A Magnet assisted segmental rotor switched reluctance machine suitable for fault tolerant aerospace applications

Sana Ullah

School of Electrical and Electronic Engineering

Newcastle University

A thesis submitted for the degree of

Doctor of Philosophy

2016

Abstract

The aerospace industry is moving towards more-electric aircraft. These electrical systems are lighter, more efficient and smaller compared to present hydraulic system. The permanent magnet electrical machine is an obvious choice to replace these hydraulic systems because of its high torque density. However for low speed applications, there are significant drag torque issues which negate some of the machine's advantages.

This thesis introduces a new permanent magnet assisted segmental rotor switched reluctance machine. This machine was first designed by using finite element software and then compared with a conventional segmental rotor switched reluctance machine, showing an increase in torque by increasing non saturation region of the stator lamination.

On this basis, a fault-tolerant permanent magnet assisted segmental rotor switched reluctance machine was designed to replace the permanent magnet machine used in the nose wheel of the aeroplane. Both two-dimensional and three-dimensional finite element analyses were conducted to analyse the dominant end winding effect.

Fault-tolerant segmental rotor switched reluctance machine was then built and tested. Static analysis was conducted to determine current-flux linkage and torque values at different rotor angles. The machine was analysed both with and without magnets to assess the effect of reverse magnetization with magnets at the stator tooth tip. Mutual inductance was also found using the same test rig. Dynamic testing of the machine was done to determine open circuit voltage and short-circuit current.

A novel pot core permanent magnet assisted inductor was also designed and compared with the conventional E-E core inductor. The magnet was used to hold the inductance of the inductor constant for high current values and the inductor was then tested to determine magnet's effect. A dominant inner loop effect was found which was proved by doing several tests.

Various recommendations were made to further improve overall performance of the machine and the inductor.

Acknowledgment

I would like to express my deepest gratitude to all those who helped me throughout this research work. Sincere thanks to my both supervisors Dr Glynn Atkinson and Dr Richard Martin for their continuous guidance throughout the development and completion of my research work.

I would like to say thanks to my parents for their backing and encouragement during this time.

Special thanks to Dr Steve McDonald for helping in Matlab.

Many thanks to all the technicians within the department.

Table of Contents

List of figures

List of tables

List of symbols and abbreviations

SRM	Conventional switched reluctance machine
SSRM	Segmental Rotor Switched Reluctance Machine
MSSRM	Magnet Assisted Segmental Rotor Switched Reluctance Machine
PM	Permanent magnet
Ψ	Flux linkage
MBI	Magnetically biased inductor
AC	Alternating current
DC	Direct current
FE	Finite element
λ	Pole pitch
t	Tooth width/thickness
FEA	Finite element analysis
3DFE	Three-dimensional finite element
2DFE	Two-dimensional finite element
MMF	Magnetomotive force (unit: Amperes.Turns)

Chapter 1 Introduction

The aerospace industry is adapting the more-electric aircraft (MEA) where some of the key hydraulic, pneumatic and mechanically actuated aircraft actuators are replaced by electro-mechanical actuators (EMA). The hydraulic actuators are heavy, inefficient and costly to maintain. By replacing them with electrical actuators, aircraft efficiency will increase and there will be a reduction in weight and improvement in quality of the system. The aerospace industry is subjected to strict safety rules, and all these replacement electrical machines must go through rigorous testing and certification before being used in any aircraft system [1]. The electrical systems found in the Boeing 787 Dreamliner require a generating capacity of 1000 KVA, with the undercarriage wheels having electric brakes [2]. The Airbus A380 [3] has electrical systems such as electrostatic hydraulic backup actuators and electrostatic hydraulic actuator.

ACTUATION2015 (Modular Electro Mechanical Actuators for ACARE 2020 Aircraft and Helicopters) is a collaborative project with 54 partners and Newcastle university is a member of this collaboration working on fault tolerant electrical drives to replace nose wheel actuators[4]. This thesis presents a new fault tolerant electrical machine designed for the nose wheel steering application of the aircraft.

Figure 1-1 shows the various systems within aeroplane which ACTUATION2015 project is investigating.

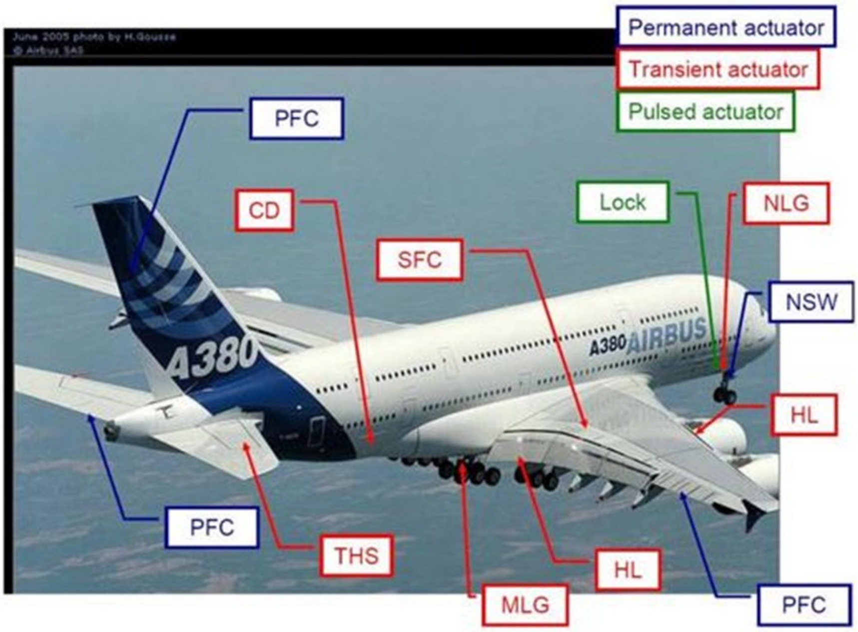
June 2005 photo by H.Gousse
© Airbus SAS

Figure 1-1: Different parts of an aeroplane with potential of replacing with EMAs [4]

1.1 Fault-tolerant electrical machine topologies in aerospace applications

Reliability and fault tolerance is the paramount requirement of all electrical systems within an aircraft. New electrical systems should be fault tolerant, with faults limited to a single component or sub systems which will not affect flight critical operations. There should be extra modules that can replace the faulty sections which results in an increase in the overall size of the system. The fault should also be stopped from propagation within a system. Thus the electrical machines that are going to replace these hydraulic systems should be fault-tolerant, smaller in size and at the same time torque-dense to reduce the mass of the system. They should have electrical, thermal and magnetic isolation between different phases. Figure 1-2 shows the development in power generation in aeroplane for the past 60 years.

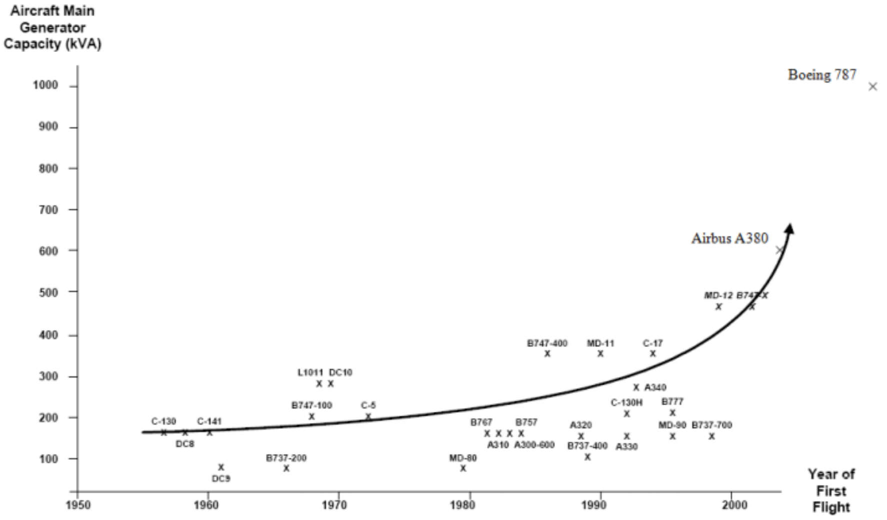

Figure 1-2:Development in power generation on an aeroplane over 60 years [5]

1.2 Candidate types of electrical machines for aerospace applications

Based on the above criteria of electrical, magnetic and thermal isolation between the lanes of the electrical machines along with the requirement of high torque/weight ratio, there are only few candidates that can qualify for the operation.

1.2.1 Squirrel cage induction machine

Squirrel cage Induction Machine (IM) is a simple cheap structure and has been used in industries for years. The disadvantage with the structure is that when fully wound, mutual interaction between phases increases. Work [6-8]has been done to improve the fault tolerant capabilities of the machine which reduces electrical and magnetic interference between phases at the expense of complicated control techniques which makes continues operation of machine possible in open circuit failure, however machine operation during short-circuit fault current is still an issue.

1.2.2 Permanent magnet machine

The permanent magnet (PM) machine could be a good option because of its smaller size and high torque density. By carefully designing with concentrated winding, the PM machine can be made fault-tolerant with a negligible effect of one phase on the next [9]. One of the basic disadvantages of the PM machines is that during short-circuit fault at lower speed, flux from the magnets induces high currents in the shorted phase which results in high drag torque. To overcome this, the healthy phase has to be overrated which leads to poor torque density [10].

1.2.3 Switched reluctance machine

The switched reluctance machine (SRM) is the best option in terms of fault-tolerant capability with a strong, robust structure with no magnets on the rotor and can withstand high temperatures. In the case of the conventional SRM, magnetic coupling occurs as the flux has to share the same stator coreback. Single tooth segmental rotor switched reluctance (SSRM) can be a good option with the flux paths shorted by small rotor segments, thus decreasing mutual coupling between two adjacent phases. Because of better electromagnetic structure, the SSRM gives 40% more torque for the same copper loss when compard to the SRM. [11].

1.3 Objectives and methodology

This thesis presents a new fault tolerant torque dense (SRM) designed for the nose wheel steering application of the aircraft to replace the PM machine. The original PM machine is a 20 poles duplex 3 phase fault tolerant machine with 230 mm outer diameter (stator outer diameter) and 20 mm stack length. The PM machine fulfils the following targets for the application requirements.

A. The starting torque should be 17 Nm or above for the complete electrical cycle.
B. The average torque should be 13.5 Nm or above at 900 rpm (rated speed).

The PM machine is able to meet the above specifications but suffers from high drag torque issues.

The objective of this thesis is to investigate the feasibility of a fault tolerant magnet-assisted segmental rotor switched reluctance machine (MSSRM) that can replace the PM machine. The new machine should have the same fixed outer diameter with considerable increase in stack length while fulfilling the required torque conditions without any drag torque issues. It also includes the design of a novel permanent magnet-assisted pot core inductor (pot core MBI) used within the drive of the MSSRM. To achieve the research objectives, the following work was conducted

1. Design of a new permanent magnet-assisted segmental rotor switched reluctance machine.
2. Comparison of the conventional 3-phase MSSRM with conventional SSRM for the same copper loss.
3. Design investigation of a fault-tolerant MSSRM based on the magnet assist idea that can achieve the same targets as that of the PM machine with considerable increase in the size and mass of the machine.
4. Investigation of demagnetisation in magnets in the fault tolerant MSSRM during fault conditions.
5. Construction of the MSSRM and testing for comparison with finite element (FE) model.
6. Development of a new pot shape inductor (Pot core Magnetically Biased Inductor (MBI)) that does not saturate early (can keep the inductance high up to high levels of current). This inductor is built, tested and used within drive of the MSSRM.
7. Recommendation for future work based on simulations and results from the experimental models.

1.4 Overview of thesis

This thesis consists of three main parts. The first part introduces a new idea of having permanent magnets at the stator tooth tip of a 3-phase SSRM. This machine was then compared with the conventional 3- phase SSRM for the same copper loss. The second part includes the design of a fault-tolerant MSSRM to replace the present PM machine used in the nose wheel of an aircraft. In the third part, a novel permanent magnet-assisted pot core inductor was investigated and manufactured which will be used in the drive to control the same MSSRM.

A brief description of each chapter is given below

Chapter 1 introduces and gives the background of the thesis. It explains the disadvantages of the heavy hydraulic systems currently in use within the aircraft. It also describes different electrical machines that can replace these hydraulic actuators. The fault tolerant capabilities of these machines are explained which have led to the investigation of the SRM for its better fault tolerant capability.

Chapter 2 discusses previous research work on SRMs and their performance. It also considers different permanent magnet-assisted SRMs and inductors along with their advantages and disadvantages. Different fault tolerant electrical drives used in the aerospace is explained.

Chapter 3 discusses previous work on different SRM topologies prior to author contribution. Different SRM topologies were compared with the existing PM machine for the same current density and outer diameter with an increase only in stack length. Final topology was chosen and three-dimensional finite element (3DFE) analysis of the machine was conducted to assess the dominant leakage inductance.

Chapter 4 introduces the magnet assist concept on the basis of which a 3-phase MSSRM was compared to a conventional 3-phase SSRM for the same copper loss using finite element analysis (FEA) software.

Chapter 5 considers the introduction of idea of magnet assistance to the fault tolerant SSRM which shows significant potential improvements in the machine performance.

Chapter 6 investigates the MSSRM to assess demagnetisation of the magnet during fault conditions and considers manual optimization technique used to improve performance of machine. Both two-dimensional finite element (2DFE) and three-dimensional finite element (3DFE) analyses were conducted to investigate end winding effect.

Chapter 7 describes the construction of the MSSRM and pot core inductor along with different test rigs to evaluate the machine.

Chapter 8 shows the concept and development of the magnet assisted pot core MBI.

Chapter 9 shows the testing of the MSSRM. The machine was tested with and without magnets to observe the effect of magnets on the stator core. Flux linkage-current, torque, mutual inductance waveform and cogging torque were obtained by using static test rig. Open circuit voltage and short circuit current waveforms were obtained by using the dynamic test rig. It also shows the testing of the permanent magnet-assisted pot core inductor.

Chapter 10 shows the conclusion of the present research and suggests future work that can be done to improve both the fault tolerant MSSRM and pot core MBI based on the practical results gained during testing of these devices.

1.5 Contribution to knowledge

The following contributions to knowledge are made in this study;

1. Introduction of magnets into the conventional SSRM, which results in an increase in the torque density of the machine by reverse-magnetizing the stator core.
2. Development of a fault tolerant MSSRM based on the above idea to design a fault tolerant MSSRM to replace the PM actuator used in the nose wheel of the aircraft.
3. Constructing and testing of the fault tolerant MSSRM with and without magnets to assess the effect of the magnets on the stator core with the introduction of magnets to it.

4. Designing a novel pot core shape MBI which will be used in the drive of the MSSRM. Magnets were introduced to the inductor which results in keeping the inductance higher up to high levels of current by the reverse magnetization of the inductor core.

1.6 Published work

The following publication have stemmed from this work;

1. S. P. McDonald, G. J. Atkinson, D. J. B. Smith, and S. Ullah, "Overcoming the challenges of drag torque in a dual-lane actuator for an aircraft," in *Electrical Machines (ICEM), 2014 International Conference on*, 2014, pp. 2120-2126.
2. S. P. McDonald, G. J. Atkinson, D. J. B. Smith, and S. Ullah,“Magnetically biased inductor for an aerospace switched reluctance drive” *in IEMDC 2015, international conference(in Press)*

A series of journal publications are currently being written for submission in early 2016.

Chapter 2 Literature review

2.1 Introduction

This chapter considers previous work on the development of the SRM. The basic working principle and the way its structure has developed over the years to improve performance are discussed. Different types of inductors are considered and the advantages of using magnets in inductors to improve performance are explained. At the end different types of fault tolerant drives used within aerospace are discussed.

2.2 Switched reluctance machine

The first switched reluctance machine (SRM) was built by Davidson in 1838 and used to propel a locomotive on the Glasgow-Edinburgh railway. The essential features of the modern SRM were described by Bedford and Hoft in 1971 and 1972 in two US patents [12, 13].

2.2.1 Basic structure and working principle of the SRM

The SRM is a simple, low cost, robust, rugged structure and is able to perform in harsh environments. This makes it a serious contender to be used in most household, electrical vehicles and aerospace applications [14]. The SRM is a variable reluctance stepping machine that is designed to efficiently convert electrical energy into mechanical energy and vice versa. It belongs to the class of machines that depends upon variation in magnetic reluctance to produce torque. SRMs have rotor and stator which are both salient and are hence it is classed as doubly salient. The stator and rotor are made of laminated iron. The rotor is a brushless toothed structure with no windings; all windings are on the stator. Because it has no windings in the rotor, the rotor's losses are very low and it can be very strong enough to allow high speed operation. Figure 2-1 shows the structure of a conventional 3-phase 6/4 SRM.

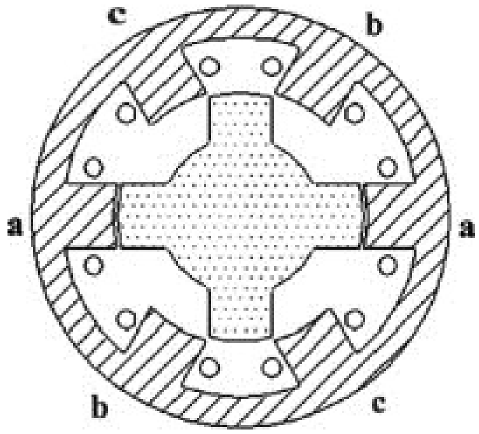

Figure 2-1: Conventional 3-phase 6/4 SRM

DC pulses of current are passed through each phase and as the flux tries to find the path of least reluctance for magnetic circuit to be completed, the rotor is pulled towards the flux region where maximum flux can flow through the rotor back to the stator, hence torque is produced. The greater the area between the aligned and unaligned inductance, the greater will be the torque produced by the machine. Figure 2-2 shows useful area between the aligned and unaligned flux linkage value.

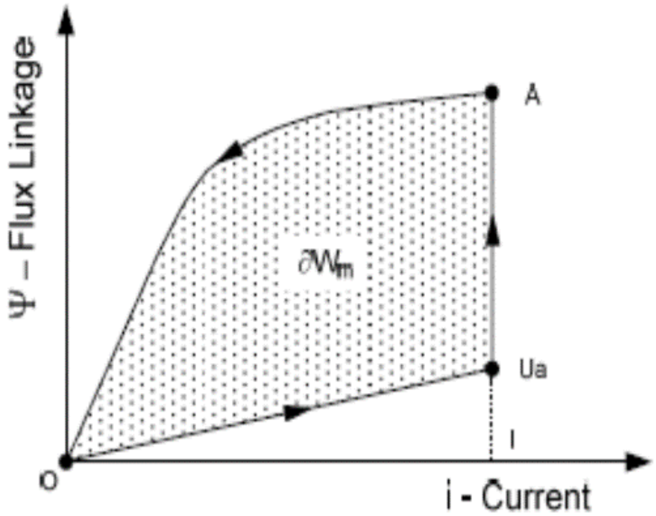

Figure 2-2: Useful working area between aligned and unaligned flux linkage [15]

The input power equation of an SRM can be written as

$$P = T\omega + i^2R + \frac{d}{dt}\left(\frac{1}{2}Li^2\right) \tag{2-1}$$

Where P is the input electrical power, Tω is the output mechanical, i^2R is the copper loss, $\frac{d}{dt}(\frac{1}{2}Li^2)$ shows rate of change of magnetic energy. By differentiating the last part of the equation, the final equation can be written as:

$$P= T\omega + i^2R + \frac{1}{2}\ i^2\frac{dL}{dt} + Li\frac{di}{dt} \tag{2-2}$$

The phase voltage equation can be written as

$$V= i\ R+ \frac{d}{dt}(Li) \tag{2-3}$$

By multiplying equation (2-3) with i (current in phase) and differentiating the last term, equation (2-3) can be written as

$$Vi= i^2R+Li\frac{di}{dt}+i^2\frac{dL}{dt} \tag{2-4}$$

By equating equation (2-2) and (2-4), the torque equation can be found given as

$$T = \frac{i^2}{2}\frac{dL}{d\theta} \tag{2-5}$$

2.3 Previous work done on the machine improvement

The SRMs are easy to construct because of their simple structure, however, the machine has following drawbacks

1. high torque ripple
2. high acoustic noise
3. low torque density

A lot of work has been done to overcome the above disadvantages in the machine.

The torque ripple of the SRM can be reduced by increasing the pole numbers[16] and in some cases this can almost double the output torque at certain speeds for the same losses [17]. Recent work by Widmer [18] shows a significant decrease in torque ripple by using a 6- phase switched reluctance machine. All these machines have the advantage of shortening the magnetic flux path, which decreases overall core losses and leakage flux. The disadvantage with such high phase machines is the use of more power switches hence increasing the overall size of the inverter. Figure 2-3 shows the inverter and machine structure of the 6 phase SRM.

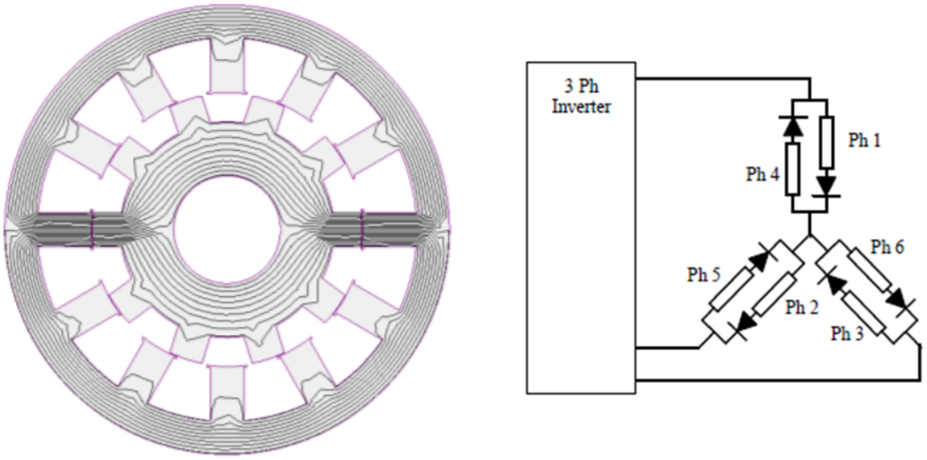

(a) **(b)**

Figure 2-3: (a) 6 phase 12-10 SRM [18] (b) 3 phase full bridge converter to drive 6 phase SRM [18]

Average torque per revolution for the conventional SRM is given by equation (2-6)

$$T=\frac{m*N_r}{2\pi}*\text{w} \tag{2-6}$$

Where m the number of phases, $\mathrm{N_r}$ is the number of rotor poles, W the energy converted into work which depends on the area between the aligned and unaligned inductance. It is clear from equation (2-6) that average torque can be increased by increasing the number of rotor poles. Desai et al [15, 19] worked on increasing the pole numbers in the conventional SRM. The number of rotor poles were made greater than stator pole which increased the average torque by 119% percent. Machines were tested with configurations of 6/8 (6 stator poles and 8 rotor poles) and 6/10. The reason for the increase in average torque in this case was the higher number of stokes per revolution resulting from an increase in the rotor pole numbers. 6/8 and 6/10 configurations gives smaller areas of aligned and unaligned inductance but increase the number of stokes per revolution, thus increasing the overall torque of the machine.

The disadvantage with such machines is that, as the rotor pole number increases, the electrical frequency of the stator also increases which results in an increase in the iron losses at higher speeds.

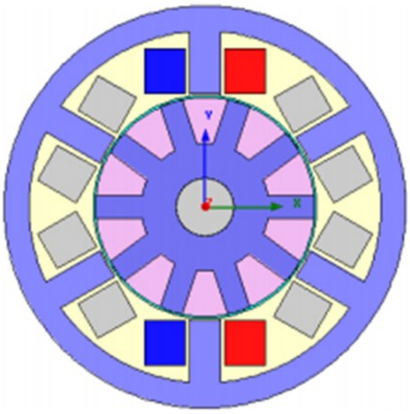

Figure 2-4: 6/10 SRM [19]

Acoustic noise is a big problem which prevents SRM from being used in many applications. This is because of high radial forces in the airgap. Although a lot of work has been done to study acoustic noise and the reasons for it [20-22], further work needs to be done to reduce overall noise of the machine.

Mecrow [23, 24] used a fully pitched switched reluctance machine to use the mutual inductance of phases rather than self-inductance for the rotation of the machine. Each slot in this case is available to only a single winding of a single phase rather than being shared by the adjacent phase. This results in an increase in magnetive motive force (MMF) per phase for given copper loss, which results in 9% increase in the output torque of the machine as compared to the conventional SRM with the concentrated windings. The disadvantage with such machine is that the end winding length of the conductor increases, which significantly increases the overall mass of the SRM. Mecrow found an overall 44% increase in the mass of copper compared to the conventional SRM with concentrated winding while the resistance per phase almost doubled.

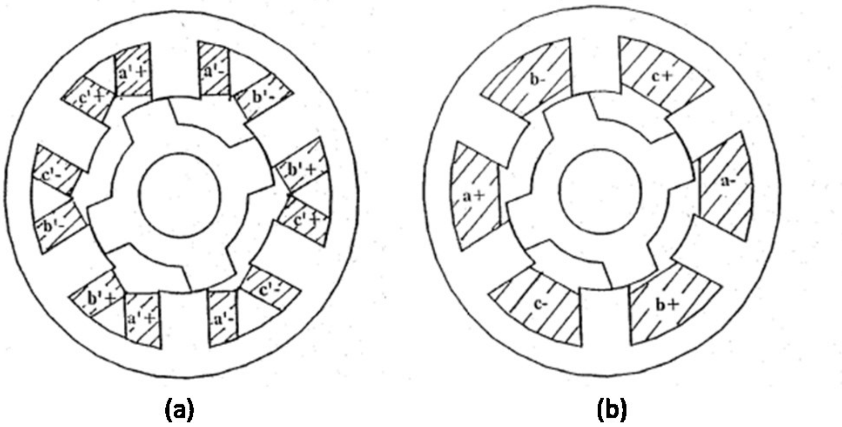

Figure 2-5: (a) Conventional SRM with concentrated windings (b) Conventional SRM with fully pitched winding [23]

2.4 Permanent magnets in SRMs

Magnets have been used in SRMs to increase the overall efficiency of machine. Lipo[25] used magnets in the stator coreback to increase field weakening performance. At higher speeds, the current cannot reach its peak value because of higher back- EMF and less time for the current to reach its rated value. By placing magnets in the stator, the flux linkage of the coil is increased specially at the aligned position which results in an increase in the torque at higher speeds. However, this will decrease the torque in constant torque region because magnets at the coreback act as an extra air gap for the flux from the main coils to flow which can decrease the inductance of the machine at aligned position. Figure 2-6 shows Lipo's SRM with magnets in the stator coreback.

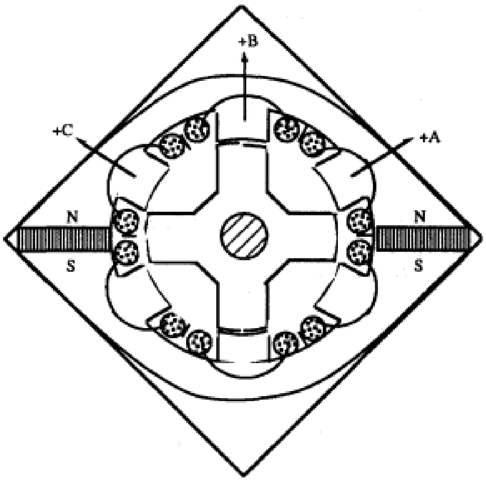

Figure 2-6: Conventional SRM with magnets in the stator [25]

Hasegawa [26] used permanent magnets along with auxiliary windings to improve the torque density of the machine. A DC current was passed through the auxiliary windings which act as an extra source of magnetic flux, but at the same time stator structure was made in such a way that flux from the main coils could flow through the stator coreback by using the area around which auxiliary windings are wound. This helps in avoiding most of the flux leakage caused by magnets when the main coil flux flows through it. Drawbacks of the model are that half of the flux still flows through the magnet which results in flux leakage as the magnets act as an extra air gap and also an extra power supply will be required to supply the DC current into auxiliary windings. It was shown that efficiency was improved by 3% while the torque was improved only up to 3 amps. Figure 2-7 shows the SRM structure with magnets and auxiliary windings in the stator.

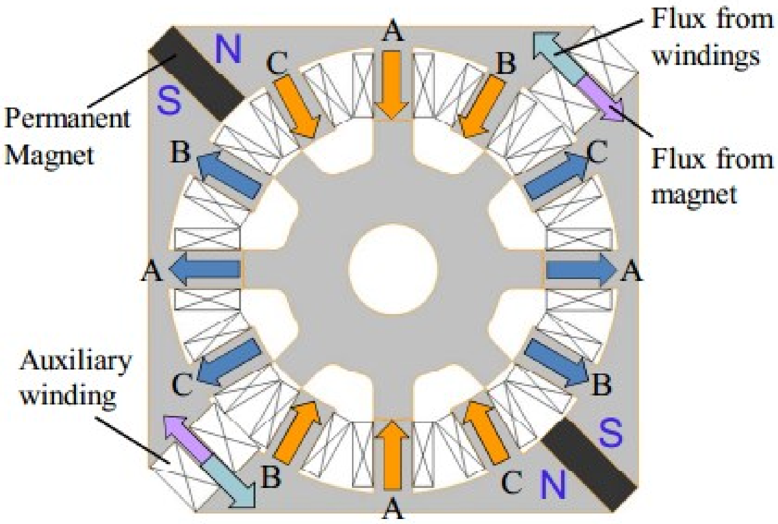

Figure 2-7: SRM with auxiliary windings and magnets at stator coreback [26]

Nakamura [27] used ferrite magnets in the stator coreback of a switched reluctance generator. No external excitation current was used as flux from the magnets provided the excitation flux. Three stacked stator structures were used which were mechanically shifted at certain angle. The results show that the efficiency of the generator was 90% percent along with an overall cheap price and greater simplicity in the generator.

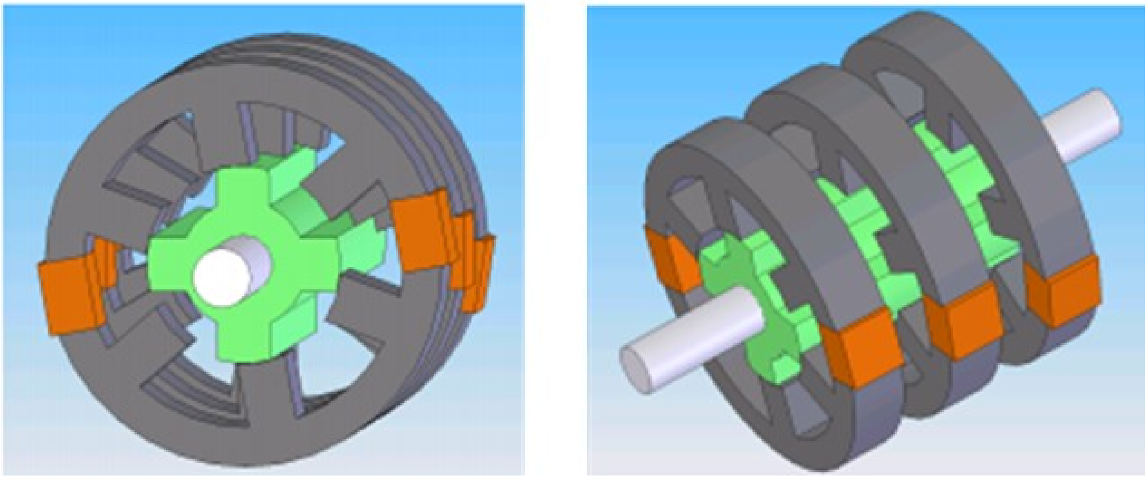

Figure 2-8: SRM generator with ferrite magnets on the stator [27]

Nakamura [28] also designed an SRM with magnets placed at the tooth tip. It was mentioned that the overall torque of the SRM with magnets increased by 25% compare to the conventional SRM of the same size and current density. Demagnetisation of the magnets and losses in magnets at higher speeds were not mentioned which can increase significantly at higher speeds with high currents.

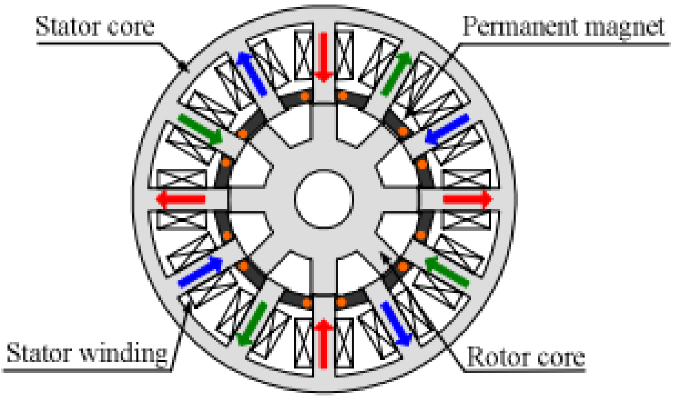

Figure 2-9: SRM with magnets at tooth tip [28]

Andrada [29] presented a new hybrid electric motor with magnets placed at the stator tooth tip. The stator is made of independent magnetic segments with magnets at the tooth tip which are short-circuited by the stator segments. The new hybrid reluctance motor was then compared with two SRMs (6/4 and 12/8 configuration) at 3000 rpm. Andrada’s comparison showed that the new machine has higher efficiency compared to other conventional machines. However, it was clear from his investigation that the other machines were smaller in size with bigger air gaps which could be the reason of having less torque, thus decreasing the overall efficiency of the other two conventional SRMs.

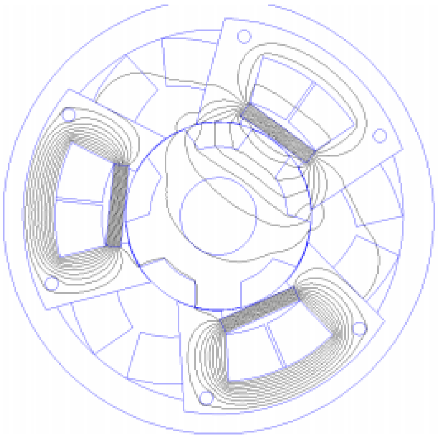

Figure 2-10: New hybrid reluctance motor [29]

Jeonwong [30] introduced the idea of stator common poles in SRMs in which magnets were placed. Flux from the magnets flows in the same direction as that of the adjacent active phase (Phase around which coil is wound). Theses magnets assist the flux from the main coils which results in an increase in aligned inductance of the active phase. Disadvantage with this structure is that magnet flux always uses the rotor poles to complete the magnetic circuit which can results in an increase cogging torque. Also this type of SRM is not suitable for high stator rotor pole combination because of common stator poles, the slot area will decrease significantly which will reduce the MMF of the machine for a given copper loss.

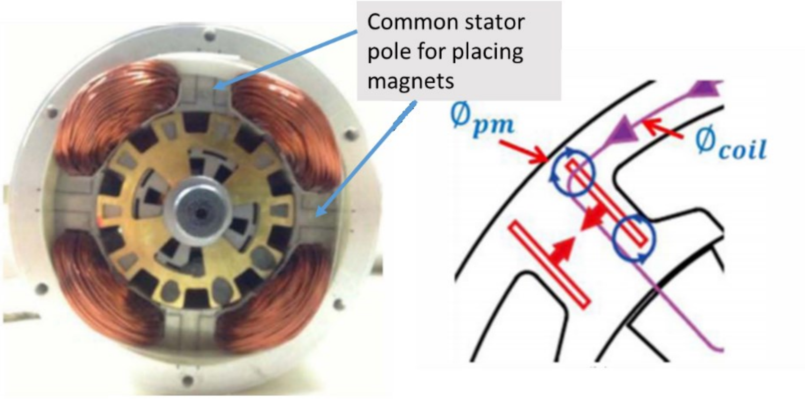

(a) (b)

Figure 2-11: (a) SRM with common stator poles having magnets (b) Magnetic path of both magnets and coil flux[30]

2.5 Segmental rotor switched reluctance machine

The segmental rotor switched reluctance machine (SSRM) is another form of SRM that has a rotor made of small segments rather than the single rigid body in conventional SRM. Horst introduced first segmental rotor design which was limited to 2 phases with unidirectional operation [31].

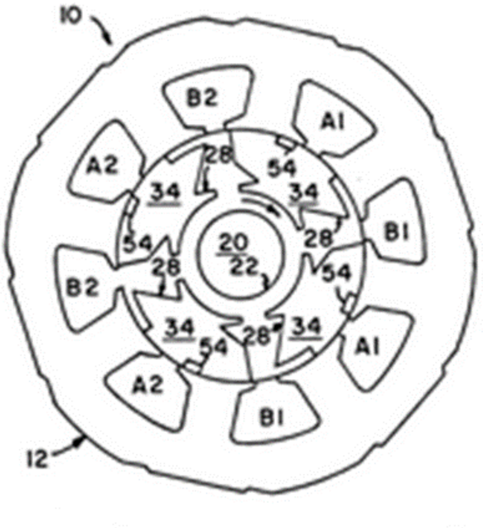

Figure 2-12: Horst's unidirectional segmental rotor design[31]

The design rules of SSRM have been fully detailed by Mecrow [11, 32, 33] who was able to develop design rules for both fully-pitched and single tooth concentrated winding SSRMs. The output torque of the SSRM was increased by 40% compared to conventional SRM for the same copper. This was because of the better magnetic utilisation of the magnetic circuit, having higher aligned inductance while keeping the unaligned inductance low. The small flux paths results in a decrease in the iron losses of the machine along with low leakage flux. Just like the conventional SRM, the problem with fully pitched winding of MSSRM is that the length of the end windings increases significantly which increases the mass and almost doubles the copper loss. [34].

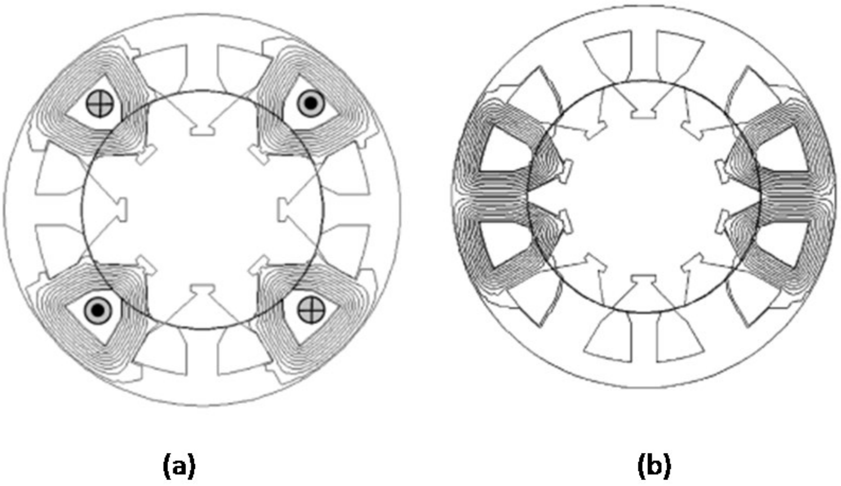

Figure 2-13: (a) Fully pitched winding SSRM and (b) Single tooth concentrated winding SSRM [35]

Problems with the SSRM design occurred during the construction where steel wedges were used to hold the rotor structure with in the shaft. This can result in extra eddy current losses within the steel wedges even though they are far away from the air gap. The mechanical strength to hold the segments can decline also as the speed of the rotor increases.

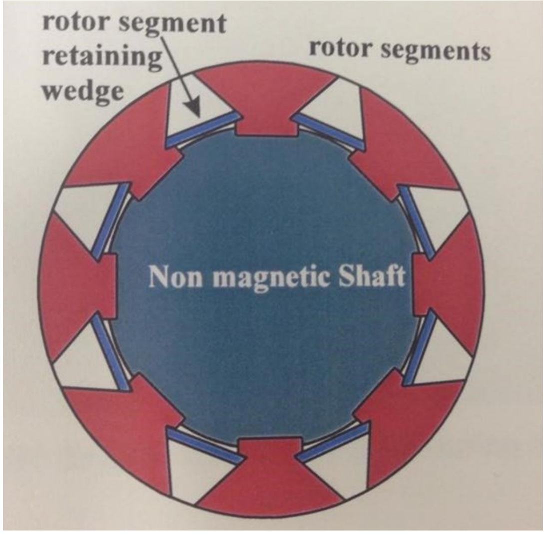

Figure 2-14: Rotor segments connected to the shaft by steel wedging [34]

As mentioned above, the rotor of SSRM consists of small segments, so it is important to place these within a mechanical structure with low permeability in order to avoid high unaligned inductance along with the extra iron losses in the rotor holding structure. Oyama [36] developed the construction process by placing these segments in aluminium structure.

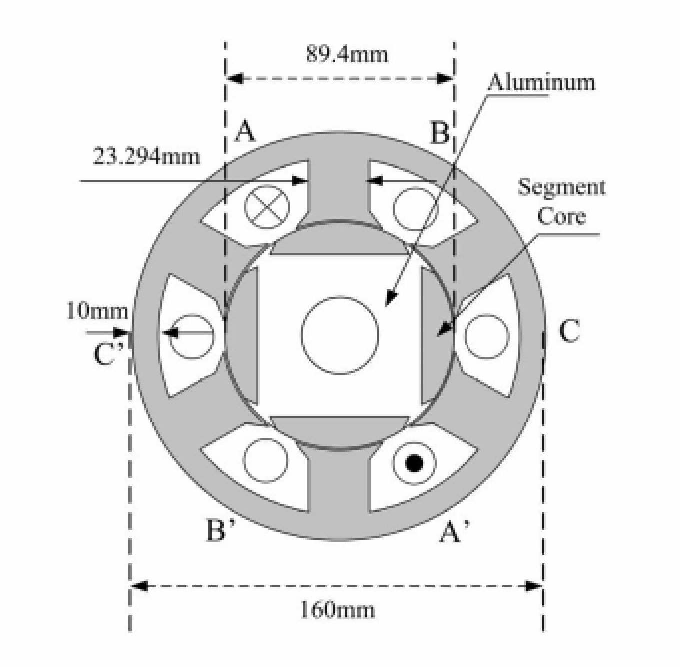

Figure 2-15: Segmental rotor SSRM placed in aluminium block [36]

The structure shows that the rotor teeth are quite large compared to those in Mecrow's SSRM. This may result in a very high unaligned inductance which can result in a decrease in the overall output torque of machine. Also the aluminium block is extended up to the air gap, it can result in an increase in eddy current losses with in the rotor holding structure.

Widmer [37] worked on increasing the pole number of SSRM to increase the average torque of the machine. A full pitched SSRM was designed with a stator and rotor pole combination of 12/16. This resulted in a 25% increase in the average torque compared to the conventional 12/10 SSRM for the same copper loss. The increase in average torque was due to increase in the number of stokes per revolution. The disadvantage of such structure is that, as the pole numbers increases, stator frequency also increases which results in almost doubling the iron losses at higher speeds.

Vandana [38] proposed a circular slot fully pitched SSRM. It was claimed that the machine performance increased by 27% compared to a conventional SSRM for given MMF. However the structure shown will greatly decrease in the slot area compared to the conventional SSRM which can result in high current density and thus high copper losses.

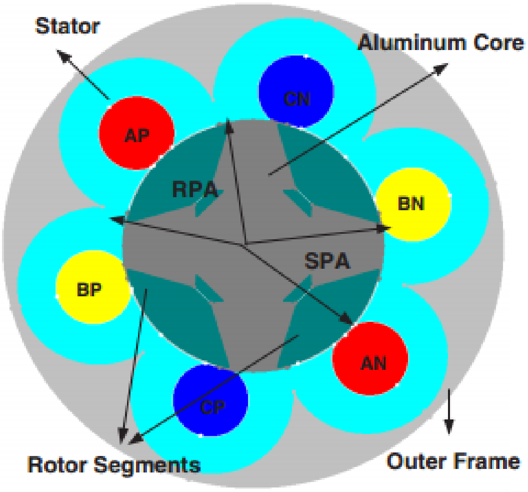

Figure 2-16: Circular slot fully pitched SSRM [38]

Widmer [39, 40] designed and built an 80kW SSRM and compared its performance with the PM machine used in the Nissan Leaf [41]. It was found that the SSRM size and mass should be increased by 30% to get the same torque performance as that of the Nissan Leaf's PM machine. However, the advantage of not having magnets within the SSRM makes it less expensive compared to other machine.

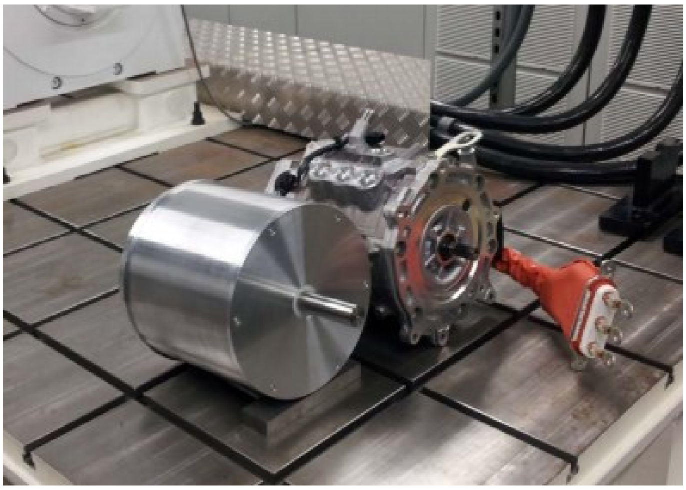

Figure 2-17: SSRM and Nissan Leaf (Interior Permanent Magnet machine)

All of the above work shows that both conventional SRMs and conventional SSRMs can be good alternatives to PM machines and IM with the advantages of low cost, simple structure and ease of construction. The structure of the machine is improved significantly throughout the years which makes it a suitable candidate for torque dense applications.

2.6 Inductor

A new type of inductor is proposed in this thesis with magnets inside it (Magnetically biased inductor (MBI)) to reverse bias the inductor core to avoid it becoming saturated earlier. This inductor will be used along with DC link capacitor to reduce current ripple in SSRM drive system. This new MBI inductor was simulated and then tested.

The MBI was first introduced in the 1960's but very few relevant studies have been published[42]. However it has recently received attention because of its advantages and the availability of advanced materials such as soft magnetic composites (SMC) with better three dimensional magnetic qualities.

Fujiwara [43] and Robel [44] introduced inductors with magnets placed in the air gap of the core. The results show an increase in 30% reduction in copper compared to a conventional inductor. However, there are three disadvantages with such structures. First is that the main flux has to pass through the magnet which is placed in the main core around which creates an extra air gap. Second is that the magnet comes in the path of external magnetic field of the coil which can demagnetise the magnet. Third is that the coil is wound around the magnet and at higher temperatures, the magnet can demagnetise easily because of higher temperature of the coil.

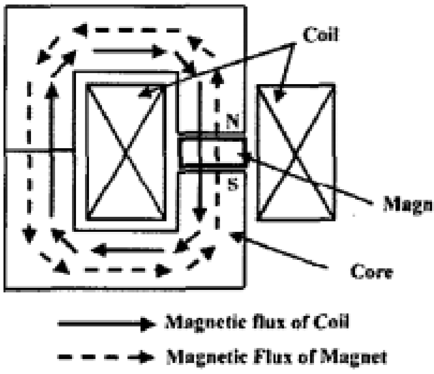

Figure 2-18: Fujiwara's choke with magnet in the centre of gap of core[43]

Aguilar [45, 46] introduced magnets into the centre core with coils on each side of the E-E core, thus avoiding the magnets being positioned in the path of the main coil flux. This also helps avoid demagnetisation. The results showed a 50% reduction in core volume compared to the conventional E-E core. The problem with such a structure is that most of the flux from the magnet gets short circuited as magnets are closer to each other. The response of inductor is very nonlinear and two coils are used instead of one which will increase the volume of the inductor.

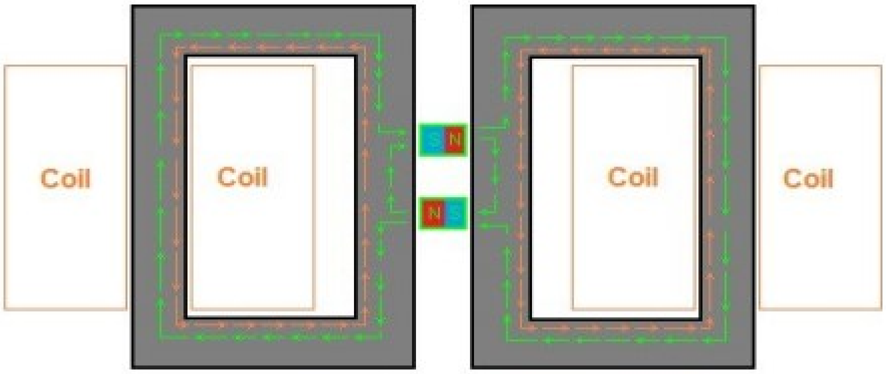

Figure 2-19: Aguilar's MBI with magnets fitted in middle of core[45]

Shane introduced magnets into core with magnet on the side of the main core [47, 48]. Again there is 50% reduction in mass of inductor. However, this design requires unconventional inductor cores with extra space for the magnets to be placed within the core.

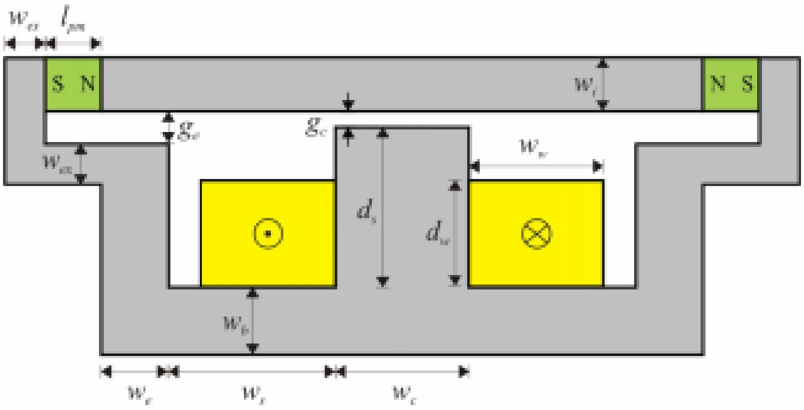

Figure 2-20: Shane's Permanent magnet assisted inductor with magnets at the side of core [48]

All the above work shows that a permanent magnet-assisted inductor can be a good option to replace conventional core inductors to reduce mass and copper loss. This is very important in aerospace applications where reduction in mass and at the same time high performance are very important.

2.7 Fault tolerant drives in aerospace applications

As discussed in the previous chapter, there are few candidates for aerospace applications in terms of fault tolerance characteristics of these machines. Krishnan did software based comparison of SRM, IM and PM[49]. PM was found to be the most torque dense among the three with SRM following. SRM has high degree of fault tolerance and can withstand high temperatures. At high temperature SRM has the best performance as PM machine magnets demagnetise with IM to be the least efficient.

Based on the rules set in [50] for a fault tolerant PM machine, Haylock designed a fault tolerant PM machine for the fuel pump applications [51]. PM machine was tested for different common fault conditions which can occur during the operation of the drive. The drive was tested and shown that remaining healthy phases continued to work and remain unaffected by short phase. It was shown that healthy phases continued to provide the target torque even under different fault conditions.

Bennett [52] worked on to replace centralized dual hydraulic motor used to control symmetry and position of the flaps and slats with individual actuators at each flap surface. Such approach helps in controlling each flap individually with the reduction of mass (by removing shaft, hydraulics and pipework). Figure 2-21 shows test rig for flaps control.

Figure 2-21 Full twin flap test rig [52]

Atkinson [53, 54] worked on electrical fuel pump to replace hydraulic mechanical pump. The advantage of electrical system is the removal of mechanical gear box along with independent control on fuel pump allowing precise fuel delivery to the engine according to its conditions. This electrical system consisted of a 4 phase fault tolerant PM machine with electrical isolation maintained up to power electronics side having 4 independent phase modules. The machine was able to run up to 30,000 rpm with significant amount of work done on design of stator to avoid high rotor loss due to non-synchronous fields because of concentrated windings [55]. Figure 2-22 shows 4 phase fault tolerant PM machine.

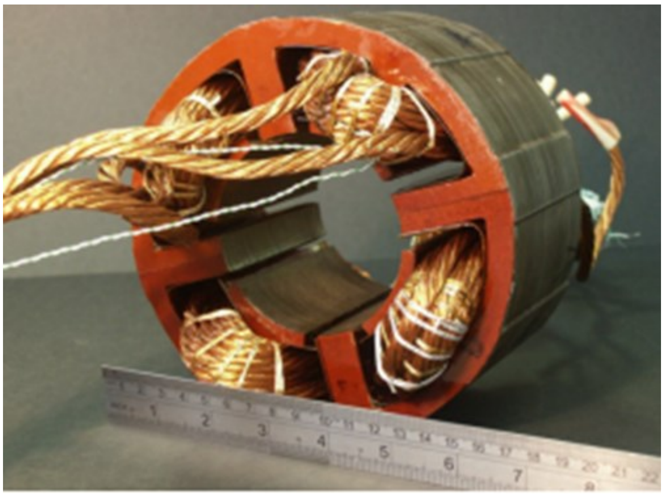

Figure 2-22: Fault tolerant 4 phase PM machine stator [55]

Bennet also worked on a dual-lane controller used to control a fault tolerant PM motor developed by Goodrich Actuation Systems [10]. During fault conditions, either half motor can provide rated torque. A dual–lane power converter was designed and manufactured for this actuator. During normal operation, both drives are simultaneously on. During single fault conditions, the failed lane can be disabled with motor providing torque by getting current from the active safe lane.

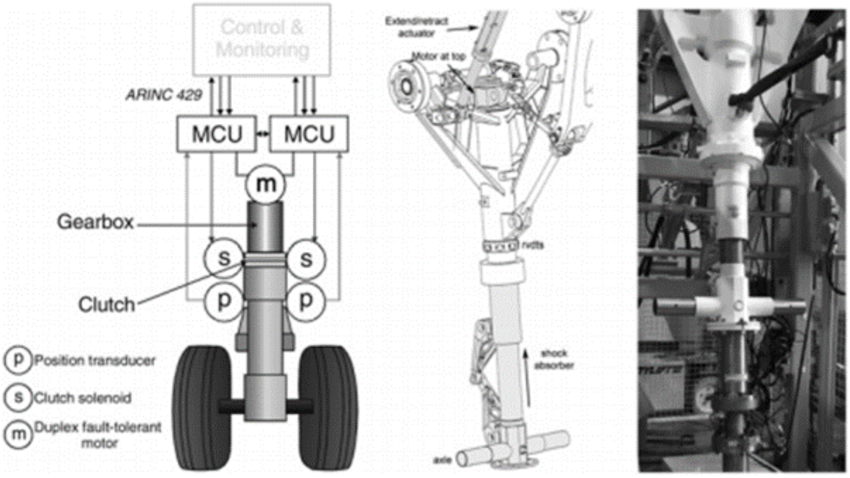

Figure 2-23: Prototype nose wheel steering actuator [10]

Dusek [56] worked on the slot pole combination of the permanent magnet machine for aerospace application. It was found that high slot pole combination results in improving the efficiency at the expense of decreasing the fault tolerant capability compared to the low slot pole combination.

Kakosimos [57] compared IM and PM machine for aerospace applications. It was found that IM efficiency is low at lower speeds because of high end ring resistance while PM efficiency decreases at higher speeds because of field weakening. It was shown that PM machine has better fault tolerant capability compared to IM. At the end, PM machine was favoured for aerospace applications. Figure 2-24 shows the testing of both IM and PM machines.

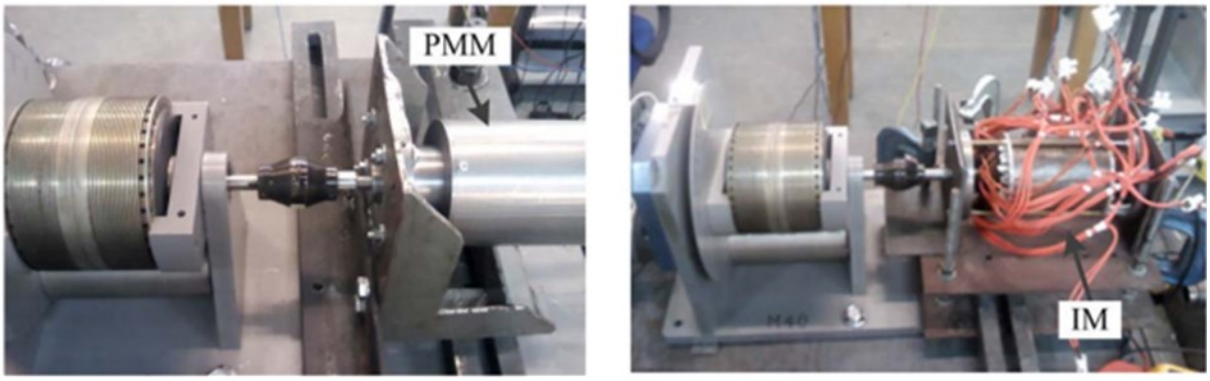

(a) **(b)**

Figure 2-24: (a) Kakosimos's PM machine (b) Induction machine

Galea [58] designed a PM machine with a full-Halbach array on the rotor. Different methods were used to enhance the performance of the machine. The machine was able to produce peak torque density of 65Nm/kg at the peak load conditions. Figure 2-25 shows the testing of PM machine.

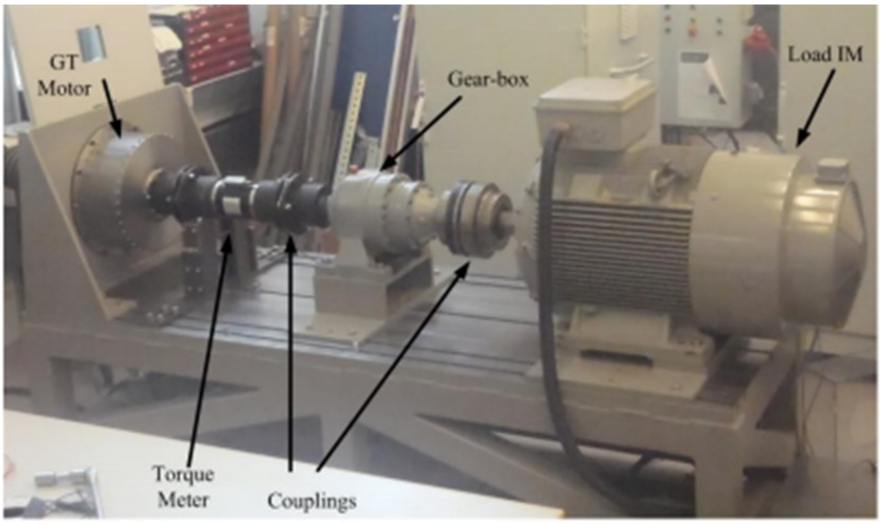

Figure 2-25: Galea's PM machine for the wheel of an aircraft

Villani designed a 5 phase PM machine for aircraft flap actuator. The machine was able to produce required torque even with failure of one or two phases under different conditions with the expense of increase of drive size because of high number of phases [59]. Figure 2-26 shows Villani's 5 phase PM machine.

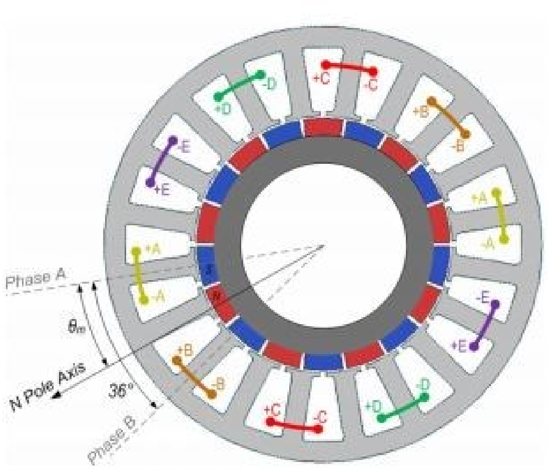

Figure 2-26: 5 phase 18 poles PM machine [59]

Richter [60-62] worked on SRMs for aerospace applications in terms of its fault tolerance performance . To overcome slight interference between different phases in conventional SRM, a spacer tooth was introduced. This does help in avoiding thermal and electrical contact between different phases at the expense of reducing electrical loading as some of slot area is occupied by the spacer tooth which results in decreasing the output torque of the machine.

Villani also designed a 5 phase SRM used for flap actuator of medium size aircraft. The work shows that the machine can provide required torque even with the failure of one or two phases [63]. The machine was not compared with PM machine of the same size. Figure 2-27 shows Villani’s 5 phase SRM.

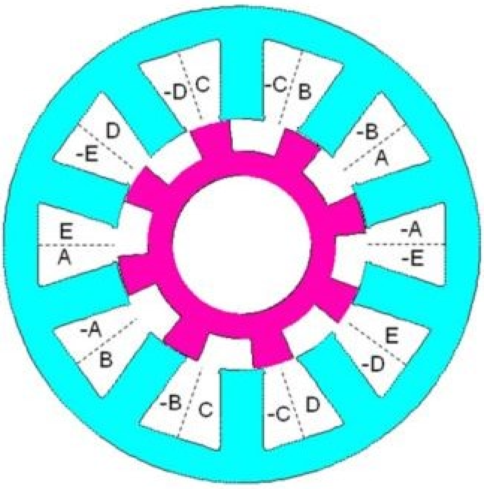

Figure 2-27: 5 phase 10/8 SRM [63]

2.8 Conclusion

The literature survey shows the previous work that has been done to improve the performance of SRM. Working principle and drawbacks of the structure is explained. The used of the magnets in the stator coreback improves the field weakening performance of the machine. The structure of the SRM was improved by using the segmental rotor design. This results in improving the electromagnetic structure of the machine and hence increasing the torque of the machine for the given copper loss. Previous work on magnet assisted inductors is also shown which decrease the copper loss and mass of the core to 50% compared to conventional E-E cores. At the end, work done on different fault tolerant drives used in aerospace is explained which shows the gradual increase in use of the electrical machines in the aerospace industry.

Chapter 3 Development of magnet free machines for aerospace applications

3.1 Introduction

This chapter outlines previous work on the development of magnet free machines for aerospace applications. This previous work sets the application in which the MSSRM topology which is described in chapter 4 has been applied. A permanent magnet machine was developed for an electric nose wheel steering application. This machine was compared with various SRM topologies by Smith [64] on the EU funded Actuation2015 (A2015) programme. Initially 2DFE analysis was conducted to compare different topologies and then 3DFE analysis was conducted to investigate end winding effect and leakage inductance. During the course of this A2015 programme, it became clear that SSRM topology would be highly suitable for aerospace applications. By way of background a summary of the A2015 work is included.

3.2 Disadvantages of the PM machine

Actuators for more electric aircraft are mostly based on the PM machines because of their high torque density. Adoption to dual lane multiphase topology is important for high reliability of these actuators. This makes both the machine and power electronics redundant to increase the reliability of the machine.

During the fault conditions, the healthy phase uses 40% extra current (above the rated current) to overcome the drag torque because of the magnets within the rotor in the PM machine [10, 64]. This significantly reduces the overall reliability of the PM machine because of overheating of the healthy phases and negates its high torque density advantage. This moves us towards those machines having good fault tolerant performance without having drag torque issues.

Synchronous wound field machines can be discounted due to the increased failure modes caused by a wound field, increased complexity in adding a dual lane structure to the field winding and increased drive components require to supply the field winding.

Induction motors (IM) can be wound for multiphase operation which would allow dual lane operation, however when fully wound there is significant coupling between lanes, which would not permit their use as a fault tolerant actuator. Winding designs with low coupling are possible but they result in a lower electric loading of the actuator and compound the already poor power density of induction machines with respect to PM machines.

SRM can be a good option with higher torque density compared to IM and at the same time less coupling between all phases. Initial investigation to the design of new SRM was done with certain design constraints which help in effective fault tolerant of the topology.

3.3 Fault tolerance

In order to act as a direct replacement for existing PM actuators, the new switched reluctance designs must meet the following constraints

3.3.1 Electrical isolation

To achieve electrical isolation there must be no electrical connection between power lanes or risk of a connection being made during fault. To achieve this drive modules, connections and coils for each power lane are physically separated by a spacer tooth and nonmagnetic spacers in the end winding regions.

3.3.2 Thermal isolation

To achieve thermal isolation, the thermal conduction paths between power lanes must be minimised. Spacer tooth acts as a thermal barrier between adjacent windings due to their low thermal resistance from coil to coreback as a good thermal path for faulted phase.

3.3.3 Magnetic isolation

Both power lanes must exhibit minimal mutual coupling to limit the power transfer between power lanes and prevent interaction between fault currents and active lane currents. Spacer teeth and concentrated winding single tooth arrangement are known to minimise coupling to a few percent (3%) of coil self-inductance [51, 65].

3.3.4 Unbalanced magnetic pull (UMP)

Unbalanced magnetic pull occurs when the radial magnetic forces on the rotor do not sum to zero at any particular operating point, resulting in a rotating or oscillating force on the rotor and stator that can increase bearing wear and create mechanical vibration and noise. This effect is caused by the arrangement of the stator windings, and is minimised by ensuring that each phase has winding symmetrically opposite to each other on the stator and the sum of the MMF along axis of magnetic alignment is zero.

3.4 Switched reluctance machine topologies

Three inherently fault tolerant SR motor topologies and one arrangement of two single lane, simplex motors in series on the same shaft have been investigated. All these machines have the same current density as that of the PM actuator with fixed outer diameter while stack length was altered to get the required torque as that of the PM actuator. Thin non-oriented silicon steel (NO2O) used in both stator and rotor with 20mm lamination thickness. The proposed SRM topology should be able to provide the following torques in two different conditions:

1) Stand still condition- where the required rated torque should be above 17Nm. As the SRM have high torque ripple, the lower value of the torque ripple must be above 17Nm throughout the complete electrical cycle of the machine. The SRM topologies were investigated around this point as the machine saturates at high current densities to achieve this rated torque with high leakage inductance.
2) At 900 rpm- where the average torque of the machine should be equal or above 13.5Nm.

3.4.1 Dual lane toothed SRM topology

Richter [66] proposed a dual lane magnetically isolated SRM for fault tolerant applications. The motor includes spacer teeth to give electrical and thermal isolation. A 16-10 (16 stator poles and 10 rotor poles) machine was presented with 4 spacer tooth. The spacer teeth results in a reduction of electrical loading of the machine, which results in lower torque density.

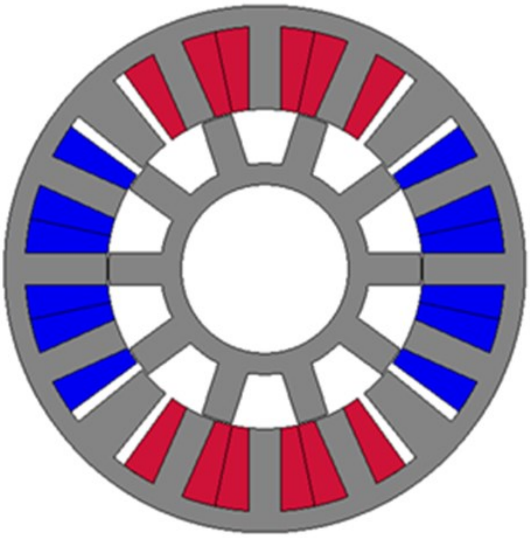

Figure 3-1: The proposed dual lane 16-10 toothed SRM with space teeth to fully isolate power lanes. Blue colour shows Lane 1 and red colour shows Lane 2

3.4.2 Two Simplex SRMs on same shaft

Rather than attempt to combine two isolated power lanes into a single stator SRM– an alternative arrangement is simple two standard, single lane SRMs in series on the same shaft. This simplex arrangement consists of two machines, both rated to give the required rated torque. Each motor is then fully utilised electrically by its respective drive and can be expected to achieve the best torque density possible. The main drawback of this design is that it will have twice the end winding length than a single, dual lane motor, which will become prohibitive to its selection for actuators of short axial length or with large winding areas. Stack length increases further as there should be a gap between the two machines to get magnetic isolation between coils of the two machines.

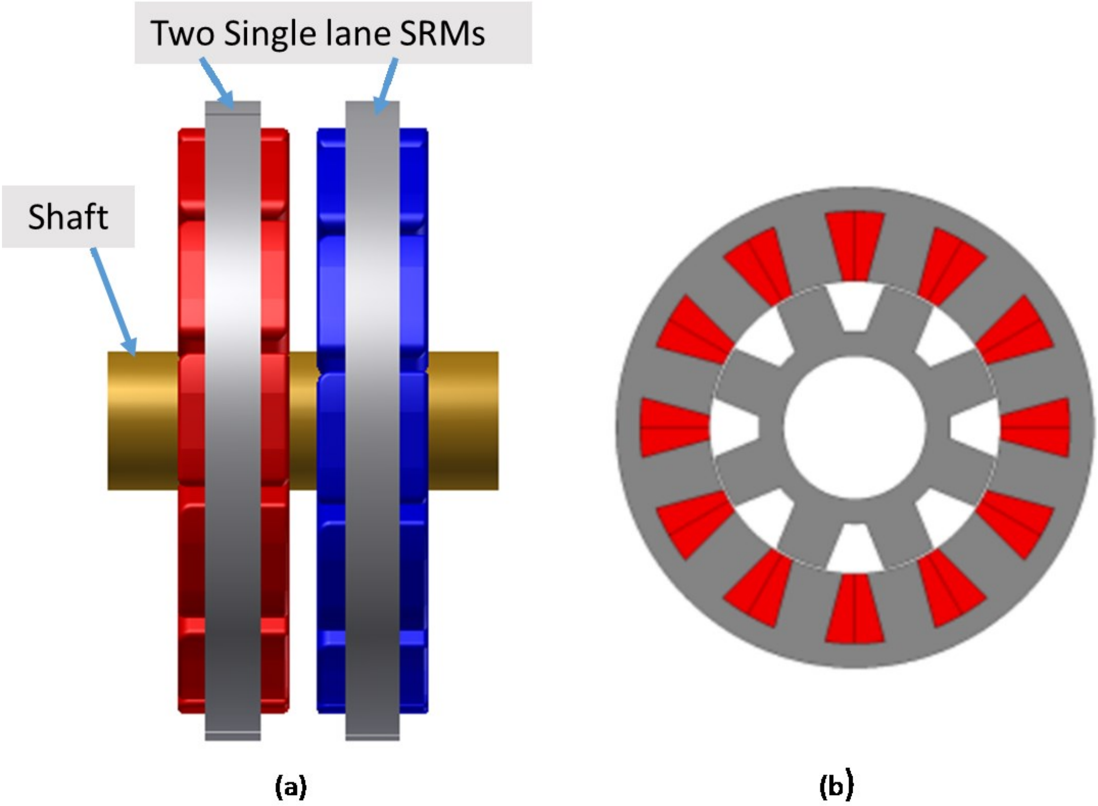

Figure 3-2: (a)Two single lane conventional SRMs on same shaft with end windings (b) 2DFE model of a single lane SRM

3.4.3 Dual lane single tooth wound segmental rotor SRM (SSRM)

Three phase SSRM[11] inherently meets the isolation requirements of fault tolerance and in a 24 tooth, 20 segment topology the windings can be arranged to ensure no UMP. Unlike the conventional SRM, the SSRM uses small rotor segments with a short flux path of each phase, thus minimizing the magnetic coupling between adjacent phases. The 24-20 arrangement is the lowest combination that can meet all the requirements and is the preferable choice of topology to keep the electrical frequency of the machine as low as possible. The windings of each power lane are distributed around the periphery of the machine in an alternating manner to balance the thermal loading of the machine when any one lane is active. Figure 3-3 shows SSRM structure.

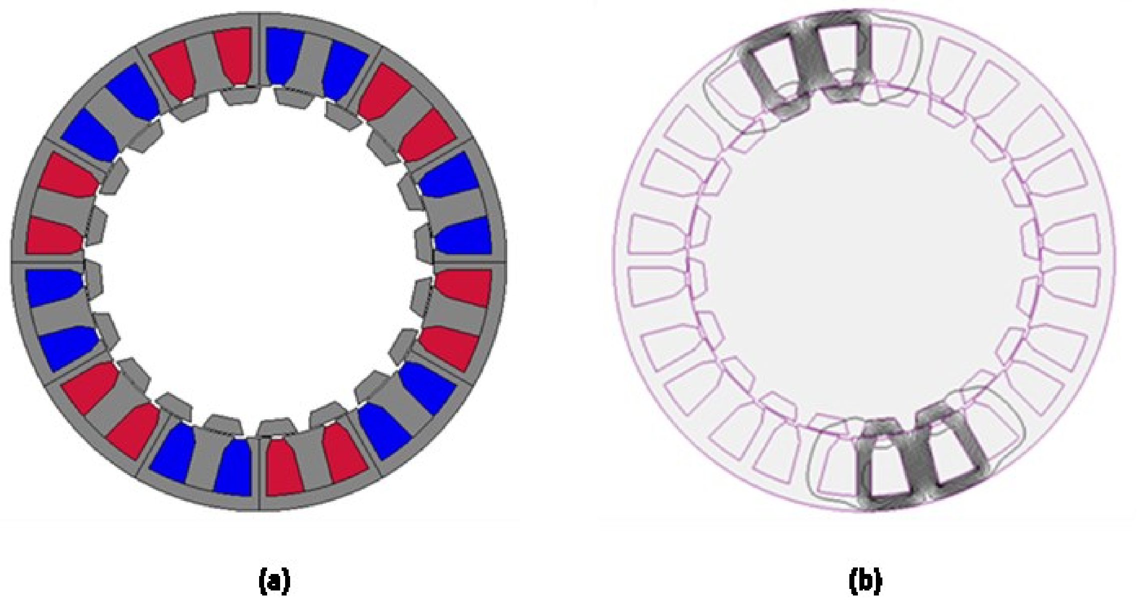

Figure 3-3: (a) 24-20 SSRM, Lane 1 phases in red, Lane 2 phases in blue (b) Flux plot of Lane 1 phase A in aligned position

3.4.4 Dual Lane Segmental H-slot SRM

Adapting the design proposed by Ruba[67] for a segmental topology, delivers the motor design shown in Figure 3-4. This design offers some potential benefits over the conventional single tooth wound segmental SRM in the above; namely the lower segment count will lead to a lower operational frequency and hence higher actuator speed in current control while the location of the return path of each coil on the outer surface of the actuator can potentially provide a better thermal path from the windings to the motor casing allowing high current densities for the same coil temperature. The lamination spurs between the machine coreback, though magnetically redundant, provide isolation between lanes and a mechanically stiff mechanism for torque transfer to the machine housing.

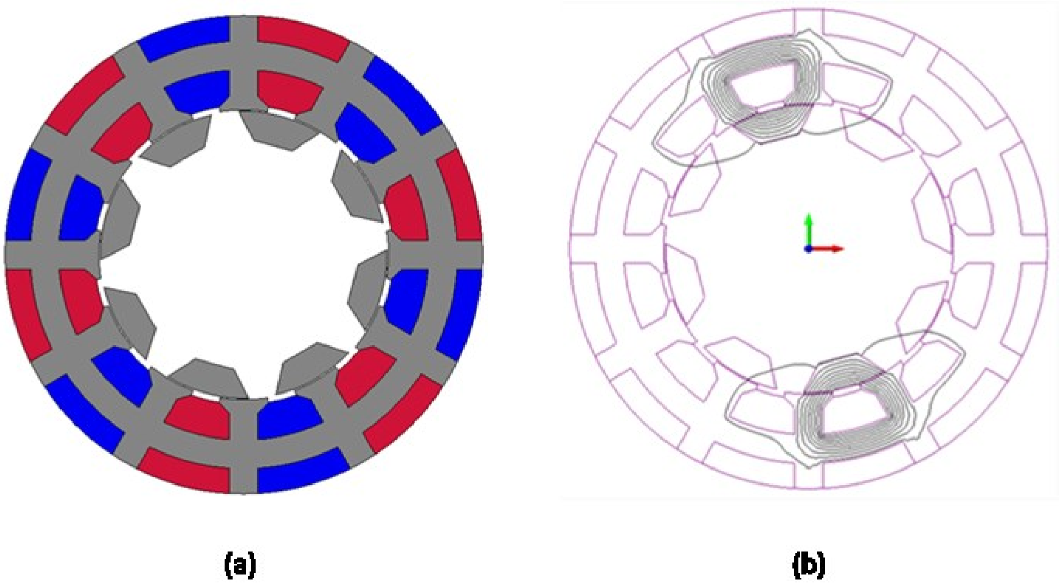

Figure 3-4: (a)Active magnetic components of 12-8 segmental H-slot SRM(b)Flux plot of Lane 1 phase A in aligned position on right

3.5 Torque Density Comparisons

To compare the various SRM topologies proposed against the PM actuator, the following design constraints were set:

- All motors to have the same outer diameter as that of the PM machine.
- All motors to have the same active length as that of the PM machine.
- All motors to operate at the same current density as that of the PM machine.
- All motors will have the same slot fill factor as that of the PM machine.
- All motors operating with perfect square current waveforms.

From these comparisons it was possible to compare the various SRM designs based on torque density, i.e. ignoring high speed operation and comparing them on their basic ability to deliver the same torque output as PM actuator for the same loading, and from the same overall package size. Table 3-1 summarizes the results of machine size and shape optimisation for the various SRMs.

Table 3-1: Comparison of SRM length oversizing required to achieve equivalent faulted performance as PM

SRM Topology	**Pu active length required vs PM**
Dual lane SRM	1.69
Single lane SRM	1.27
Dual lane SSRM	1.02
Dual lane H-slot SRM	1.30
PM machine	1.00

3.6 Proposed SRM for aerospace application

In Table 3-1, a clear contender is SSRM with only 2% increase in stack length as compared to the PM actuator. Optimisation of the SSRM leads to the specifications in Table 3-2. From 2DFE analysis, the proposed SSRM topology is able to achieve both the targets at different critical speeds.

Table 3-2: Direct comparison of PM to SSRM

Parameter	PM	SSRM
Max Speed (rpm)	900	900
Rated Torque, low Speed (Nm)	17	19.6
Rated Torque, high speed (Nm)	17	17.1
Drive Dc link Voltage (V)	480	480
Rated peak current (A)	11 (fault)	11 (healthy or fault)
Turns	211	352
Electrical Frequency @9500rpm (Hz)	150	300
RMS Current Density (A/mm^2)	26.1 (fault)	26.1
Outer Diameter (mm)	230	230
Active Length (mm)	20	20

Fill factor of the fault tolerant SSRM should be the same as that of PM machine to keep the mass of the machine low as the mass density of the copper is high compared to the steel. The machine has high copper loss for the given fill factor, however the actuator will operate for a short time so efficiency is not the prime target.

3.7 FE analysis of the SSRM

Based on the above work, it is clear that SSRM is the best choice but 3DFE analysis was conducted to analyse the end winding effect and leakage flux. As the stack length of the machine is small compared to the outer diameter of the machine, high electrical loading can result in an increase in the unaligned inductance as most of the flux uses the corresponding stator tooth (tooth around which the coil is wound) to complete the magnetic circuit. Because of smaller stack length, the length of the end windings is almost the same as that of the active winding (used within the slot) length which can result in significant increase in the unaligned inductance. This part shows both 2DFE and 3DFE results of the model to assess the difference the performance of the machine. Figure 3-5 shows quarter of the SSRM with end windings.

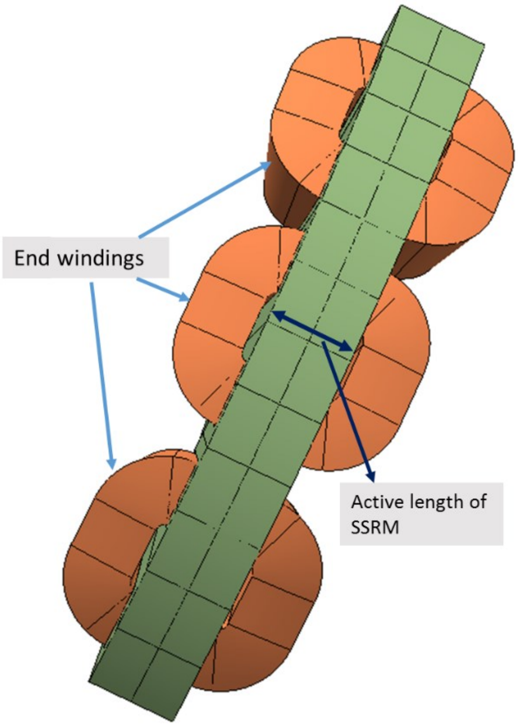

Figure 3-5: Top view of the quarter SSRM showing stach length and end winding length

3.7.1 2DFE and 3DFE static analysis

Both 2DFE and 3DFE static analysis of the machine were conducted to investigate end winding effect and leakage flux effect on the inductance value of the SSRM. Figure 3-6 shows the torque values at different rotor angles when rated current passed through the coil. Figure 3-7 shows the flux linkage of the machine at the aligned and unaligned position of both models. Based on the flux linkage values at aligned and unaligned position, the average torque for different current values is found shown in Figure 3-8.

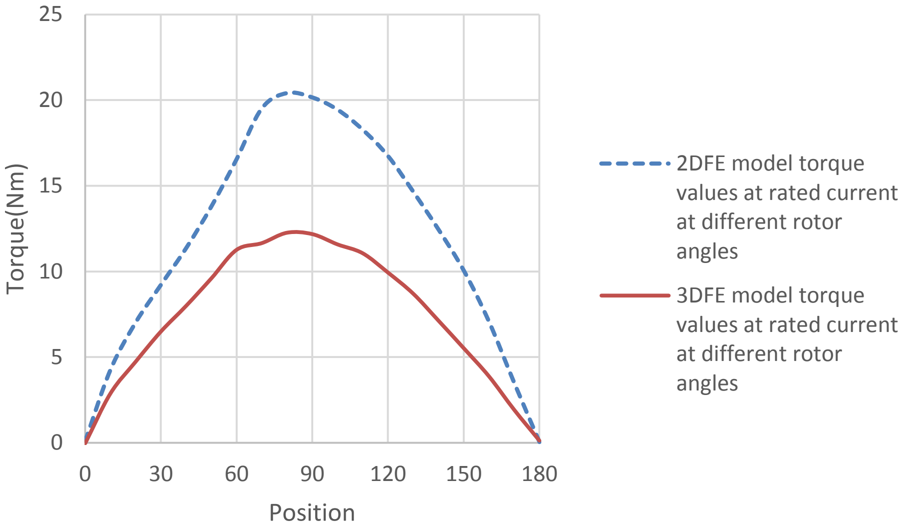

Figure 3-6: Torque of 2DFE and 3DFE SSRM models at different rotor at rated current

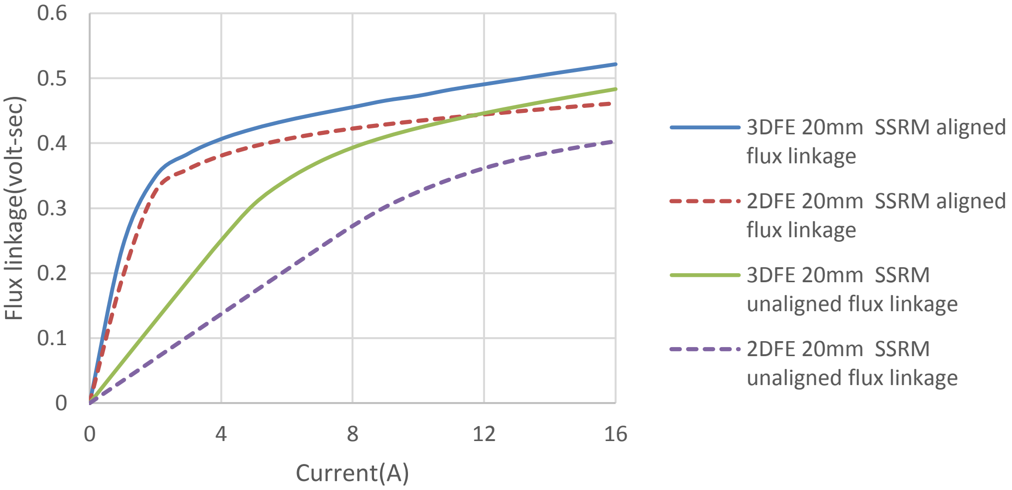

Figure 3-7: Aligned and unaligned flux of 2DFE and 3DFE SSRM models

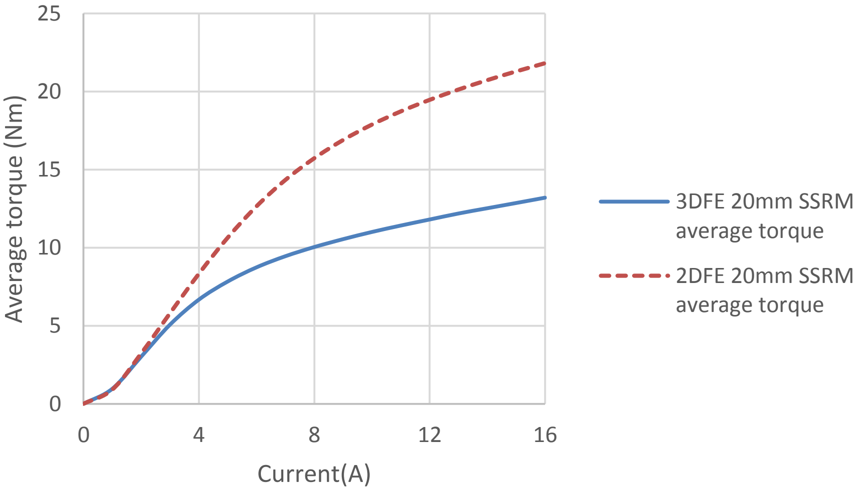

Figure 3-8: Average torque for different values of current in 2DFE and 3DFE models

3.7.2 Conclusion from 2DFE and 3DFE static analysis

The SSRM 2DFE and 3DFE models were investigated to analyse the effect of end windings and leakage flux. From 3DFE static analysis (shown in previous figures) it is clear that the torque of the SSRM decreases significantly. Disadvantage with the large end windings and short stack length is that at unaligned position, the 3D flux path is significant compared to the 2D path, hence increasing the flux linkage. By the introduction of end windings to the model, the average torque decreases by 39% at the rated current of 11 Amps peak.

3.8 30mm SSRM

In order to get the same holding torque as that of the PM machine, the stack length of SSRM was increased to 30 mm. But this results in 50% increase in volume compared to the PM actuator which is significantly higher. Figure 3-9 shows the flux linkage at the aligned and unaligned position from 3DFE static analysis when the size of SSRM was increased to 30 mm. Based on the area between the aligned and unaligned flux linkage, the average torque of 30mm SSRM for different values of current was found shown in Figure 3-10. Increase in the stack length of the machine results in decrease in the end winding effect. The average torque decreases by 16% at rated current due to the end winding effect. By assuming ideal condition with no effect of the high inductance (found from 3DFE model) on the drive at lower speed, 2DFE motion analysis was conducted. The torque values (all values found from 2DFE motion analysis in one complete cycle) were then multiplied by the decrease torque factor (found from 3DFE model which will be 0.84 in this case as torque decrease by 16%). Figure 3-11 shows resultant torque waveform at the rated current which shows the lower value of the torque ripple above 17 Nm.

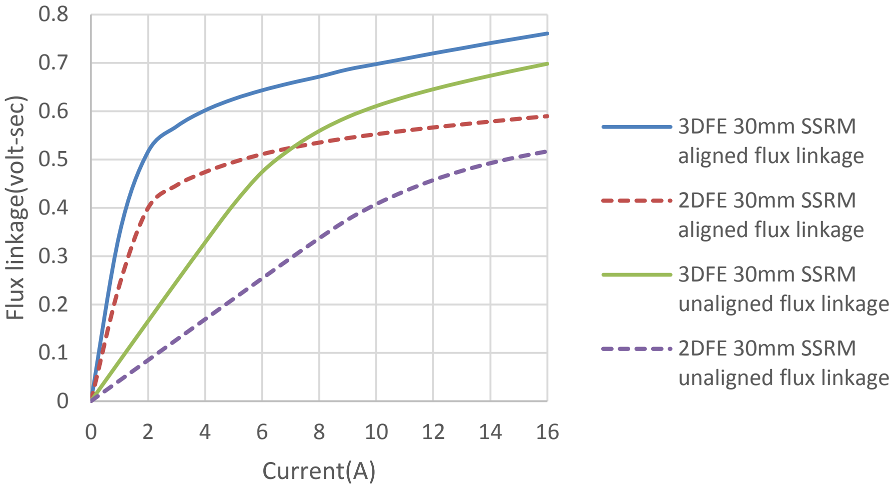

Figure 3-9: 30mm SSRM Aligned and Unaligned flux linkage

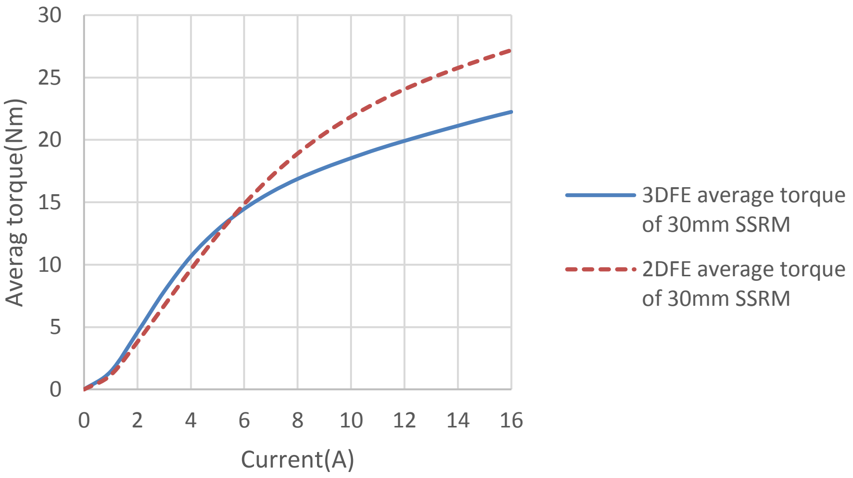

Figure 3-10: Average torque of 3DFE 30mm SSRM for different values of current

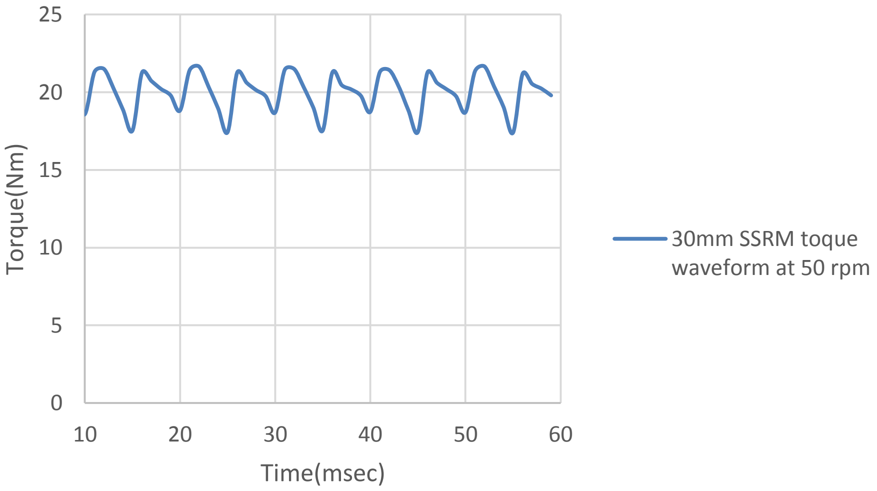

Figure 3-11: 30mm SSRM torque waveform at 50 rpm

3.9 Mass comparison

Figure 3-12 shows the mass comparison between the SSRM and PM actuator. Fault tolerant SSRM mass increased by 22% when the stack length was increased by 50% compared to PM machine mass. Fault tolerant SSRM was left at this point as the replacement to PM machine because even optimization will hardly decrease the overall mass and volume of the machine.

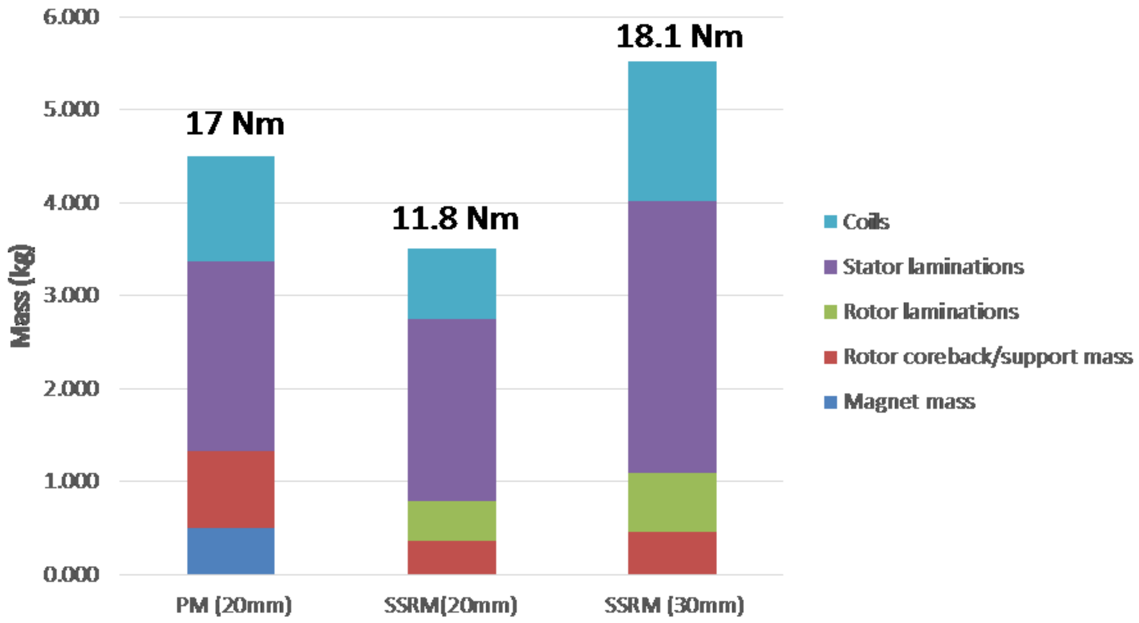

Figure 3-12: Mass comparison of different parts of the PM and SSRM with different stack length

3.10 Conclusion

Different SRM topologies were investigated which leads to the conclusion of SSRM as the best one to replace PM actuator for the aerospace application. However dominant end winding effect resulted in 39% decrease in torque compared to the 2DFE model. To overcome this problem, the fault tolerant SSRM stack length was increased by 50% compared to the PM machine to achieve the target torque at rated current. This resulted in 22% increase in the mass of the machine compared to the base machine (PM machine). The 30mm SSRM is able to achieve the holding torque but high increase in mass of the machine does not make it suitable for aerospace applications. It also shows that by increasing the stack length of the machine, the enwinding effect decreases which shows SSRM can be a good option for high stack length machines. All the above work leads to the idea of applying the magnet assist concept to SSRM to overcome the drawbacks of end winding effect by increasing the unsaturated region of the machine and at the same time investigating the fault tolerant capability of the MSSRM.

Chapter 4 Applying the magnet assist concept to conventional segmental rotor topology

This chapter explains the basic concept of the magnet assist to a conventional 3- phase SSRM (called as MSSRM). It shows how a conventional SSRM works and the effect of the magnet assist which can improve the performance of the machine. The MSSRM was compared with a conventional SSRM for the same copper loss (1 kW) while keeping the tooth width to slot pitch ratio (t/λ) constant. Operating point of the magnet and demagnetisation within the magnet of the MSSRM was investigated. 2DFE analysis was conducted to compare both machines for the given copper loss.

4.1 Working principle of the SSRM

The operating range of the conventional SSRM is limited only to the first quadrant of the B-H curve. In terms of its structure, the machine consists of rotor segments with coil wound around the main tooth (big tooth) in the stator. The magnetic circuit of the machine is completed by the flow of flux from the main tooth, through the rotor segment and shorted by two small teeth on either side of the main tooth. Figure 4-1 shows structure of a conventional SSRM.

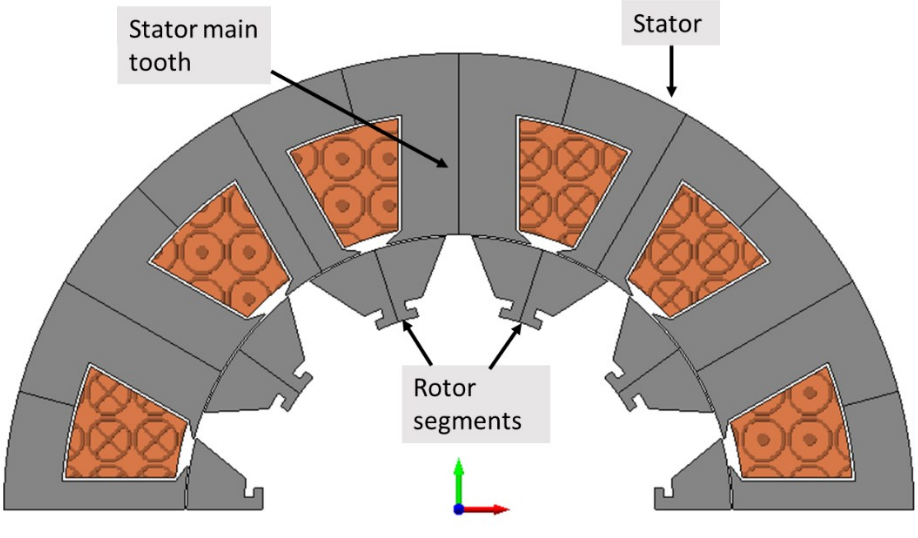

Figure 4-1: Conventional SSRM

At the unaligned position, the unaligned inductance is very low because of high air gap reluctance. At the aligned position, flux from the main coils flows through small rotor segments because of its high permeability which results in an increase in the aligned inductance. The tooth width to slot pitch ratio (t/λ) is important in determining the area between the aligned and unaligned inductance. In conventional SRM, t/λ is limited to a maximum of 0.5[16]. In comparison, in the SSRM t/λ can be increased up to 0.67 with higher aligned inductance while still keeping the unaligned inductance low, thus resulting in 40% more torque compared to a conventional SRM for the same copper loss [11]. Figure 4-2 shows flux from the coil at the aligned and unaligned position while Figure 4-3 shows the aligned and unaligned flux linkage of a conventional SSRM.

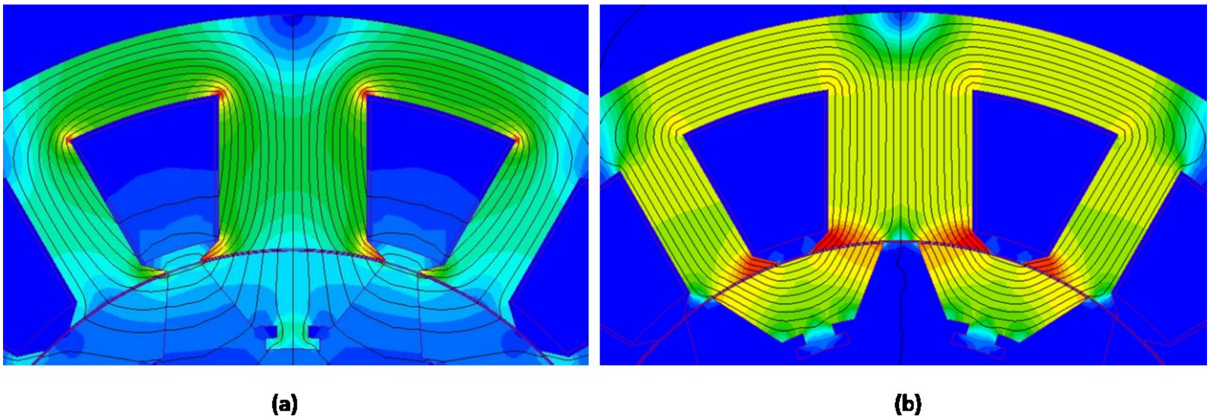

Figure 4-2:(a) Coil flux at the unaligned position (b) coil flux at the aligned position of the conventional SSRM

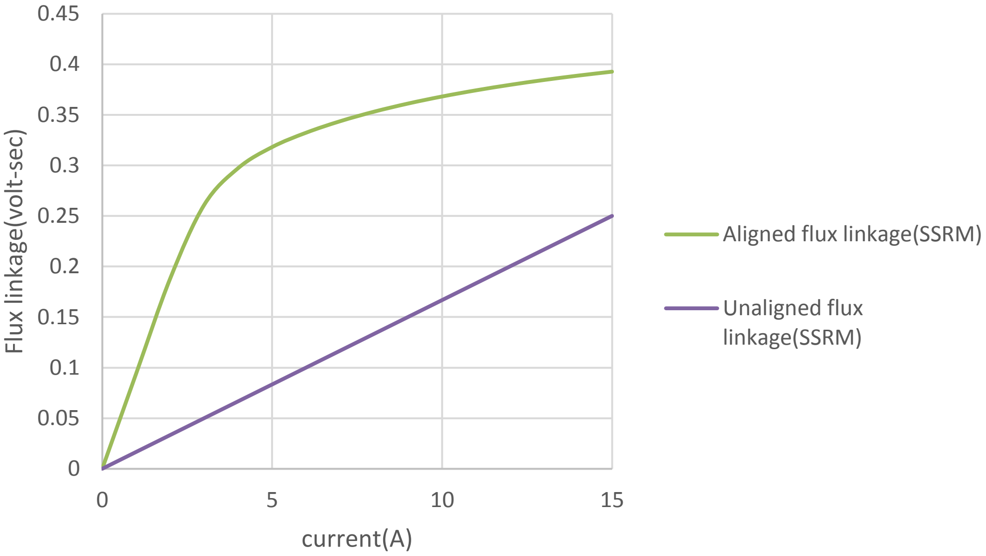

Figure 4-3: Aligned and unaligned flux linkage of the conventional SSRM

4.2 Drawback with SRM and SSRM

The torque of the SRM and SSRM is dependent on the area between the aligned and unaligned inductance. At the unaligned position because of high air gap, the unaligned flux linkage remains low. However at the aligned position, inductance is limited by the magnetic properties of lamination material. At the aligned position, for lower values of current there is a linear increase in flus linkage but at higher currents, the laminations saturate which results in very small increase in flux linkage for high current values. This results in decrease in the torque of the machine at high electrical loading.

4.3 Introduction of magnet assist idea to SSRM

The operating range of the SSRM can be extended by the introduction of magnets. By placing magnets at the stator tooth tip, with flux from the magnets opposing the main coil flux, the operating range of the machine can be extended to third quadrant of the B-H curve. This process reverse magnetises the stator core material which results in it taking longer for the stator core to become saturated (especially at the aligned position where inductance is limited by the saturation of the material), hence increasing the overall area between the aligned and unaligned inductance. This results in an increase in machine torque.

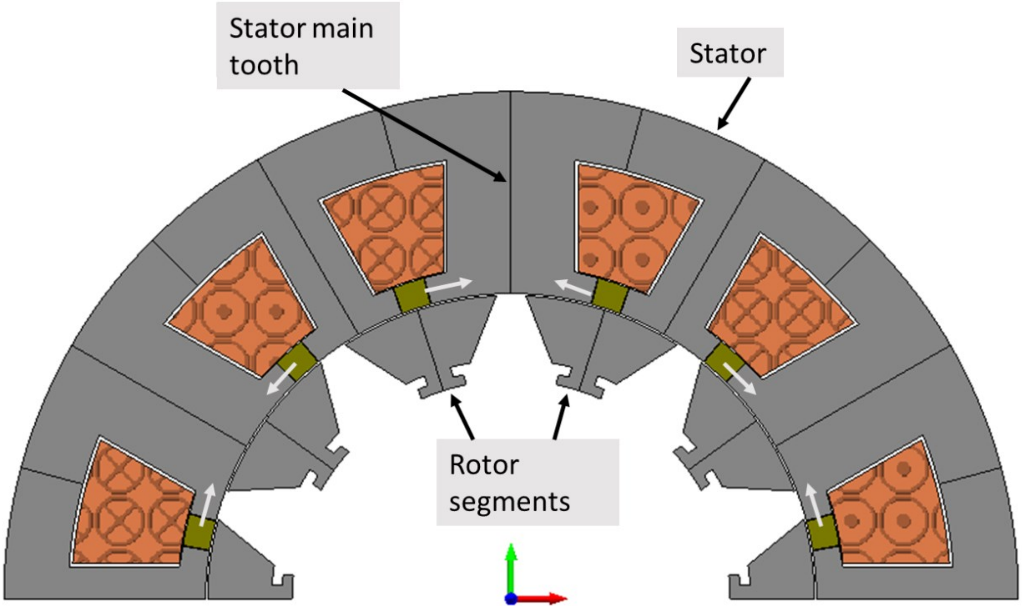

Figure 4-4: Magnet added to conventional SSRM(MSSRM) with arrows showing direction of magnets

Figure 4-5 shows the saturated and unsaturated range of the conventional SRM, SSRM and MSSRM within the B-H curve while Figure 4-6 shows flux from the magnets at the aligned and unaligned positions. Figure 4-7 shows flux linkage from the SSRM with magnets at the stator tooth tip.

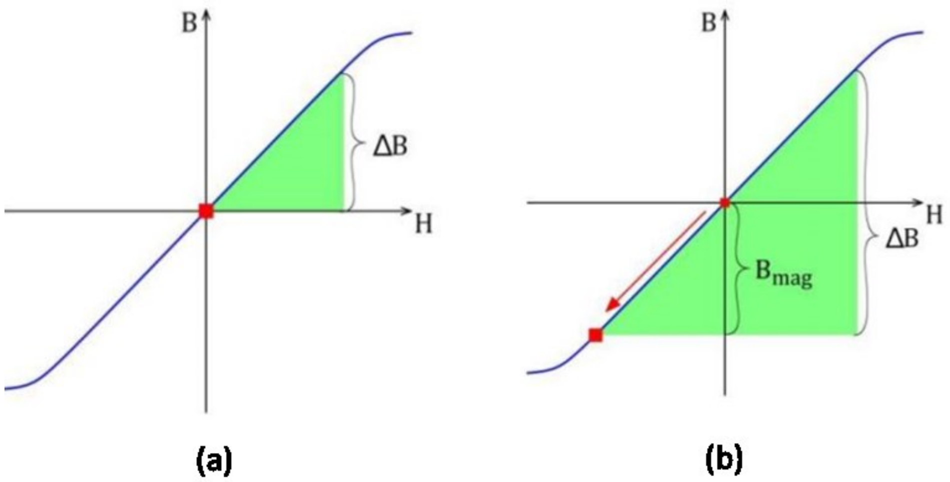

Figure 4-5: a) B-H curve for conventional SRM and SSRM which is limited to the quadrant only b) B-H curve for new magnet assisted SSRM which is extended to third quadrant

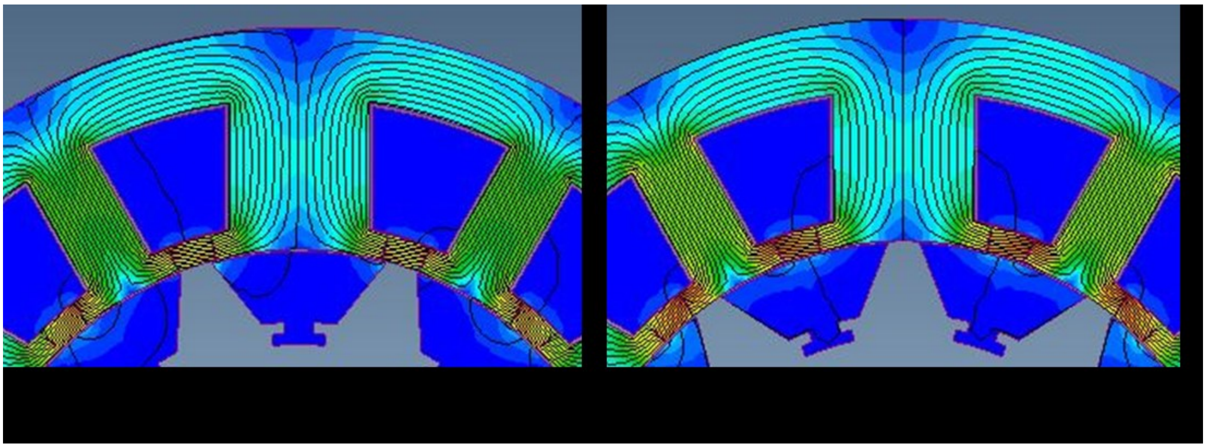

Figure 4-6: (a) Flux from magnets at the unaligned position (b) flux from magnets at the aligned position

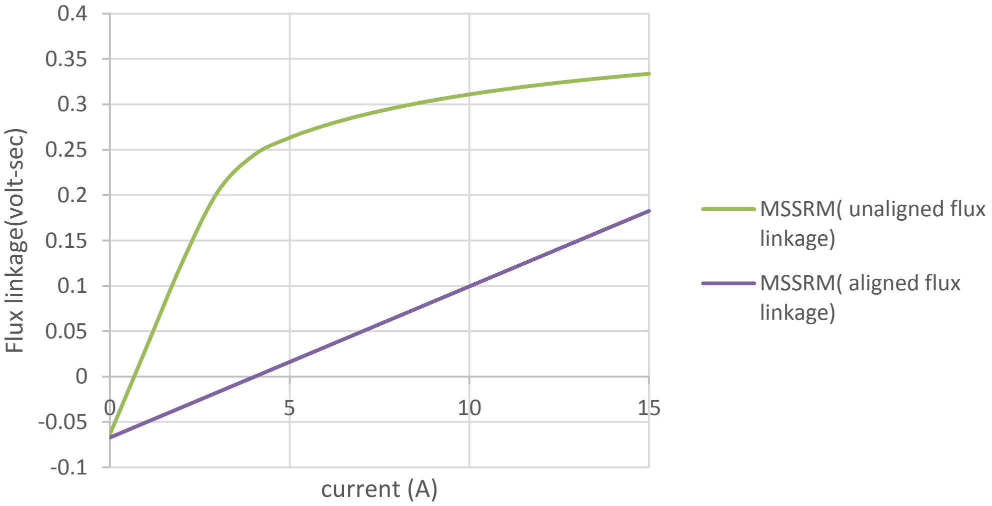

Figure 4-7: Aligned and unaligned flux linkage of the magnet assist SSRM (MSSRM)

The advantage of placing the magnets at the stator tooth tip is that flux from the main coils does not pass through the magnets, which can act as an extra air gap for coil flux. Also, by placing the magnets at that position, all the flux from the magnets is short-circuited by the stator coreback, and thus there is no cogging torque.

4.4 Choice of type of magnet

Magnet placed at the stator tooth tip has to overcome two problems:

1) Flux from the main coils will flow in the opposite direction to the magnet flux, so the magnet should be strong enough to withstand high external fields.
2) Since the magnet is placed at the stator tooth tip, it should withstand high temperatures as it will be far away from any type of cooling which will be available round the stator.

Samarium cobalt can be a good option for magnet material as it can withstand high temperatures up to 350 degree Celsius.

4.5 Comparison of magnet assist SSRM (MSSRM) with conventional SSRM

To show the idea works, a 3-phase magnet assist SSRM (MSSRM) was compared with a conventional 3-phase SSRM for the same copper loss by using FE software (Infolytica magnet). Both machines were compared on the basis of following rules:

1. t/λ ratio for both the machines was kept constant (0.67).
2. 12-10 single tooth wound machine topologies were chosen for both designs.
3. Outer diameter (150mm) and stack length (60mm) of both machines were kept constant.
4. Copper loss for both the machines was kept constant (1 kW)
5. Rated current value of both machines kept constant(30 Amps peak)
6. 2DFE static analysis was conducted to compare flux linkages and torque values per phase.

4.6 SSRM FE static analysis

The SSRM was simulated using FE software. Table 4-1 shows the dimensions and copper loss in SSRM.

Table 4-1: Parameters of SSRM

Characteristics	SSRM
Outer diameter of stator (mm)	150
Outer diameter of rotor (mm)	89.7
Air gap length (mm)	0.3
Stack length of the machine (mm)	60
tooth width to slot pitch ratio	0.67
Main tooth thickness (mm)	18.94
Small tooth thickness (mm)	9.47
stator coreback thickness (mm)	9.47
Average length of each coil (mm)	188.52
slot area (mm^2)	279.97
Copper loss(watts)	333.33
fill factor	0.46
MMF required for given copper loss (A-turns)	2547.46
Peak value of current(A)	30
Number of turns/phase	240
Resistance/phase (Ω)	0.74
Flux density in the tooth (T)	1.8

4.6.1 2DFE static analysis

2DFE static analysis of SSRM was conducted by passing current through each phase and rotor was rotated at different angles to measure torque and flux linkage. Figure 4-8 shows single main tooth with rotor segments at the aligned position with mesh size.

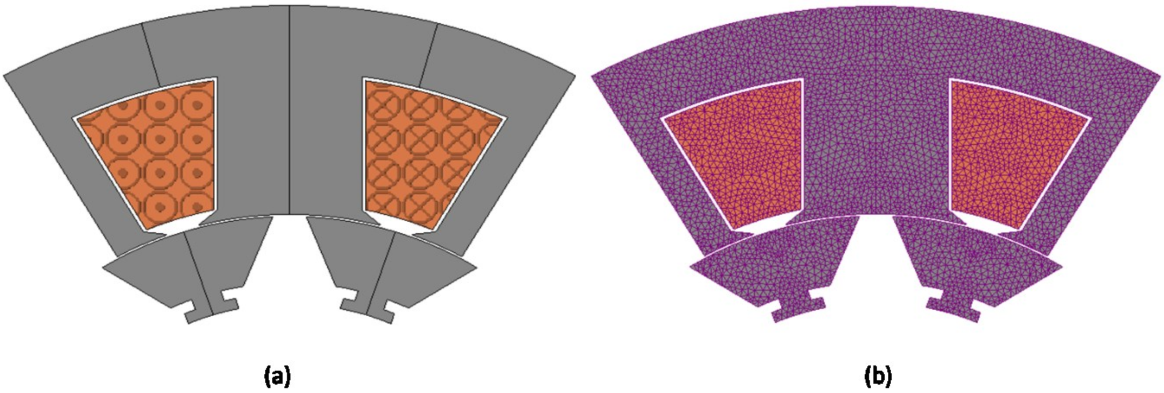

Figure 4-8: (a) single main tooth 2DFE model of SSRM (b) Mesh size of the 2DFE SSRM model

Figure 4-9 shows the torque of the SSRM at the rated current. Figure 4-10 shows the aligned and unaligned flux linkage of the SSRM. Figure 4-11 shows average torque of the SSRM at different current values derived from flux linkage-current waveform.

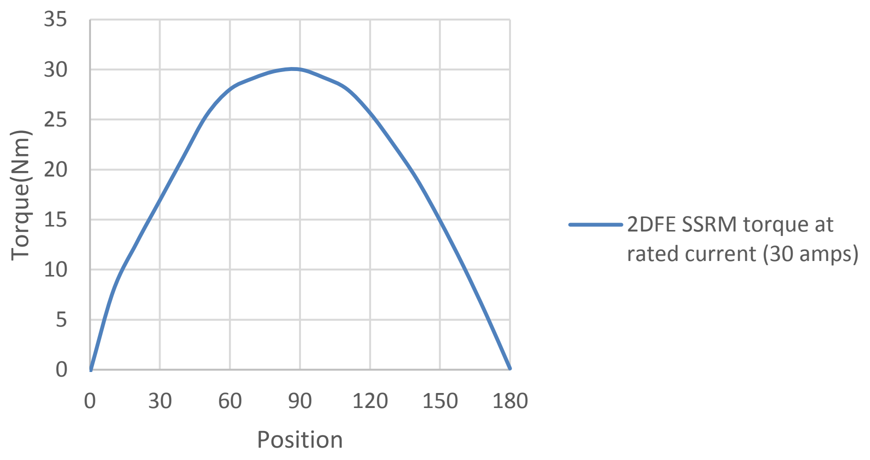

Figure 4-9: Torque of the SSRM at rated current when only one phase energized

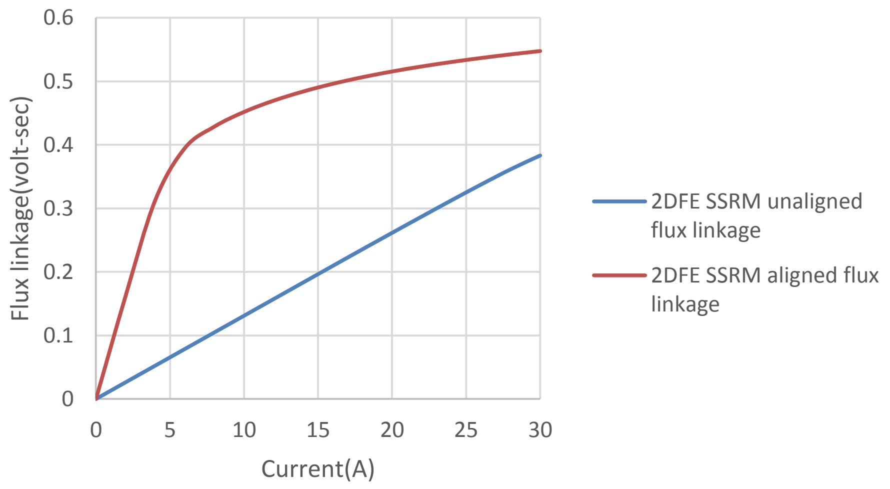

Figure 4-10: Aligned and unaligned flux linkage of 2DFE SSRM model

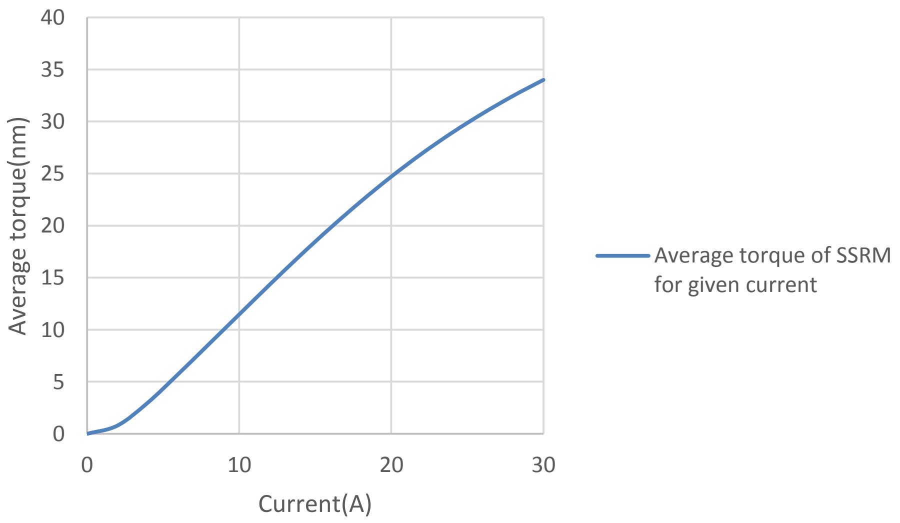

Figure 4-11: Average torque of the SSRM for different values of current

4.7 MSSRM FE static analysis

MSSRM was analysed by using 2DFE software. The magnet used for simulation in the MSSRM was the Recomma 33E (Samarium cobalt) [68] with an operating temperature range up to 350°C.

4.7.1 Choosing thickness of magnet

Before finalising the MSSRM dimensions, its magnet thickness was varied while keeping the copper loss constant in order to find the thickness of magnet required to achieve the maximum torque for given copper loss. Choosing a thicker size of the magnet will not help in getting higher torque as the stator core can be reverse-magnetized up to a certain value above which copper loss will increase without an increase in torque. To choose the right size of magnet, its thickness was varied between 2 to 4.5 mm until the maximum torque was obtained while keeping the copper loss constant. A thickness of 3.5mm was considered to be suitable one giving the maximum torque. Figure 4-13 shows the output torque against magnet thickness.

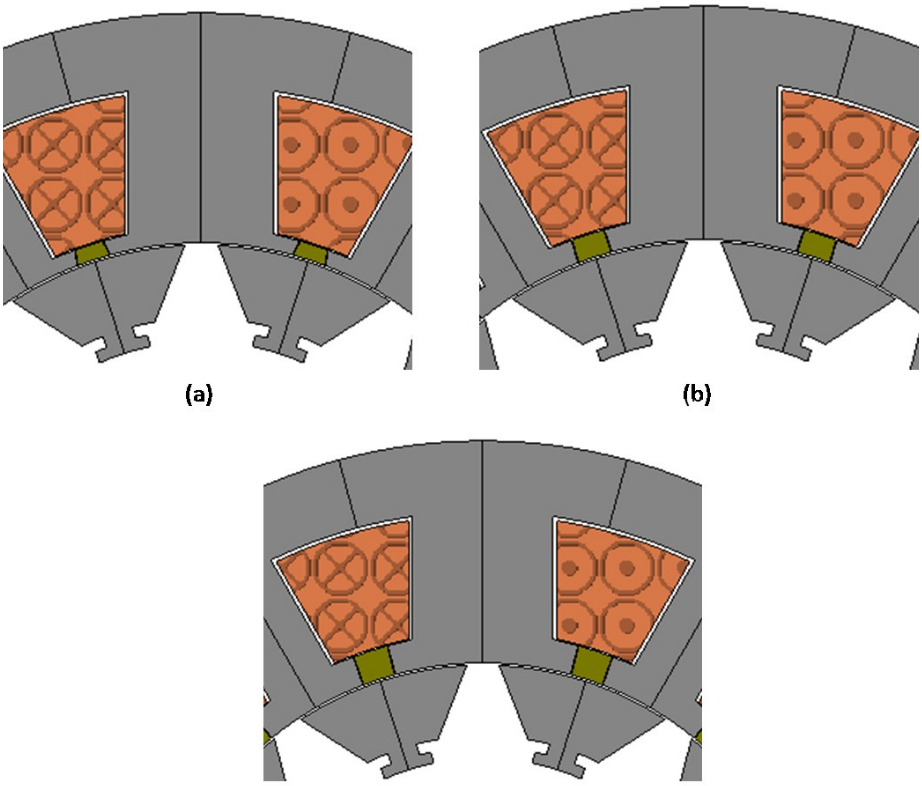

(a) (b)

(c)

Figure 4-12: (a) Magnet of thickness 2mm(b) Magnet of thickness 3mm (c) Magnet of thickness 4mm

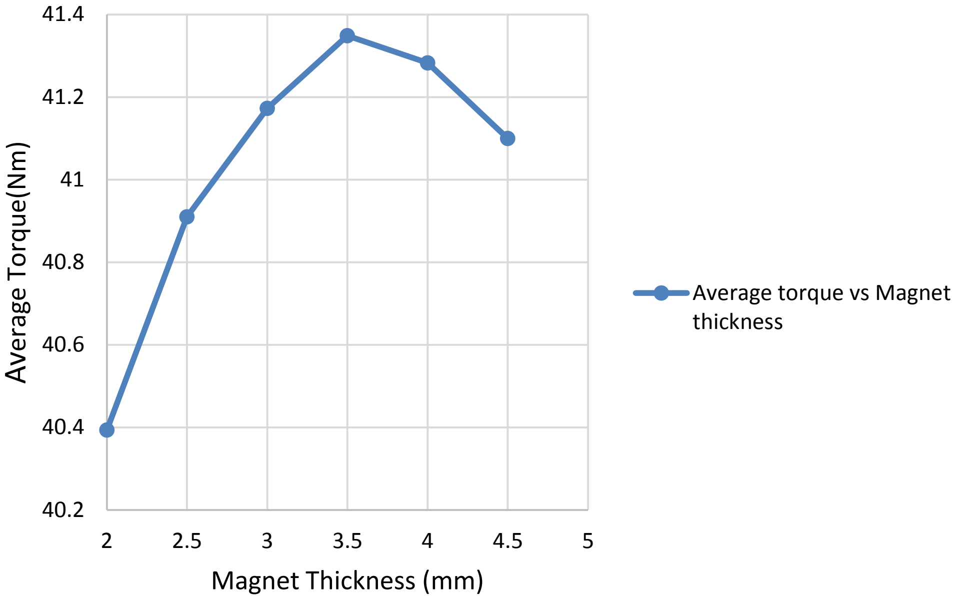

Figure 4-13: Average torque for different thicknesses of magnet while keeping copper loss constant

Demagnetisation within the magnet at rated current was found by using the FEA software. Figure 4-14 shows the demagnetisation prediction of demagnetisation at 100°C. The FEA software shows the magnet does not get demagnetise at all rotor angles.

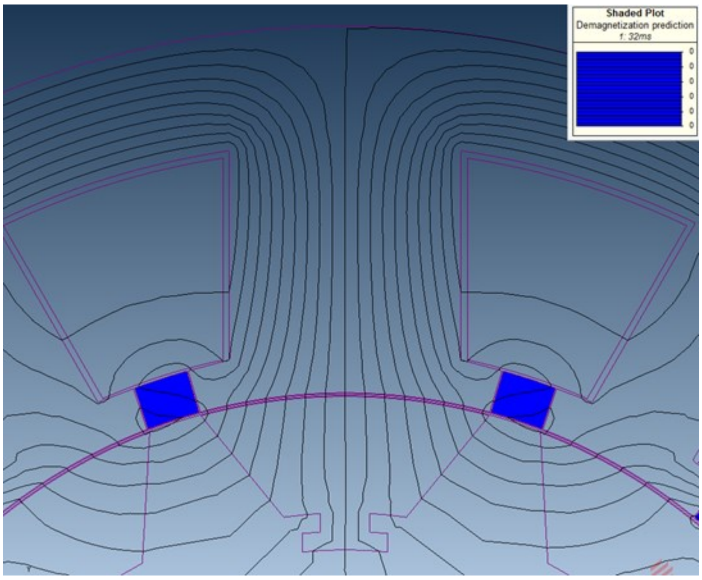

Figure 4-14: Demagnetisation prediction within magnet at the unaligned position

Introduction of the magnets tooth tip results in decreasing the slot area.

Based on the thickness of the magnet, the final dimensions of the MSSRM are shown in Table 4-1

Table 4-2: MSSRM and SSRM dimensions

Characteristics	**MSSRM**	**SSRM**
Outer diameter of stator(mm)	150	150
Outer diameter of stator(mm)	89.7	89.7
Air gap length(mm)	0.3	0.3
Stack length of the machine(mm)	60	60
tooth width to slot pitch ratio	0.67	0.67
Main tooth thickness(mm)	18.94	18.94
Small tooth thickness(mm)	9.47	9.47
stator coreback thickness(mm)	9.47	9.47
slot area(mm^2)	252.42	279.97
Average length of each coil(mm)	189.25	188.52
Copper loss/phase(watts)	333.33	333.33
fill factor	0.46	0.46
Peak value of current(A)	30	30
MMF required for given copper loss(A-turns)	2413.20	2547.46
Number of turns/phase	228	240
Resistance/phase(Ω)	0.74	0.74
Flux de4nsity in the tooth(T)	1.6	1.8

4.7.2 Operating point of the magnet

The magnet at the stator tooth tip pushes the flux against the main flux. At higher values of MMF because of the high external magnetic field, the operating point of the magnet can significantly change.

For this reason it is important to find the operating point of the magnet. The operating point should be above half of the residual flux density (B_r) of the magnet in order to take the maximum advantage of the magnet [69]. At the same time, demagnetisation at the edges (which is hard to avoid) should be as low as possible.

Within the stator structure, an air gap of 0.1 mm was assumed on both side of the magnet between the stator and the magnet as in practice it would be hard to insert the magnet within the stator structure if there was less space available. By assuming the worst conditions in which all the flux from the coil uses magnet as a short flux path, the magnetic circuit of the stator can be drawn as shown in Figure 4-15

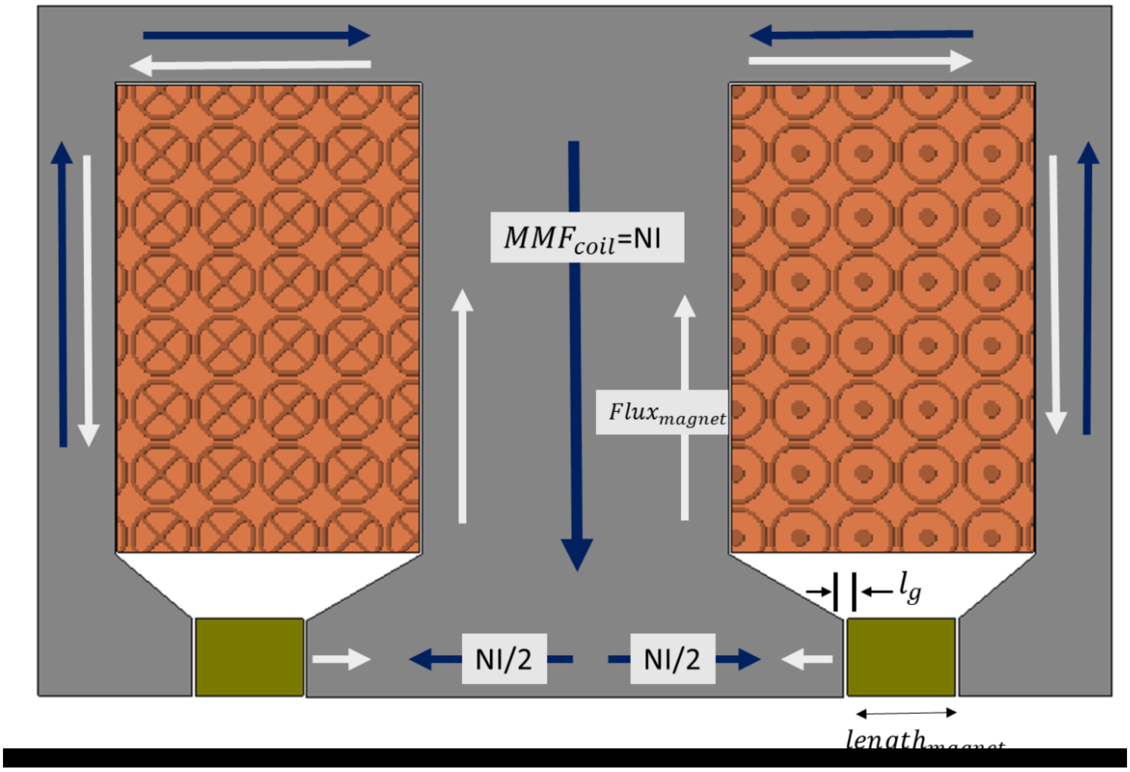

Figure 4-15: Magnetic circuit of the stator during worst case

By using Ampere’s Law, the equation for the entire magnetic structure can be written as follows [69]

$$\int Hdl = 0 \tag{4-1}$$

$$H_m l_m + H_g l_g + {}^{NI}/_{2} = 0 \tag{4-2}$$

$$H_m = \frac{-(H_g l_g + {}^{NI}/_{2})}{lm} \tag{4-3}$$

$$H_m = \frac{-(\frac{B_g\, l_g}{\mu_o} + {}^{NI}/_{2})}{l_m} \tag{4-4}$$

where H_m is the magnetic field strength of the magnet, l_m is the length of the magnet, ${}^{NI}/_{2}$ represents the MMF of the coil (half of its value is taken as half of the MMF which will oppose each magnet), μ_o is the permeability of free space ($4\pi * 1e^{-7}\ H/m$), B_g is the flux density within the air gap between magnet and the stator and l_g is the length of the air gap between the stator and the magnet. Assuming that the value of B_g 1T, with l_m equals 5mm (found from the FEA model), the value of H_m was found using equation (4-4)

$$H_m = -3.7\text{e}5(\text{A/m}) \tag{4-5}$$

The operating point of the magnet can be found by using equation (4-6). By using magnet data sheet with given μ_r(1.06) and B_r(1.12) values at 100°C

$$B_m = B_r + \mu_r \mu_o H_m \tag{4-6}$$

$$B_m = 0.62 \text{ T} \tag{4-7}$$

The operating point of magnet is well above half of the residual flux density ($\frac{B_r}{2}$) of the magnet.

4.7.3 2DFE static analysis

2DFE static analysis of the MSSRM was conducted by putting current into each phase and rotor was rotated at different angles to measure torque and flux linkage. Figure 4-16 shows single slot pole combination of 2DFE model of the MSSRM with mesh size used during simulations. Figure 4-17 shows the torque waveform of the MSSRM at rated current when rotor was rotated at different angles. Figure 4-18 shows the flux linkage of the 2DFE MSSRM at the aligned and unaligned positon. The flux linkage values were moved to first quadrant which makes the comparison with the conventional SSRM model easier. The rest of the thesis follows the same procedure of moving the MSSRM flux linkages values to the first quadrant. From flux linkage-current values, the average torque for given current is found shown in Figure 4-19.

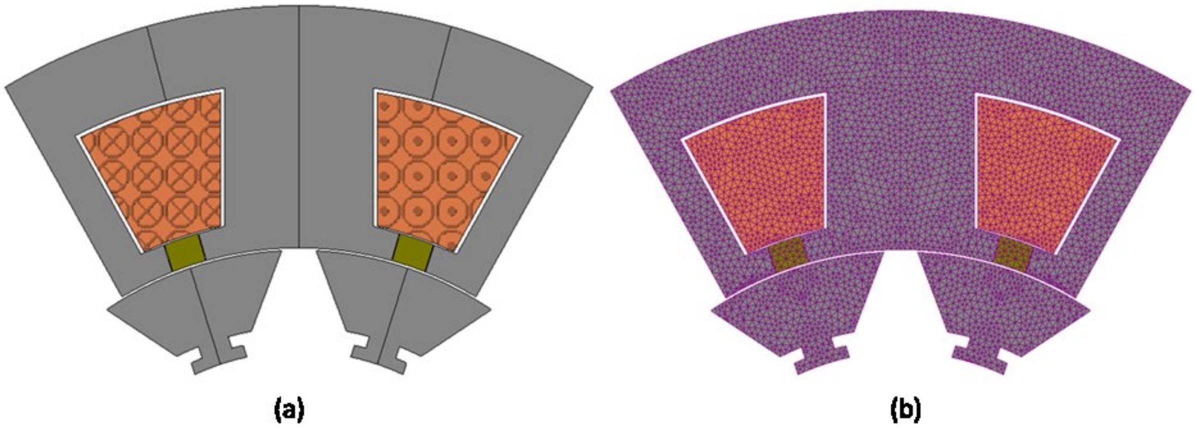

Figure 4-16: (a) single main tooth of the MSSRM with magnets (b) Mesh of the 2DFE model

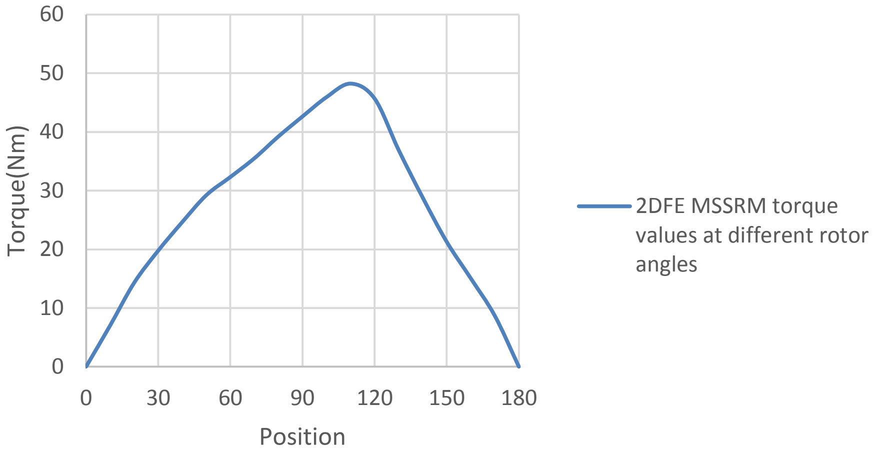

Figure 4-17: Torque values of MSSRM when rated current passed through coil at different rotor angles

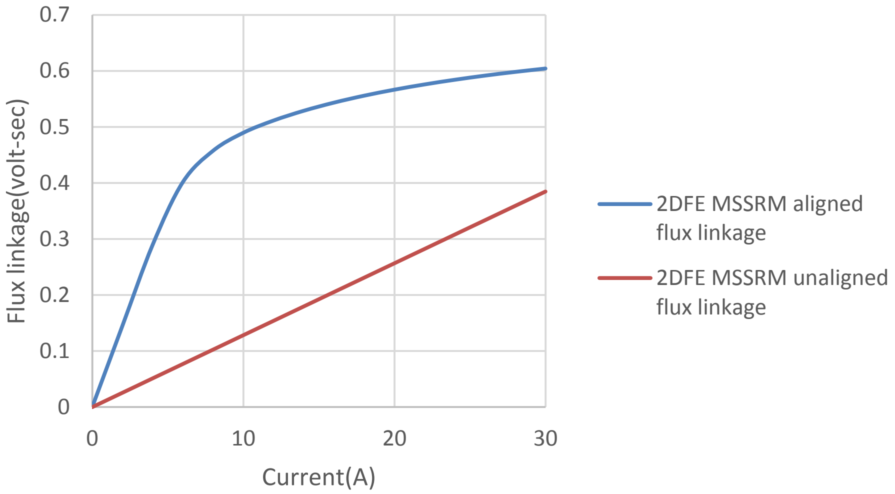

Figure 4-18: Aligned and unaligned flux linkage of MSSRM

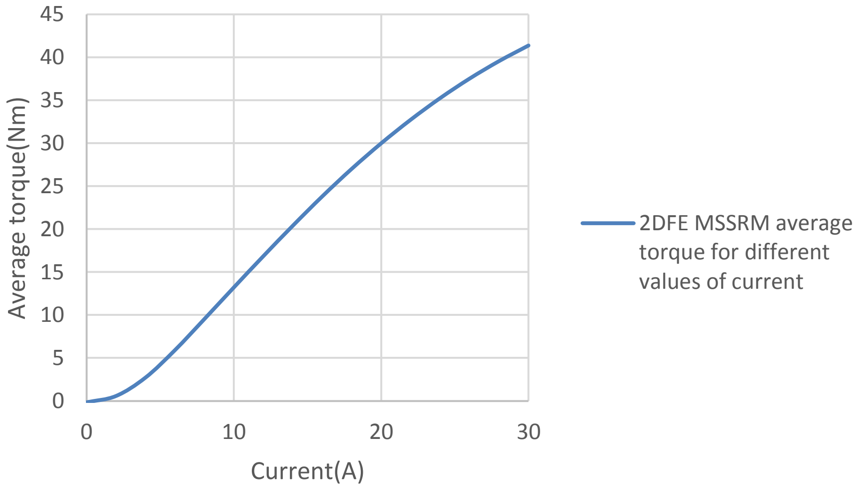

Figure 4-19: Average torque values of MSSRM for different values of current

4.8 Comparison of the MSSRM and SSRM based on the 2DFE model results

Based on the above work, the MSSRM and SSRM can be compared for the same copper loss on the basis of the 2DFE models. Figure 4-20 shows the flux linkage values of both models at the aligned and unaligned positions. It can be seen that the unaligned flux linkage remains the same for both models, however, the MSSRM has higher aligned flux linkage. The use of magnet avoids the stator laminations from becoming saturated at high current values by reverse magnetizing it, thus getting high aligned flux linkage for high values of current.

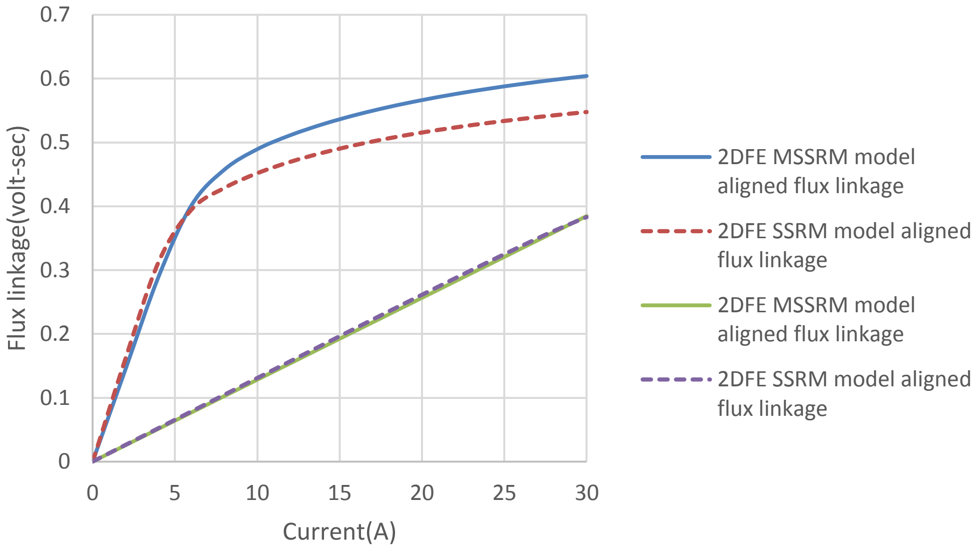

Figure 4-20: MSSRM and SSRM 2DFE models aligned and unaligned flux linkage

Figure 4-21 shows the average torque for different values of current in the two models based on the area between the aligned and unaligned flux linkage. Results show an 18% increase in average torque of the MSSRM compared to the SSRM in the 2DFE models.

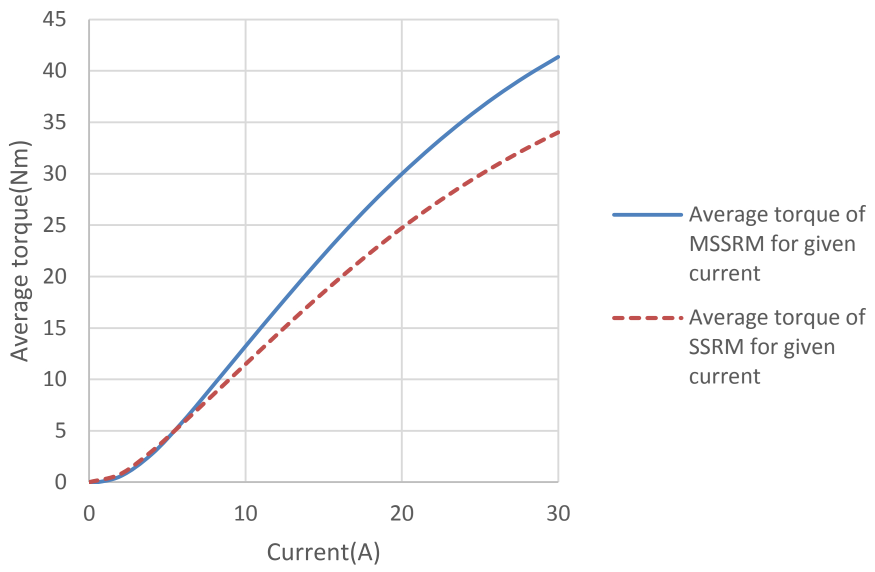

Figure 4-21: Average torque of 2DFE SSRM and MSSRM models for different values of current

4.9 Magnetization orientation of the MSSRM

In the case of the conventional SSRM, the coils are wound in such a way that flux from one coil is in the opposite direction to that in the adjacent stator main tooth coil in order to avoid the smaller stator tooth from becoming saturated when two phases are conducting simultaneously for a short period[34]. The new MSSRM was investigated for the same purpose to assess the effect of the magnetic field when coils and magnets are in different orientations. 2DFE motion analysis was conducted to find the output torque values with different orientation of the magnet and coil directions.

Figure 4-22 shows the symmetrical orientation (dot-cross, dot-cross) of the MSSRM coils along with magnet directions, while Figure 4-23 shows the asymmetrical orientation (dot-cross, cross-dot) of coils along flux direction. In both cases, flux from the magnet flows in the opposite direction to that of main coil.

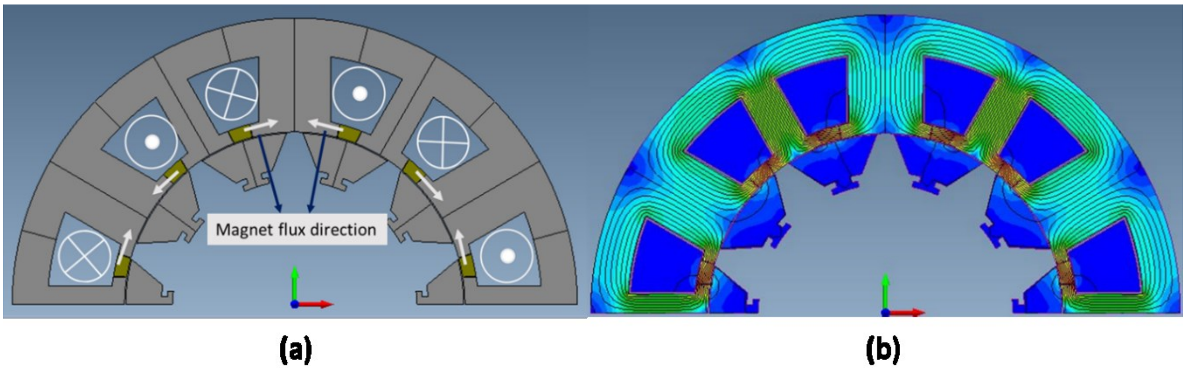

Figure 4-22: Symmetrical orientation of coils (a)dot-cross, dot-cross coil combination (b)Flux from magnets only

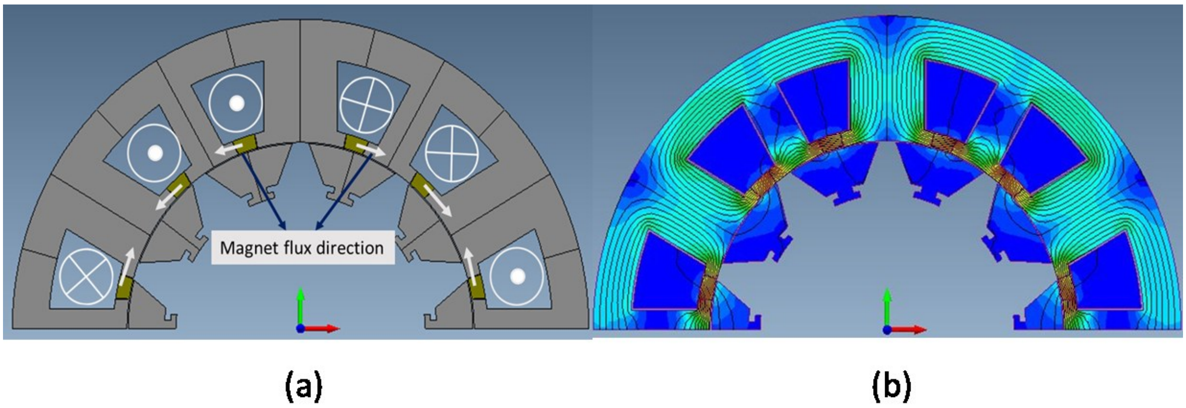

Figure 4-23: asymmetrical orientation of coils (a)dot-cross, cross-dot coil combination (b)Flux from magnets only

Figure 4-24 shows the output torque values for both coil combinations at the rated current when only one phase is excited. Figure 4-25 shows the flux linkage at the aligned and unaligned position for the symmetrical and asymmetrical coil combinations.

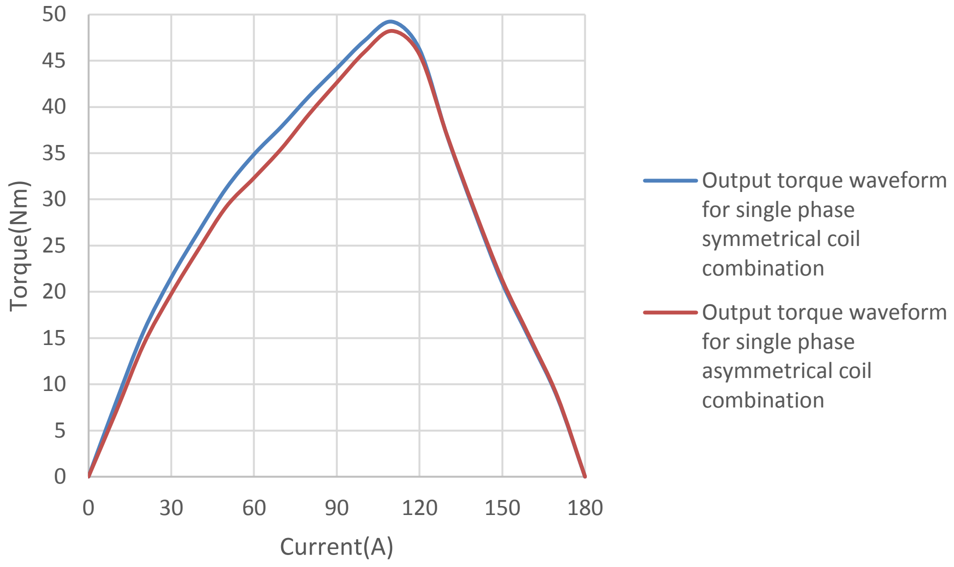

Figure 4-24: Static torque at rated current (30 Amps)

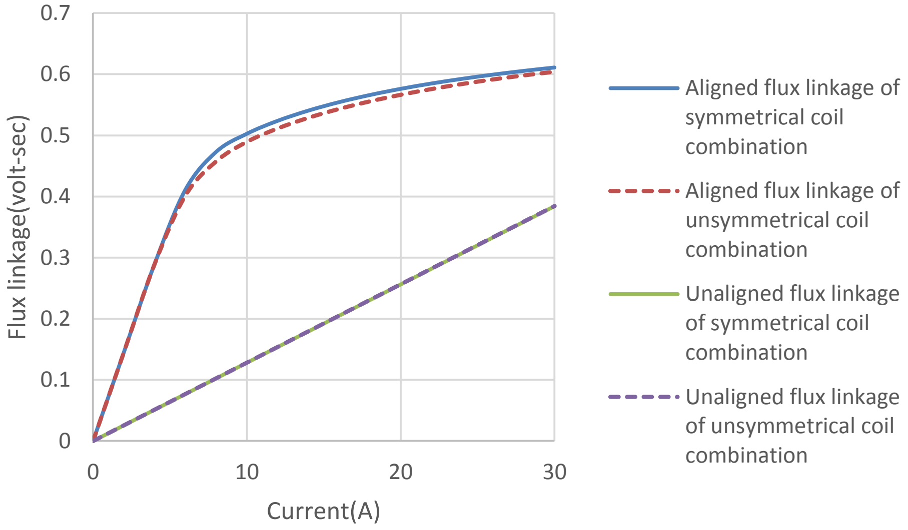

Figure 4-25: Aligned and unaligned flux linkage for even and odd symmetry of MSSRM

It is clear from Figure 4-24 and Figure 4-25 that the MSSRM with flux in all phases moving outward or inward gives higher torque. However, during normal operation when two coils conduct at same time, the smaller tooth saturates earlier in the case of the symmetrical coil combination. This is because the flux from both the phases shares the same small tooth, with flux from both coils moving in the same direction, which results in earlier saturation of the smaller tooth and hence a decrease in aligned inductance. Figure 4-22 shows that the small tooth is reversed-magnetized by the magnet flux, but the magnet flux is still not strong enough to avoid it from becoming saturated when the main coil flux flows through the same tooth. In case of the MSSRM with asymmetrical coil combination, magnet flux (Figure 4-23) is not reverse-magnetizing the small tooth, but the opposing flux from the adjacent phases is strong enough to avoid the small tooth from becoming saturated early when two phases are conducting at same time. This results in an average increase in torque of 6% of the MSSRM with asymmetrical coil combination as compared to the MSSRM with symmetrical coil combination, when both 2DFE models were run at 100 rpm for the same copper loss (Figure 4-26).

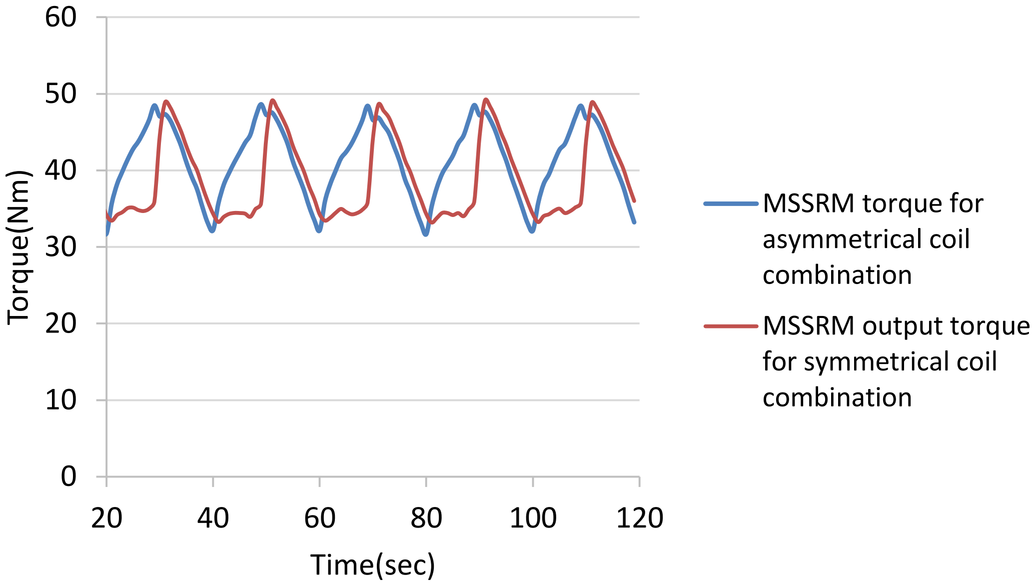

Figure 4-26: Torque waveform of the MSSRM at 100 rpm

4.10 Conclusion

The chapter explains the development of the MSSRM. The MSSRM was compared with a conventional 3-phase SSRM for the same copper loss. First 2DFE static analysis of the SSRM was conducted. Then 2DFE MSSRM model was analysed for the same copper loss. Magnet thickness was varied to find the best thickness of magnet required for the given copper loss. Operating point of the magnet was found which was above half of the residual flux density at the rated current. Demagnetisation within the magnet was found by using the FEA software which shows the magnets has no demagnetisation throughout the complete electrical cycle at the rated current. On the basis of flux-current waveforms, the MSSRM achieves 18% more torque compared to the SSRM for the same copper loss. This is as a result of high aligned inductance of the MSSRM because magnets avoid the stator from becoming saturated earlier, hence giving high output torque. Magnetization orientation of the MSSRM was investigated to observe the effect of the magnets on the machine saturation under different coil orientation which showed asymmetrical coil and magnet combination gives high torque.

Chapter 5 Developing the MSSRM for aerospace applications

5.1 Introduction

In chapter 4 a new motor topology, the magnet assist segmental rotor switched reluctance machine (MSSRM) was introduced. The MSSRM was shown to offer an improvement in torque density when compared with magnet free counterpart, the SSRM. In parallel with this work, other research work was going in the school to replace the fault tolerant PM actuator with magnet free SRM which is discussed in chapter 3. However from the 3DFE analysis, it was found that the machine torque significantly decreases. Therefore the work was directed towards MSSRM which can be a good option to improve torque performance of the SSRM having magnets in it.

In this chapter, the MSSRM is applied to the actuator specifications from chapter 4 and initial investigation was done by using both 2DFE and 3DFE models of MSSRM and was further developed to show its suitability for aerospace application.

5.2 Introducing magnets to fault tolerant SSRM

Previous chapter shows that fault tolerant SSRM cannot replace PM actuator because of low average torque which results in an increase in volume and mass of the machine to achieve the target. This leads to the use of MSSRM which gives higher torque compared to the conventional SSRM for the same copper loss as discussed in chapter 4. For initial investigation, all the parameters of the MSSRM kept similar to that of the fault tolerant SSRM with magnets placed at the stator tooth tip. Recomma 33E (Samarium Cobalt) was used which can withstand temperatures up to 350°C. This magnet should be able to withstand high temperatures during fault conditions without getting permanently demagnetised as there is no cooling system available.

A magnet of thickness 3mm was placed at the stator tooth tip of the fault tolerant SSRM. Placing of magnets at tooth tip reduces slot area which results in reducing the number of turns in each slot to 340 for the given current density. As the adjacent phase is dead during normal operation of the machine (dual lane), magnet can be placed with North Pole facing the main tooth (big tooth). Both 2DFE and 3DFE analyses were carried out to investigate the end winding effect.

Figure 5-1 shows the structure of fault tolerant MSSRM with magnets at the tooth tip of the stator. Figure 5-2 shows magnet thickness and Figure 5-3 shows the magnet flux paths in on the next page.

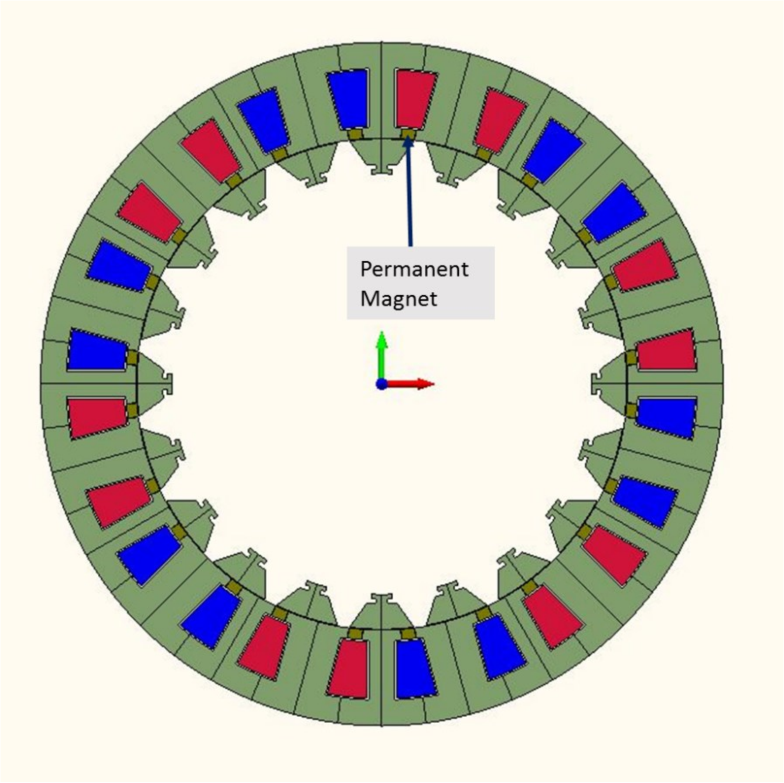

Figure 5-1: : Fault tolerant MSSRM with magnet at the tooth tip of stator

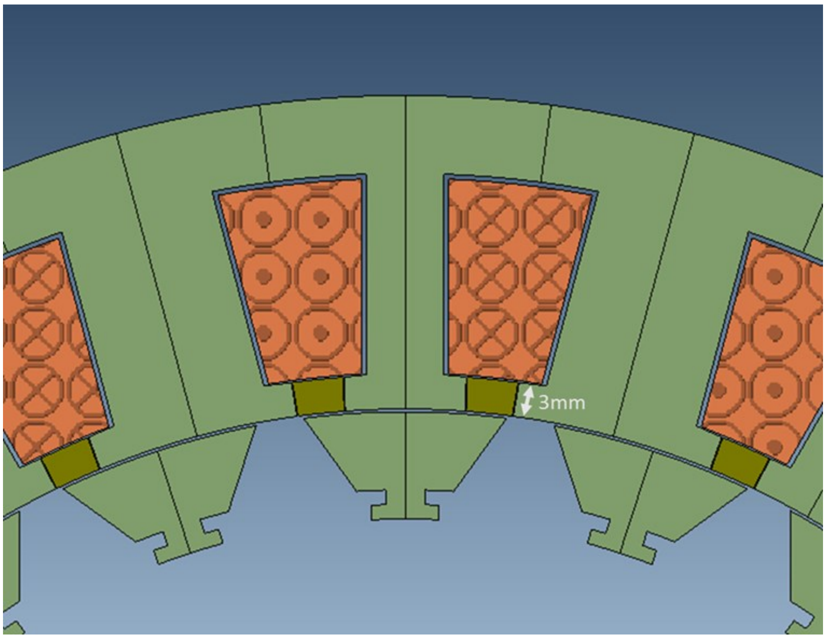

Figure 5-2: Magnet thickness

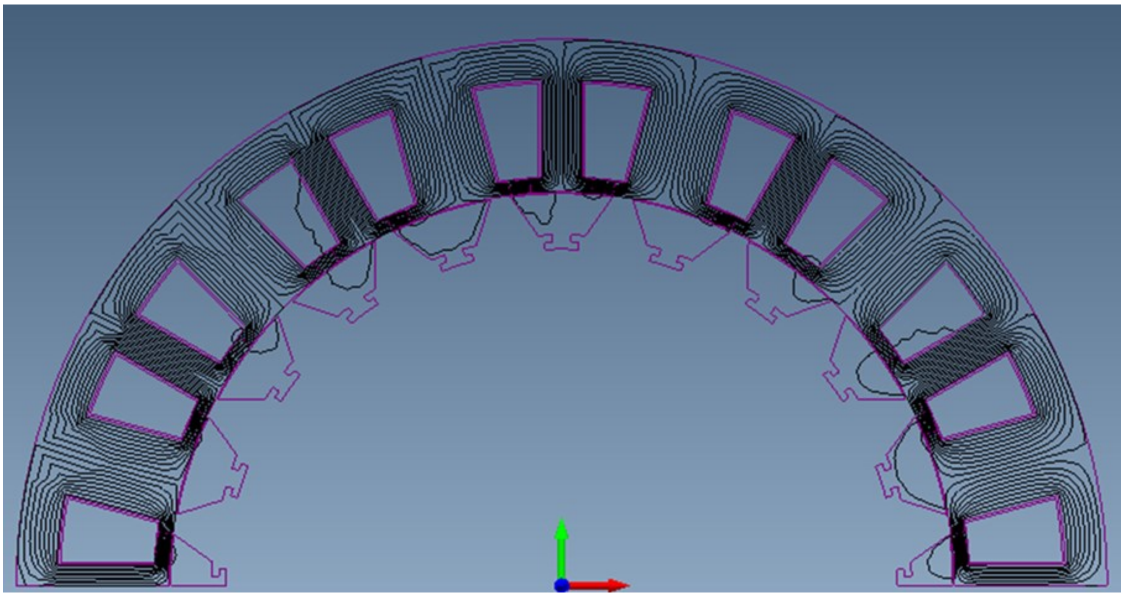

Figure 5-3: Flux from the magnets placed at stator tooth tip

5.3 2DFE results and comparison with SSRM

2DFE analysis of the MSSRM was conducted to investigate the performance of the machine. Figure 5-4 shows the aligned and unaligned flux linkage of the fault tolerant MSSRM which was compared with the fault tolerant SSRM model. It is clear from Figure 5-4 that the aligned flux linkage of the MSSRM increases significantly because of the magnets reverse magnetizing the stator core. At lower values of current, the unaligned flux linkage remains low because of less number of turns within the MSSRM stator, however at high currents, the unaligned flux linkage remains linear rather than getting saturated as in the case of SSRM. This is because of magnets avoiding the demagnetisation of the stator tooth even at the unaligned position. This results in an increase in the unaligned flux linkage, however because of the higher aligned flux linkage, there is a significant increase in torque of the MSSRM. Figure 5-5 shows resultant torque at rated current while rotating the rotor at different angles. Figure 5-6 shows average torque for different values of current found from the area between the aligned and unaligned flux linkage. The Fault tolerant SSRM stator core saturates at higher current while the MSSRM stator core remains unsaturated for higher values of current which results in 23% increase in average torque for the rated current.

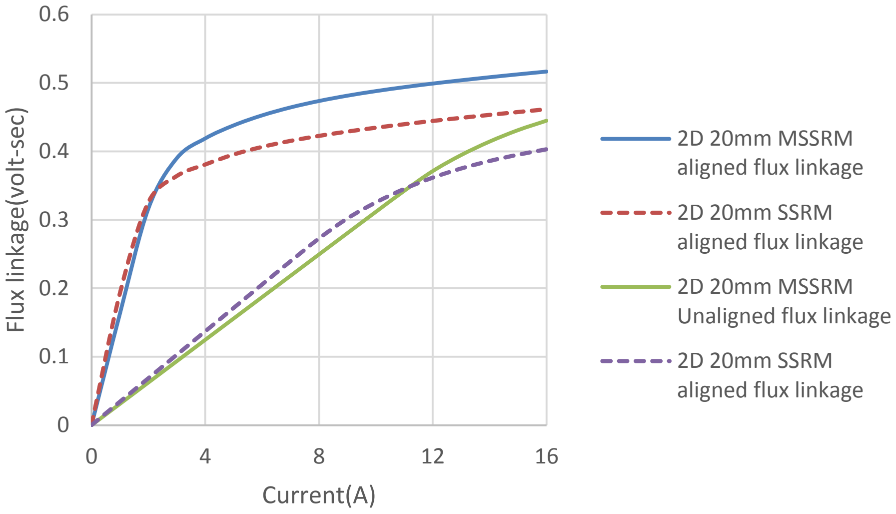

Figure 5-4: Aligned and unaligned flux linkage of 20mm SSRM and MSSRM

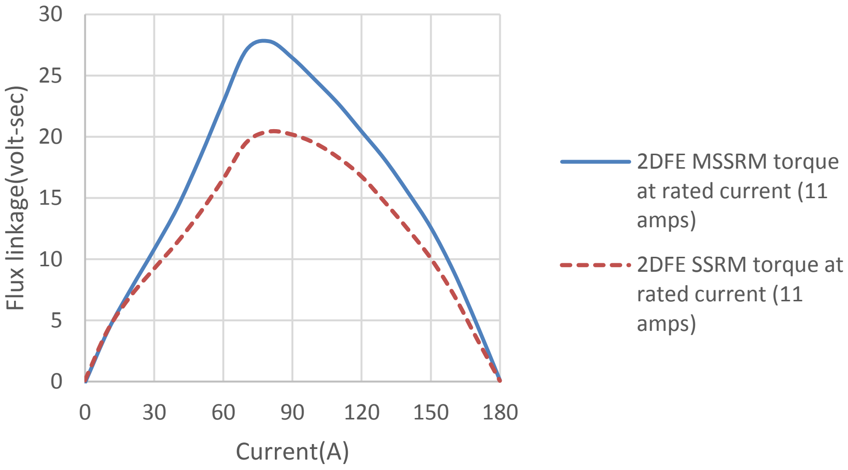

Figure 5-5: Torque at different angles of both 2DFE SSRM and MSSRM models

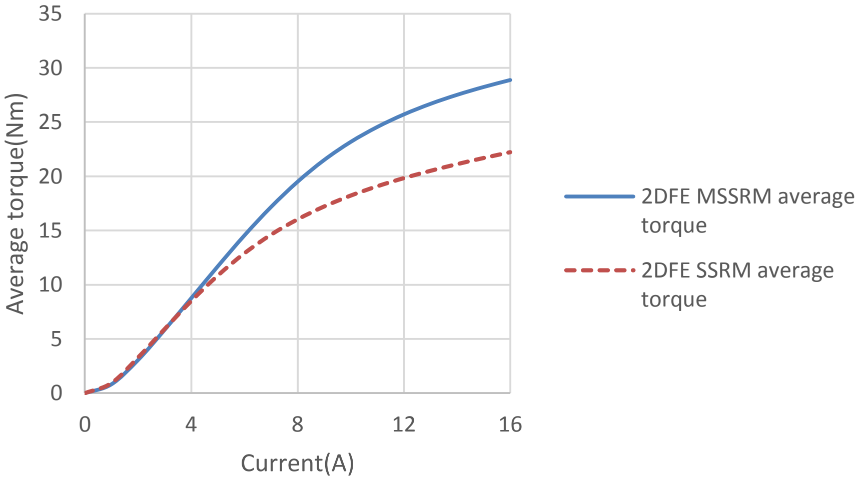

Figure 5-6: Average torque of 2DFE MSSRM and SSRM for different values of current

5.4 3DFE results and comparison of the MSSRM with SSRM

3DFE analysis of the fault tolerant MSSRM was conducted. Figure 5-7 shows the aligned and unaligned flux linkages of both SSRM and MSSRM models with 20mm stack length while Figure 5-8 shows torque of both machine when rated current(11 Amps) was passed through a single phase.

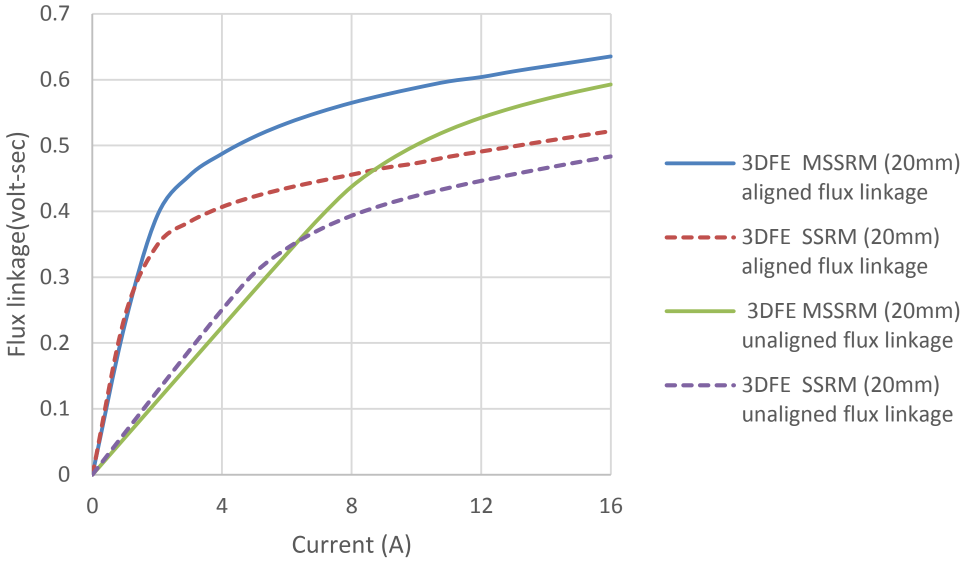

Figure 5-7: Aligned and unaligned flux linkage of MSSRM and SSRM

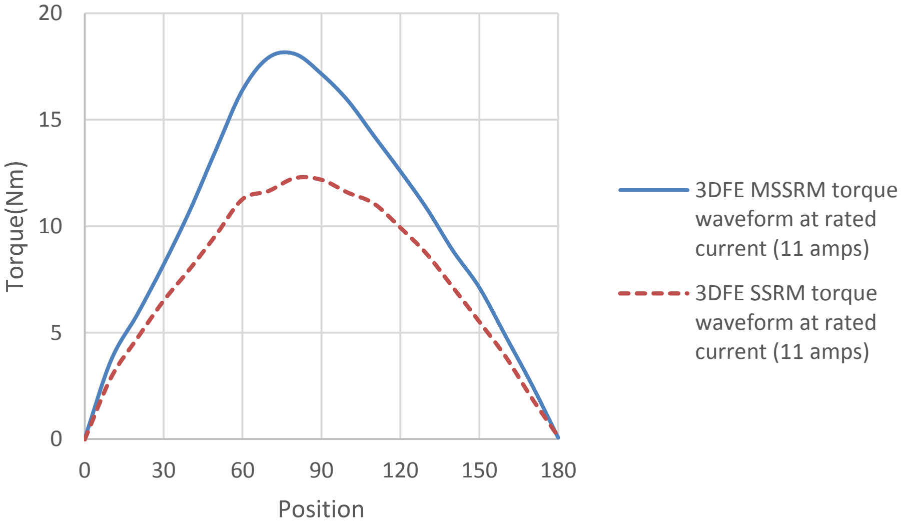

Figure 5-8: Torque at different angles of both 3DFE SSRM and MSSRM models

The fault tolerant MSSRM unaligned flux linkage increases significantly and remains linear throughout the current range as compared to the SSRM which saturates after 10 Amps. This is because the magnets avoid saturation of the stator tooth even at the unaligned position. This can result in a decrease in the torque of the machine because of increase in the unaligned flux linkage but it is compensated by high increase in the aligned flux linkage as stator tooth does not saturate early which results in keeping the aligned flux linkage high up to high values of current. Based on the aligned and unaligned flux linkage waveform, average torque of the MSSRM for different values of current is found shown in Figure 5-9. At the rated current, there is 29% increase in average torque of the fault tolerant MSSRM compared to fault tolerant SSRM for same current density.

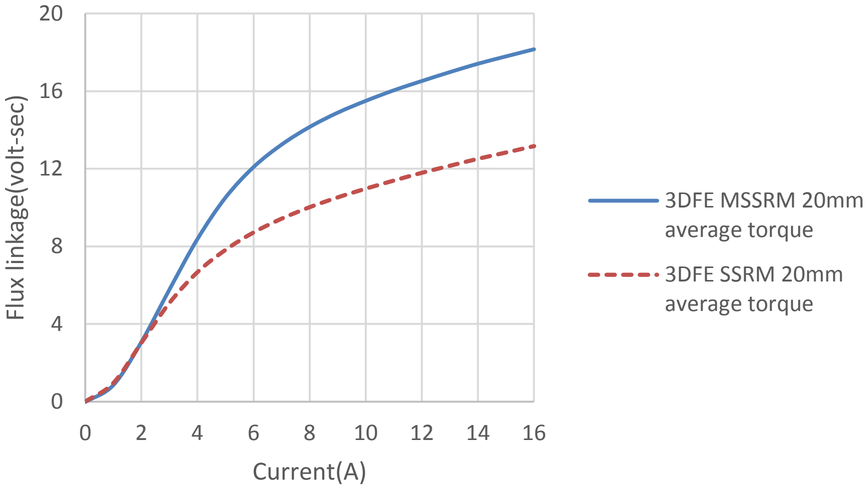

Figure 5-9: Average torque of 3DFE MSSRM and SSRM for different current values

5.5 Comparison of MSSRM on the basis of 2DFE and 3DFE results

Previous chapter shows that SSRM average torque decreases by 39% when end winding effect and leakage flux was included (3DFE results). The MSSRM was analysed on the same basis. Figure 5-10 shows average torque of the MSSRM from 3DFE and 2DFE models which shows a decrease in 32% torque at rated current. Compared to SSRM, this decrease in torque is 8% less compared to its 3DFE model because of the high aligned inductance due to the reverse magnetization of the stator core by magnets.

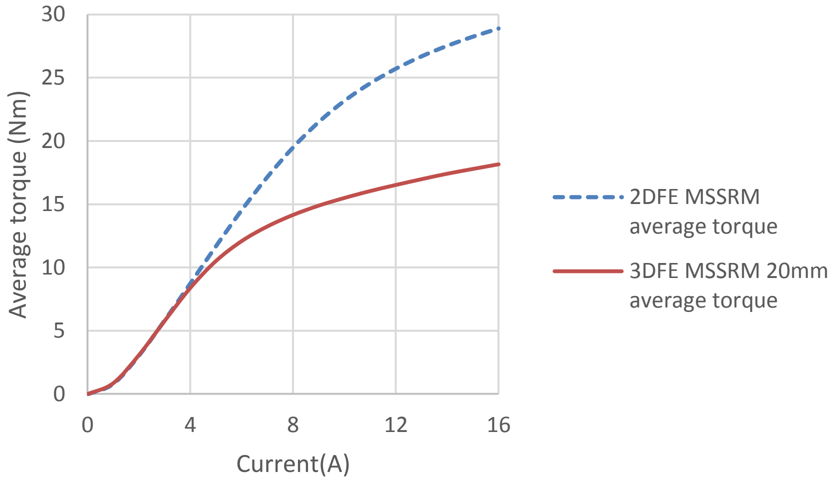

Figure 5-10: Average torque from 2DFE and 3DFE MSSRM models for different current values

5.6 Torque waveform of the machine at lower speed (stand still condition)

By assuming ideal condition with no effect of the high inductance (found from 3DFE model) on the drive at lower speed, 2DFE motion analysis of the fault tolerant MSSRM was conducted. Torque values found from 2DFE model were then multiplied by the decrease torque factor (as torque decrease shown in the above figure) to include the effect of end winding and leakage flux found from 3DFE model. Figure 5-11 shows torque waveform of the MSSRM at 50 rpm.

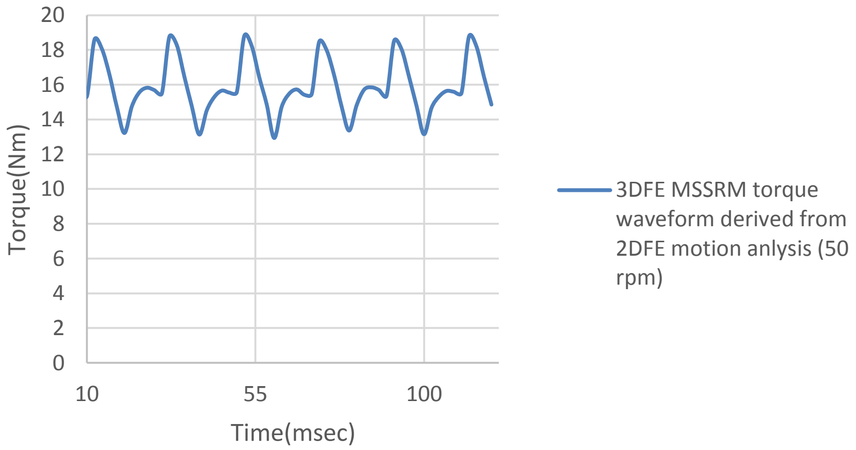

Figure 5-11: Torque wavfrom of MSSRM at 50 rpm based on the inclusion of 3DFE results

It is clear from the above figure that lower value of the MSSRM is still significantly lower than the target torque of 17 Nm throughout the complete electrical cycle of the machine.

5.7 Mass comparison

The new MSSRM was compared with the fault tolerant SSRM (20mm and 30mm stack length) and PM machine (20mm stack length). Figure 5-12 shows the mass of different parts of all the machine. The MSSRM overall mass increased only by 1.6% compared to the conventional SSRM (20mm) for the same volume. The mass of MSSRM is still 30% less than the PM machine. The MSSRM uses only 12% of magnet mass compared to the PM machine for the same active length.

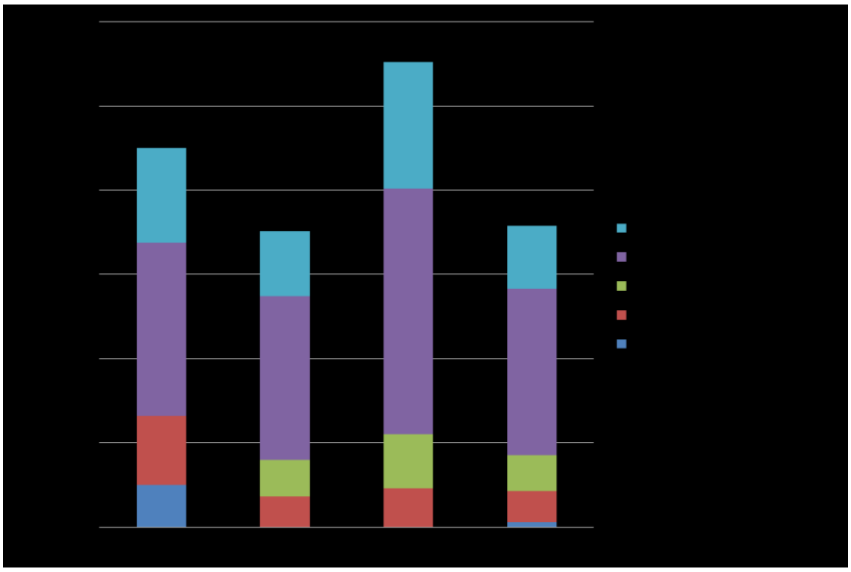

Figure 5-12: Mass of different parts of machines

5.8 Conclusion

The idea of magnets assist was introduced to the conventional SSRM designed to replace the PM actuator. Both 2DFE and 3DFE analyses of the new fault tolerant MSSRM were conducted. From 2DFE results, it was found that 23% more torque was produced by the MSSRM at rated current compared to conventional fault tolerant SSRM. 3DFE analysis shows as increase in 29% average torque compared to SSRM at the rated current. Motion analysis of the machine were carried out at rated current by assuming ideal condition (low speed) with no impact of the high inductance on the drive. It was found the lower value of the torque ripple of the MSSRM is still below the target torque value. The MSSRM mass was then compared with PM machine and SSRM which shows only 1.6% increase in mass compared to SSRM for the same volume. The MSSRM uses only 12% of PM machine magnet mass. Overall mass of MSSRM is still 30% less compared to PM machine for the same active length. This shows that the MSSRM can be good option to replace the SSRM which has high end winding effect which results in significant decrease in torque of the machine. Further investigation to the design of the MSSRM will be discussed in the next chapter to improve the performance of the machine.

Chapter 6 Design investigation

6.1 Introduction

From the previous chapter it is clear that the proposed fault tolerant MSSRM can be a good option on the basis of torque density compared to the SSRM. This chapter describes the work carried out to improve the design of the machine. The demagnetisation of magnets after placing them at the stator tooth tip is demonstrated under the fault conditions. Manual optimization of the machine was conducted by using 2DFE software to improve its performance. 3DFE analysis was conducted to investigate end winding effect. Machine performance at the critical speeds under ideal conditions was determined and the machine mass was compared with those of the SSRM and PM machine.

6.2 Operating point and demagnetisation of the magnets

Instead of optimising the machine from the start, it is important to investigate the demagnetisation and operating point of the magnet. As the fault tolerant MSSRM has very high current density with no cooling system, the temperature of the magnets during worst operating conditions was assumed to be 200°C. In fault condition, 1.5 times of rated current (11 Amps peak) can flow through the coils for a short time which can change the operating point of the magnet. At the same time, magnet can come under high external fields (form the coils) which can result in demagnetisation of the magnet. Flux from the coil divides into two parts which uses the small stator tooth to complete the magnetic circuit after passing through small rotor segments at the aligned position. At the unaligned position, the air gap length increases which can result in flux from the coils using both air gap and magnet to complete the magnetic circuit. An airgap of 0.1mm on either side of magnet was assumed as in practice, it is not possible to insert the magnets within the stator structure without a gap between the stator and magnet. By assuming worst condition in which the flux from the coil uses only magnet as a short magnetic flux path, the operating point of the magnet can be found by using equation (6-1) and (6-2).

$$H_m = \frac{-(\frac{B_g\, l_g}{\mu_o} + {}^{NI}\!/_{2})}{l_m} \tag{6-1}$$

$$B_m = B_r + \mu_r \mu_o H_m \tag{6-2}$$

where H_m is the magnetic field strength of the magnet, l_m is the length of the magnet, ${}^{NI}\!/_{2}$ term presents the MMF of the coil (half of its value is taken as half of the MMF which will oppose each magnet), μ_o is the permeability of free space ($4\pi * 1e^{-7}\ H/m$), B_g is the flux density within the airgap between magnet and the stator and l_g is the length of the air gap between the stator and the magnet.

By assuming fault condition, 1.5 times the rated root mean square (RMS) current was passed through the coils with the magnet of a temperature of 200°C, operating point and demagnetisation within the magnet were found. Assuming that the value of B_g 1T with l_m equals 4.8mm (found from the model), the value of H_m was derived using equation (6-1)

$$H_m\text{=-}5.66e^{5}\ \text{(A/m)} \tag{6-3}$$

Recomma 33E (samarium cobalt) has residual flux density (B_r) of 1.1T at 200°C, μ_r equals 1.05 and the value of H_m already found was inserted into equation (6-2)

$$B_m\text{=}0.35\text{T} \tag{6-4}$$

Hence the operating point of the magnet is well below the half of the residual flux density ($\frac{B_r}{2}$).

FEA software can be used to predict the amount of demagnetisation within the magnet. The software was used to analyse the demagnetisation by assuming the magnet temperature to be 200°C. Figure 6-1 shows the demagnetisation within the magnet while considering the temperature of the magnet is 200°C in fault conditions.

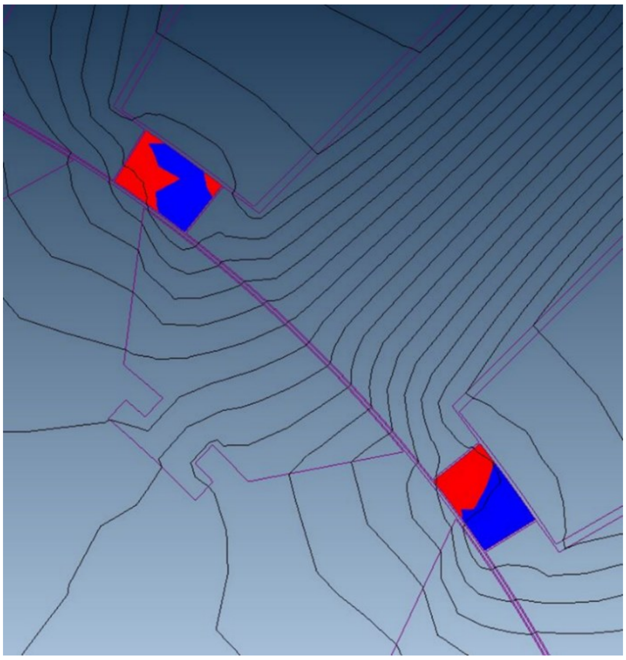

Figure 6-1: Predicted demagnetisation of the magnet when a high fault current flows through the stator with a magnet temperature 200°C

The blue area shows the safe area of magnet while the red area shows the demagnetised region of the magnet. It is clear from this figure that more than half of the magnet becomes demagnetised at high MMF.

6.2.1 Placement of the magnet above the stator tooth tip

In order to avoid the demagnetisation, various feasible shape magnet structures were investigated to decrease demagnetisation within the magnet. At the end, magnets were moved up the stator which was found as the only solution to avoid the demagnetisation. This leads to increase overall length of the magnet i.e. 10mm, thus increasing the resistance of the magnet to external magnetic field. The disadvantage of doing this is that the slot area decreases, which reduces the MMF per slot for fix current density and fill factor. Figure 6-2 shows quarter section of the fault tolerant MSSRM when the magnets were moved up the stator.

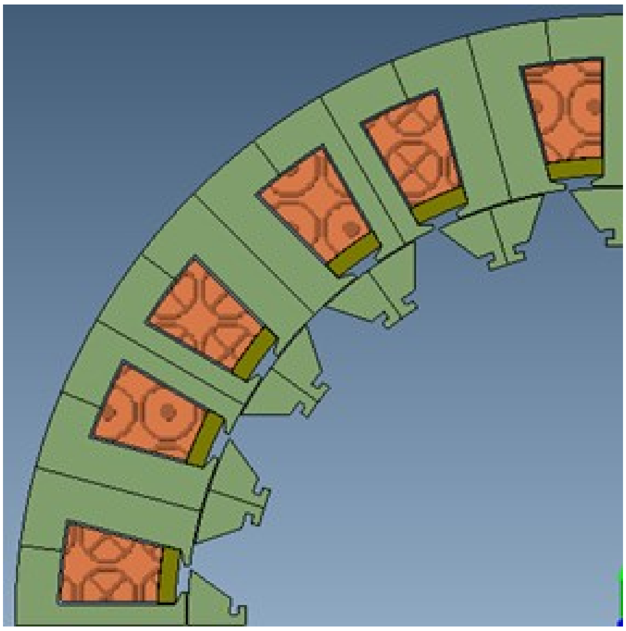

Figure 6-2: MSSRM with magnet moved up the stator

In order to get the required rated torque, the stack length of the machine was increased by 25%. The reason for choosing this stack length is because it will make mass of the machine almost equal to that of the PM machine even though the overall volume of the machine increases. The MSSRM was then optimised to reduce the overall mass and to increase the average torque of the machine.

6.2.2 New operating point of the magnet and demagnetisation

As the magnet was moved up, the overall length increased to 10mm. By using new magnetic circuit, the operating point of the magnet was found to be 0.74 T at 200°C. FEA software was the used to predict the demagnetisation within the magnet at 200°C.

Figure 6-3 shows the demagnetisation of the magnet when 1.5 times the rated RMS current flows through the coils.

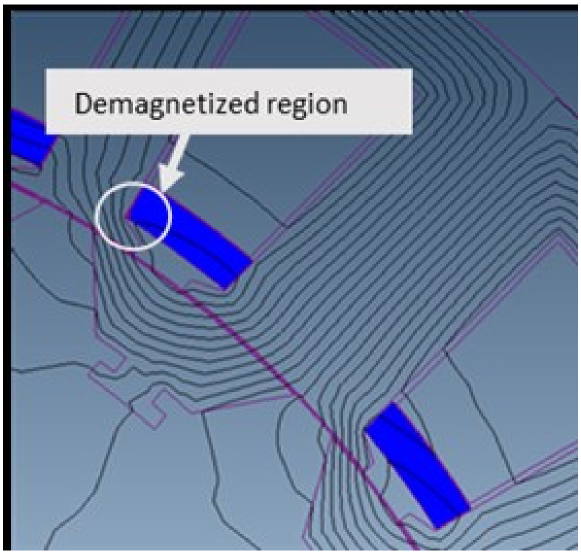

Figure 6-3: Demagnetisation in magnet when 16.5 amps of current flows through coil at 200°C

It is clear from the above figure that only a small area of the magnet becomes demagnetised (red area at the edges) while most of the magnet is safe (blue area) at all rotor angles.

6.3 Airgap between magnet and stator tooth tip

With rectangular shape magnet, as its radial distance from the centre increases, the distance of the outer surface of the magnet from the stator increases. It will increase the distance of the top of the magnet from the stator tooth, which will change the operating point of the magnet. In the FEA model, a gap of 0.2 mm was left at the top between magnet and stator. Figure 6-4 shows the increase in distance between stator and the magnet. This airgap was assumed in both 2DFE and 3DFE analyses of the machine.

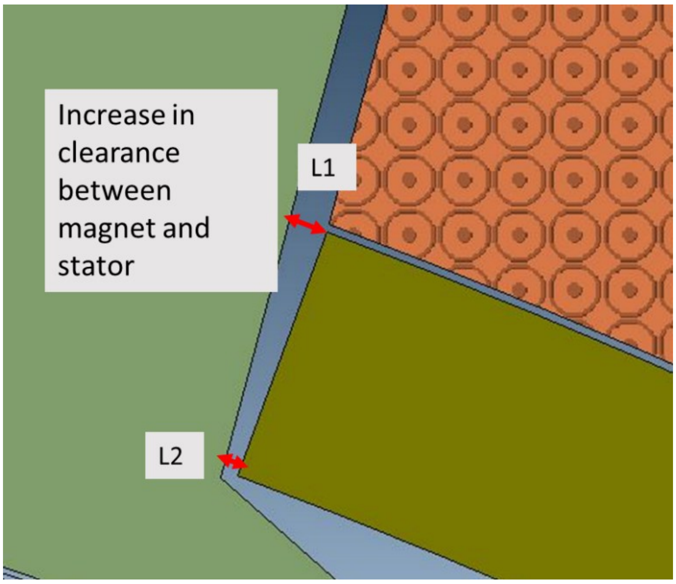

Figure 6-4: Increase in clearance between stator tooth and magnet(L1>>L2)

6.4 Optimisation of the MSSRM

Various parameters of the proposed model were changed to optimise the machine and keeping the current density, fill factor and outer diameter constant as that of the PM machine to achieve the target torques.

First the machine was optimized by using 2DFE software and the optimized model was simulated by using 3DFE software to determine the end winding effect and the effect of leakage flux which can result in decreasing the torque of the machine.

6.4.1 Choosing the best t/λ ratio

Tooth width to slot pitch ratio (t/λ) of fault tolerant MSSRM was varied with magnet thickness kept constant (3mm) to find average torque for the given current density and rated current. Figure 6-5 shows the variation in tooth width with changing t/λ. As the t/λ ratio decreases, the slot area increases which decreases the stator tooth thickness. In the case of the conventional SSRM, the thickness of the small stator tooth, stator core back and rotor coreback should be half of that of main stator tooth thickness (stator tooth around which coil is wound). The t/λ of the SSRM should be 0.67 to achieve maximum torque for the given copper loss [11] . However, by moving the magnets up the stator and at the same time magnet reverse magnetize the stator, the dimensions of the MSSRM can be varied to achieve high torque for a given current. Thus various parameters of the MSSRM were changed to improve the performance of it.

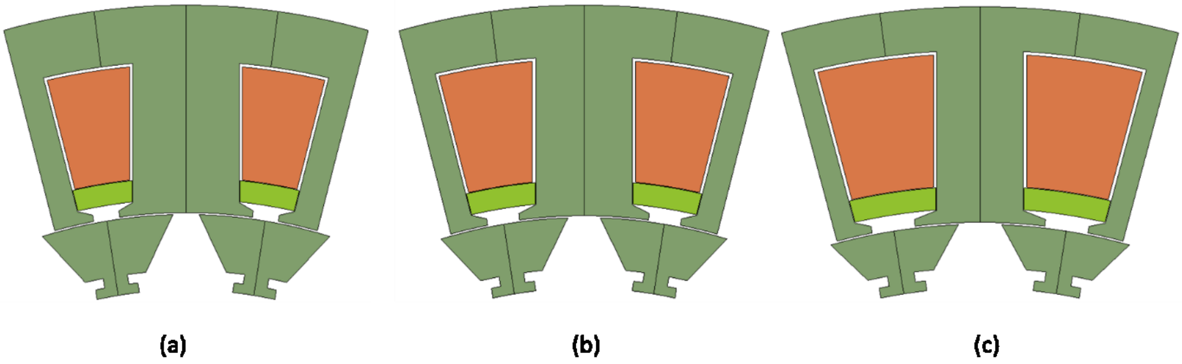

Figure 6-5: Effect on tooth thickness and slot area as tootht width to slot pitch rati0 changes (a) 0.67 t/λ (b)0.6 t/λ (c) 0.55 t/λ

Table 6-1 shows the parameters of the MSSRM for given t/λ ratio. 0.6 was chosen as it gives the maximum average torque for the given current density.

Table 6-1: Parameters of the MSSRM for different t/λ ratios

t/λ	**0.67**	**0.6**	**0.55**
Fill Factor	0.35	0.35	0.35
current density(A/mm^2)	26.1	26.1	26.1
Slot area(mm^2)	212.65	240.15	320.58
Rated current Peak(A)	11	11	11
Number of turns	260	297	341
Average Torque at 50 rpm(Nm)	22	23.1	22.2

6.4.2 Effect of changing magnet thickness

The thickness of the magnet was varied from 2 to 4.5mm to find the maximum torque at a certain thickness of magnet while keeping t/λ 0.6. Figure 6-6 shows the resulting average torque with different magnet thicknesses while keeping the current density constant.

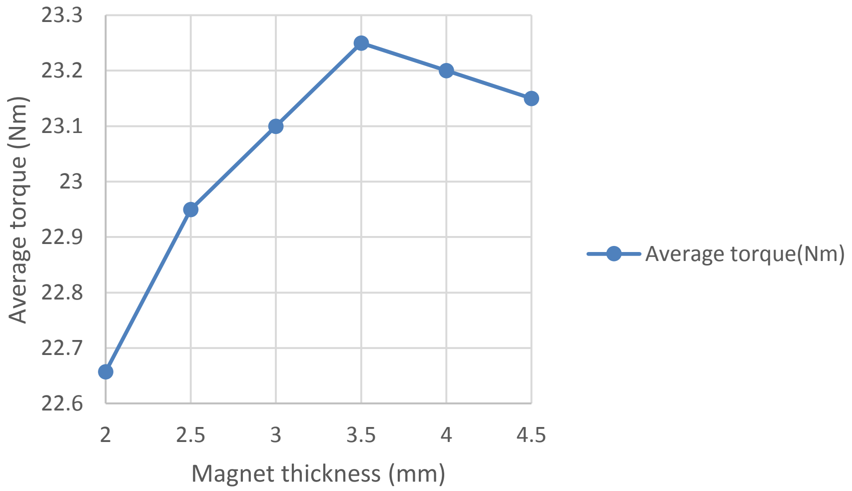

Figure 6-6: Effect on average torque of different thicknesses of magnets when machine was run at 50 rpm while keeping current density constant

It is clear from the above figure that a thickness of 3.5mm of the magnet gives the highest value of average torque.

6.4.3 Effect of change in stator coreback thickness

As the magnet moves up, electric loading of the machine decreases because of the lower slot area. Thus the stator coreback can be reduced in size according to the new electric loading. At the same time, magnet reverse magnetized the stator coreback. Figure 6-7 shows the resultant torque values from 2DFE models of the machine when the stator coreback was varied. As the stator coreback thickness decreases, the slot area increases which results in an increase in electric loading and hence increase in the average torque of the machine while magnet keeps avoiding saturation of the stator coreback.

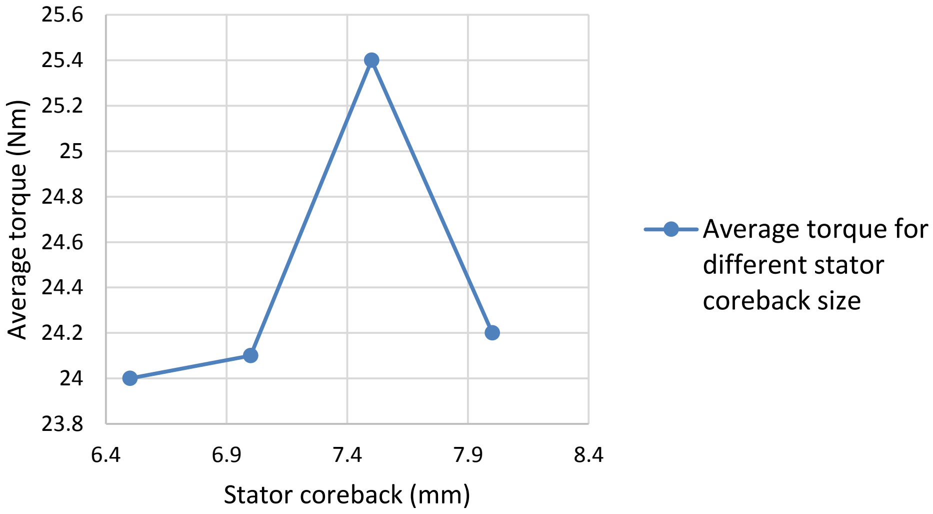

Figure 6-7: Effect of stator coreback thickness on average torque at 50 rpm

It is clear from Figure 6-7 that the average torque increases by 5% when the coreback was decreased to 7.5 mm. Hence 7.5 mm was chosen as the stator coreback thickness.

6.4.4 Effect of change in rotor coreback thickness

Just as with the stator coreback, the rotor coreback was also varied from 6.5 to 8 mm to see the effect on torque values. Figure 6-8 shows the resulting average torque when the rotor coreback thickness was varied while keeping the stator coreback thickness at 7.5 mm, t/λ at 0.6, and magnet thickness at 3.5 mm. Thick rotor coreback results in an increase in unaligned inductance which results in decrease in the torque of the machine.

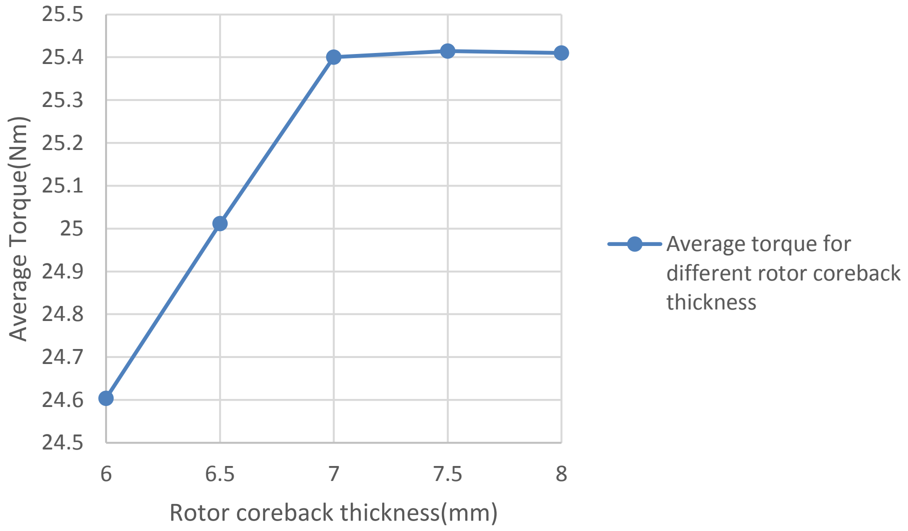

Figure 6-8: Effect of rotor coreback thickness on average torque at 50 rpm

It is clear from Figure 6-8 that torque hardly increases if the rotor coreback is above 7mm. Hence 7mm was chosen as the final stator coreback thickness.

Within the process of optimisation, the average torque increases by 8% (25.4 Nm) compared to original model (23.1 Nm) with decrease in lower value of torque ripple by only 2%. By decreasing the stator coreback thickness, the slot area increases which increases the number of turns for the given current density to 310. Figure 6-9 shows final dimensions of the machine.

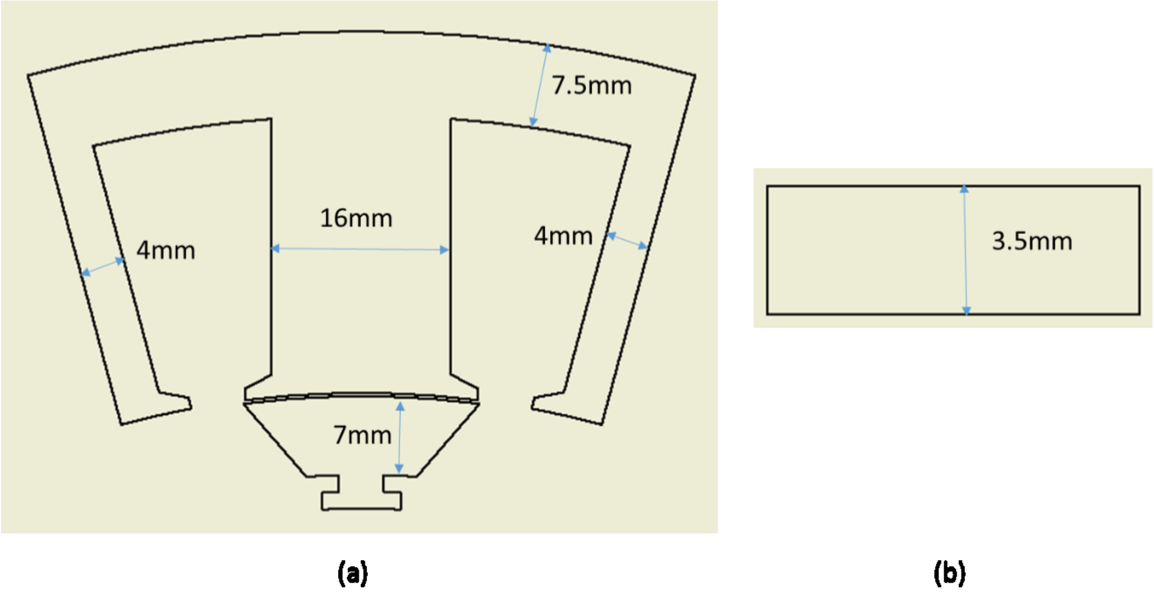

Figure 6-9: (a) Dimensions of stator and rotor with half of the small stator tooth thickness (b) magnet thickness

6.5 FE analysis of MSSRM

Both 2DFE and 3DFE models were simulated to investigate the end winding effect and leakage flux of the machine which results in decreasing the performance of the machine. Figure 6-10 shows 3DFE model with end windings and the mesh used within FEA model.

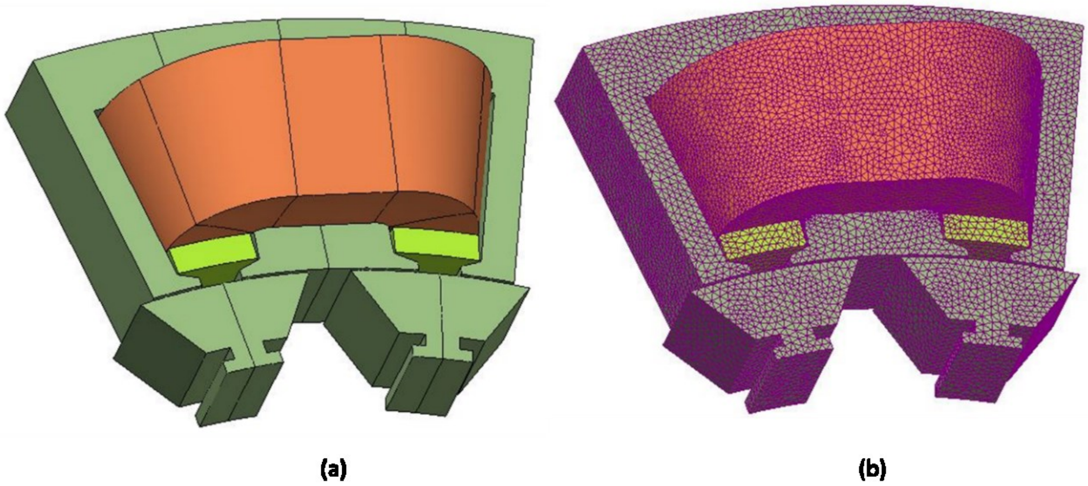

Figure 6-10: (a) Single tooth with winding of 3DFE stator model with rotor poles (b) single tooth with winding of 3DFE model with mesh

Figure 6-11 shows the 2DFE and 3DFE models torque values when rotor was rotated at different angles while Figure 6-12 shows the aligned and unaligned flux linkage of both 2DFE and 3DFE models .

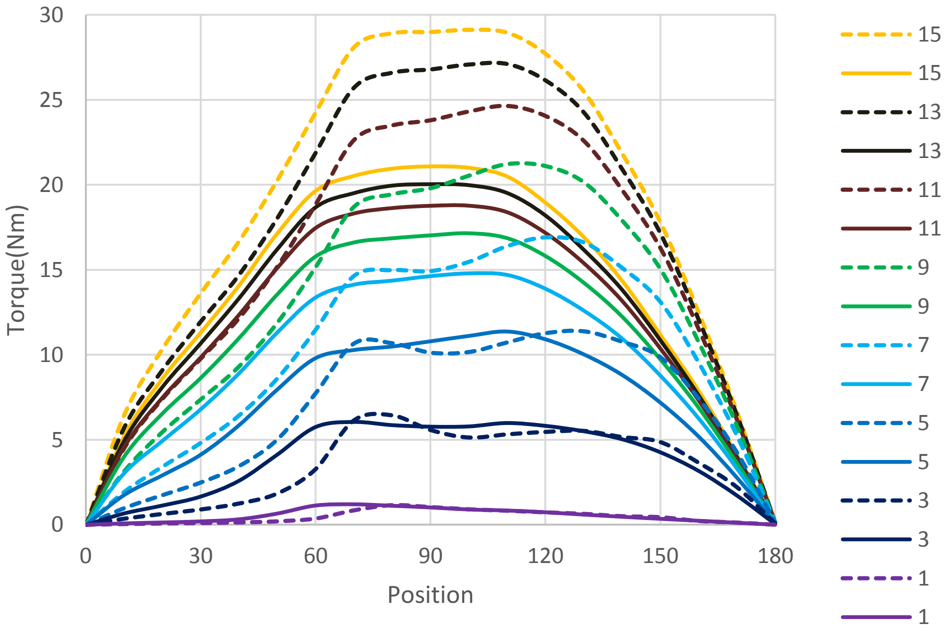

Figure 6-11: Torque values from the 3DFE and 2DFE models. Solid lines presents 3DFE model torque values while dashed lines presents 2DFE model torque values at different rotor angles for different current values

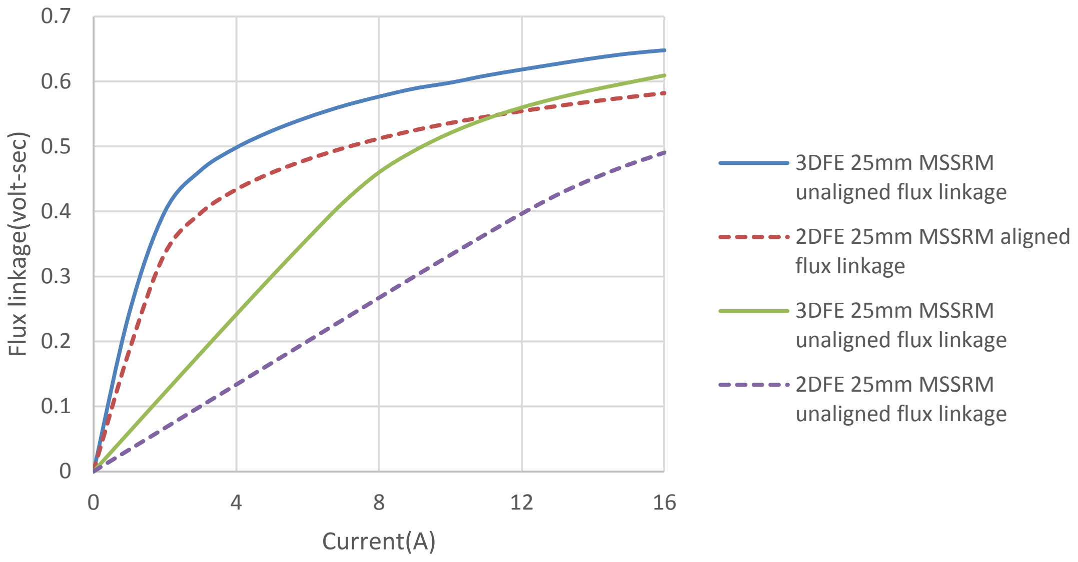

Figure 6-12: Aligned and unaligned flux linkage of 2DFE and 3DFE MSSRM

It is clear from torque waveform that there is a significant decrease in torque when 3DFE analysis of the machine was conducted. The reason for it can be found in Figure 6-12. There is an increase in aligned flux linkage in the 3DFE model results compared to the 2DFE model aligned flux linkage, however increase in the unaligned flux linkage in 3DFE model is significantly high and the main stator tooth even starts to saturate after 8 Amps. This shows the impact of the end windings which are almost of the same size as that of active windings within the slot. Base on the area between the aligned and unaligned flux linkage, the average torque of the machine was found shown in Figure 6-13. Average torque of MSSRM decreases by 23% compare to the 2DFE model at rated current.

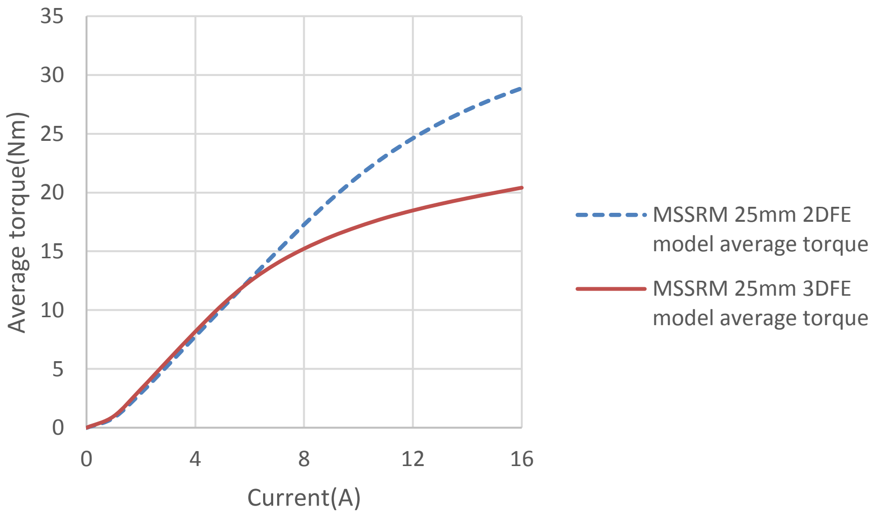

Figure 6-13: Average torque for different values of current of 2DFE and 3DFE MSSRM models

6.6 Torque of the MSSRM at critical speeds

The torque waveforms of the proposed fault tolerant MSSRM when two phases conducting at the same time were obtained by using 2DFE motion analysis models. Ideal current waveforms with no impact of the high inductance (found from 3DFE model) on the drive was assumed, 2DFE motion analysis was conducted to find the lower value of torque ripple at two critical speeds i.e. at 50 rpm and 900 rpm. From 3DFE model, it is clear that the average torque decreases because of high unaligned inductance, this decrease torque factor was multiplied with 2DFE model motion analysis torque waveform values throughout the complete electrical cycle. This helps in finding the lower value of torque ripple easily as 3DFE motion analysis is time consuming.

Figure 6-14 shows torque waveform when rated current flows through the coils. It is clear that the MSSRM cannot achieve the target torque at lower speed, however by increasing the current to 13 Amps, the lower value of torque ripple above 17 Nm can be achieved. Figure 6-15 shows torque waveform of the MSSRM at 900 rpm found by using the same assumptions mentioned above. The MSSRM is able to achieve torque (14.2 Nm) above the target torque (13.5 Nm) with torque ripple of 40%.

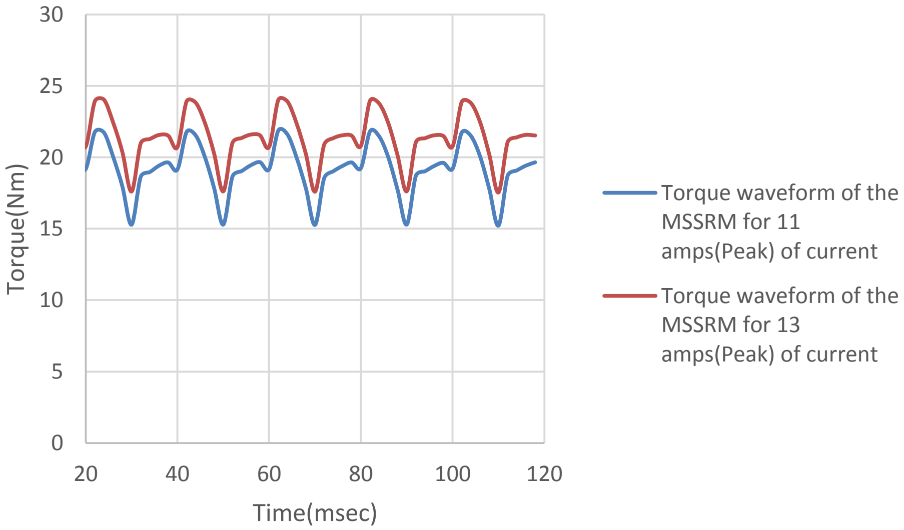

Figure 6-14: Torque wavform at lower speed (50 rpm) for different values of current

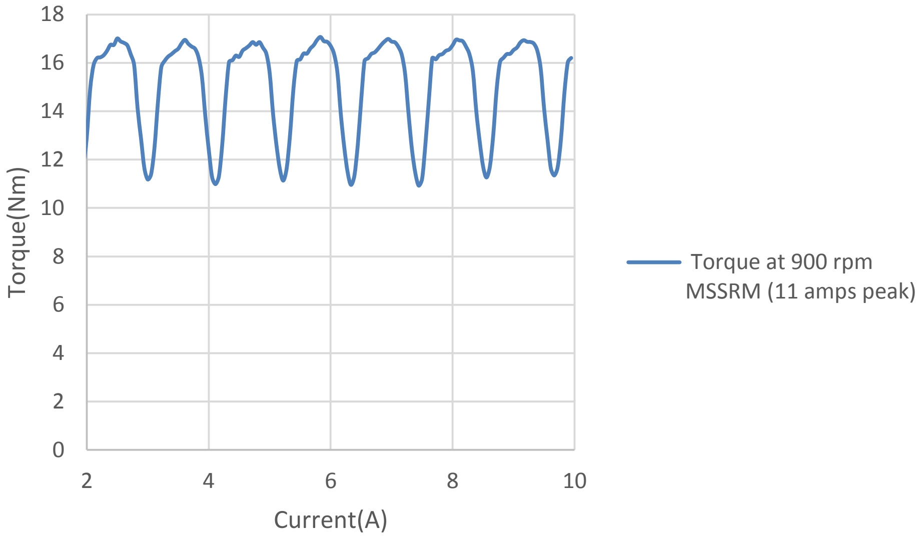

Figure 6-15: Average torque of the MSSRM at 900 rpm with 35(elect degree) advance

6.7 Losses in the MSSRM

Losses within the machine were found in order to determine the efficiency of the machine

6.7.1 DC winding loss

The fault tolerant MSSRM will work at lower speeds with high current density and high torque requirement from the machine at lower speed (stand still condition) which results in dominant DC loss. A single turn within the proposed MSSRM has 50mm length in the slot and with a mean length of 53mm round the end windings. By assuming copper conductivity to be $58.13\text{x}10^{6}\Omega^{-1}m^{-1}$ at $200C^{\circ}$, the winding loss found shown in Table 6-2. Losses in the magnet found using FEA software amounted to 3.99 watts.

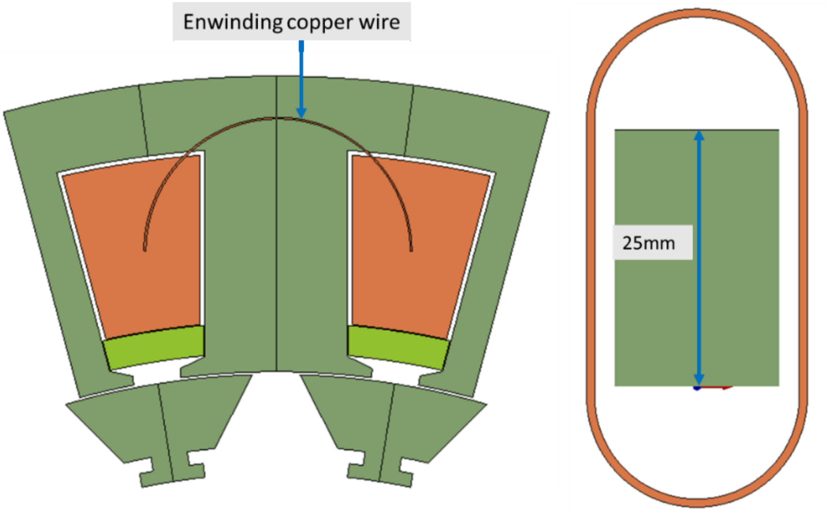

Figure 6-16: Winding arrangment, stator cross section(left), tooth cross section(right)

Table 6-2: Copper loss of the MSSRM when copper temperature is 200°C

Resistance/phase at 200°C (Ω)	6.62
slot area	250
Average length of each turn(mm)	103
fill factor	0.35
number of turns/slot	310
Area of one conductor (mm^2)	0.28
current(rms value)(A)	9.19
Copper loss/phase (watts)	560

6.7.2 Iron loss

Iron loss within machine was found using FEA software. The FEA software uses Steinmetz equation.

$$P = K_h f^{\alpha} B^{\beta} + K_e(s f B)^2 \qquad (6\text{-}5)$$

Where K_h is hysteresis and K_e is eddy current coefficient, α and β are frequency and flux density exponents respectively. The losses were multiplied by the "build factor" of 1.6[70]. The build factor considers effect of manufacturing on constructed machines.

Table 6-3 shows losses in different parts of the machine at 900 rpm.

Table 6-3: Iron losses of MSSRM at 20°C

	Hysteresis losses (watts)	Eddy current losses (watts)
stator losses(watts)	20.80	5.60
Rotor losses(watts)	5.64	1.11
total loss(watts)	26.44	6.71
total iron loss(watts)	33.14	

6.7.3 AC losses

AC losses of the MSSRM were found by running the FEA model at 900 rpm. Four solid conductors at four different points within the slot were assumed and simulations were done to find the conductor which gives maximum AC loss. The conductor close to main stator tooth and magnet was found to give the maximum AC loss. For worst case scenario, this loss was assumed in all conductors which was then multiplied by the number of turns and number of slots to get the resulting AC loss of 2.79 Watts.

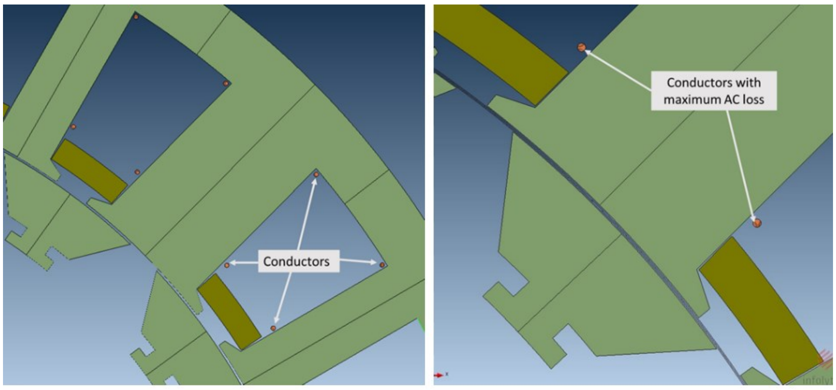

(a) (b)

Figure 6-17: (a) Four conductors at different positions within the slot area (b) Conductor having maximum AC loss

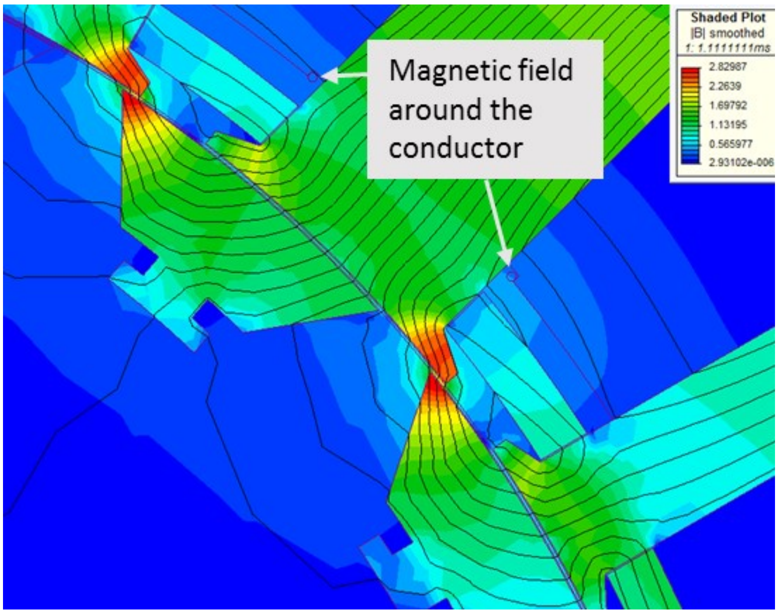

Figure 6-18: Rotor angle at which flux density across conductor is maximum

AC losses were also found using the following expression [71]

$$P_{ac}=\frac{\pi}{64}.\sigma.\text{l}.\ d^4.\frac{dB^2}{dt} \qquad (6\text{-}6)$$

where σ is the conductivity of the copper wire, l is the length of the wire, d is the diameter of the coil, B is the flux density across the coil which varies with time.

AC losses in this case were found to be 3.75 Watts. Both results show very small AC losses, thus avoiding the use of the stranded wire (normally used to avoid ac losses). Figure 6-19 shows variation of flux density in conductor in one complete electrical cycle which can be used to calculate the AC losses by using equation (6-8).

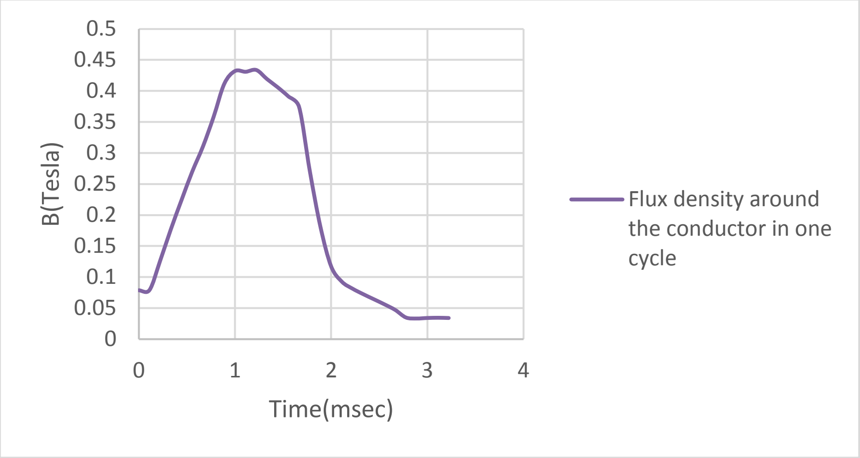

Figure 6-19: Variation of magnetic field in the conductor in one complete cycle

6.8 Efficiency of MSSRM

The efficiency of the MSSRM at 900 rpm was found for a copper temperature of 20°C. There is a decrease in current value as speed increases for a fixed voltage of 480 V as current cannot reach its rated value rapidly at high speeds because of higher back EMF and inductance. Table 6-4 shows all of the losses and the overall efficiency of the machine.

Table 6-4: Efficiency of MSSRM at 900 rpm (200°C)

Resistance/phase at 200°C (Ω)	6.62
Current(rms value)(A)	6.62
Copper loss in 3 phases (watts)	868
Iron loss(watts)	31.44
Magnet loss(watts)	3.99
AC loss(watts)	2.79
Total Loss(watts)	906.22
Speed(rpm)	900
Torque(Nm)	18.2
Mechanical Output power(watts)	1339.26
Efficiency (%)	65

6.9 Mass comparison

All three machines were compared on the basis of the mass of different parts of the machine. FEA software gives the mass of different parts of the machine after simulation. Figure 6-20 shows the masses of different parts of the three machines.

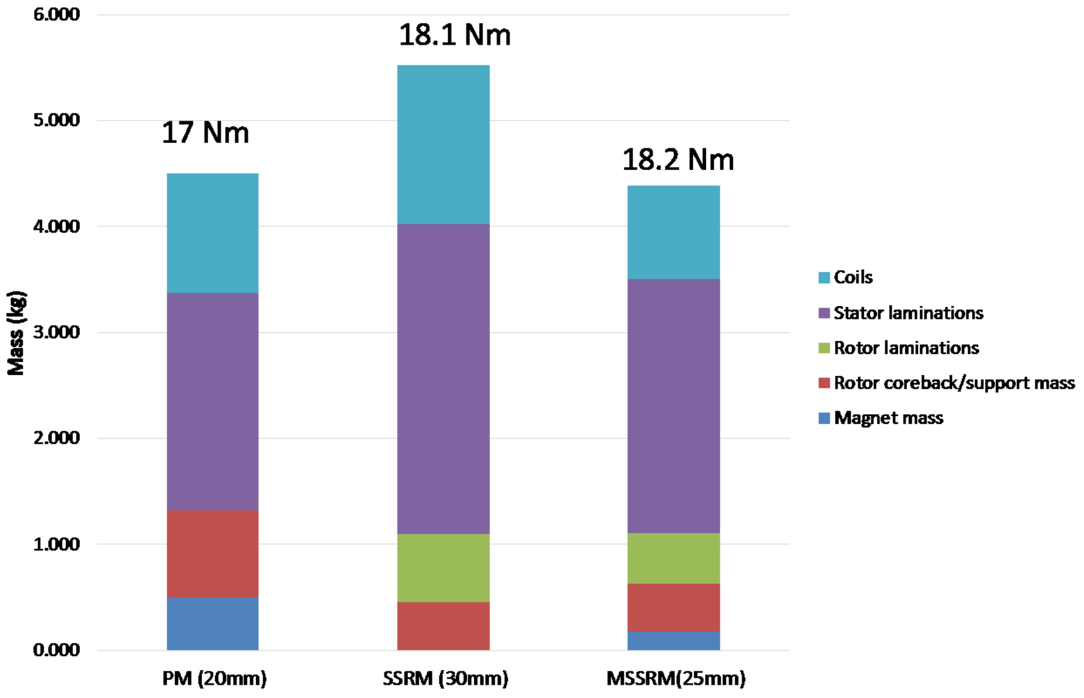

Figure 6-20: Mass of different parts of three machines

The MSSRM mass is still 2% less compared to the PM machine, while the mass of the SSRM is 15% higher than the PM machine. The real difference between the MSSRM and PM machine lies in the mass of the magnet which in the MSSRM decreases by 68% compared to the PM machine. Figure 6-21 shows the comparison of the magnet mass.

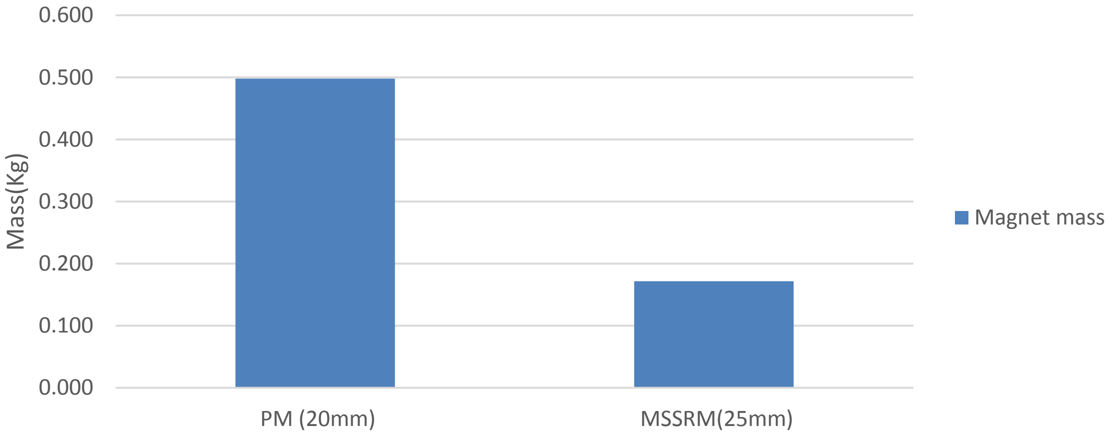

Figure 6-21: Mass of the magnets in the PM and MSSRM machines

6.10 Conclusion

The fault tolerant MSSRM design was investigated under fault conditions which results in demagnetisation of the magnet. Magnets were moved up the stator to avoid the demagnetisation by increasing the overall active length of the magnet. By moving the magnets up, electric loading of the machine reduces, therefore active length of the machine was increased to get more torque. Different parameters within the model were changed to increase average torque of the machine for given fixed conditions. From 3DFE analysis, it is concluded that MSSRM at lower speed can achieve the target torque if the rated current is increased to 13 Amps (peak) to achieve the standstill torque condition. In terms of stack length, the MSSRM size only increases by 25% to that of PM machine. As compared to SSRM, the active length is 25% less. The mass of MSSRM is still 2% less than the PM machine. The MSSRM uses only 32% of the PM machine magnet mass. The mass of the proposed model is 21% less as compared to 30mm fault tolerant SSRM.

Chapter 7 Novel permanent magnet assisted cylindrical shape inductor

7.1 Introduction

This chapter explains the design and working principal of a new permanent magnet assisted pot core inductor which will be used in the switched reluctance drive to reduce current ripple. Design was improved by using the FEA software to see the different parameters which can affect the inductance value. The inductor was designed based on the area available within the drive system. It was then compared with the conventional E-E core magnetically biased inductor (MBI) on the basis of inductance value for the same copper loss and core mass.

7.2 Basic idea

Just like conventional SRM's, the working area of a conventional inductor is limited to the first quadrant of B-H curve. Considering the linear region of the inductor, when current is passed through the coil of a conventional inductor, the flux density within the inductor core rises from 0 to maximum flux density (B_{sat}), where B_{sat} is the maximum allowable flux density of the core above which the core saturates. The value of B_{sat} depends on the material from which the core is made.

For a simple inductor, inductance L with a given winding number N and core cross-sectional area A_c , the relationship between the current range ΔI and the flux density range ΔB is given by:

$$\mathrm{L.\Delta I = N.\Delta B.A_c} \tag{7-1}$$

For a simple inductor, equation (7-1) holds until the material begins to saturate. The value of ΔB varies from 0 to B_{sat} for conventional inductors.

By the introduction of magnets, the working range of inductor can be extended to the third quadrant, hence increasing the unsaturation range of the inductor. The flux from the magnets should be opposing to the main flux from the coil. By passing current in the coil, the flux density of the core will not increase from 0 to B_{sat} but from $-B_{bias}$ to B_{sat}, thus increasing the unsaturated linear region of the core.

Figure 7-1 shows the maximum working range of conventional and MB inductor.

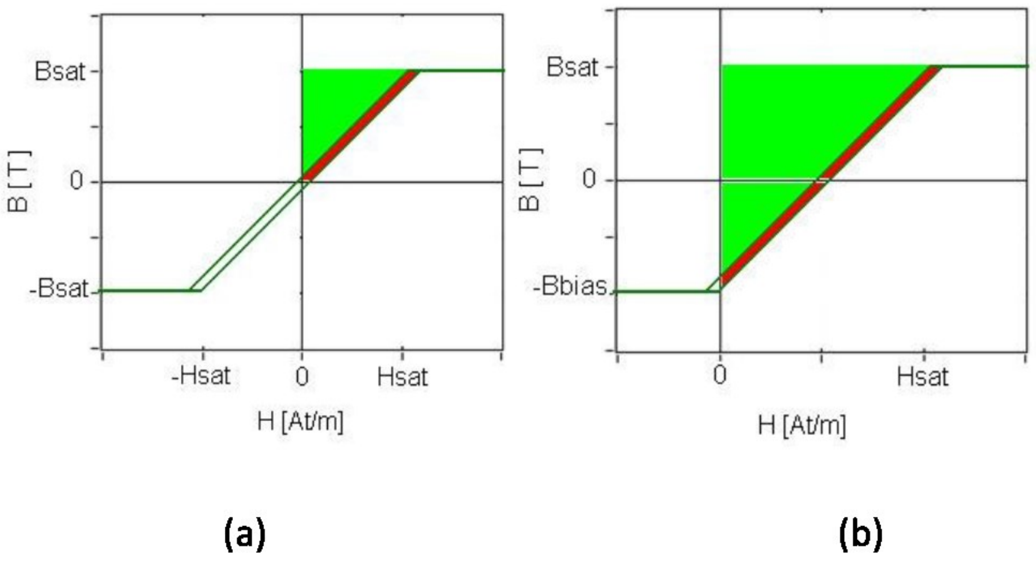

Figure 7-1: (a) Working area of conventional inductor (b) Extended working area of MB inductor

7.3 Initial design and working principal

Initial design of the pot core MBI is shown in Figure 7-2. The design consists of a central main core with coils wound around it. The flux from the main central core flows through the first endcap, air gap plate and second endcap back to the main central core. Permanent magnets are placed within the magnet plates along with the air gap plate with the direction of the flux from the permanent magnets opposing the main flux from the coils.

Direction of flux path through the inductor is shown in Figure 7-3. Because of the bigger axial length of the magnets, overall reluctance of the magnet path is higher than smaller air gap plates, thus the flux from the main coils will flow through the air gap plates through the air gap region.

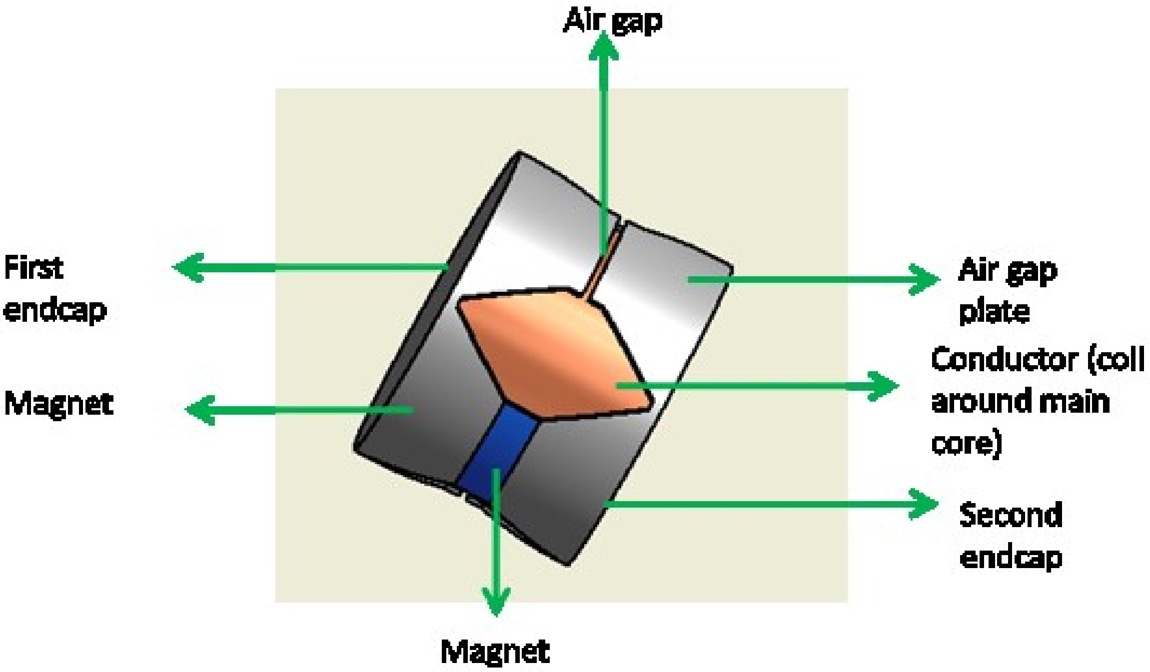

Figure 7-2: Initial design of pot core MBI

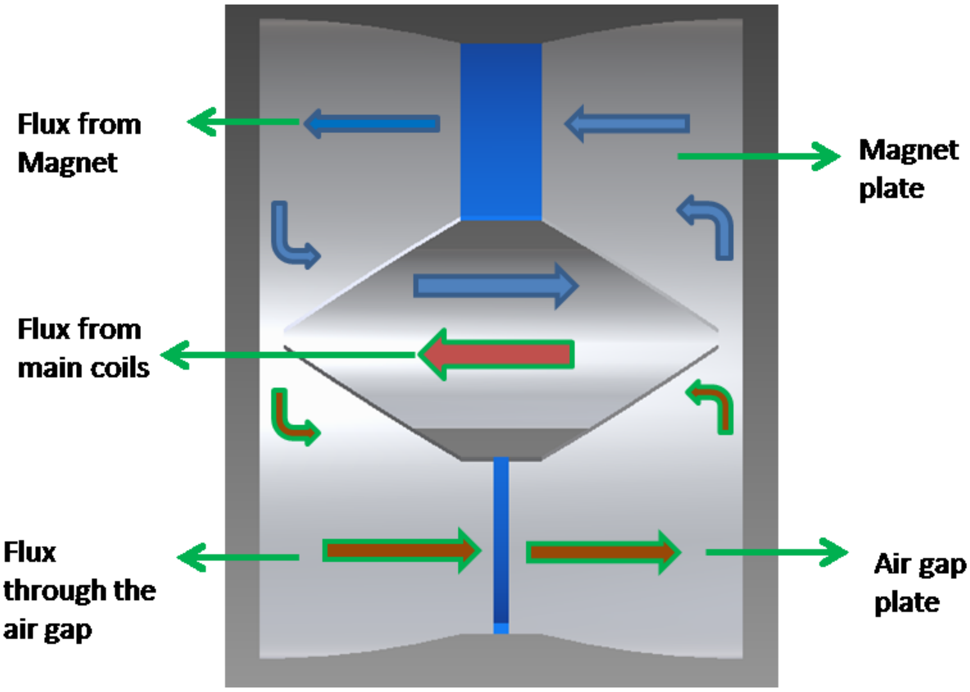

Figure 7-3: Flux paths of pot core MBI

7.4 Design parameters

The dimensions of the inductor are chosen according to the limited area available within the drive system. Material used during simulation for the core of the inductor is insulated powder (SMC). Dimensions of pot core MBI were chosen on the same basis as that of E-E core. In conventional E-E core, the main core width is double to that of side cores with air gaps, with area of inductor equals product of width of main tooth and length of the inductor.

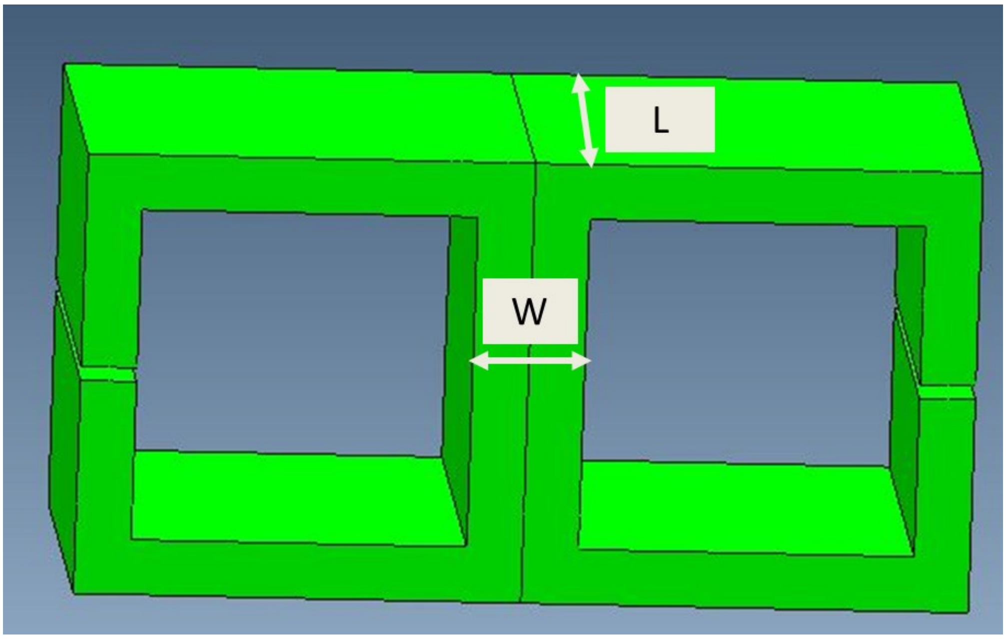

Figure 7-4: Dimesions required to find the cross sectional area of E core inductor

$$A_c\text{=W*L} \tag{7-2}$$

On the same idea, the pot core flux divides into four different sections (sections can be increased). As the structure is round shape, the value of Ac (cross sectional area of the inductor) is given by the equation (7-3)

$$A_c\text{=}2\pi(D/2)t_{endcap} \tag{7-3}$$

Where D is the diameter of the central main core, t_{endcap} is the thickness of the endcap which comes into contact with the main core. Figure 7-5 shows a simple structure of pot core inductor.

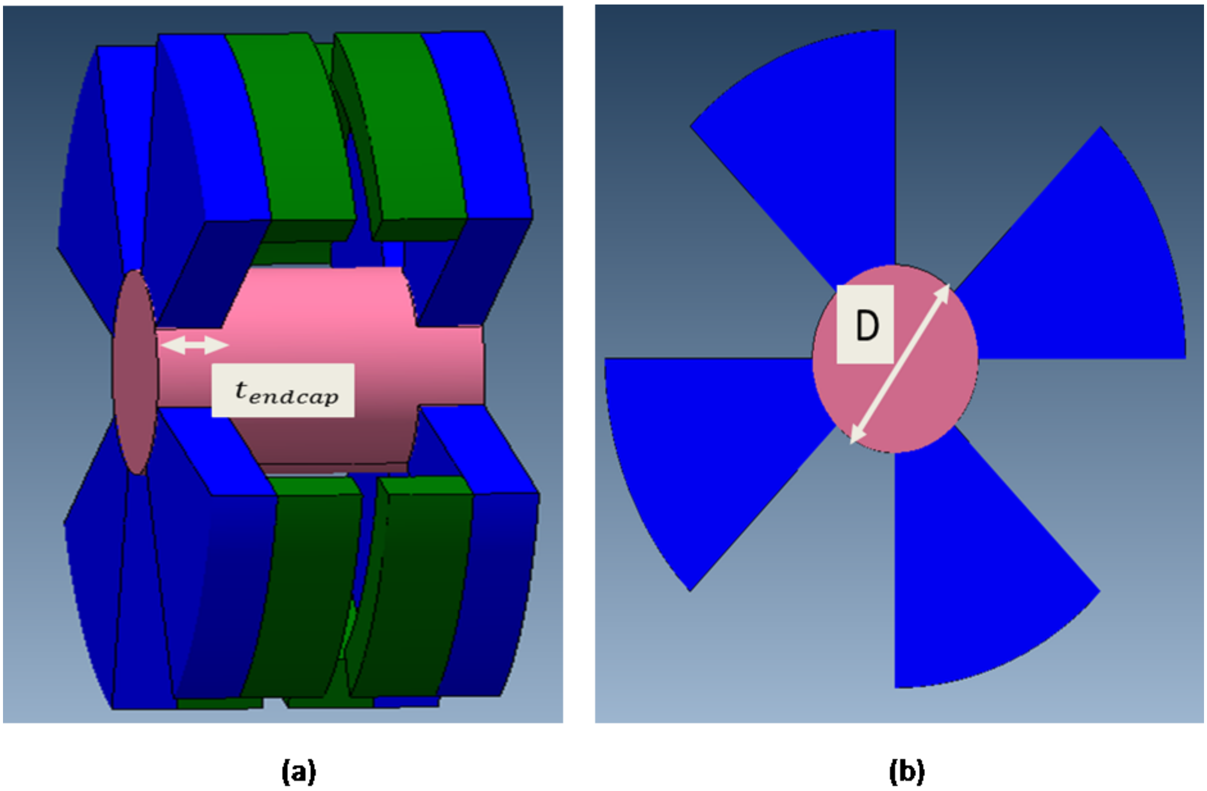

Figure 7-5: (a) side view of pot core MBI with end plate thickness (b) front view with diameter of main core

7.5 SMC Material

Soft magnetic composite (SMC) material is an isotropic powder that is commonly used nowadays in making small machines and inductors. Though permeability of the material is much lower than laminated steel, better three dimensional (3D) magnetic properties of the material makes it suitable for complex structures which is hard to make with laminated steel [72]. The material is made up of small powder particles which helps in reducing eddy current losses by providing small path for the flow of eddy currents, thus increasing overall resistance of the material at higher frequencies and reduction in iron losses.

7.6 Different designs of pot core MBI and their characteristics

Different design of the pot core MBI were simulated by using FEA software to see the characteristics of the inductor. Design was then improved by considering some of the drawbacks which some of the designs have and the shape was changed to improve the performance of the inductor.

7.6.1 Separate magnet and air gap plate

In this case the magnet and air gap plates are placed separately. Structure of such pot core MBI is shown in the Figure 7-6.

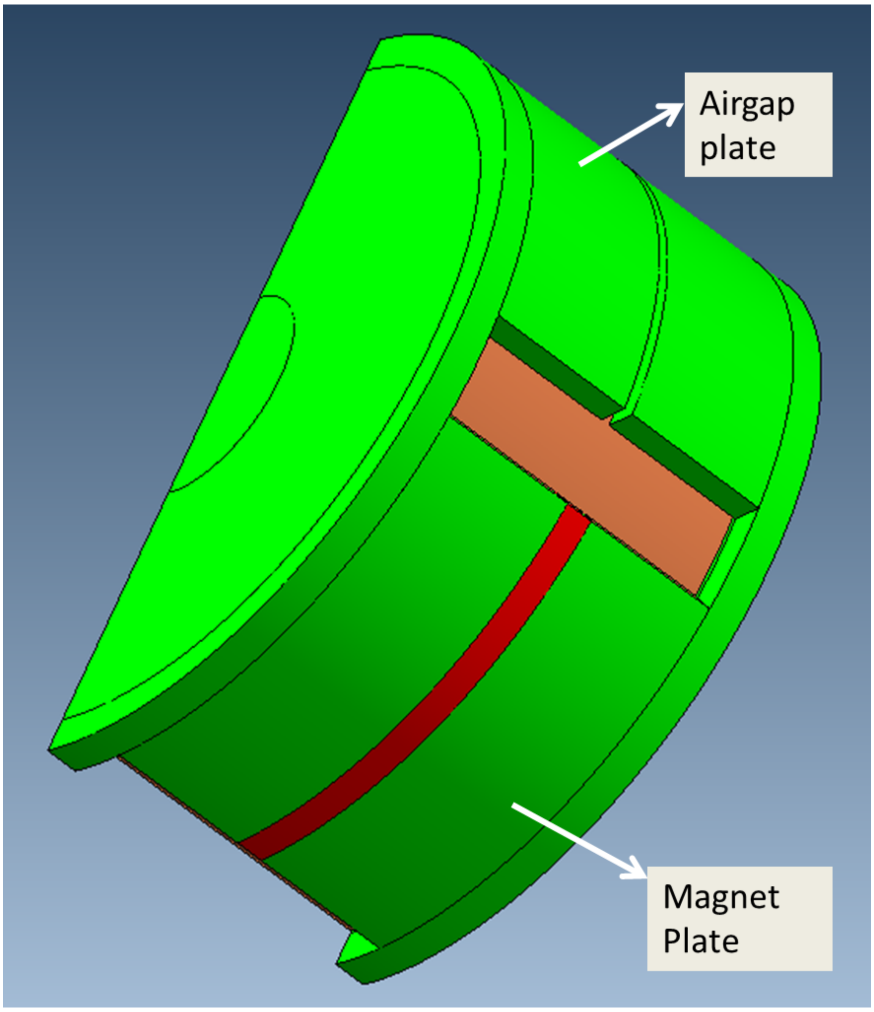

Figure 7-6: Pot core MBI with airgap and magnet separately placed

The disadvantage with such a structure is that only the core is reverse magnetised. When current flows through the main coil, most of the flux flows through the air gap plates and as the air gap flux is not reverse magnetised, it becomes saturate early, thus lowering the inductance value at higher currents. By placing the magnet and air gap plate separately, overall size of magnets increases. To place a single piece of magnet with such size in an inductor during the construction is not a cost effective method. Circular magnets are expensive and easy to break. Also if the rectangular magnets are used, this will increase the overall outer diameter of the inductor as most of the inductor will be bulging out from the sides.

Flux paths when no current flows through the coil and when current flows through the coil is shown in Figure 7-7.

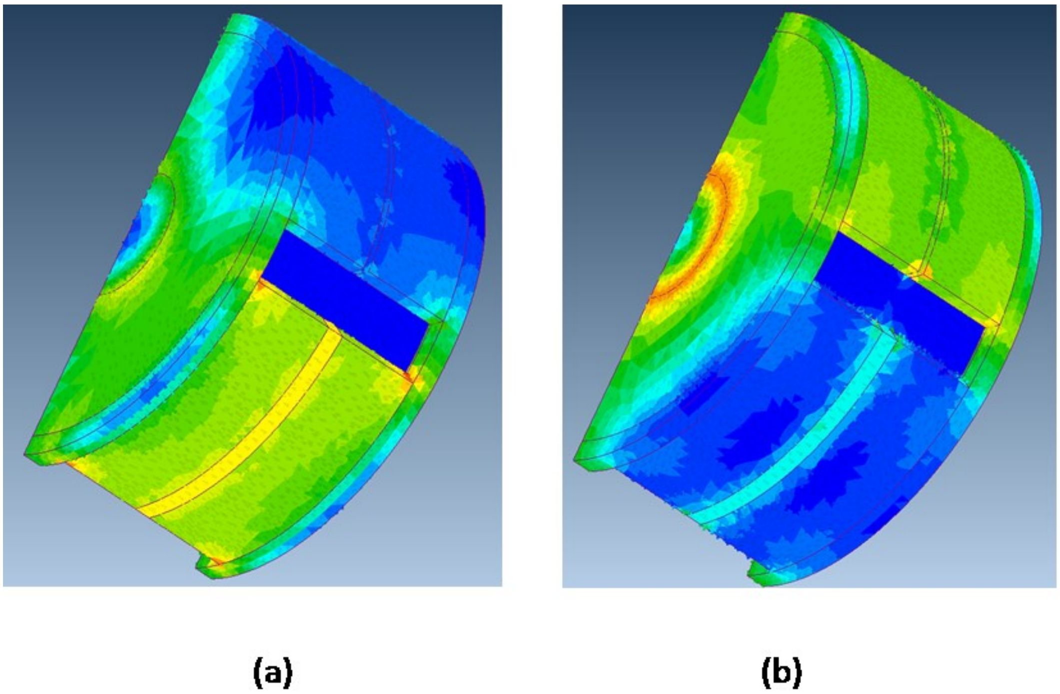

Figure 7-7: (a) When no current flows through the coils (flux from the magnets only) (b) when flux though the coils and hence all flux from coils flows through the airgap plates

7.6.2 Air gap and magnet plates together

In order to overcome the disadvantages of the above structure, both air gap and magnet plates were made together. The single long magnet from above structure was divided into two small magnets. The air gap plate was also divided into two with half of the plate placed on each side of the magnet.

This helps in avoiding disadvantages with the separate plate’s structure. The magnets are smaller in size with full use of endcap area in all directions around main central core. Smaller size magnets also help in ease of construction with less magnet bulging out from the corners.

The structure was further improved to make the size of the magnets as smaller as possible while keeping inductance constant for higher values of current.

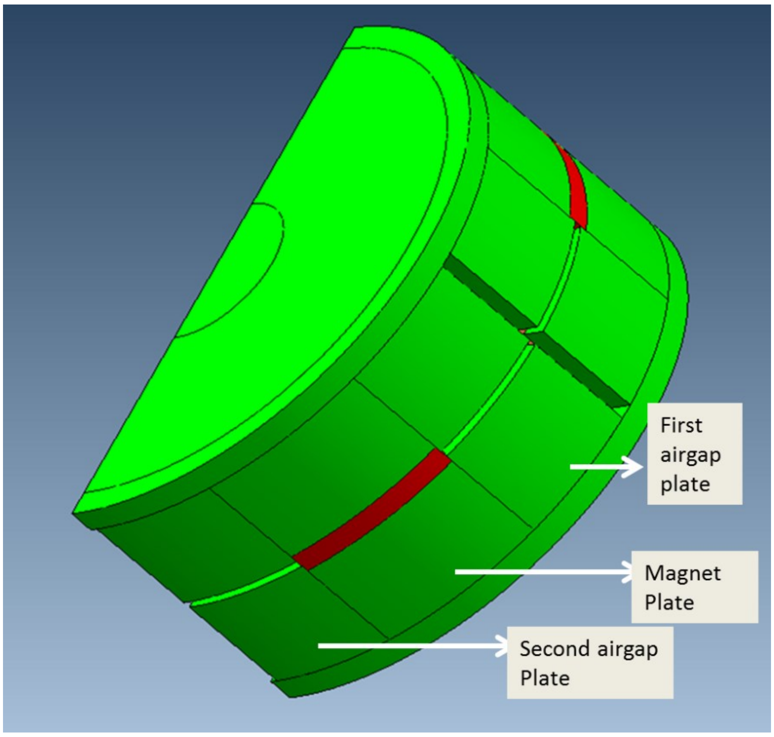

Figure 7-8: Air gap plate and magnet plate together

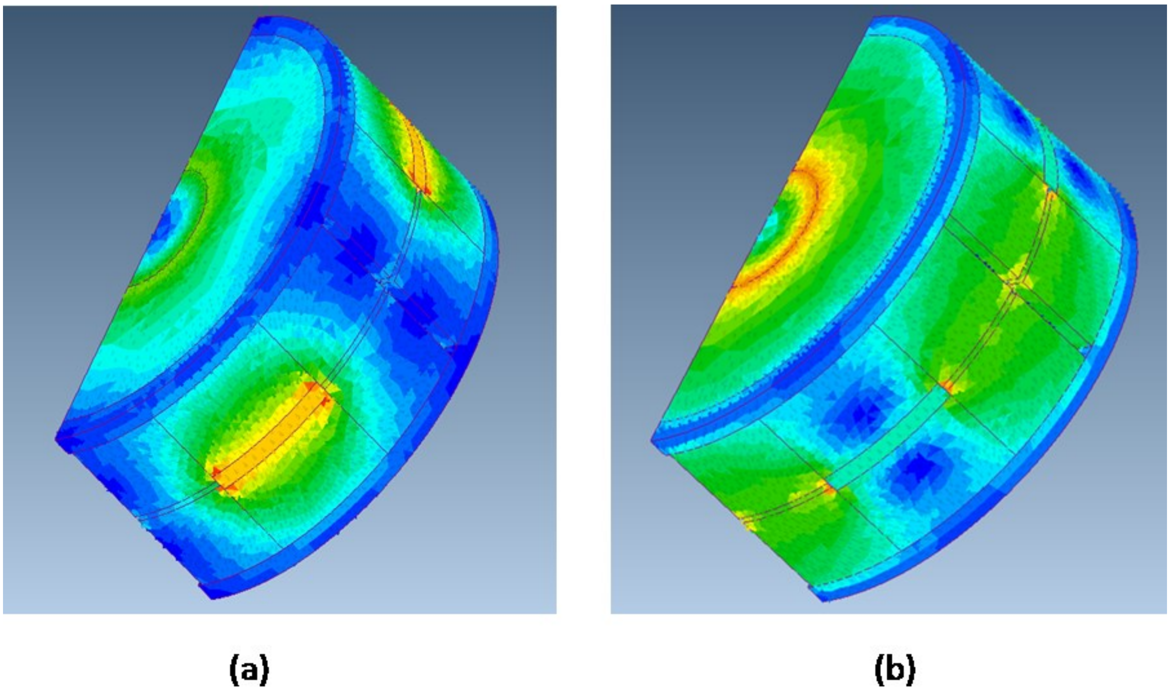

Figure 7-9: (a) Flux from the magnets only (b) flux from the magnets and main coil together

Figure 7-8 and Figure 7-9 show structure of the inductor with magnet plates in the centre while the air gap plates at the sides. The disadvantage with such structure is that most of the flux from the magnets passes through the magnet plates to the centre main core without flowing through the air gap plates, hence not reverse magnetizing the airgap plates. This results in earlier saturation of inductor again.

7.7 Changing magnet position and core structure

At this stage the inductor endplate thickness was changed at 3 different positions as the outer diameter of the end plate increases. This is because the endcap circumferential area increases as the distance from the central core increases, thus to make its area mathematically equal to 1/4th of the main core area (the flux from the main core flows through 4 different air gap plates then back to the other side of the main core). Figure 7-10 shows the resultant half structure of the inductor when extra core area was removed.

Magnets were moved on the sides with air gap plate in the centre. The position of the magnet was changed to see the effect on the inductance for different magnet numbers at different positions.

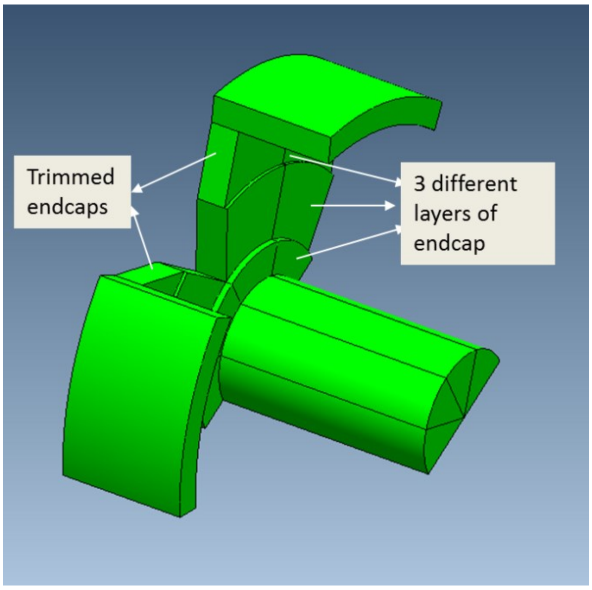

Figure 7-10: Resultant core structure after trimming the endcaps

Different topologies of the inductor were then simulated by changing the number of magnets and the position of the magnets. Figure 7-11 shows different structures of the same inductor where the magnet position was changed. Direction of the magnet flux and the flux from the main coil is shown in each figure.

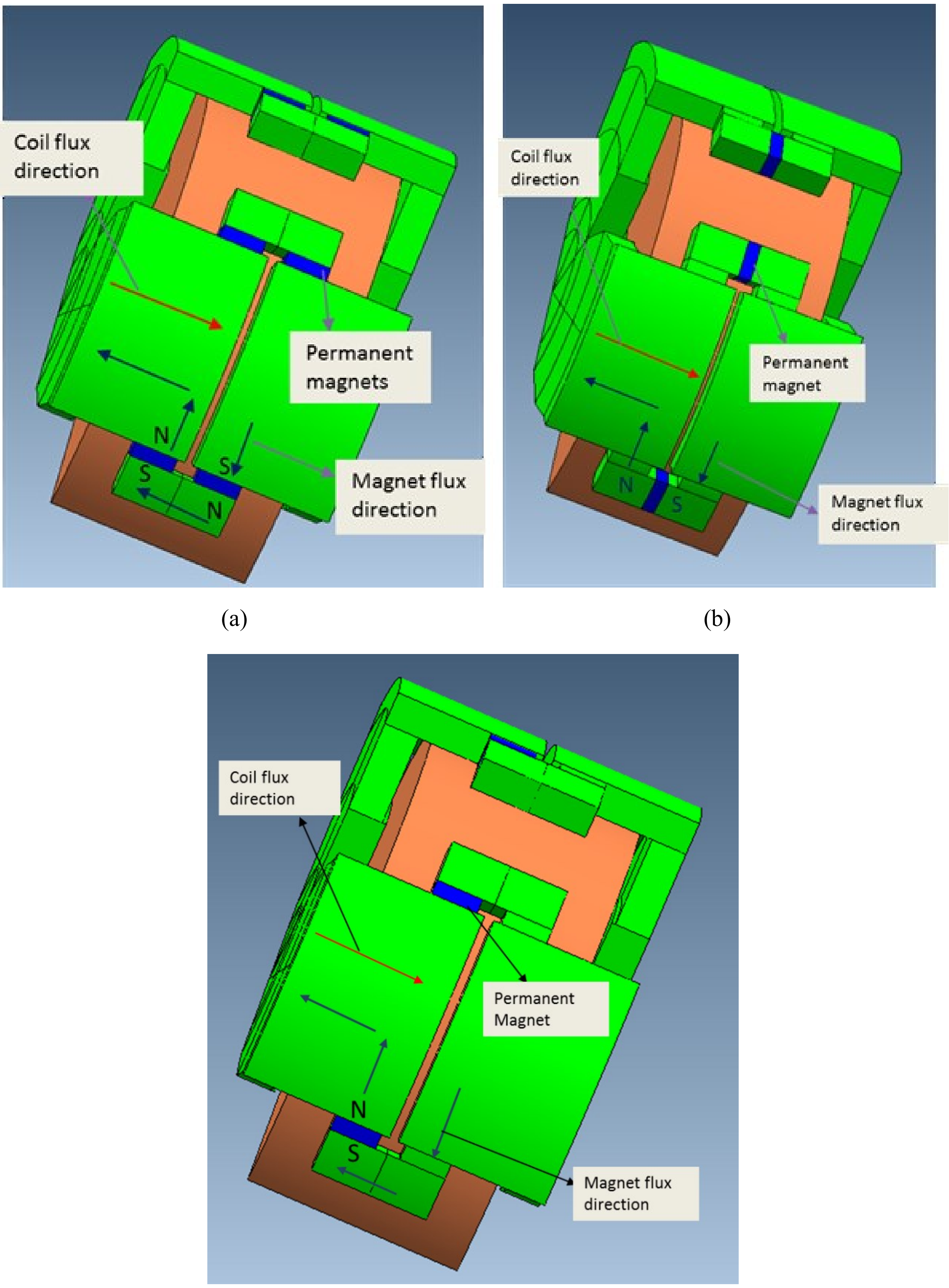

(a) (b)

(c)

Figure 7-11: (a) Four magnets on each side of single airgap plate (b) Single magnet in perpendicular to airgap (c) Magnet perpendicular to airgap

Within all the above structures, the number of turns (150 turns) and the cross sectional area of the core was kept constant ($314mm^2$) and the inductance values was measured. Figure 1-11 shows the resultant inductance values for all three inductors. It is clear that inductors with 2 magnets (both magnets is parallel and perpendicular to airgap) keeps the inductance value higher as compared to the inductor with 4 magnets on a single airgap plate.

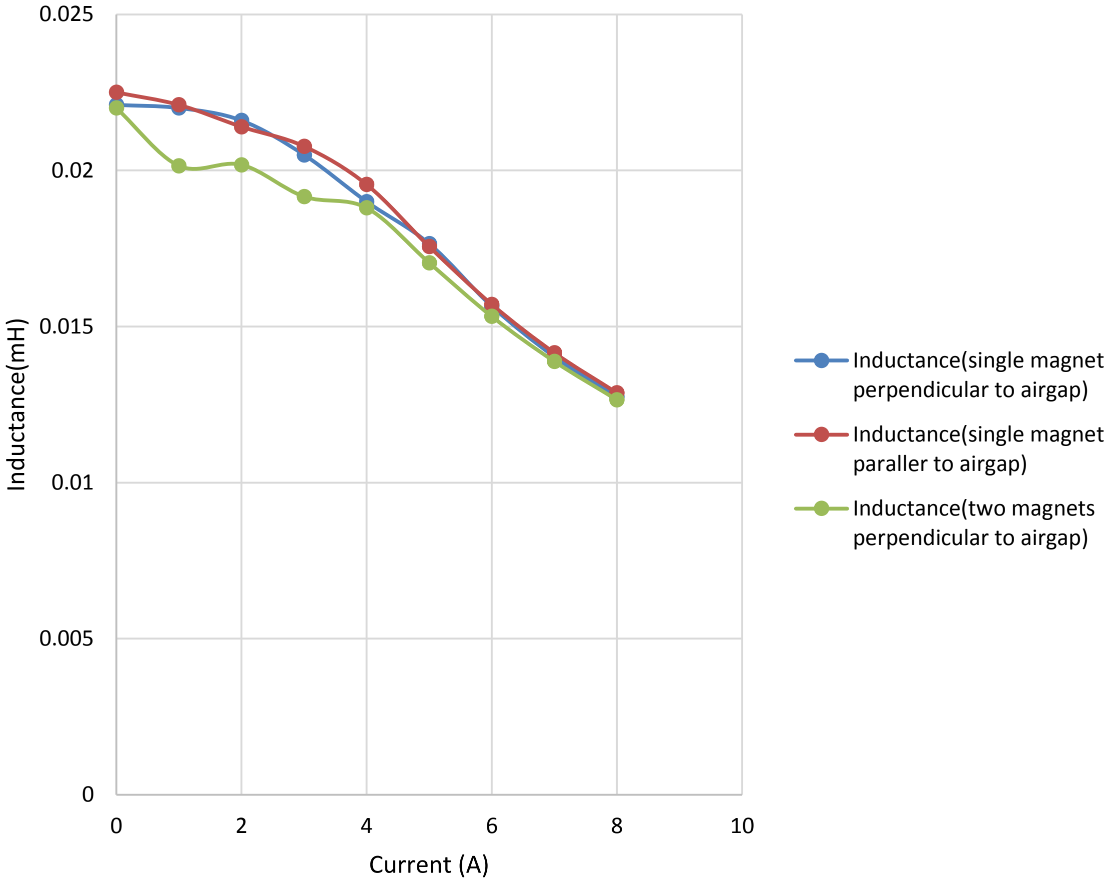

Figure 7-12: Inductance values for given current values and core area

For further analysis, inductor with single magnet in parallel to the airgap plate was taken as within the physical design, it is easier to build such inductor with magnet plate far away from the main coil flux.

7.8 Optimization of the inductor

Optimization of inductor was done by varying the core area of the inductor while keeping the number of turns constant i.e. 150 turns. The resultant inductance values for different values of current is shown in Figure 7-13. Table 7-1 shows the dimensions of the resultant inductor with copper loss and the resultant copper cross sectional area along with fill factor is shown.

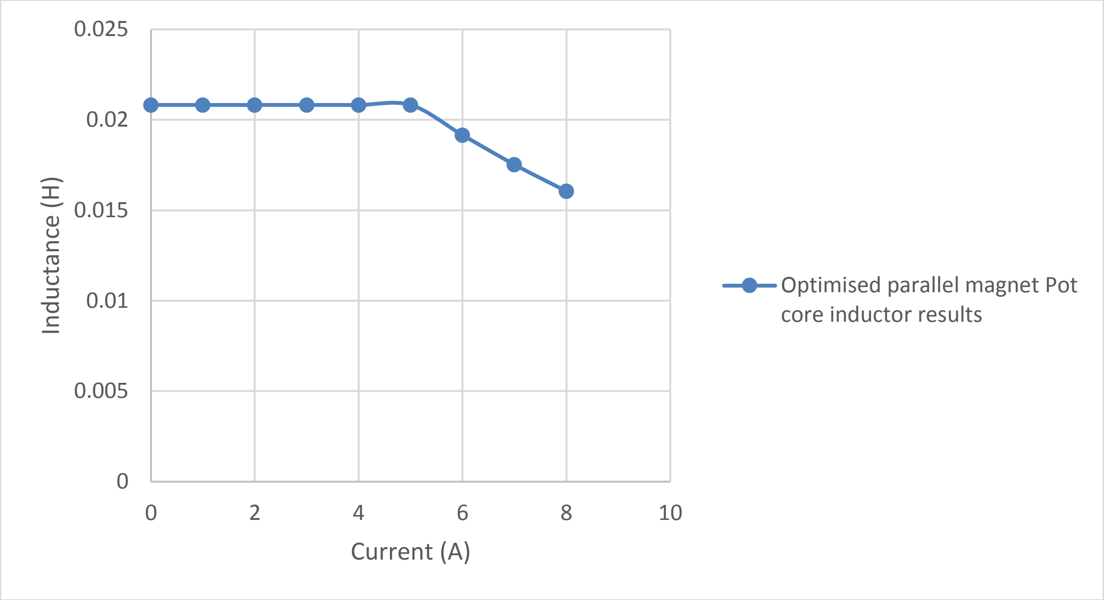

Figure 7-13: Inductance of MBI pot core inductor with magnet parallel to airgap

Table 7-1: Parameters of optimised MBI pot core inductor

Copper area(mm^2)	662.12
Number of turns	150.00
Area of one conductor(mm^2)	1.54
Conductivity at 20°C (S)	5.7e7
Resistance(Ω)	0.26
Copper loss at 7 amps(watts)	12.63
Fill factor	0.35
core mass(Kg)	0.53
Magnet mass (kg)	0.00
Copper mass (Kg)	0.89

7.9 Comparison of E-E core, MBI E-E core and pot core MBI

Conventional E-E core and E-E core with magnets (MBI E core) were compared with pot core MBI for the same copper loss and core mass as it is the conventional way of comparing two inductors[43, 47]. Core mass of the pot core shape increases because of extra core mass required for magnets to be placed. For E-E core, the central core width was considered double of the air gap cores on both sides. The air gap length was considered the same as that of MBI pot core inductor. Magnets of the same mass and dimensions were placed in E-E core with magnets to investigate the effect of the magnets on the inductance value of the E-E core. All three of them were then compared on the basis of the same copper loss and core mass.

Figure 7-14 shows E-E core with and without magnets placed in the core.

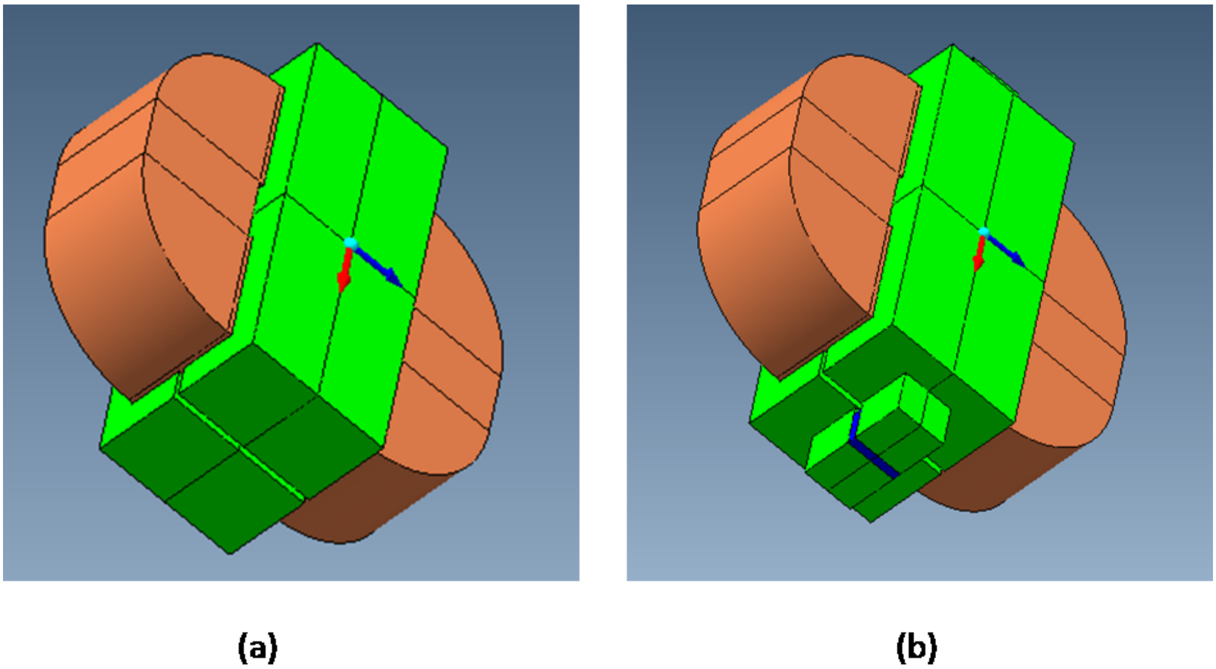

Figure 7-14: (a) E-E core without magnets (b) E-E core without magnets

The cross sectional area of E-E core with and without magnets was chosen in such a way that it gives a copper loss similar to that of Pot core MBI. It is clear from the above figure that most part of the copper is outside the main core which can result in leakage flux and can results in increase in EMI effects.

Figure 7-15 shows the inductance values for all the three cores. It is clear from the figure that the inductance of pot core is higher and constant for higher current values compared to other inductors.

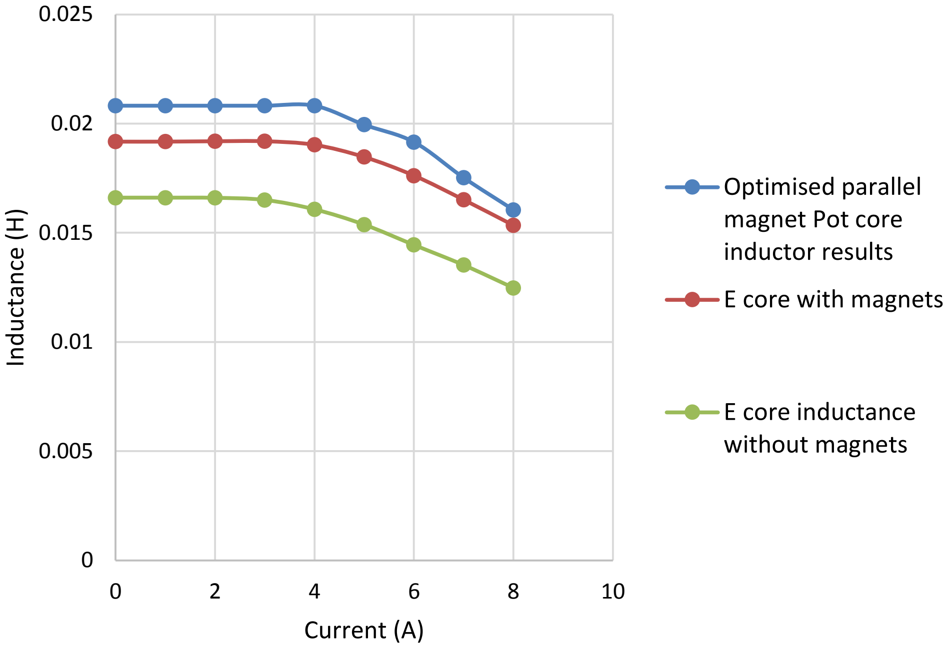

Figure 7-15: Inductance comparison of three cores

Figure 7-16 shows the mass comparison for different parts of the inductor. It is clear that pot core inductor has greater core mass compared to E-E core. But the overall mass of the pot core is less because of reduced copper mass.

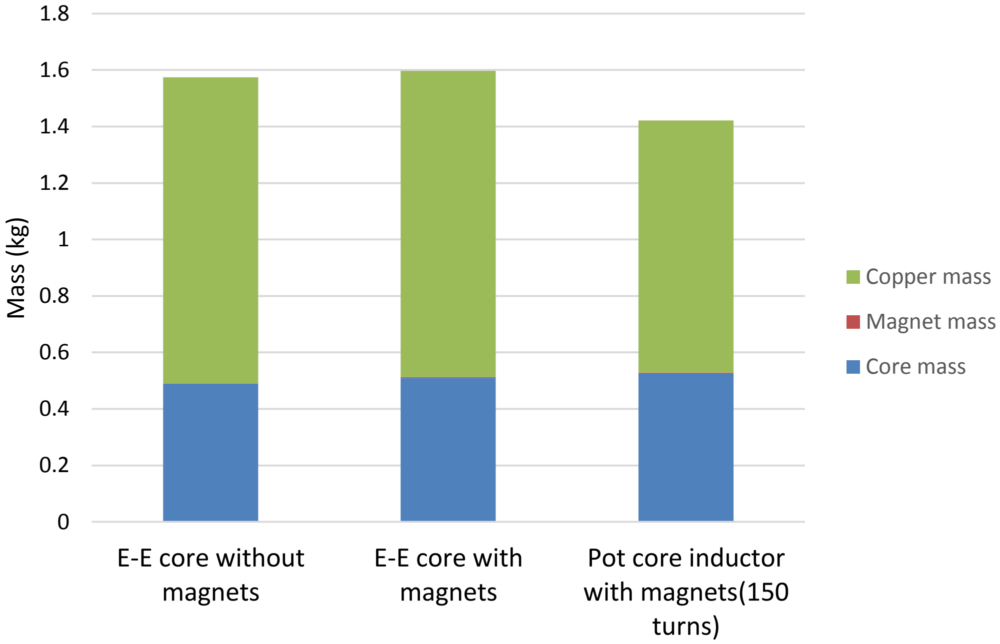

Figure 7-16: Mass comparison of different parts of three inductors

7.10 Iron losses at rated drive current

Iron losses of pot core inductor was found using FEA software. Current values that were passed through the coil were the same as that expected in the drive system during working operation i.e. 0 to 3.7 Amps DC with a ripple current of up to 4A peak value. The resultant copper and iron losses along with the losses in the magnet is shown in Table 7-2. Iron loss was multiplied by ‘build factor’ of 1.6 to increase the accuracy of the result while doing the practical analysis[70].

Table 7-2 : Losses in inductor at operating point

Copper loss at 7 Amps peak(watts)	12.63
Iron loss(Hysteresis + Eddy current losses)(watts)	4.21
Magnet losses(watts)	5.50E-04
total loss(watts)	16.83
Frequency of current (Hz)	1000.00

7.11 Conclusion

A new permanent magnet assisted pot core inductor was designed and the structure was developed by investigating different drawbacks within the structure. Final design was chosen and then improved to decrease the overall mass of the inductor. Magnets were placed at different positions to get the maximum inductance up to higher current values from the inductor. It was then compared with a conventional E-E core with and without magnets on the basis of same copper loss and same core mass. MBI pot core inductor gives 22% and 7.5% high inductance compared to E-E core without and with magnets respectively. Iron losses and magnet losses were found by using FEA analysis.

Chapter 8 Construction of MSSRM

This chapter outlines the construction of fault tolerant magnet assisted segmental rotor switched reluctance machine (MSSRM) and pot core magnetic biased inductor (MBI). The first part covers the construction of MSSRM and the second part is about the construction of pot core MBI. The machine and inductor were both constructed by the technicians in the school.

8.1 Stator construction

The stator was constructed from a stack of N020 laminations[1] bonded by Ultimeg 2002L epoxy. The lamination was 0.2 mm thick and supplied in square sheets of length 270 mm. The stack length of 25 mm consisted of 119 laminations, giving a stacking factor of 95%. The stack was then compressed and heated for 3 hours at 160°C to cure the epoxy at its highest strength.

An Electrical Discharge Machining (EDM) wire erosion machine (Figure 8-1) was used to cut the stator as single component.

The magnets and copper wire were separated by a small key way of diameter 1.5 mm with a natural glass fibre laminated plastic (tufnol) was inserted (Figure 8-3).

---

[1] From SURA (www.sura.se)

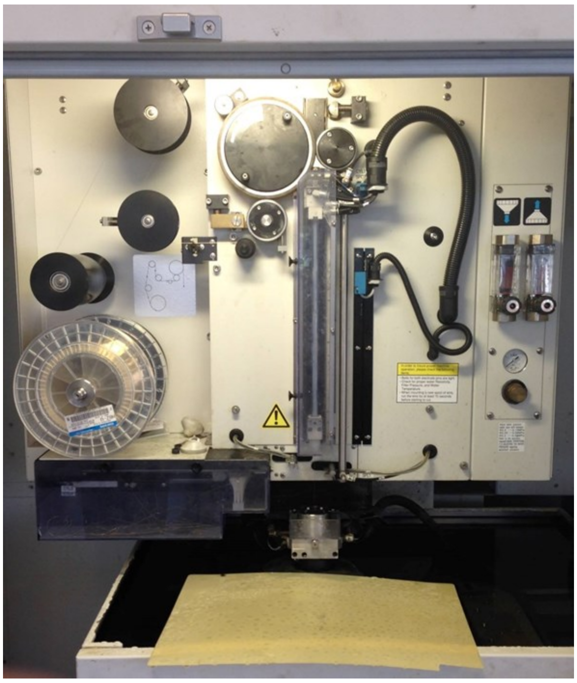

Figure 8-1: EDM Machine

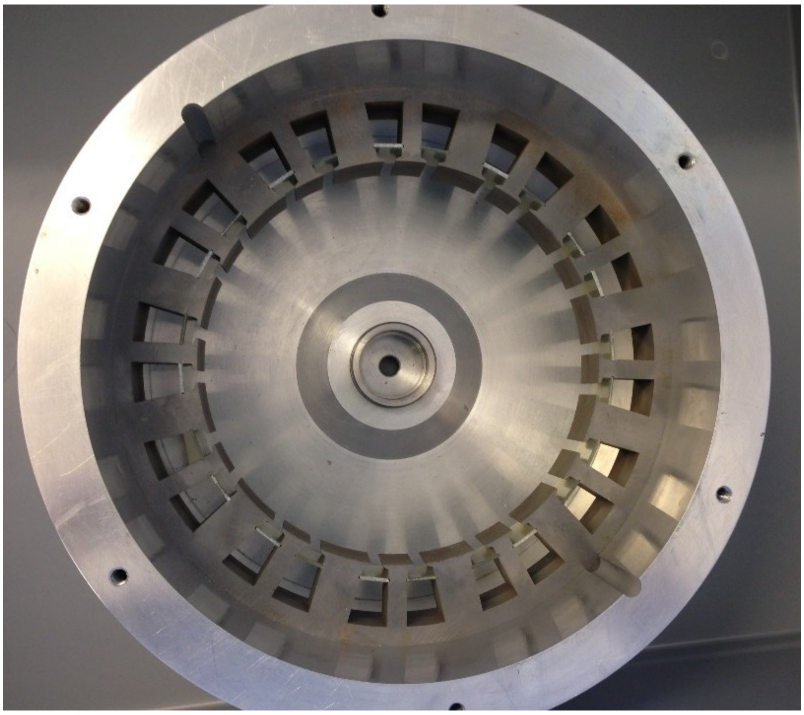

Figure 8-2: Stator within the aluminium casing

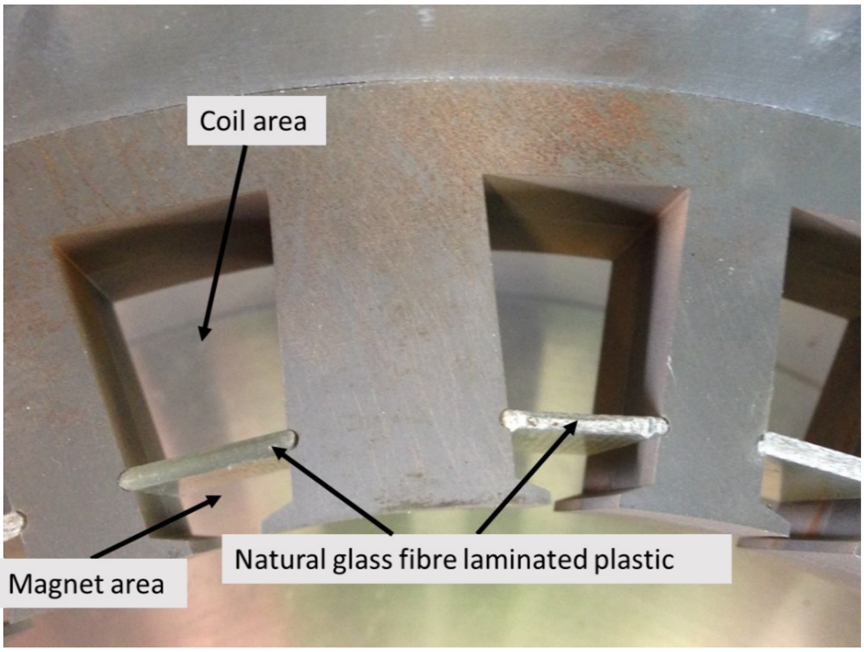

Figure 8-3: Natural glass fibre laminated plastic to separate copper wire from magnet

8.2 Rotor construction

Like the stator, the rotor was made from a stack of N020 laminations, again with a stacking factor of 95%. Rather than making separate rotor segments in the start, a single ring with additional outer diameter was manufactured (Figure 8-6). This ensured the rotor structure fitted into its supporting ring concentrically. Once in place, the rotor was finally machined by using lathe to separate the segments.

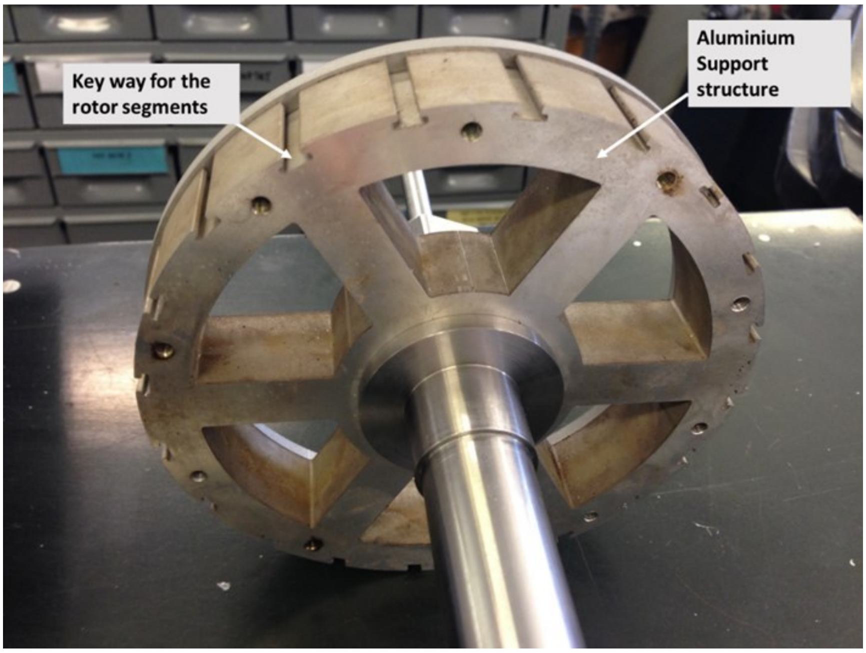

Figure 8-4: Aluminium rotor support structure

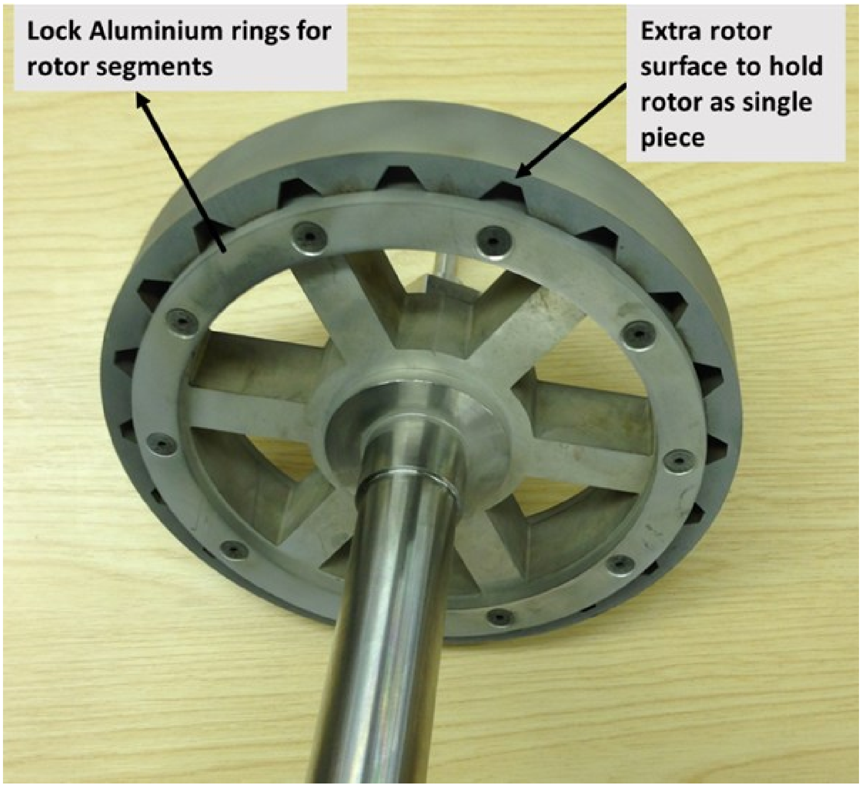

Figure 8-5: Laminated rotor ring in prior to final machining

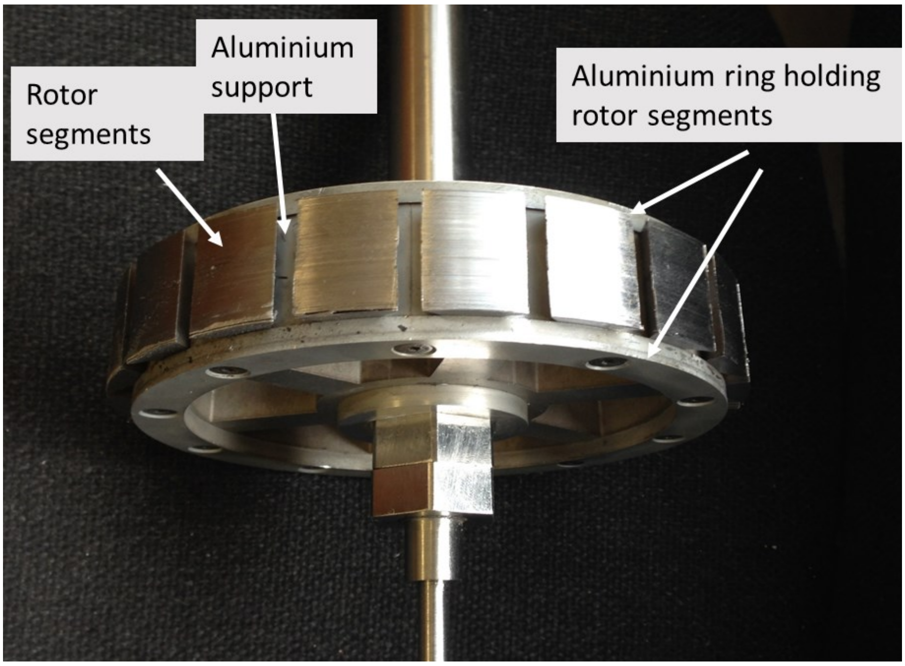

Figure 8-6: Finished aluminium support and shaft

8.3 Stator windings

The machine was wound with the stator inside its casing. Coils were wound around a wooden-former and then placed into each slot. A disadvantage of this method is that the coil opening needs to be large enough to go within the stator tooth edges which results in an increase in overall winding length of each coil and thus result of each coil.

Magnetemp CA-200 wire[2] with a diameter of 0.6mm was used which has a temperature capability up to 200°C. The wire is insulated with polyamide.

The slot wedge was inserted after placing the coil to prevent the coil from moving and coming into contact with the magnets. Type K thermocouples were placed at the top and in centre of a single coil of phase A to measure the temperature of the coil.

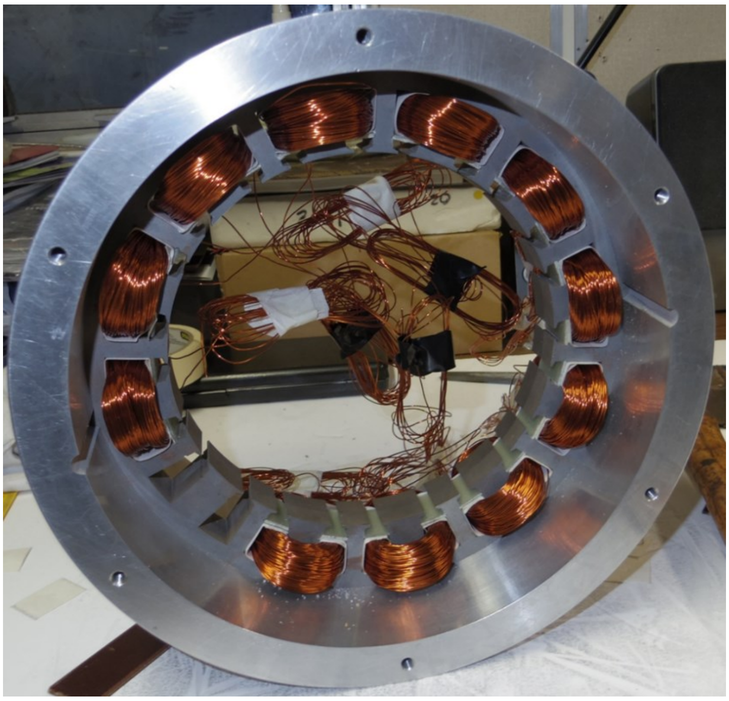

Figure 8-7: Windings being inserted into the stator slots

---

[2] From superior Essex (http://www.spsx.com/)

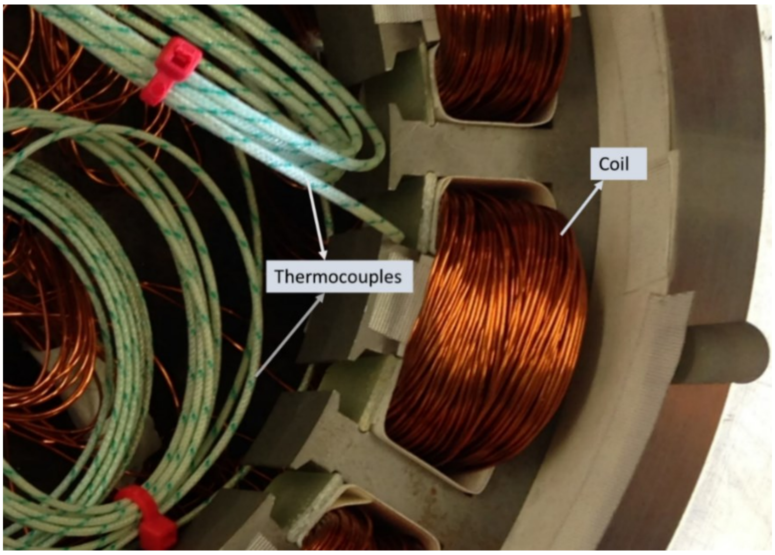

Figure 8-8: Single tooth concentrated windings with thermocouples

8.4 Permanent magnets

The dimensions of permanent magnets[3] were chosen to allow easy insert inn into the stator coils. A gap of 0.1mm was left on either side of the magnet, FE simulations include this gap. The magnets are samarium cobalt (Recomma 33E) were produced by Arnold Magnetic Technologies. The magnets alternate in their direction of magnetization around the circumference of the stator. A gauss meter was used to confirm the correct alignment of the magnets.

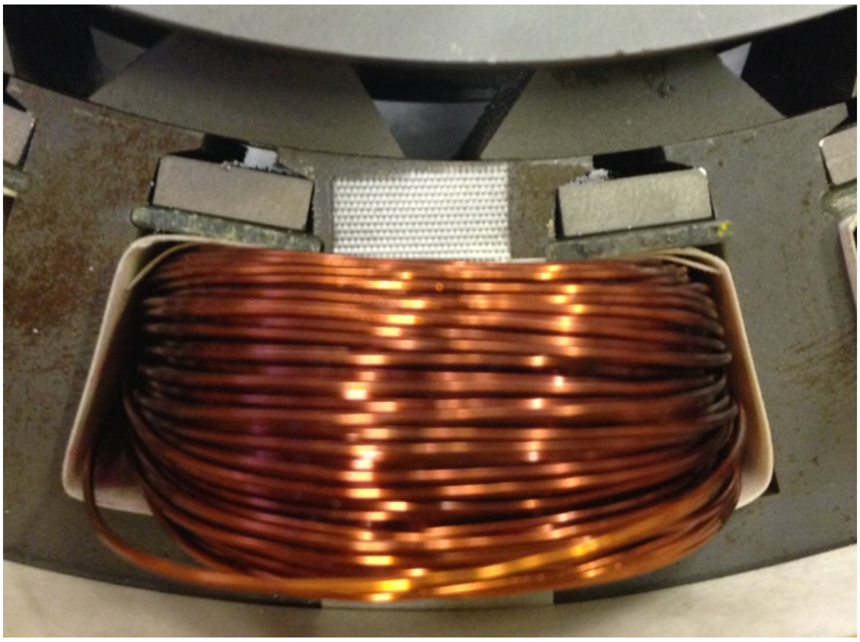

Figure 8-9: Magnets in situ

---

[3] From Arnold magnetics technologies (http://www.arnoldmagnetics.com/)

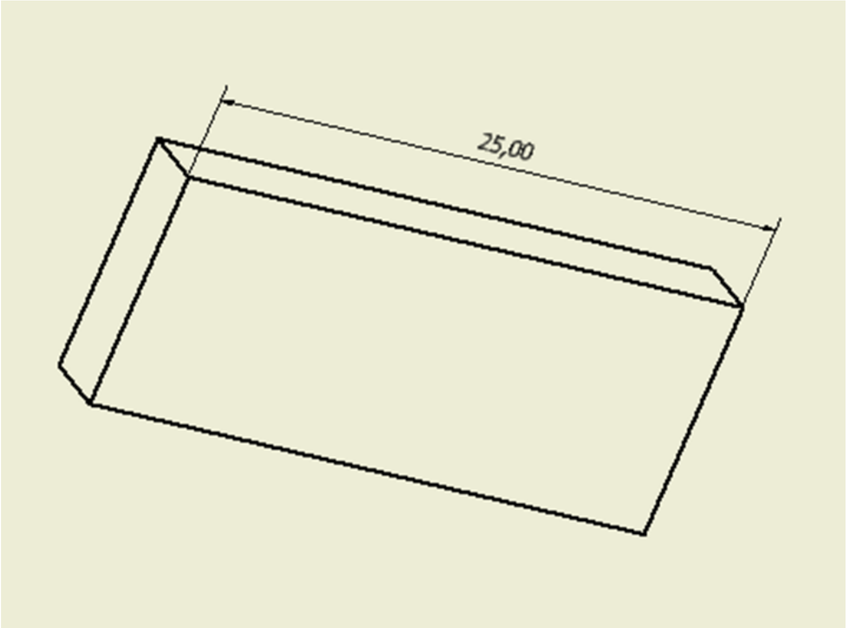

Figure 8-10: Length of the magnet (mm)

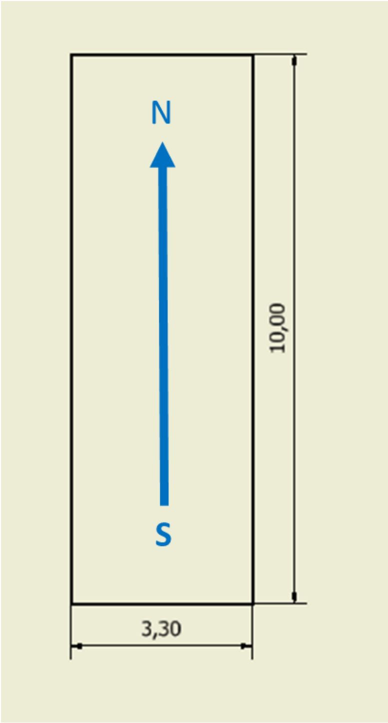

Figure 8-11:Width, height (mm) and magnetization direction of magnet

8.5 Static torque test rig

Static torque measurements were carried out on the machine using the test rig shown in Figure 8-12. The machine shaft is connected via a torque transducer to a dividing head to accurately position and lock the rotor.

During static torque test, shaft twisting could result in an inaccurate position reading of the dividing head, hence the actual rotor position was obtained from the motor mounted resolver.

Constant DC and pulsed current can be applied to the machine, in this way both torque – angle and flux linkage – current data can be collected using the same test rig.

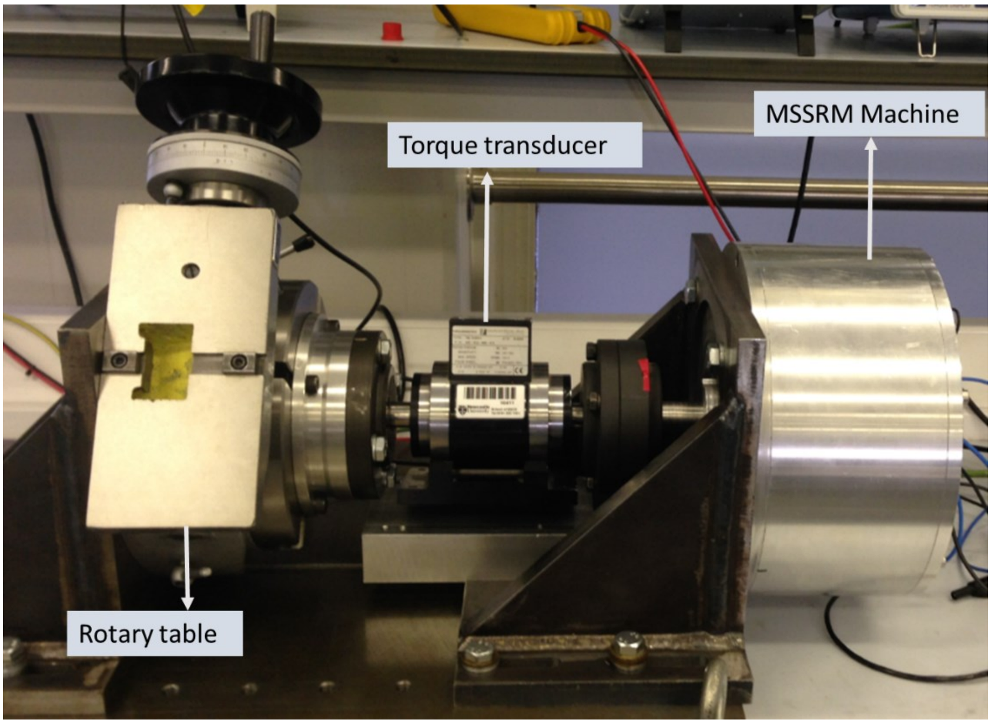

Figure 8-12: Static test rig with torque transducer and rotary table

8.6 Dynamic test rig

The back EMF and short-circuit current of the machine was measured using the dynamic test rig shown in Figure 8-13. The test machine is driven via the torque transducer by an induction machine. In this test the back EMF and short-circuit fault current was measured.

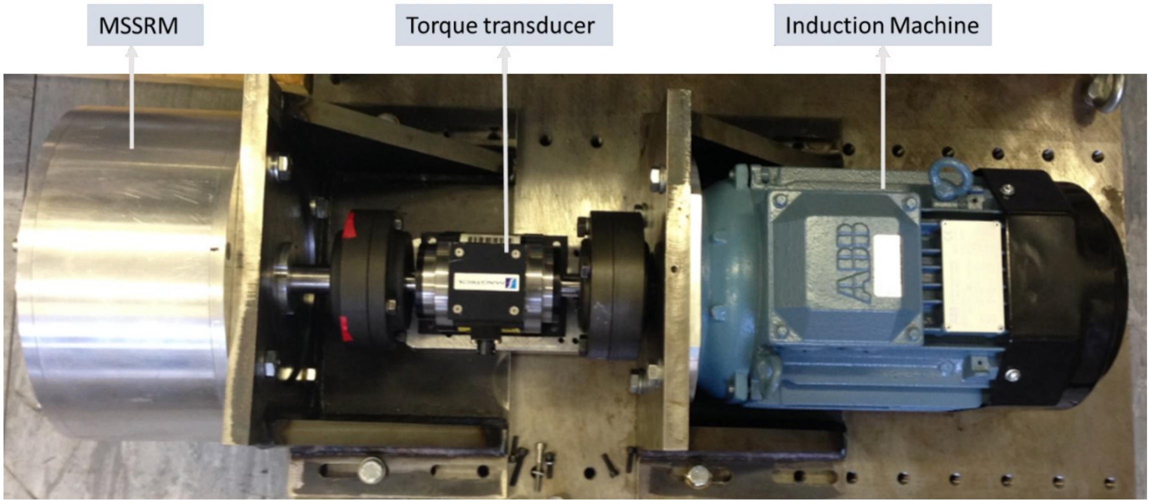

Figure 8-13: Dynamic test setup of MSSM with induction machine

8.7 Inductor construction

The inductor was constructed from soft magnetic composite (SMC)[4] material. Two segments were machined by EDM which were joined together by glue after inserting coil. Figure 8-14 shows an inductor half segment before trimming its sides while Figure 8-15 shows the separate segments after trimming it from sides with different thickness of layers around endcap.

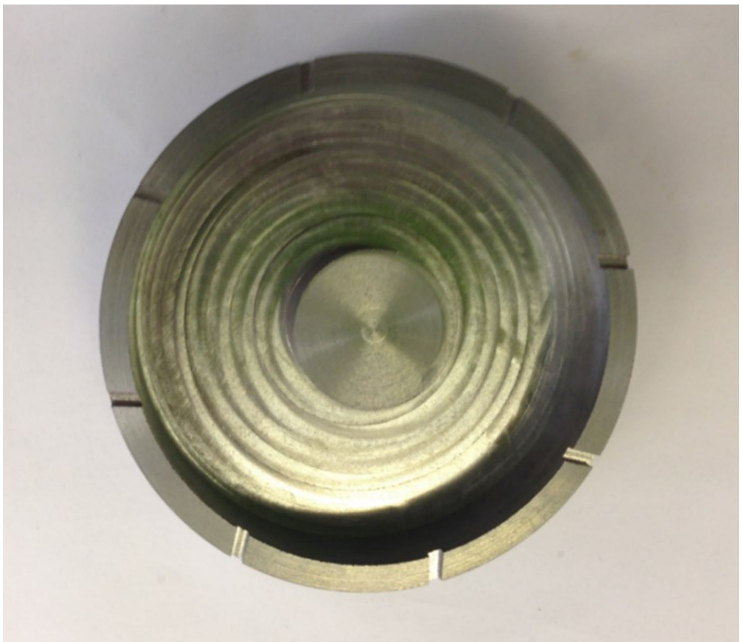

Figure 8-14: Half of the inductor

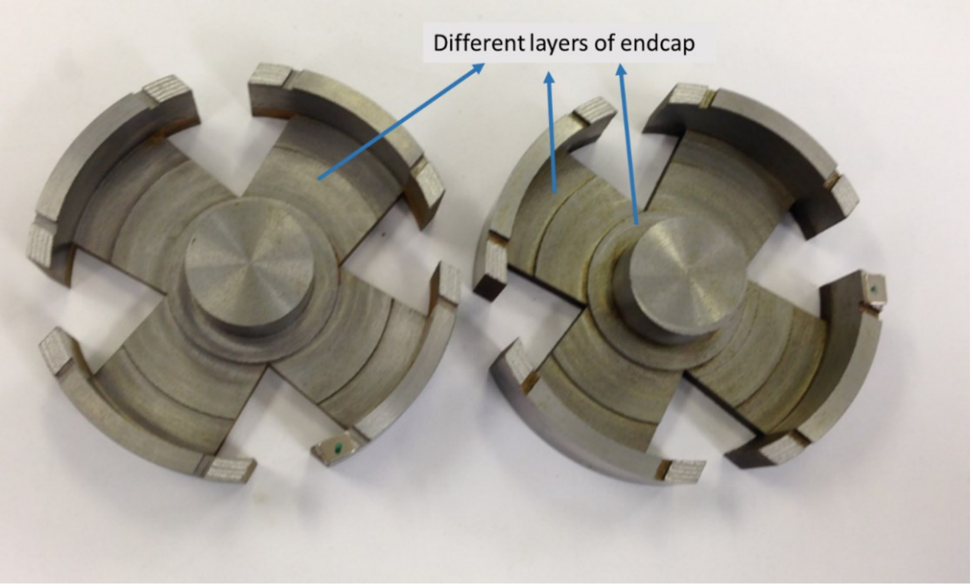

Figure 8-15: Both inductor segments after trimming from sides

---

[4] From Hoganas(https://www.hoganas.com/)

Figure 8-16 shows full inductor after putting coil and magnets within the inductor structure.

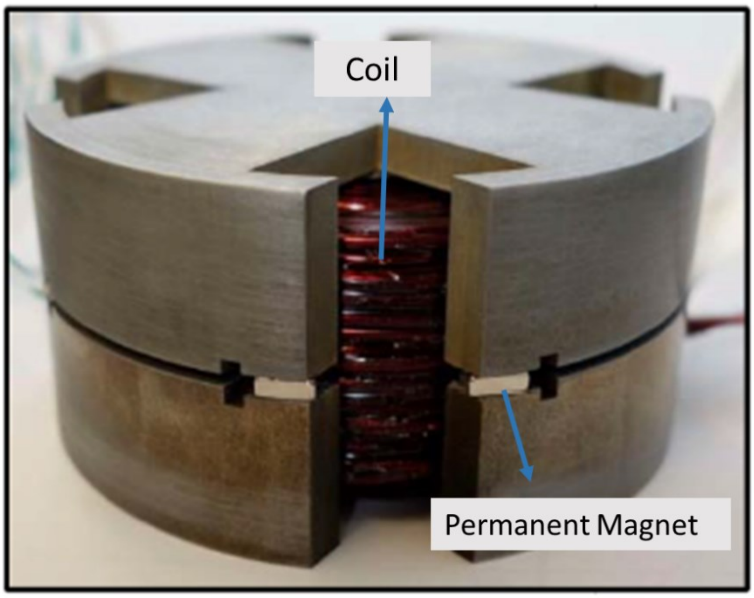

Figure 8-16: Inductor with magnets and 250 turns coil

8.8 Conclusion

The fault tolerant MSSRM and pot core MBI were constructed. Magnet length was chosen in such a way that it can fit well within the required space by considering the tolerance during construction. In the case of the MSSRM, instead of making the rotor as single pieces in the start, it was made as a single body and placed within an aluminium structure and was later on cut into segments. Both the inductor and machine windings were done separately on a wooden frame. Static testing was done by connecting the machine to rotor locker and dynamic testing was done by connecting it into an induction machine.

Inductor was made from two separate segments and then glued together after fitting the coil. Magnets were then fitted into magnet slots which fitted well within the required space.

Chapter 9 Testing and results

9.1 Introduction

This chapter presents the validation of the idea of introducing magnets into the conventional SSRM, which will result in the improvement of the torque density of the machine. A static test rig was used to obtain the flux linkage–current characteristics and torque at different rotor angles. The same test rig was used to measure cogging torque and the mutual flux linkage between different phases. Open circuit voltage and short-circuit current was found from dynamic testing. The whole procedure can be divided into the following sections.

1. Flux linkage–current waveform without magnets
2. Torque waveform without magnets
3. Flux linkage-current waveform with magnets
4. Torque waveform with magnets
5. Comparison of MSSRM with and without magnets
6. Mutual flux linkage
7. Cogging torque
8. Open circuit voltage test
9. Short-circuit current test

9.2 Phase resistance

Resistance of each phase was found at 25°C temperature. The resistance found in this case was 21% higher than that predicted, with a difference of only 1% between different phases. This increase in resistance was because of winding the coil on a separate wooden frame with extra length for manual insertion. This will result in an increase in copper loss by the same proportion. Thermal analysis was conducted at the end. The level of resistances found in different phases of the machine are shown in Table 9-1. This increase in resistance of the windings is because the coils were made on a separate wooden frame while considering the stator tooth edges which resulted in an increase in average length of the coil.

Table 9-1: Predicted and measured resistance values in different phases at 25°C

	$R_{Ph}(\Omega)$
Predicted	3.96
Phase A measured	5.01
Phase B measured	5.05
Phase C measured	5
Phase X measured	5
Phase Y measured	5.05
Phase Z measured	5.03

9.3 Static test

A static test was conducted to find the torque and flux linkage of each phase at different rotor angles, which closely predicts dynamic performance and 3DFE model of the machine. This was accomplished by connecting the rotor of the machine to a rotary table via torque transducer. A position encoder was connected to the rotor shaft to accurately measure rotor position, as a high number of rotor poles results in large variations in exact position with a small amount of vibrations in the shaft caused by the magnetic pull when a current is passed through coil, since the test rig is not always strong enough to hold the shaft completely stationary at higher currents. A static analysis was conducted without magnets first and then magnets were inserted into the stator slots and the process was repeated. The rotor was rotated by 1°(mechanical) which is equal to 20°(electrical) for one complete electrical cycle, which gives both positive and negative torque values.

9.3.1 Static test without magnets

9.3.1.1 Flux linkage–current analysis

The rotor was rotated and the flux linkage of each phase at different positions was found. DC voltage was applied to each phase and the current was monitored. This was done for all the phases within the machine for each lane phase (dual lane motor).

The flux linkage of each phase was found using equation (9-1)

$$\Psi = \int_{o}^{t} [v - iR] dt \tag{9-1}$$

where Ψ is the flux linkage, R is the resistance of each phase, v is the voltage applied across each phase and i is the current flowing through the coil.

Figure 9-1 shows the flux linkages of lane 1, phase A. The results show very little variations in flux linkage in all phases in both lanes 1 and 2 at the aligned and unaligned position. Figure 9-2 shows the flux linkage of phase A at different angles.

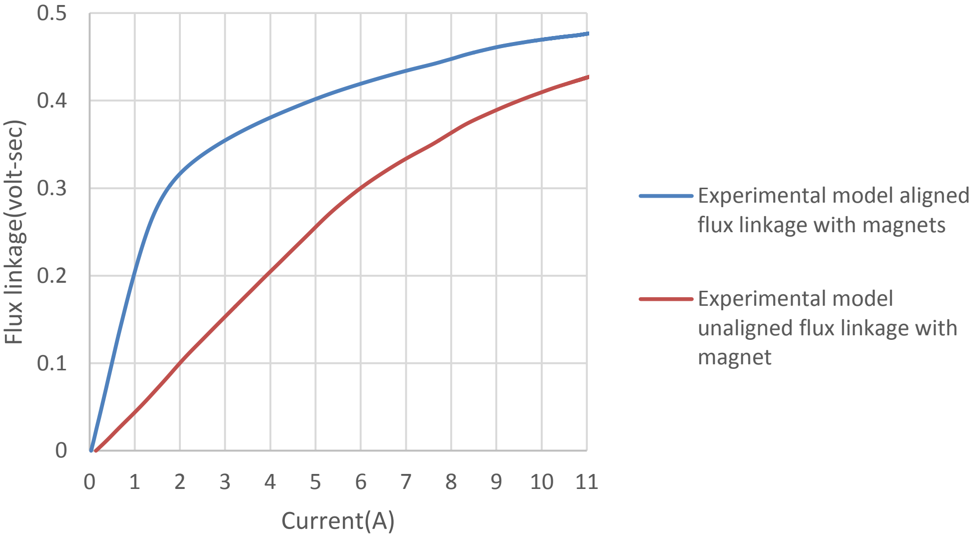

Figure 9-1: Phase A aligned and unaligned flux linkage without magnets

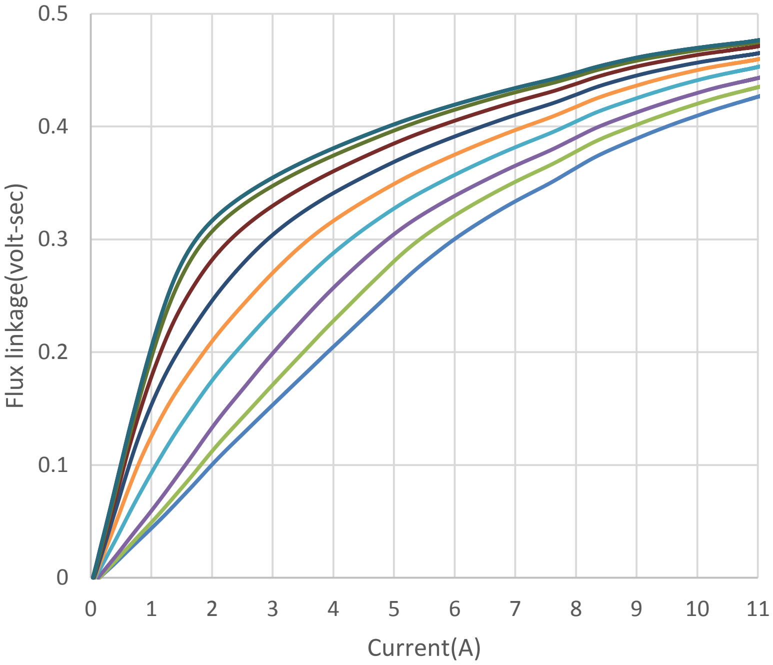

Figure 9-2:Flux linkage of phase A at different rotor angles(mechanical) with no magnets in the stator

9.3.1.2 Comparison of flux linkage–current waveform in FEA and experimental model (without magnets)

Flux linkage values from the experimental model were then compared with those from the FEA model to identify variations between the unaligned and aligned flux linkage area, which will help in predicting potential problems during the construction of the machine. Figure 9-3 shows the resulting flux linkage values of the experimental and 3DFE models at the aligned and unaligned positions.

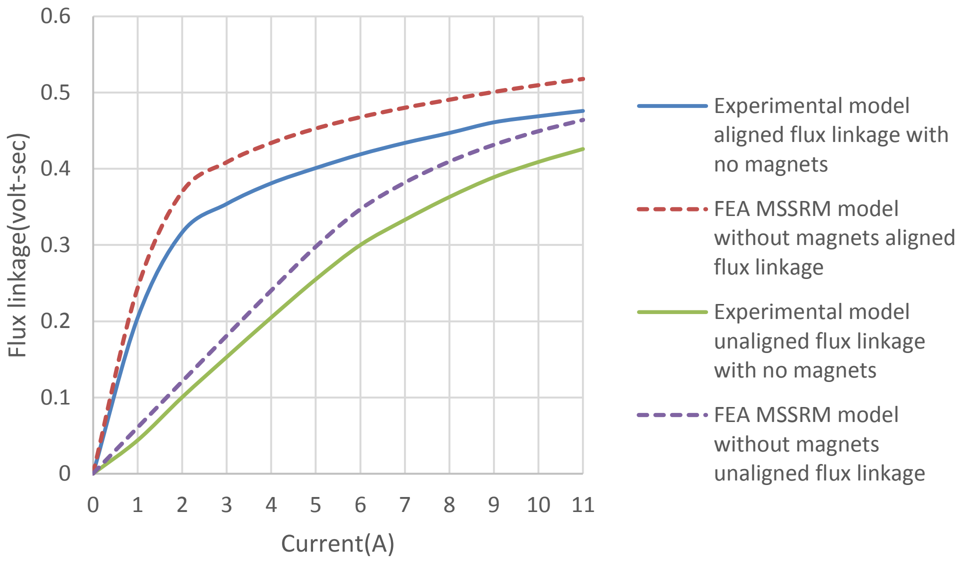

Figure 9-3: Comparison between FEA and experimental model with flux linkages at aligned and unaligned position without magnets in the stator

It is clear from Figure 9-3 that the experimental model unaligned flux linkage is much lower than that of the FEA model. The aligned flux linkage of the experimental model also decreases by the same proportion. As the linear increase in the flux linkage at the aligned position for lower values of current is dependent on the air gap, a bigger air-gap could result in a decrease in the aligned flux linkage for lower current values.

To confirm that the air-gap of the experimental model is bigger compared to the FEA model, a number of 3DFE models were run, increasing the air-gap between the rotor and stator. The FEA results comes close to the experimental results when air gap length increased to 0.41mm. Figure 9-4 shows the aligned and unaligned flux linkage of the revised FEA model compared with the experimental model.

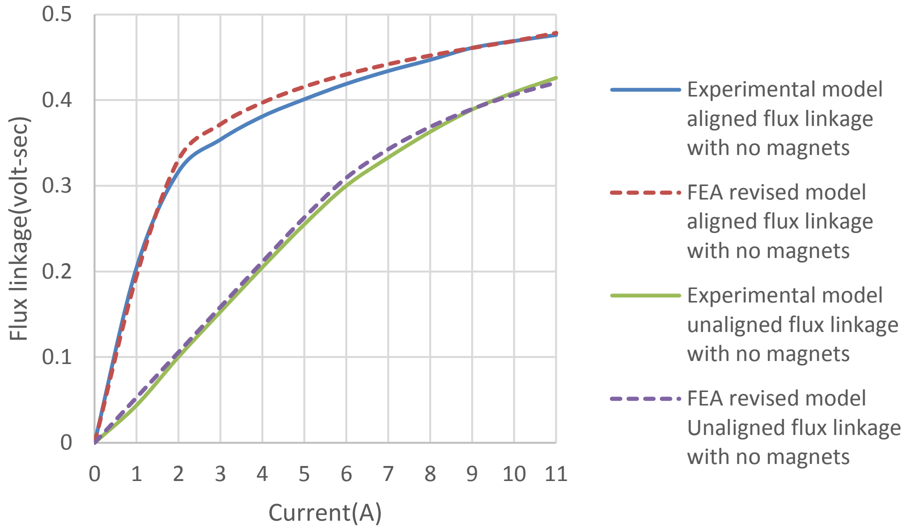

Figure 9-4: Aligned and unaligned flux linkage of experimental and revised FEA model with no magnets

From the flux linkage waveform, the average torque of the MSSRM without magnets was found and compared with the revised and original FEA model for different values of current. Figure 9-5 shows the average torque for different current values.

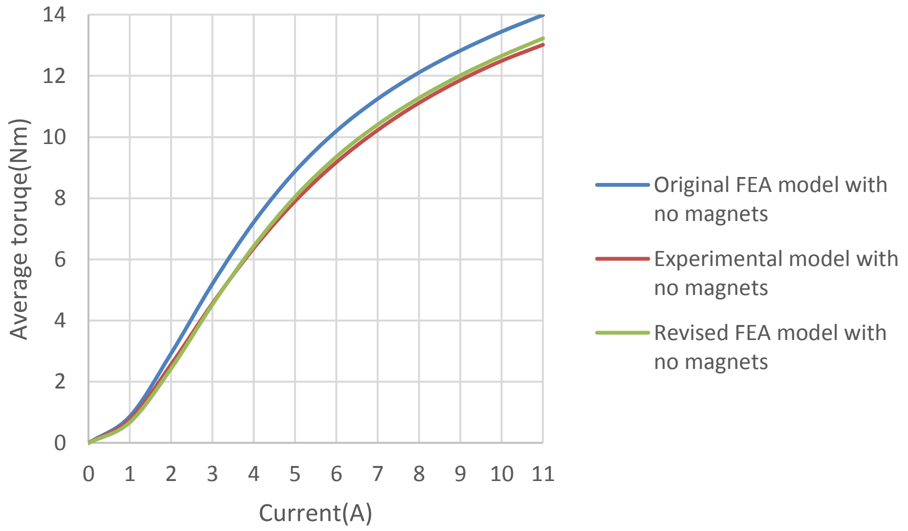

Figure 9-5: Average torque of original, revised and experimental model with no magnets

The revised model shows a decrease in the difference in average torque from 8% (original FEA model) to 1.5% with the revised FEA model at rated current of 11 Amps.

9.3.1.3 Static torque analysis with no magnets

Figure 9-6 shows the static torque of the machine when moving the rotor at different angles and tension measured within the shaft. Current pulses were passed through coils of each phase and the rotor was rotated to find the torque at each angle while varying the current values. From the torque results, experimental model was compared with revised FEA model at different rotor angles.

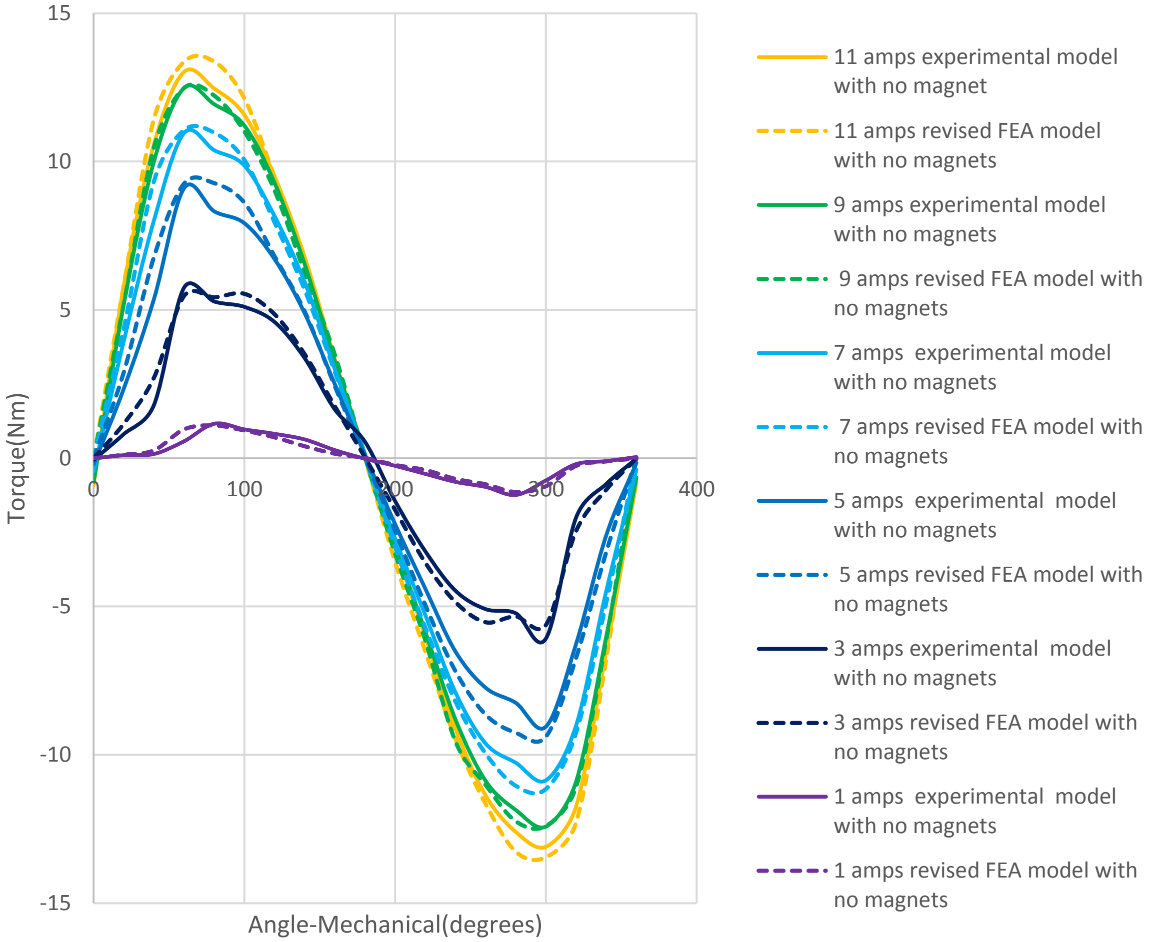

Figure 9-6: Static torque measurement for different levels of current in each phase with no magnets in stator. Solid lines shows experimental results while dotted lines show revised FEA model results

It is clear from Figure 9-6 that the torque of the machine is almost comparable with the revised FEA model with 0.4% difference in peak values as current values increases.

9.3.2 Static test with magnets

This time magnets were placed in the stator tooth to investigate the behaviour of the MSSRM with magnets used to avoid demagnetisation of the stator core at higher currents. The same procedure as before was followed to find the flux linkage-current waveform and for comparison with the original FEA model for all phases.

9.3.2.1 Flux linkage–current analysis

The flux linkages of all phases was found. Figure 9-7 shows the flux linkage values of phase A while Figure 9-8 shows values in phase A at different rotor angles.

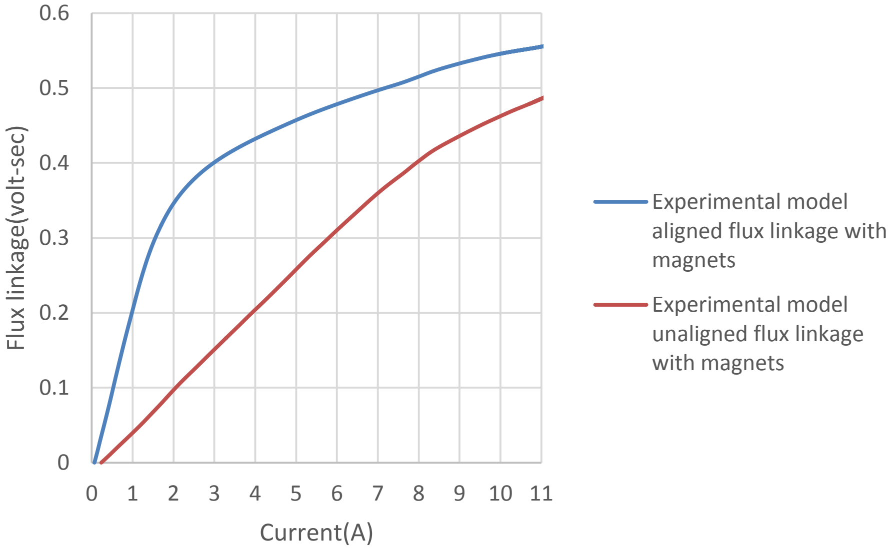

Figure 9-7: Experimental model aligned and unaligned flux linkage of phase A with magnets

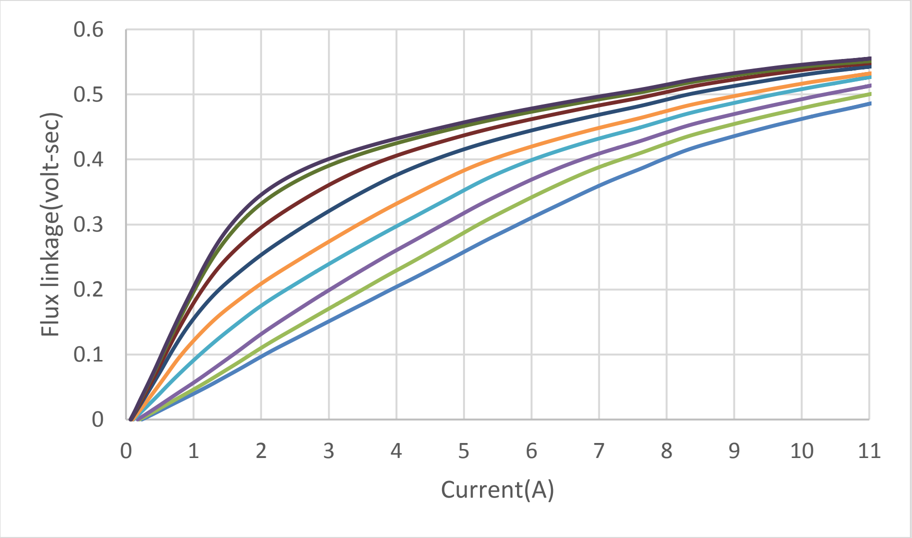

Figure 9-8:Experimental model flux lux linkage at different rotor angles with magnets in the stator in phase A

9.3.2.2 Comparison of FEA and experimental model flux linkage–current analysis including magnets

Figure 9-9 shows a comparison between experimental and FEA model results when magnets were put into the stator. As expected from the MSSRM without magnets, there is a clear decrease in flux linkage both at unaligned and aligned position because of bigger air-gap.

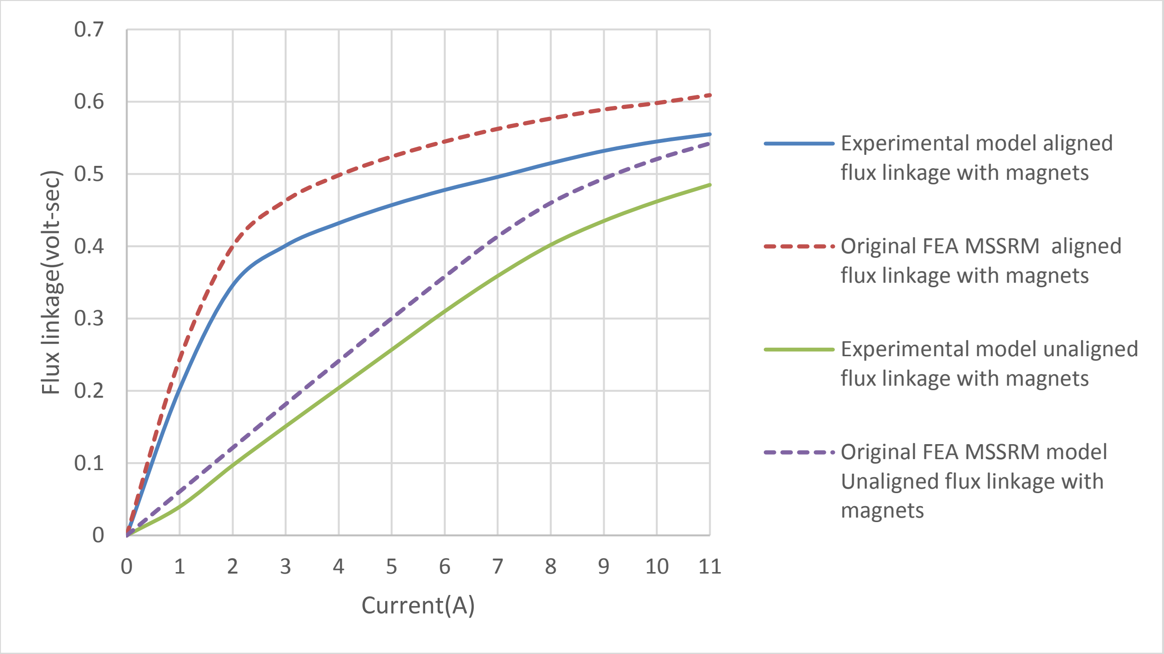

Figure 9-9: Comparison between FEA and experimental model with flux linkages at aligned and unaligned position with magnets in the stator

By using the same air-gap between the stator and the rotor in revised FEA model with magnets as done with without magnets model version(discussed in previous section), the values of the aligned and unaligned flux linkage were found, and are shown in Figure 9-10. By using the flux linkage-current waveform, the average torque of the experimental MSSRM with magnets was compared with the revised and original FEA models and the results are shown in Figure 9-11. There is clearly less difference between the average torque values from 8% in the original FEA model to 1.8% in the revised model.

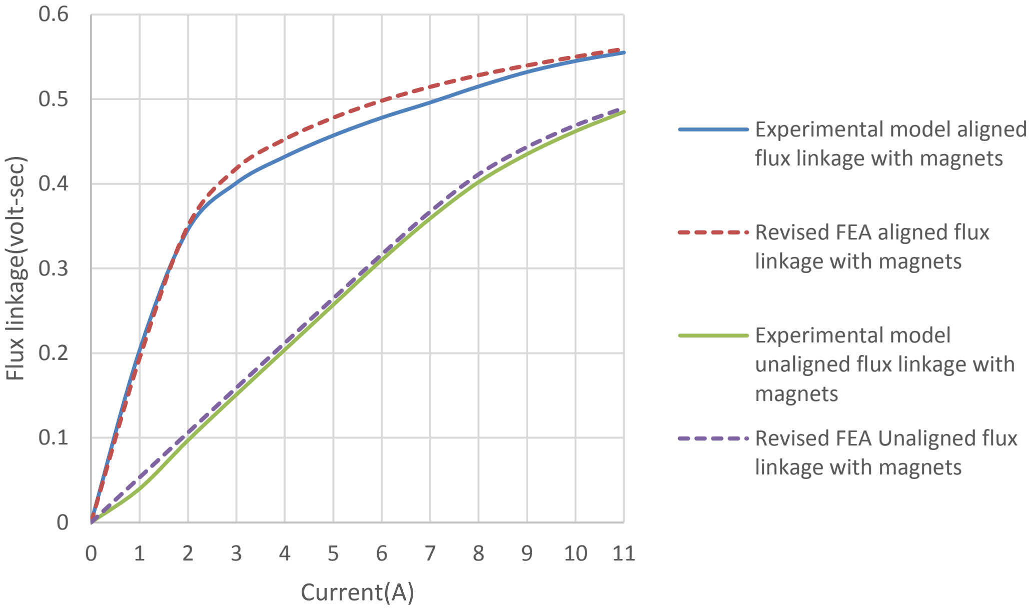

Figure 9-10: Experimental and revised FEA model aligned and unaligned flux linkage with magnets

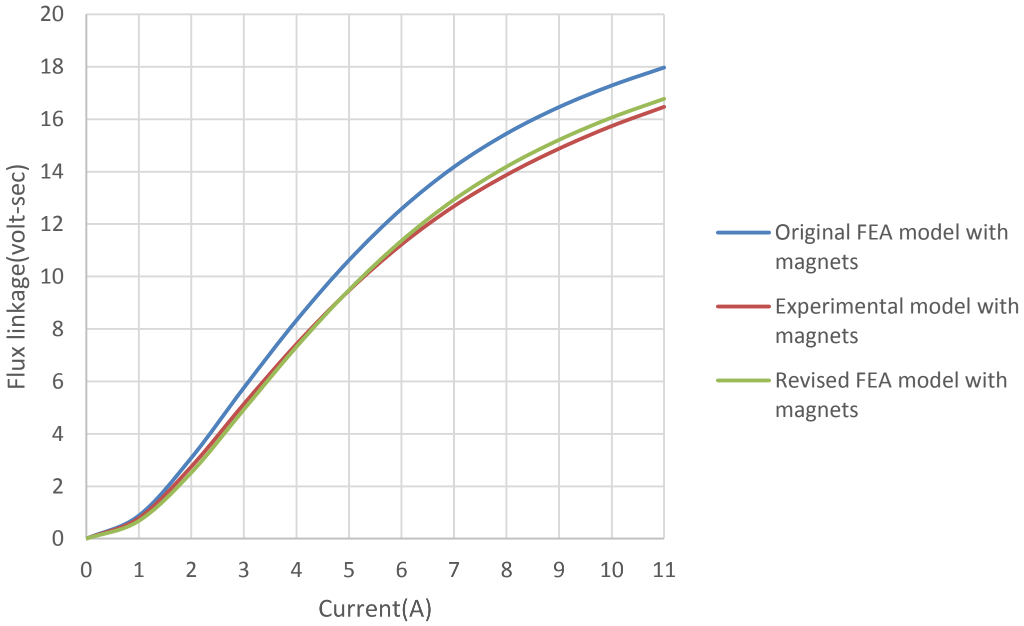

Figure 9-11: Average torque of original, revised and experimental model with magnets

9.3.2.3 Static torque analysis with magnets in the stator

Figure 9-6 shows the static torque of the machine when the rotor is at different angles. Current pulses were passed through the coils of each phase and the rotor was rotated to find the torque at each angle. The torque values results of the experimental model were compared with those of the revised FEA model at different rotor angles.

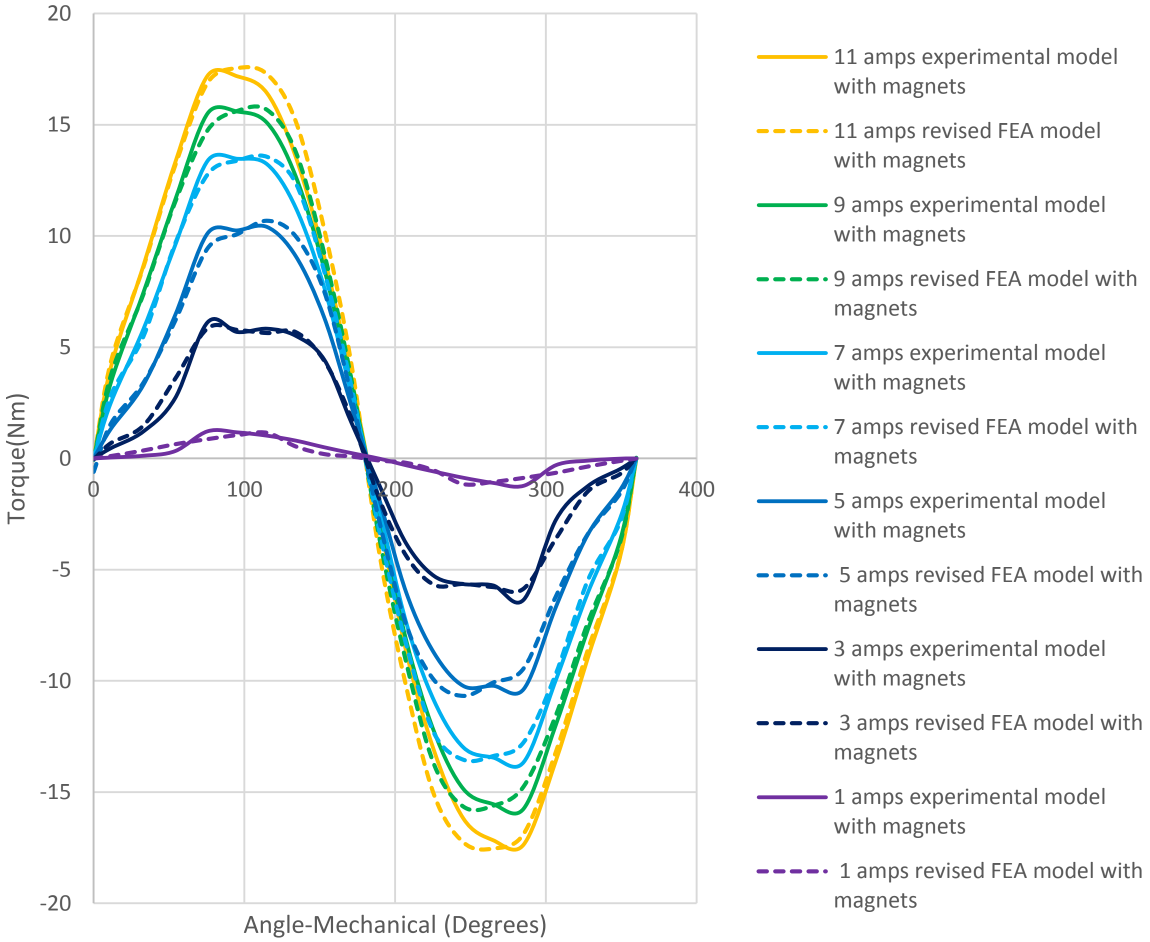

Figure 9-12: Static torque measurement for different levels of current in each phase with magnets in the stator. Solid lines shows experimental results while dotted lines shows revised FEA model results

9.4 Comparison of the MSSRM with and without magnets

The performance of the MSSRM with magnets was compared with the MSSRM without magnets to determine if there was an improvement after the introduction of magnets.

9.4.1 Flux linkage–current waveform comparison

Based on the previous analysis, the flux linkage–current waveform in two machines was compared as shown in Figure 9-13.

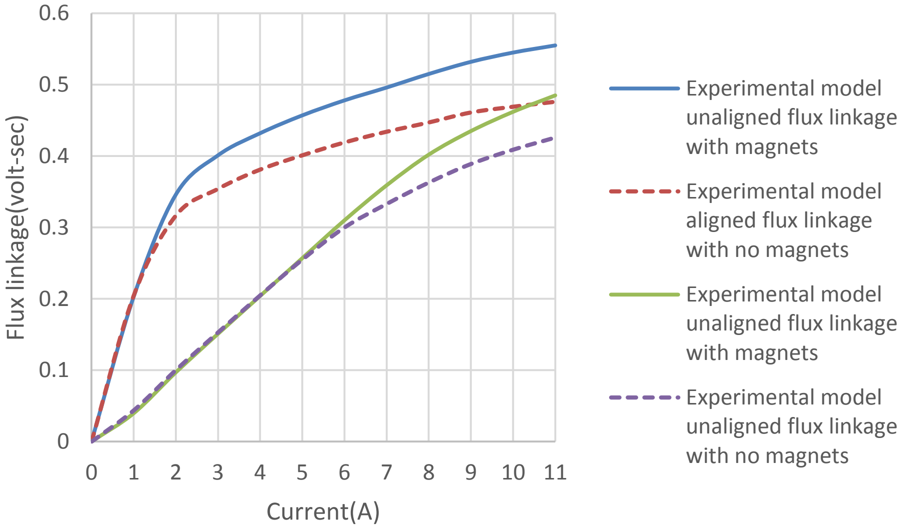

Figure 9-13: Flux linkage waveform of MSSRM with and without magnets

It is clear from above the figure that the MSSRM with magnets has high unaligned flux linkage at high current values. This is because magnet keeps the stator core reverse-magnetized at the unaligned position, thus avoiding it from becoming saturated even at high currents. Meanwhile in the MSSRM without magnets, there is saturation even at the unaligned position at higher currents.

A substantial difference occurs at the aligned position, where the MSSRM without magnets saturates much earlier compared to the stator with magnets, which results in significant increase in the aligned flux linkage of the MSSRM with magnets as compared to MSSRM without magnets.

9.4.2 Torque comparison

The torque values of the MSSRM with and without magnets were compared for the rated current of 11 amps. Figure 9-14 shows the torque values at rated current while Figure 9-15 shows the average torque for different current values found from the aligned and unaligned flux linkage values.

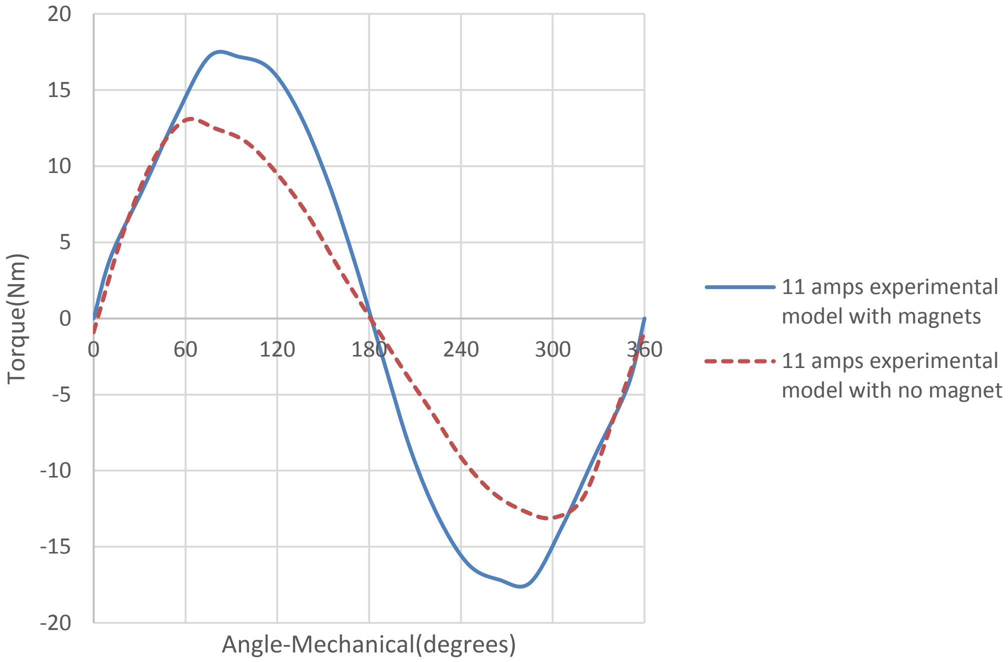

Figure 9-14: Torque comparison at rated current of MSSRM with and without magnets

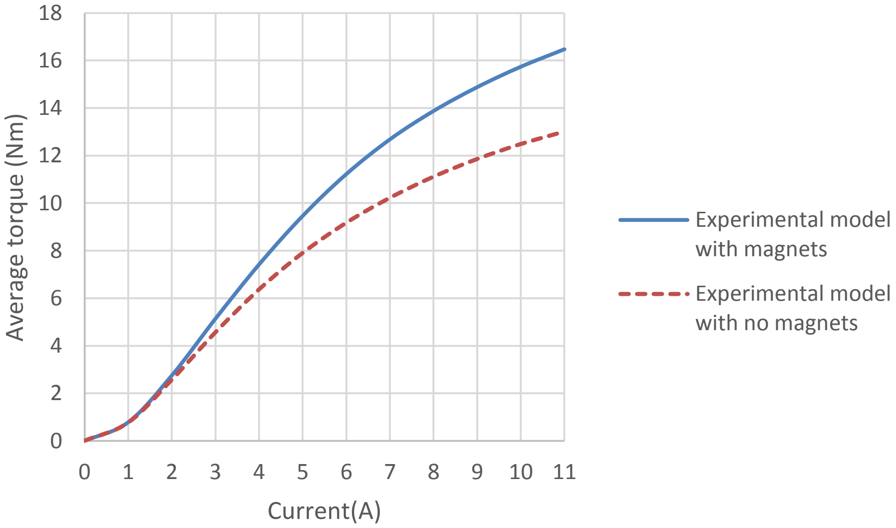

Figure 9-15: Average torque at different current values for MSSRM with and without magnets

9.5 Conclusion on the effect of magnets

From the above analysis it is clear that the introduction of magnets significantly improves the overall performance of the machine. The MSSRM with magnets has high unaligned inductance compared to without magnets, and this is because the magnets prevents the saturation of the stator core at the unaligned position and hence the flux linkage remains linear. In the case of the MSSRM without magnets, the stator tooth becomes saturated even at the unaligned position at higher currents and thus there is a decrease in unaligned flux linkage at higher currents. The presence of magnets within the stator structure causes a big increase in aligned flux linkage, which results in an overall increase in the torque of the machine. From the flux linkage-current waveforms, the overall increase in average torque was found to be 21% in the MSSRM with magnets compared to without magnets model for the rated current.

From the torque values, it is clear that the experimental model cannot reach the required torque value in the stand still condition. Based on the decrease in the torque values, from revised FEA model, it was found that the current has to be increased to 16 Amps to increase the lower value of torque ripple above 17Nm.

9.6 Mutual flux linkage

During fault conditions, the fault phase should have a minimum impact on the remaining healthy phases (in this case, the adjacent phase of lane 2) (Figure 9-16). As the inductance of the SRM changes as the position of rotor position varies, mutual inductance was found by varying rotor position. This time, current pulses were passed through lane 1 phase (Phase A in this case) and voltage was measured across adjacent lane (lane 2) phase (phase X). The magnetic circuit now acts like a transformer. The voltage across the secondary coil (coil X) can be found using equation (9-2)

$$V_{sec}=i_{sec}R_{sec}+L_m\frac{di_p}{dt} \tag{9-2}$$

Since there is no current flowing in the secondary coil, equation (9-2) can be rewritten as:

$$V_{sec}=L_m\frac{di_p}{dt} \tag{9-3}$$

where V_{sec} is the voltage found across the adjacent phase and i_p is the current through phase A. This equation was used to determine the mutual inductance in phase X.

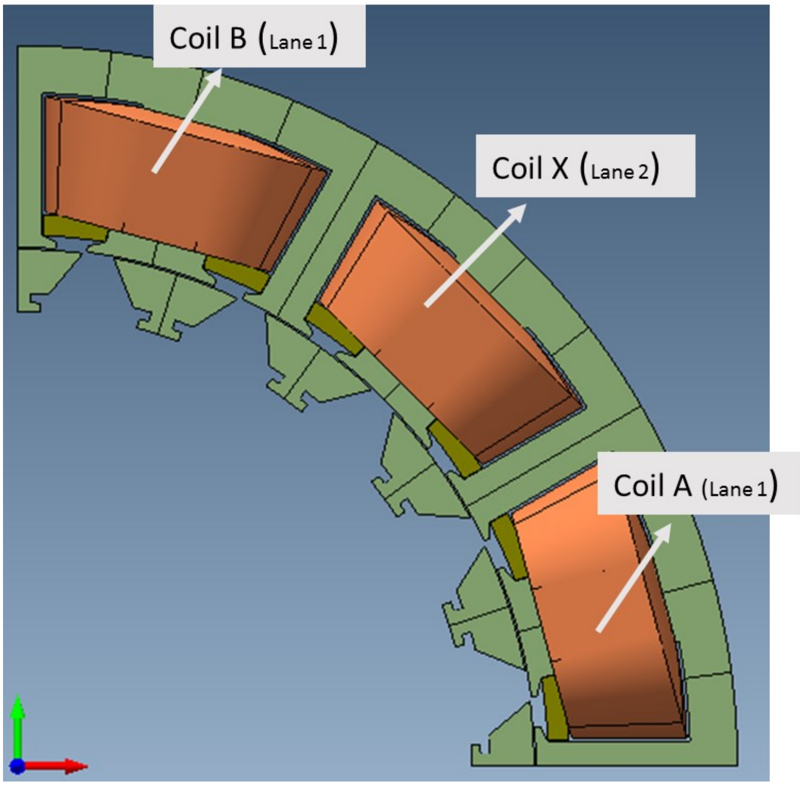

Figure 9-16: Lane 1 and 2 phases

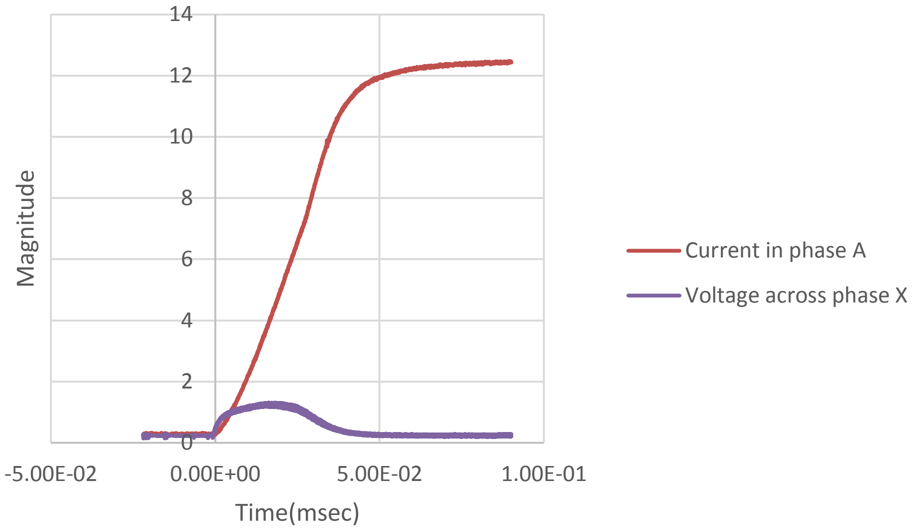

Figure 9-17: Voltage across phase X when current flows through phase A

The results were then compared with those of the FEA model. In this case, the revised FEA model was used as it closely predicts the experimental model. Figure 9-18 shows mutual flux linkage in adjacent phase when the rotor was at the aligned and unaligned position.

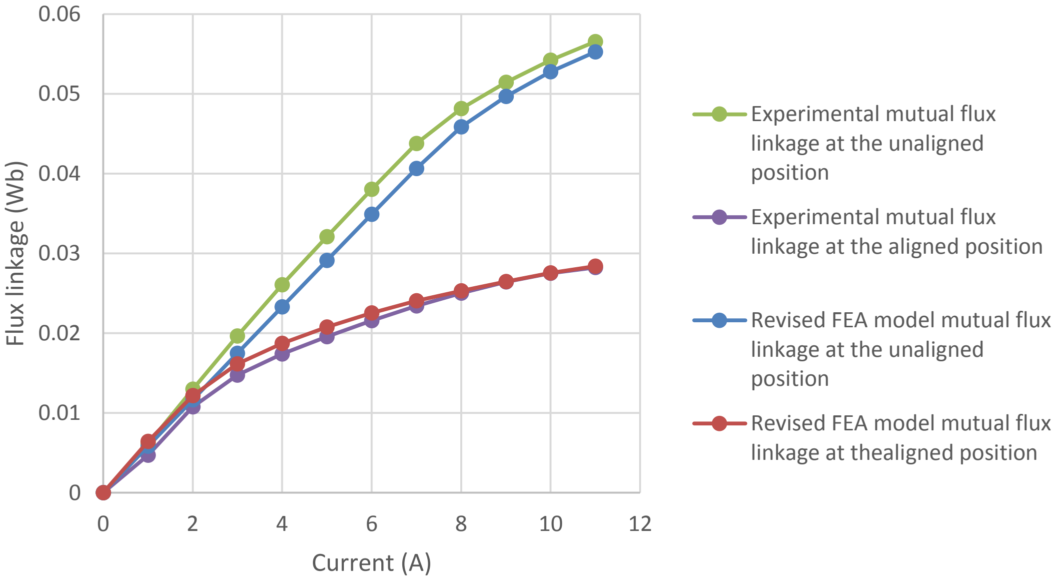

Figure 9-18: Compariosn of mutual flux linkage found across the adjacent phase from the revised FEA and experimental model

The experimental results show an increase in 1.8% mutual flux linkage at the unaligned position compared to revised FEA model at rated current. In this case mutual inductance is 9% in adjacent phase compared to the self-inductance value of conducting phase (Phase A).

Flux linkage in the next phase of the same lane (Phase B in this case) was also found by using the same method. In the MSSRM the flux is short-circuited by segments, and hence there is almost no magnetic interaction between two phases excited by the same lane. Again current was passed through phase A and the voltage across phase B was found. However no variations in voltage were found. From the FEA model, the flux linkage value found is 5 mH which is 0.73% of the self- inductance.

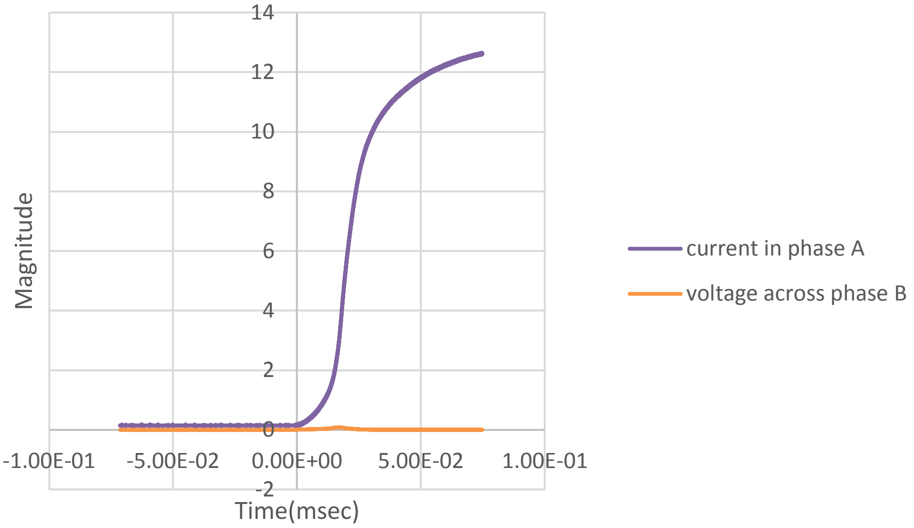

Figure 9-19: Voltage induced in phase B by the flow of current in phase A

9.7 Cogging torque

Cogging torque was measured using static test rig by rotating the rotor without passing any current through the stator coils. Because of very low cogging torque, there were high fluctuations within torque meter values during testing. To make the process easier, the highest fluctuated value (which will include error) of the torque meter at a certain angle was taken. Figure 9-20 shows the cogging torque at 900 rpm using the revised 2DFEA model while Figure 9-21 shows cogging torque values which is 8mNm from experimental model. The results show a 30% increase in the peak cogging torque.

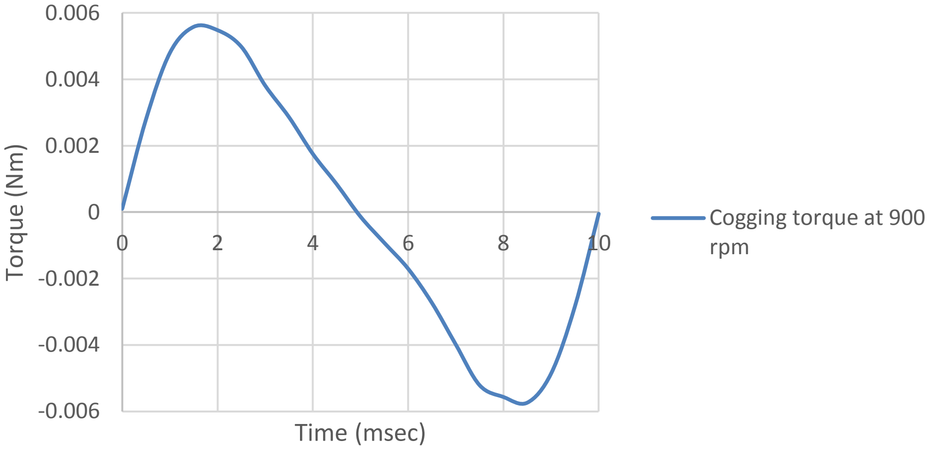

Figure 9-20: FEA model cogging torque at 900 rpm

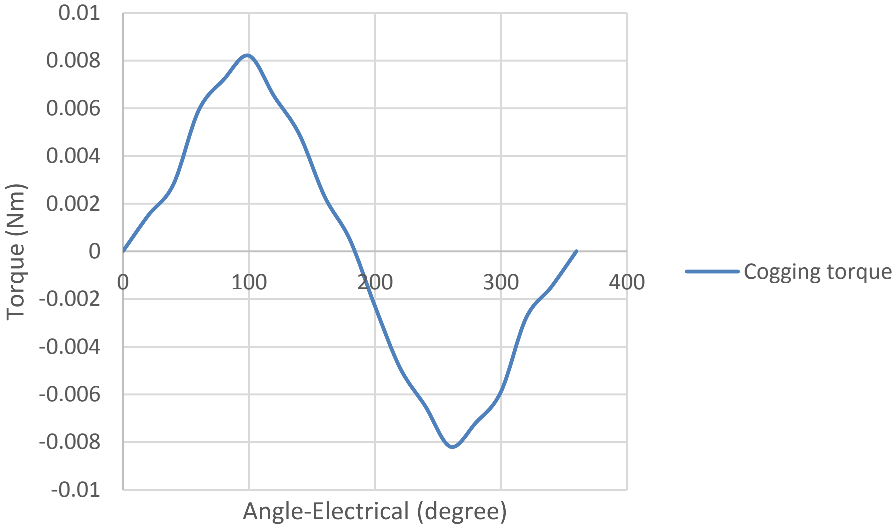

Figure 9-21: Cogging torque values at different electrical angles

9.8 Back EMF measurement

An open circuit test was conducted by using the dynamic test rig with rotor of the MSSRM rotated at 900 rpm to analyse the back EMF induced in the coils. This was done because some of the flux from magnets uses the rotor as short magnetic path, thus inducing voltage in the rotor segments. The MSSRM was rotated at the rated speed (i.e. 900 rpm). Figure 9-22 shows the back EMF values at 900 rpm from the experimental model for phases A and X respectively. The peak per-phase back EMF values measured were 5.02 and 5.34V (phase average) in two phases; this is only 1.8% of the base PM machine back EMF. The FEA model gives a similar waveform with a peak value of 5.2V (Figure 9-23); which is almost in the middle of the two measured values.

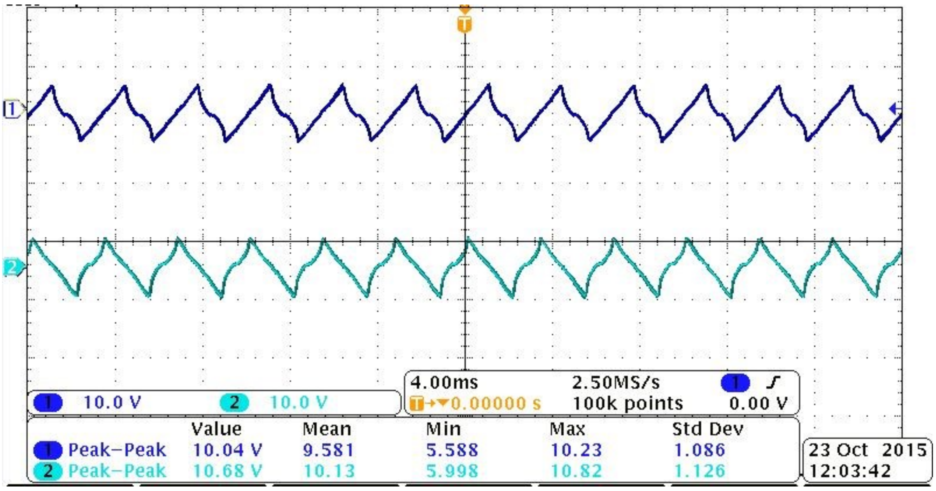

	Value	Mean	Min	Max	Std Dev
1 Peak−Peak	10.04 V	9.581	5.588	10.23	1.086
2 Peak−Peak	10.68 V	10.13	5.998	10.82	1.126

Figure 9-22: Back EMF across phase A and X at 900 rpm (Experimental model)

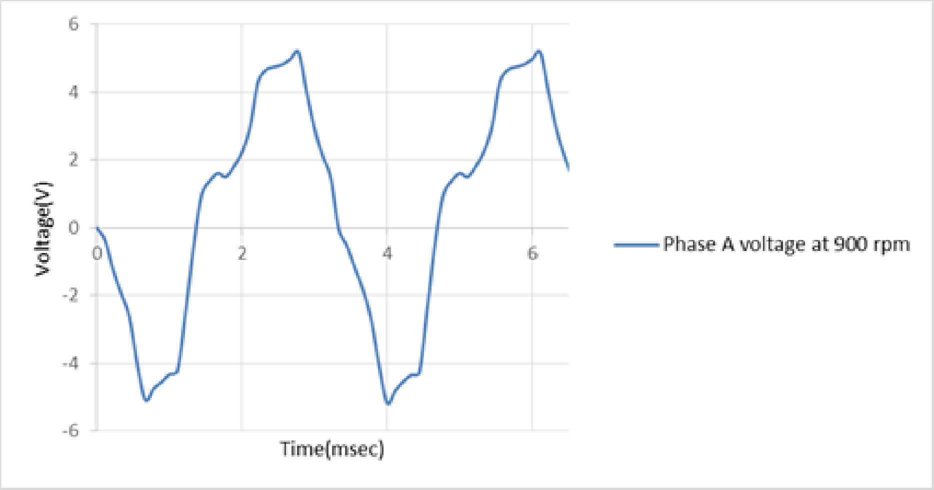

Figure 9-23: Back EMF across phase A at 900 rpm (Revised FEAmodel)

9.9 Short-circuit current test

A short-circuit test was conducted by short circuiting one of the phases and then rotating the rotor of MSSRM at 900 rpm. Figure 9-24 shows the measured short-circuit current under this condition. This is also replicated in 3D FEA and the associated prediction is shown in Figure 9-25. The peak value of short circuit current found in each phase of the prototype was 167mA; this is only 2.3% of the base PM machine short-circuit current. The FEA model gives a similar waveform with a peak value of 172mA.

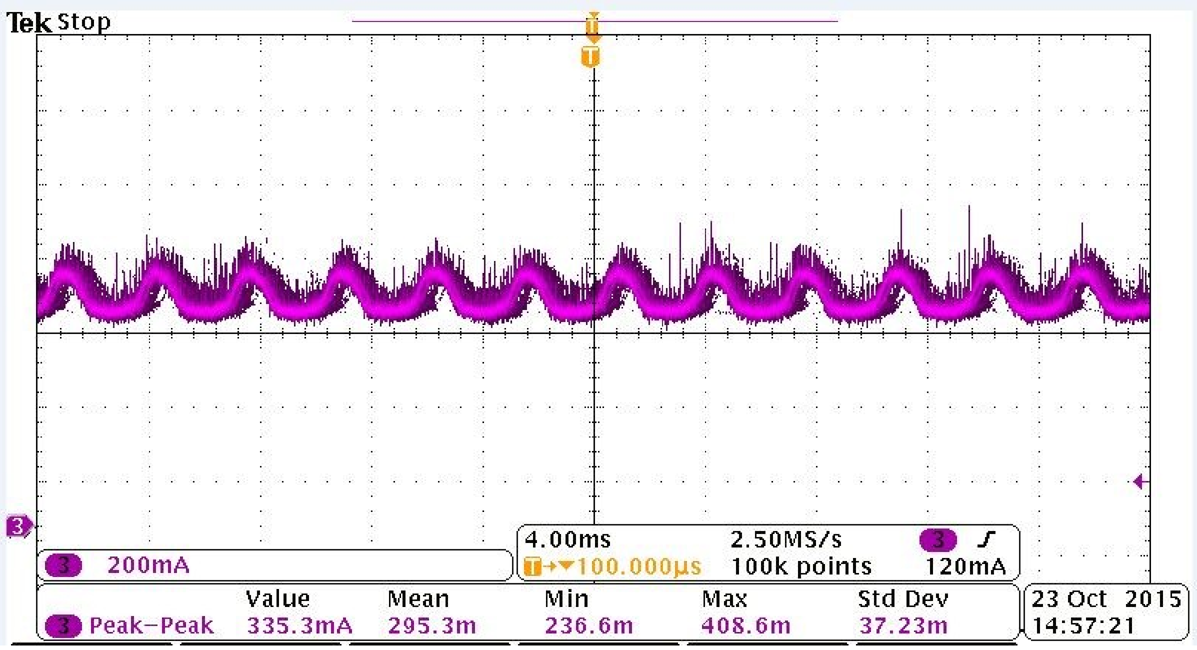

Figure 9-24: Short circuit current in phase A at 900 rpm (Experimental model)

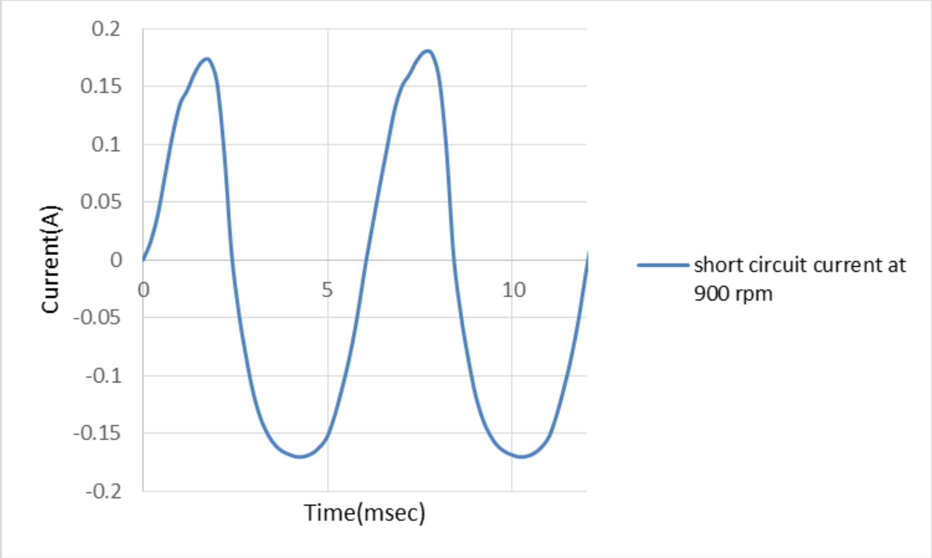

Figure 9-25: Short circuit current of phase A at 900 rpm (Revised FEA model)

9.10 Thermal analysis

Resistance in the prototype was found to be 21% higher than that in the FEA model due to the winding technique used during the winding of the machine. This results in a rapid increase in temperature of the coil. Two thermocouples were placed at two different positions

1. The upper end of coil
2. In the middle of the coil

A 5 Ampere (DC current) was passed in the coil. The temperature in the coil reached to 80°C in 30 seconds which then remained stable.

Then the DC current was increased to 11 Amps (peak value of the rated current) and the temperature of coil reached to 200°C after 1 minute and 48 seconds. Thereafter the temperature continued to increase which results in damage to one of the phase coils (Figure 9-27). This rapid increase in temperature of the coil indicates that the machine fill factor should be increased (by increasing the cross sectional area of the coil) to reduce the resistance of the coil which will result in increase in mass of the machine. A better winding technique (discussed in chapter 10) should be used to avoid rapid increase in temperature. Figure 9-26 shows increase in temperature when rated current flows through the coil while Figure 9-27 shows damage to one of the phase when the rated current applied for longer time. The machine was rewound with bigger diameter of copper wire.

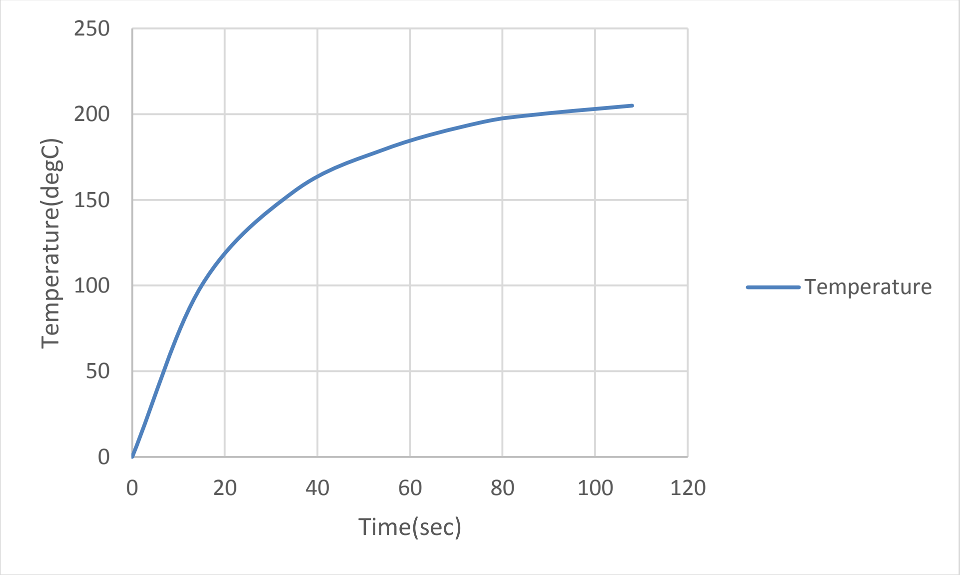

Figure 9-26: Thermal test results

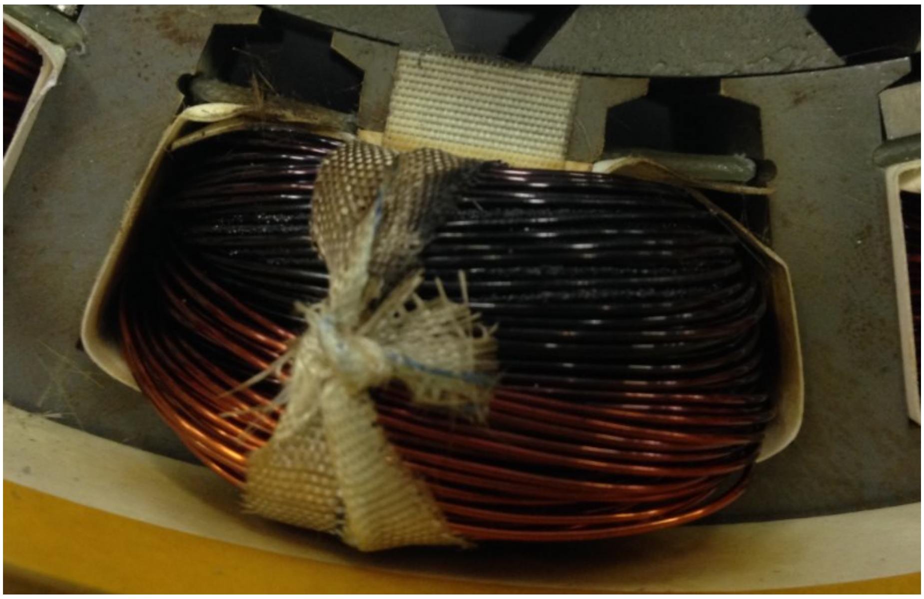

Figure 9-27: Damage to one of the coils due to overheating

9.11 Inductor measurements

This section shows different practical results obtained from the pot core MBI.

9.12 Inductance measurement

Inductance of pot core MBI was measured passing DC current pulses through coil and resultant voltage and current through coil was found. By using equation (9-4) inductance across of coil was calculated (Psi-I test).

$$\Psi = \int_o^t [v - iR]dt \tag{9-4}$$

where Ψ is the flux linkage, R is the resistance of the coil, v is the voltage applied across each phase and i is the current flowing through the coil.

9.13 Testing methodology

In order to validate the results, a conventional E-E core inductor was tested first by using Psi-I method in which DC voltage is applied across coil and by measuring rise and fall in current w.r.t voltage, inductance was calculated. Hameg LCR bridge and Biologic potentiostat were also used (which work on the principle of subjecting sinusoidal voltage with certain frequency, measuring magnitude and relationship of current to find impedance from which inductance can be measured) and compared with Psi-I test results. Hameg LCR has limited bias up to 200mA maximum. The Biologic Potentiostat Hameg LCR bridge both can read resistance at test frequency. Table 9-2 shows resultant inductance values found from all three methods. Figure 9-29 shows inductance values from Psi-I test. As expected there is a gradual decrease in inductance as current increases.

Figure 1-28: E core inductor-21.12 mH

Table 9-2 : Inductance values from all 3 methods

Conventional E-E core inductor		
Hameg bridge at 20Hz	Psi-I	Biologic Potentiostat at 20Hz
24.797mH	25mH	24.6mH

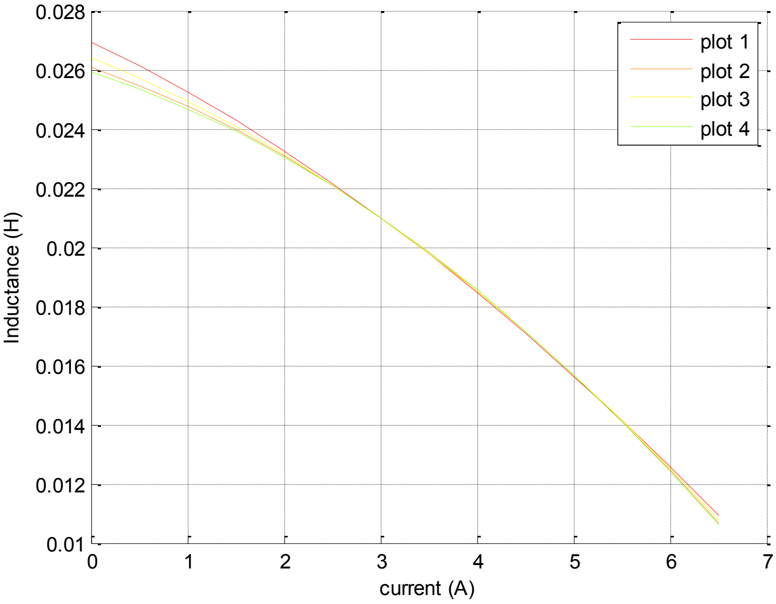

Figure 9-29: Inductance values from psi –I test with repeated dc pulses

9.14 MBI inductor with 150 turns

MBI pot core inductor with 150 turns was tested by using the same method as that applied to conventional E-E core inductor. Figure 9-30 shows psi-I results of inductor without magnets and Figure 9-31 shows inductance of inductor using Psi-I method. DC resistance found was 0.218 Ω.

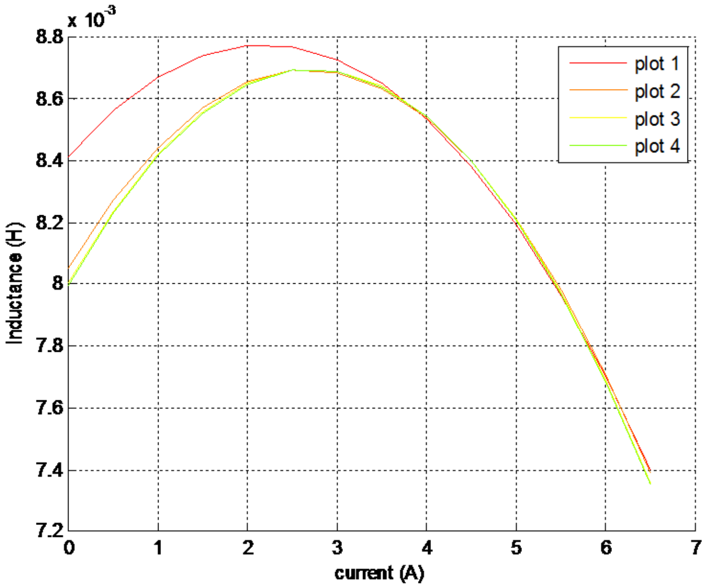

Figure 9-30: Inductance without magnets in the core(150 turns)

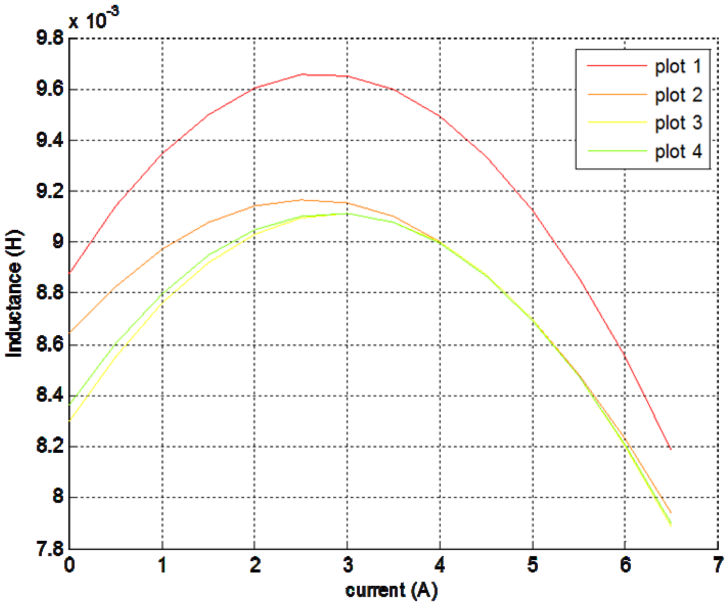

Figure 9-31: inductance with magnets in the core(150 turns)

Table 9-3: Test results from all three methods for 150 turns inductor

Inductance measurement using 3 methods		
Hameg bridge at 20 Hz	Psi-I with magnet bias	Biologic Potentiostat at 20Hz
6.48mH	8.2mH	6.56mH
0.231Ω	0.218Ω	0.253Ω

Measured inductance from the Psi-I test is higher compared to the Hameg and biologic potentiostat measurements. Also from Figure 9-30 and Figure 9-31 there is an increase in inductance as current varies from 1 to 5 Amps which is very unpredictable.

From both figures it is clear that inductor with magnets has higher inductance compared to inductor without magnets. The inductance shows a very nonlinear response with an increase in inductance for the starting current values and then rapid decrease. There is a big difference in measured and FEA model values which can be a reason of minor loop effect due to the presence of biased DC current which is very common in most of the inductors having small hysteresis loop [73].

To investigate the minor loop effect, the test was modified by putting larger AC currents over the DC bias level required. Resultant values showing increase in inductance values as AC current increases at any DC bias level.

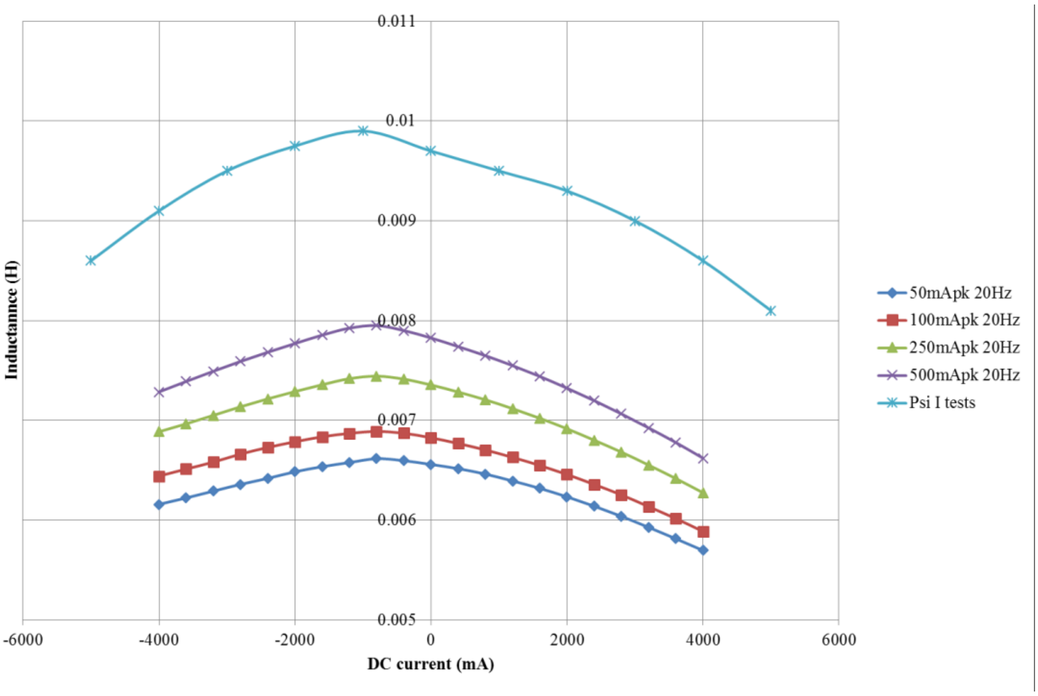

Figure 9-32: Measured inductance values with effect of minor loop as AC current increases for 150 turns

9.15 Inductance value at 250 turns

Due to lower inductance value at 150 turns because of minor loop effect, the number of turns were increased to 250 to increase inductance value as inductance is proportional to the square number of turns. Because of circular coil, more turns can be put into the available space. By using FEA model, MBI was compared with E-E core with magnets for 250 turns which shows MBI have better inductance compared to E-E core with magnets. Figure 9-33 shows inductance values for both 150 and 250 turns in MBI and E-E core with magnets inductors by using FEA software. Resultant increase in copper loss and mass of inductor is shows in Table 9-4

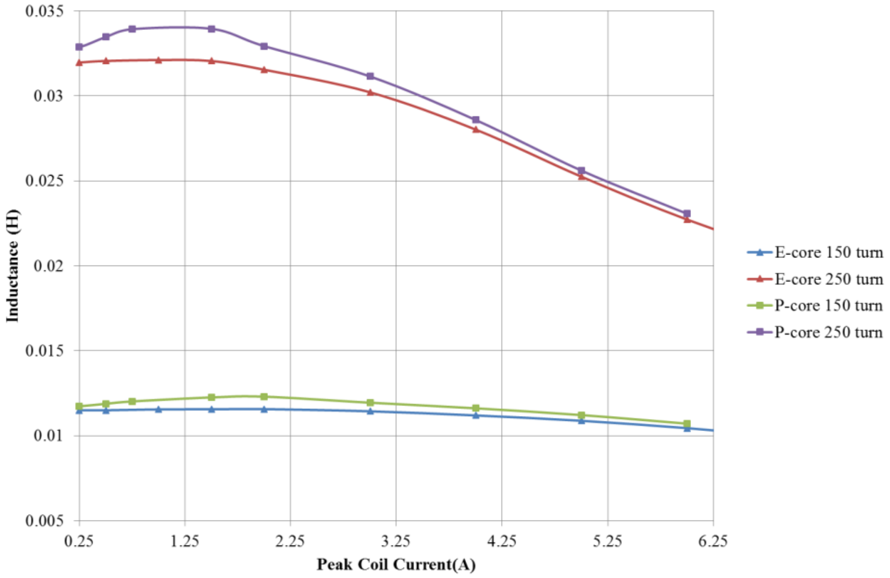

Figure 9-33: comparison of E-E core with magnets to MBI with different turns by using FEA software

Table 9-4: Copper loss and resultant masses of each component as number of turns increases

Copper area(mm^2)	662.12
Number of turns	250.00
Area of one conductor(mm^2)	1.54
Conductivity at 20°C (S)	5.7e7
Resistance(Ω)	0.43
Copper loss at 7 amps(watts)	21.05
Fill factor	0.58
core mass(Kg)	0.53
Magnet mass (kg)	0.00
Copper mass (Kg)	1.49

DC resistance measured using psi-I test was 0.406Ω. Figure 9-34 shows inductance values using Psi-I method.

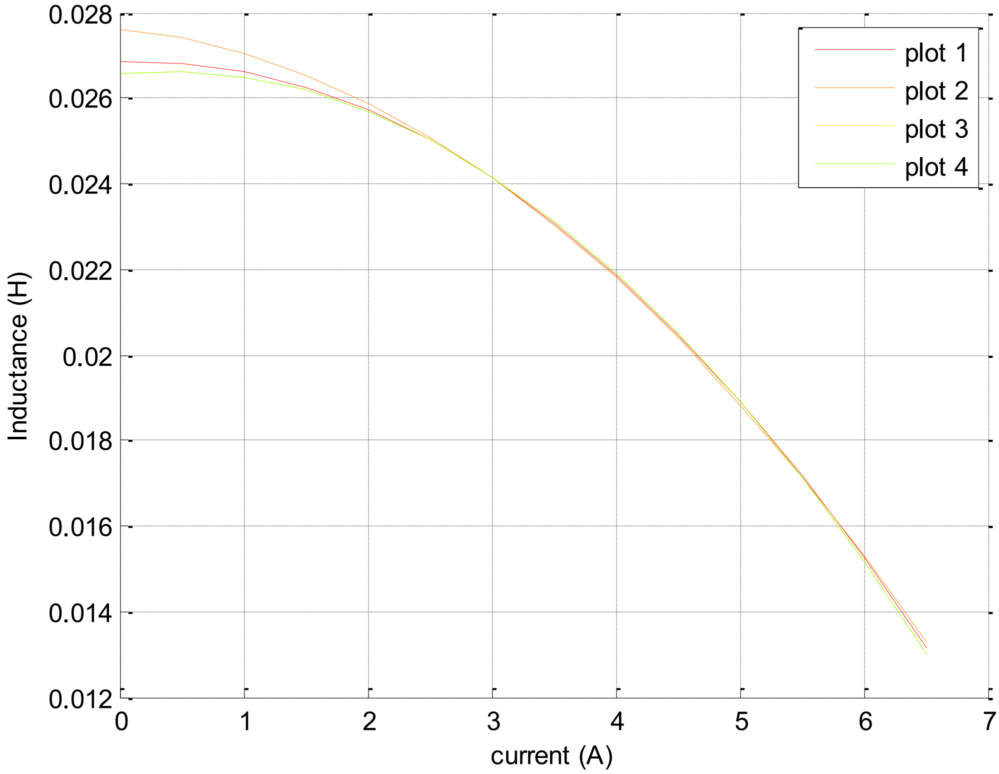

Figure 9-34: inductance with magnets in the core(250 turns)

Table 9-5: Test results from all three methods for 150 turns inductor

Inductance measurement using 3 methods(250 turns)		
Hameg bridge at 20 Hz	Psi-I with magnet bias	Biologic Potentiostat at 20Hz
19.59mH	27mH	19.8mH
0.493Ω	0.406Ω	0.529Ω

Again Psi-I test shows greater inductance value as compared to other two methods with a difference of 35% between other two methods and Psi-I method.

Just like MBI with 150 turns, MBI with 250 turns have minor loops effect which was found by following same procedure as mentioned above and result is shown in Figure 9-35.

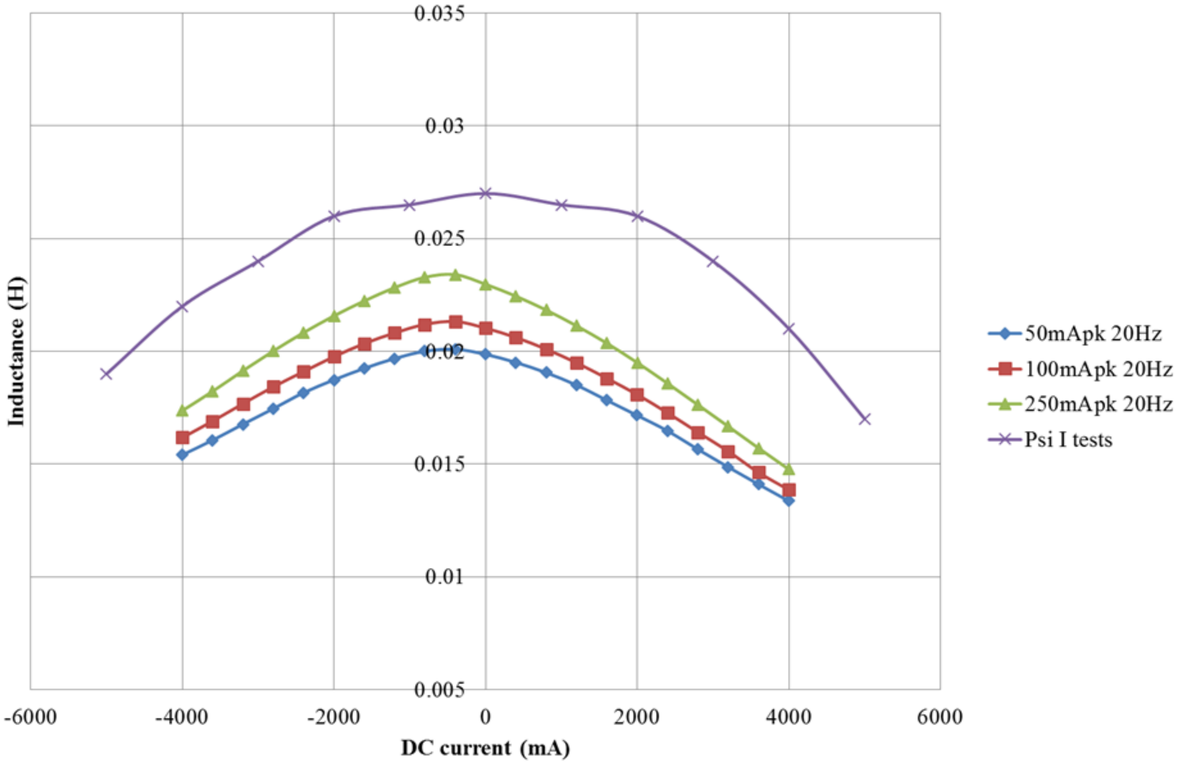

Figure 9-35: Measured inductance values with effect of minor loop as AC current increases for 250 turns

9.16 Conclusion

Testing of machine was conducted using a static and dynamic test rig. Current-flux linkage waveform, mutual flux linkage and cogging torque were found using the static test rig. The results showed a decrease in both the aligned and unaligned position which was assumed to be due to a bigger air gap between the stator and the rotor because of lower inductance values when low current flows through the coil at the aligned position. More FEA simulations were conducted to verify the situation and a revised model was used as the baseline and was then compared with experimental model under different conditions. Flux linkage-current waveforms of the MSSRM with and without magnets show an increase in 21% torque by the introduction of magnets into the machine. Magnets prevents earlier saturation of the stator core, which results in significant increase in aligned inductance and hence the torque of the machine. Mutual inductance was found by varying the position of the rotor. Mutual flux linkage found in adjacent phase was 9% of the excited phase self- inductance. Cogging torque was found by rotating the rotor at different angles and measure the torque value from the torque meter. Because magnet flux is shorted by the stator core, cogging torque found was almost zero. Open circuit voltage and short-circuit current were found by using dynamic test rig which showed 20% and 12% increase in measured values compared to the revised 2DFEA model respectively.

Open circuit voltage and short-circuit current is only 5% and 3% compared to that measured in the based PM machine respectively. Thermal analysis was conducted by removing the magnets from one phase and then passing current through that phase and this resulted in very rapid increase in temperature of the coil.

Tests results show a clear improvement in inductance by adding magnet into the magnetic circuit. Effect of minor loop on inductance value is dominant which was shown by passing AC current of different magnitude with biased dc current value (limited by measuring equipment). Number of turns were increased from 150 to 250 to increase inductance with copper loss still only 21.05 watts. This results in increasing the inductance from 6mH to 19mH.

Chapter 10 Conclusion and future work

The principle aim of this work was to design a dual lane, torque dense fault tolerant switched reluctance machine (SRM) for an aerospace application. SRMs with a short stack length and high electrical loading result in high leakage inductance, which decreases the performance of the machine. The concept of magnet assist was introduced which increased the torque developed by the machine. A magnet assisted fault tolerant SSRM was constructed, tested and shown to be a viable concept and an improvement at the current state of the art in terms of fault tolerance and torque density [54, 60, 74].

10.1 Background

The aerospace industry is moving towards more electric aircraft which will improve the performance and efficiency of new and future aircraft. Aerospace electrical machines must be torque dense and fault tolerant. The PM machine is seen as a good option but has the disadvantage of high drag torque, which is more dominant in low speed actuators. Induction machine shows to have a high mutual inductance between phases and little limit on the magnitude of a short-circuit fault, barring them from fault tolerant applications.

SRMs are a good option with natural fault tolerance and high temperature capability but suffer from low torque density. SSRMs are a better option, with minimum mutual coupling between phases and high torque density than a conventional SRM. However the torque density of the SSRM is still less than a PM machine.

10.2 Magnet assist applied to SSRM

The operating range of the conventional SSRM is limited to the first quadrant of the B-H curve. By the introduction of magnets around the stator tooth tip, with flux from the magnets opposing the main coil flux, the operating range can be extended to the third quadrant of the B-H curve. This will result in less saturation at the aligned position, hence increased the area between the aligned and unaligned inductance curves. By way of proof, 2DFE simulations were carried out and a conventional SSRM was compared with a magnet assist SSRM for the same copper loss. Results showed there was indeed an increase of 18% torque for the MSSRM.

10.3 Fault tolerant MSSRM for aerospace application

Previous work on the magnet free SRMs for aerospace applications shows that fault tolerant is best achieved using the segmented topology, SSRM. The SSRM topology has a higher torque density and much lower interaction between the phases when compared to the conventional

SRM. However, due to the aspect ratio of the design specifications, the short stack length and high electric loading resulted in a SSRM with a 40% reduction in expected performance due to the end effects.

To solve the problem, the magnet assist concept was applied to the same fault tolerant SSRM. From the 3DFE analysis, it was found that the MSSRM gives 29% more torque compared to the conventional SSRM at the rated current. This improvement led to the further investigation of the MSSRM for this application.

The fault tolerant MSSRM was simulated under fault conditions to investigate the demagnetisation within the magnets. By using 2DFE software, it was found that magnets can demagnetise at high temperature as expected with the current density of this application. To avoid demagnetisation, magnets were moved up the stator tooth which resulted in decreasing the slot area and decrease in electric loading of the machine for the given current density. To increase the torque, stack length was increased by 25%, which results in the MSSRM mass being almost equal to the PM machine. Various parameters i.e. t/λ, stator coreback thickness, rotor coreback thickness and magnet thickness were varied to optimize the machine performance, this give an 8% improvement in torque. 3DFE analysis of the final optimized model was carried out and showed the machine cannot achieve the stall torque required (first critical torque) at the rated current of 11 Amps, however allowing for an increase in current to 13Amps, will achieve the standstill torque and the current when rotating can be dropped. This feasible MSSRM was then constructed.

10.4 Testing of the fault tolerant MSSRM

Testing of the MSSRM was initially carried out without the magnets, and then with to assess the effect of magnet assist on the machine. Experimental results were obtained for both cases and then compared to their FEA analysis.

The results showed a reduction in equal proportion of both the aligned and unaligned flux linkage, which was attributed to a larger than expected air-gap. FEA analysis was carried out and seemed to confirm a larger air-gap of 0.41mm. This was confirmed in the simulation both with and without the magnets.

From the measured current-flux linkage tests, calculating the torque from the area enclosed shows 21% more torque for same copper loss and current density with the magnet assist in place. Results confirmed that the MSSRM will be able to achieve 90% of the target torque at rated current. To achieve the target torque, the current should be increased to 16 Amps, this is feasible.

Mutual inductance was measured between adjacent and far phases. Experimental results show a 9% mutual inductance between adjacent phases, this is across lane linkage and must be minimal for fault tolerance. The 9% figure is however deemed acceptable [53, 54]. There was no magnetic interaction found between phases of the same lane due to the physical separation and minimal coupling at a distance offered by the SSRM structure.

Cogging torque was measured as only 8mNm. This is negligible when compared to PM machine.

Open circuit voltage tests were carried out using a dynamometer test rig at 900 rpm. The open circuit induced EMF 7Vrms, this is only 5% of that experienced by the comparable PM machine and highlights the inherent fault tolerance of the MSSRM topology. Short-circuit fault testing was also carried out. The short-circuit current was measured at 0.21Arms, which is only 3% of the PM machine short-circuit current, again a demonstration of the MSSRMs inherent fault tolerance.

10.5 Suitability for aerospace application

Based on the above work, magnet assist SSRM can be a good option to replace the PM machine. In general, the following key points makes the MSSRM a suitable contender;

1) The MSSRM has a very simple and robust structure which is easy to construct.
2) The MSSRM uses much less magnet compare to the PM machine which can be reduced even more by improved optimization techniques which will reduce the price of the machine. In this case, the MSSRM uses only 32% of the magnet mass used in the PM machine.
3) Flux from the magnets within the MSSRM uses the stator coreback as a short path for completing the magnetic circuit which results in negligible cogging torque. Compare to this, the permanent magnets in the rotor of a PM machine results in very high cogging torque.
4) As magnets use the stator coreback as short magnetic path, EMF induced in the rotor because of the magnets in the stator is very small. This results in very low open circuit voltage. In this case, the open circuit voltage is only 5% compared to the PM machine.
5) As the back EMF is very low, very little current is induced in the stator coils. In this case, its only 3% compared to the PM machine which results in high drag torque in the case of PM machine.
6) In the MSSRM, magnets are not in the main flux path when moved up the stator tooth which results in avoiding it from demagnetisation at high electric load. In the case of

PM machines, magnets are always in the path of external magnetic field which can demagnetise it under fault conditions.

7) The torque density of the MSSRM is high compared to the conventional SRM and SSRM. In this case, the mass of the MSSRM is almost the same as that of the PM machine while achieving 90% of its average torque.
8) Mutual coupling between the phases can be further reduced by improved designing.
9) The performance of the machine can significantly increase if the stack length of the machine increases.

10.6 Magnet assisted pot core inductor

A novel magnet assisted pot core inductor was designed. The structure was improved by using FEA software to investigate the improvement in inductance when magnets are places at different positions within the inductor core. Pot core inductor was simulated and compared with E-E core with and without magnets for same copper loss, core mass and cross sectional area of core. Mass of pot core inductor was 9% less (because of less copper mass) than E-E core with magnets with an average 22% higher inductance over the whole inductance curve. Mass of pot core inductor was 11% less than E-E core with magnets with an average 7.5% higher inductance over the whole inductance curve. Testing results shows greater decrease in inductance because of minor loop effect which was found and then shown within the test results. Number of turns were increased from 150 to 250 which increased inductance from 6mH to 19mH.

10.7 Future work

Based on analysis of both MSSRM and pot core MBI, work can be done in future to improve machine and inductor performance. Few changes in structure that can be done are follows

10.7.1 Compressed coils

To improve the efficiency of the MSSRM, compressed coils can be used. A conductor of bigger diameter can be used and then compressed to give the coil a higher fill factor and lower resistance which can reduce the dominant copper loss.

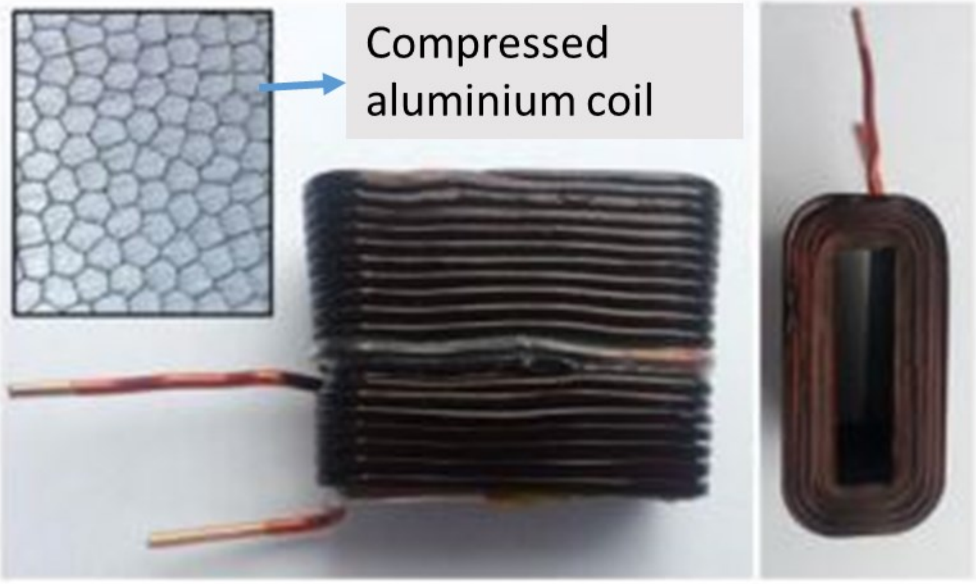

Figure 10-1: Compressed aluminium coil for aerospace application [75]

10.7.2 Segmented stator structure

To increase the fill factor and use a compressed coil, a segmented stator structure is a good solution. The stator can be made from small segments with sufficient area for the coil to be constructed on an aluminium frame, compressed, and then placed within the given slot by sliding over top of the main thick tooth of the stator.

Magnets were placed at the stator tooth tip since high temperatures due to small fill factor was expected. By using the above two concepts, magnets can be placed at the tooth tip without being demagnetised as long as temperature of the machine is kept low. Moving the magnets down the stator tooth tip will further increasing the slot area and hence the efficiency of the machine. Figure 10-1 and Figure 10-2 shows the structure of the segmented stator [75].

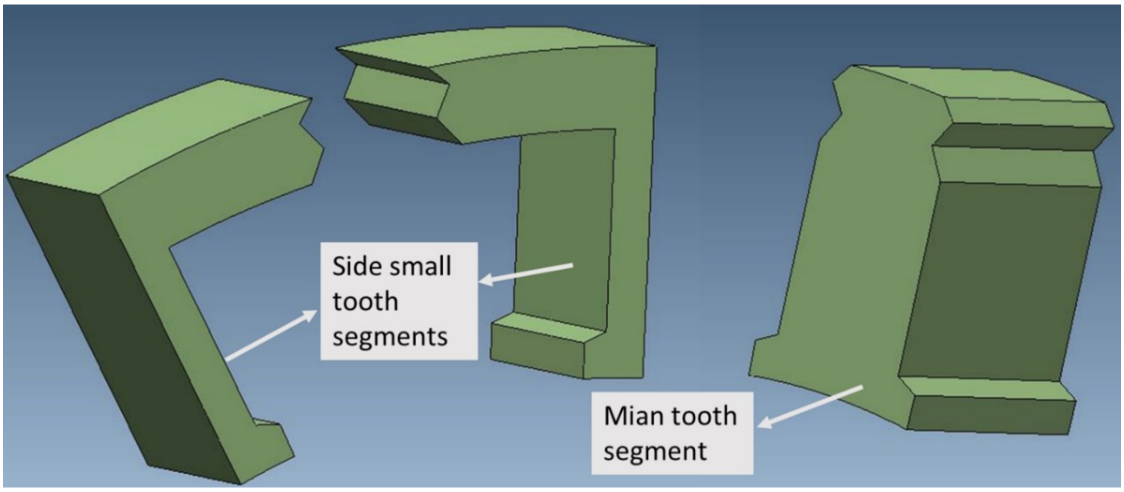

Figure 10-2 : segmented stator structure with stator tooth segments divided into parts

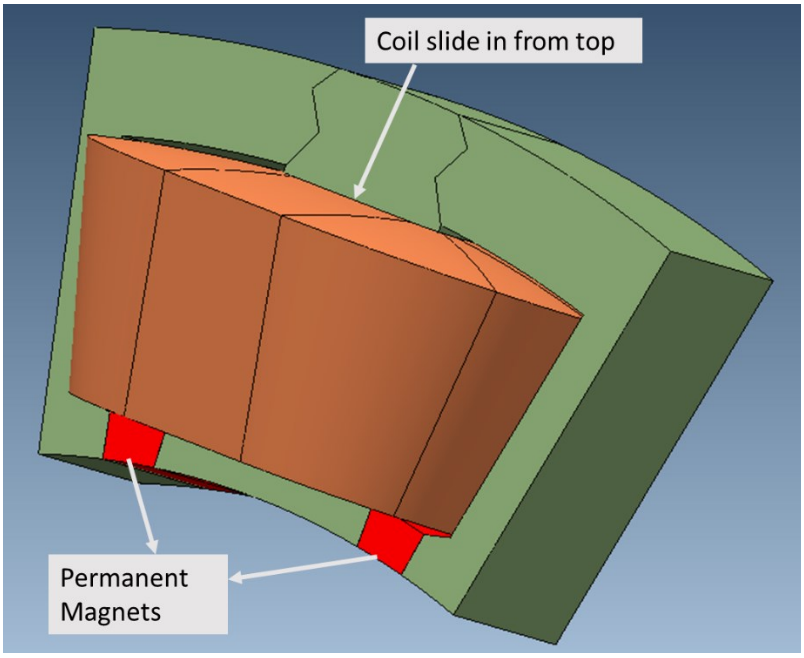

Figure 10-3: Compressed coil slides into main tooth from top and then joins small segment to main tooth

10.7.3 Lamination material

Non-oriented silicon steel (N020) was used to make the stator and rotor with saturation flux density of 1.8T. Because of the small size of the machine with a high MMF requirement to produce the required rated torque, the N020 laminations saturating point is low enough which results in the saturation of the material at lower currents, and thus a decrease in torque. To overcome this problem, steel with higher magnetic saturation, such as cobalt iron steel can be used. Such a kind of steel has high saturation induction (up to 2.22T) which results in avoiding the saturation of materials at higher currents. This type of steel is available in very thin laminations, which also reduces the iron losses of the machine [76].

10.7.4 Simulation procedure

Another way of avoiding the early saturation of the machine is to increase t/λ ratio, which results in an increase in the overall thickness of the stator and rotor, hence avoiding earlier saturation. From 2DFE analysis, a lower t/λ ratio results in higher torque, however, variation in saturation should also be investigated in 3DFE model.

Manual optimization was conducted while developing the machine. Better optimization techniques can be used to improve machine performance.

10.7.5 Inductor design and simulation techniques

As with the MSSRM, the pot core MBI performance can be also be improved by using better optimization techniques. Interaction between the PM flux and main coil flux can result in a high saturation level and design can be improved to avoid this effect by changing the orientation of the magnet in the core.

References

[1] D. D. Bell, "Contrasting the medical-device and aerospace-industries approach to reliability," in *Reliability and Maintainability Symposium, 1995. Proceedings., Annual*, 1995, pp. 125-127.

[2] A. Wechesler, "Improving fault tolerant drives for aerospace applications," Newcastle university 2013.

[3] C. Zhong, L. Yingpeng, C. Miao, S. Lei, and L. Jianxia, "Design and implementation of a high performance aeronautical active power filter," in *IECON 2010 - 36th Annual Conference on IEEE Industrial Electronics Society*, 2010, pp. 2032-2037.

[4] http://www.actuation2015.eu/.

[5] R. De Maglie, G. Osvald, J. Engstler, A. Engler, and J. P. Carayon, "Optimized 70kW power inverter dedicated to future aircraft applications," in *Power Electronics and Applications, 2009. EPE '09. 13th European Conference on*, 2009, pp. 1-10.

[6] R. L. A. Ribeiro, C. B. Jacobina, A. M. N. Lima, and E. R. C. da Silva, "A strategy for improving reliability of motor drive systems using a four-leg three-phase converter," in *Applied Power Electronics Conference and Exposition, 2001. APEC 2001. Sixteenth Annual IEEE*, 2001, pp. 385-391 vol.1.

[7] C. B. Jacobina, I. S. Freitas, T. M. Oliveira, E. R. C. da Silva, and A. M. N. Lima, "Fault tolerant control of five-phase AC motor drive," in *Power Electronics Specialists Conference, 2004. PESC 04. 2004 IEEE 35th Annual*, 2004, pp. 3486-3492 Vol.5.

[8] F. Barrero, J. Prieto, E. Levi, R. Gregor, S. Toral, M. J. Duran*, et al.*, "An Enhanced Predictive Current Control Method for Asymmetrical Six-Phase Motor Drives," *Industrial Electronics, IEEE Transactions on,* vol. 58, pp. 3242-3252, 2011.

[9] B. C. Mecrow, A. G. Jack, J. A. Haylock, and J. Coles, "Fault-tolerant permanent magnet machine drives," *Electric Power Applications, IEE Proceedings -,* vol. 143, pp. 437-442, 1996.

[10] J. W. Bennett, B. C. Mecrow, D. J. Atkinson, C. Maxwell, and M. Benarous, "A fault tolerant electric drive for an aircraft nose wheel steering actuator," in *Power Electronics, Machines and Drives (PEMD 2010), 5th IET International Conference on*, 2010, pp. 1-6.

[11] B. C. Mecrow, E. A. El-Kharashi, J. W. Finch, and A. G. Jack, "Segmental rotor switched reluctance motors with single-tooth windings," *Electric Power Applications, IEE Proceedings -,* vol. 150, pp. 591-599, 2003.

[12] B. BD, US Patent No.3678352 1971.

[13] Horst, US Patent No.3679953, 1972.

[14] R. Krishnan, *Switched Reluctance Motor Drives*: Industrial Electronics Series, CRC Press 2001

[15] P. C. Desai, M. Krishnamurthy, N. Schofield, and A. Emadi, "Switched Reluctance Machines with higher rotor poles than stator poles for improved output torque characteristics," in *Industrial Electronics, 2009. IECON '09. 35th Annual Conference of IEEE*, 2009, pp. 1338-1343.

[16] T.J.Miller, *Switched Reluctance Motors and Their Control*: Oxford: Clarendon Press, 1993.

[17] A. M. Michaelides and C. Pollock, "A new magnetic flux pattern to improve the efficiency of the switched reluctance motor," in *Industry Applications Society Annual Meeting, 1992., Conference Record of the 1992 IEEE*, 1992, pp. 226-233 vol.1.

[18] J. D. Widmer, R. Martin, C. M. Spargo, B. C. Mecrow, and T. Celik, "Winding configurations for a six phase switched reluctance machine," in *Electrical Machines (ICEM), 2012 XXth International Conference on*, 2012, pp. 532-538.

[19] P. C. Desai, M. Krishnamurthy, N. Schofield, and A. Emadi, "Design and performance evaluation of a novel 6/10 Switched Reluctance Machine," in *Electric Machines and Drives Conference, 2009. IEMDC '09. IEEE International*, 2009, pp. 755-762.

[20] C. Lin and B. Fahimi, "Prediction of radial vibration in switched reluctance machines," *IEEE Trans. Energy Convers,* vol. 28, pp. 1072-1081, 2013.

[21] J. O. Fiedler, K. Kasper, and R. W. De Doncker, "Calculation of the acoustic noise spectrum of SRM using modal superposition," *Industrial Electronics, IEEE Transactions on,* vol. 57, pp. 2939-2945, 2010.

[22] M. N. Anwar and I. Husain, "Radial force calculation and acoustic noise prediction in switched reluctance machines," *Industry Applications, IEEE Transactions on,* vol. 36, pp. 1589-1597, 2000.

[23] B. C. Mecrow, "New winding configurations for doubly salient reluctance machines," in *Industry Applications Society Annual Meeting, 1992., Conference Record of the 1992 IEEE*, 1992, pp. 249-256 vol.1.

[24] B. C. Mecrow, "New winding configurations for doubly salient reluctance machines," *Industry Applications, IEEE Transactions on,* vol. 32, pp. 1348-1356, 1996.

[25] L. Yuefeng, F. Liang, and T. A. Lipo, "A novel permanent magnet motor with doubly salient structure," in *Industry Applications Society Annual Meeting, 1992., Conference Record of the 1992 IEEE*, 1992, pp. 308-314 vol.1.

[26] Y. Hasegawa, K. Nakamura, and O. Ichinokura, "Basic consideration of switched reluctance motor with auxiliary windings and permanent magnets," in *Electrical Machines (ICEM), 2012 XXth International Conference on*, 2012, pp. 92-97.

[27] K. Nakamura and O. Ichinokura, "Super-multipolar permanent magnet reluctance generator designed for small-scale renewable energy generation," in *Electrical Machines (ICEM), 2012 XXth International Conference on*, 2012, pp. 489-494.

[28] K. Nakamura, K. Murota, and O. Ichinokura, "Characteristics of a novel switched reluctance motor having permanent magnets between the stator pole-tips," in *Power Electronics and Applications, 2007 European Conference on*, 2007, pp. 1-5.

[29] P. Andrada, B. Blanque, E. Martinez, and M. Torrent, "New hybrid reluctance motor drive," in *Electrical Machines (ICEM), 2012 XXth International Conference on*, 2012, pp. 2689-2694.

[30] J. Jeongwon, H. Jin, and L. Cheewoo, "Novel permanent-magnet-assisted switched reluctance motor (II): Concept, design, and analysis," in *Electrical Machines and Systems (ICEMS), 2013 International Conference on*, 2013, pp. 609-614.

[31] G.A.Horst, "Isolated segmental switched reluctance motor," United states Patent, 1992.

[32] B. C. Mecrow, J. W. Finch, E. A. El-Kharashi, and A. G. Jack, "Switched reluctance motors with segmental rotors," *Electric Power Applications, IEE Proceedings -,* vol. 149, pp. 245-254, 2002.

[33] B. C. Mecrow, E. A. El-Kharashi, J. W. Finch, and A. G. Jack, "Preliminary performance evaluation of switched reluctance motors with segmental rotors," *Energy Conversion, IEEE Transactions on,* vol. 19, pp. 679-686, 2004.

[34] E. A. K. El-Kharashi, "Segmented Rotor Switched Reluctance Motors," Newcastle University 2003.

[35] J. D. Widmer and B. C. Mecrow, "Optimized Segmental Rotor Switched Reluctance Machines With a Greater Number of Rotor Segments Than Stator Slots," *Industry Applications, IEEE Transactions on,* vol. 49, pp. 1491-1498, 2013.

[36] J. Oyama, T. Higuchi, T. Abe, and K. Tanaka, "The fundamental characteristics of novel switched reluctance motor with segment core embedded in aluminum rotor block," in

Electrical Machines and Systems, 2005. ICEMS 2005. Proceedings of the Eighth International Conference on, 2005, pp. 515-519 Vol. 1.

[37] J. D. Widmer and B. C. Mecrow, "Optimised Segmental Rotor Switched Reluctance Machines with a greater number of rotor segments than stator slots," in *Electric Machines & Drives Conference (IEMDC), 2011 IEEE International*, 2011, pp. 1183-1188.

[38] R. Vandana, N. Vattikuti, and B. G. Fernandes, "A Novel High Power Density Segmented Switched Reluctance Machine," in *Industry Applications Society Annual Meeting, 2008. IAS '08. IEEE*, 2008, pp. 1-7.

[39] J. D. Widmer, R. Martin, and B. C. Mecrow, "Optimisation of an 80kW Segmental Rotor Switched Reluctance Machine for automotive traction," in *Electric Machines & Drives Conference (IEMDC), 2013 IEEE International*, 2013, pp. 427-433.

[40] J. D. Widmer, "Segmental Rotor switched reluctance machines for use in automotive traction," 2013.

[41] O. T. Ishikawa S. Sato Y., Abe M. and Tamai K, "Development of High Response Motor and Inverter System for the Nissan LEAF Electric Vehicle," presented at the SAE 2011 World Congress & Exhibition, Detroit, Michigan, United States, 2011.

[42] A. R. Aguilar and S. Munk-Nielsen, "Design, analysis and simulation of magnetic biased inductors with saturation-gap," in *Power Electronics and Applications (EPE'14-ECCE Europe), 2014 16th European Conference on*, 2014, pp. 1-11.

[43] T. Fujiwara and H. Matsumoto, "A new downsized large current choke coil with magnet bias method," in *Telecommunications Energy Conference, 2003. INTELEC '03. The 25th International*, 2003, pp. 416-420.

[44] R. Wrobel, N. McNeill, and P. H. Mellor, "Design of a high-temperature pre-biased line choke for power electronics applications," in *Power Electronics Specialists Conference, 2008. PESC 2008. IEEE*, 2008, pp. 3171-3177.

[45] A. R. Aguilar and S. Munk-Nielsen, "Method for introducing bias magnetization in ungaped cores: “The Saturation-Gap”," in *Applied Power Electronics Conference and Exposition (APEC), 2014 Twenty-Ninth Annual IEEE*, 2014, pp. 721-725.

[46] A. Revilla Aguilar, S. Munk-Nielsen, M. Zuccherato, and Thougaard, "Size Reduction of a DC link Choke Using Saturation-gap and Biasing with Permanent Magnets," in *PCIM Europe 2014; International Exhibition and Conference for Power Electronics, Intelligent Motion, Renewable Energy and Energy Management; Proceedings of*, 2014, pp. 1-8.

[47] G. M. Shane and S. D. Sudhoff, "Design and optimization of permanent magnet inductors," in *Applied Power Electronics Conference and Exposition (APEC), 2012 Twenty-Seventh Annual IEEE*, 2012, pp. 1770-1777.

[48] G. M. Shane and S. D. Sudhoff, "Permanent magnet inductor design," in *Electric Ship Technologies Symposium (ESTS), 2011 IEEE*, 2011, pp. 330-333.

[49] R. Krishnan and A. S. Bharadwaj, "A comparative study of various motor drive systems for aircraft applications," in *Industry Applications Society Annual Meeting, 1991., Conference Record of the 1991 IEEE*, 1991, pp. 252-258 vol.1.

[50] A. G. Jack, B. C. Mecrow, and J. A. Haylock, "A comparative study of permanent magnet and switched reluctance motors for high-performance fault-tolerant applications," *Industry Applications, IEEE Transactions on,* vol. 32, pp. 889-895, 1996.

[51] J. A. Haylock, B. C. Mecrow, A. G. Jack, and D. J. Atkinson, "Operation of a fault tolerant PM drive for an aerospace fuel pump application," in *Electrical Machines and Drives, 1997 Eighth International Conference on (Conf. Publ. No. 444)*, 1997, pp. 133-137.

[52] J. W. Bennett, B. C. Mecrow, A. G. Jack, D. J. Atkinson, S. Sheldon, B. Cooper*, et al.*, "A prototype electrical actuator for aircraft flaps and slats," in *Electric Machines and Drives, 2005 IEEE International Conference on*, 2005, pp. 41-47.

[53] G. J. Atkinson, B. C. Mecrow, A. G. Jack, D. J. Atkinson, P. Sangha, and M. Benarous, "The Analysis of Losses in High-Power Fault-Tolerant Machines for Aerospace Applications," *Industry Applications, IEEE Transactions on,* vol. 42, pp. 1162-1170, 2006.

[54] G.J.Atkinson, "High power fault tolerant motors for aerospace applications," 2007.

[55] G. J. Atkinson, J. W. Bennett, B. C. Mecrow, D. J. Atkinson, A. G. Jack, and V. Pickert, "Fault tolerant drives for aerospace applications," in *Integrated Power Electronics Systems (CIPS), 2010 6th International Conference on*, 2010, pp. 1-7.

[56] J. Dusek, P. Arumugam, T. Hamiti, and C. Gerada, "Selection of slot-pole combination of permanent magnet machines for aircraft actuation," in *Electrical Systems for Aircraft, Railway, Ship Propulsion and Road Vehicles (ESARS), 2015 International Conference on*, 2015, pp. 1-5.

[57] P. E. Kakosimos, A. G. Sarigiannidis, M. E. Beniakar, A. G. Kladas, and C. Gerada, "Induction Motors Versus Permanent-Magnet Actuators for Aerospace Applications," *Industrial Electronics, IEEE Transactions on,* vol. 61, pp. 4315-4325, 2014.

[58] M. Galea, Z. Xu, C. Tighe, T. Hamiti, C. Gerada, and S. Pickering, "Development of an aircraft wheel actuator for green taxiing," in *Electrical Machines (ICEM), 2014 International Conference on*, 2014, pp. 2492-2498.

[59] M. Villani, M. Tursini, G. Fabri, and L. Castellini, "High Reliability Permanent Magnet Brushless Motor Drive for Aircraft Application," *Industrial Electronics, IEEE Transactions on,* vol. 59, pp. 2073-2081, 2012.

[60] E. Richter, "High temperature, lightweight, switched reluctance motors and generators for future aircraft engine applications," in *American Control Conference*, 1988, pp. 1846-1851.

[61] E. Richter, A. V. E. Ferreira, and C. Ruckstader, "An Integrated Electrical Starter/Generator System for Gas-Turbine Application, Design and Test Results "," in *Proc. ICEM*, 1994, pp. 286-291.

[62] E. Richter, "Switched reluctance machines for high performance operations in a harsh environment-a review paper," in *Proc. ICEM Conf*, 1990, pp. 18-24.

[63] M. Villani, M. Tursini, G. Fabri, and L. Di Leonardo, "A switched-reluctance motor for aerospace application," in *Electrical Machines (ICEM), 2014 International Conference on*, 2014, pp. 2073-2079.

[64] S. P. McDonald, G. J. Atkinson, D. J. B. Smith, and S. Ullah, "Overcoming the challenges of drag torque in a dual-lane actuator for an aircraft," in *Electrical Machines (ICEM), 2014 International Conference on*, 2014, pp. 2120-2126.

[65] B. C. Mecrow, A. G. Jack, D. J. Atkinson, S. Green, G. J. Atkinson, A. King*, et al.*, "Design and testing of a 4 phase fault tolerant permanent magnet machine for an engine fuel pump," in *Electric Machines and Drives Conference, 2003. IEMDC'03. IEEE International*, 2003, pp. 1301-1307 vol.2.

[66] A. V. Radun, C. A. Ferreira, and E. Richter, "Two channel switched reluctance starter/generator results," in *Applied Power Electronics Conference and Exposition, 1997. APEC '97 Conference Proceedings 1997., Twelfth Annual*, 1997, pp. 546-552 vol.1.

[67] M. Ruba, I. Bentia, and L. Szabo, "Novel modular fault tolerant switched reluctance machine for reliable factory automation systems," in *Automation Quality and Testing Robotics (AQTR), 2010 IEEE International Conference on*, 2010, pp. 1-6.

[68] http://www.arnoldmagnetics.com/uploadedFiles/Products/Samarium_Cobalt/Recoma_Grade_pdfs/Recoma%2033E%20-%20130911.pdf.

[69] J. Pyrhonen, *Design of Rotating Electrical Machine*, 2nd Edition ed.: John Wiley & Sons, 2014.

[70] P. A. Hargreaves, B. C. Mecrow, and R. Hall, "Calculation of Iron Loss in Electrical Generators Using Finite-Element Analysis," *Industry Applications, IEEE Transactions on,* vol. 48, pp. 1460-1466, 2012.

[71] C. R. Sullivan, "Computationally efficient winding loss calculation with multiple windings, arbitrary waveforms, and two-dimensional or three-dimensional field geometry," *Power Electronics, IEEE Transactions on,* vol. 16, pp. 142-150, 2001.

[72] https://www.hoganas.com/globalassets/media/sharepoint-documents/BrochuresanddatasheetsAllDocuments/Somaloy_Technology.pdf. *Somaloy® Technology*.

[73] J. D. Pollock, W. Lundquist, and C. R. Sullivan, "Predicting inductance roll-off with dc excitations," in *Energy Conversion Congress and Exposition (ECCE), 2011 IEEE*, 2011, pp. 2139-2145.

[74] J. W. Bennett, B. C. Mecrow, D. J. Atkinson, C. Maxwell, and M. Benarous, "Fault-tolerant electric drive for an aircraft nose wheel steering actuator," *IET Electrical Systems in Transportation,* vol. 1, pp. 117-125, 2011.

[75] J. D. Widmer, C. M. Spargo, G. J. Atkinson, and B. C. Mecrow, "Solar Plane Propulsion Motors With Precompressed Aluminum Stator Windings," *Energy Conversion, IEEE Transactions on,* vol. 29, pp. 681-688, 2014.

[76] http://www.vacuumschmelze.com/index.php?id=126&L=2. *cobalt steel*

Appendix 1

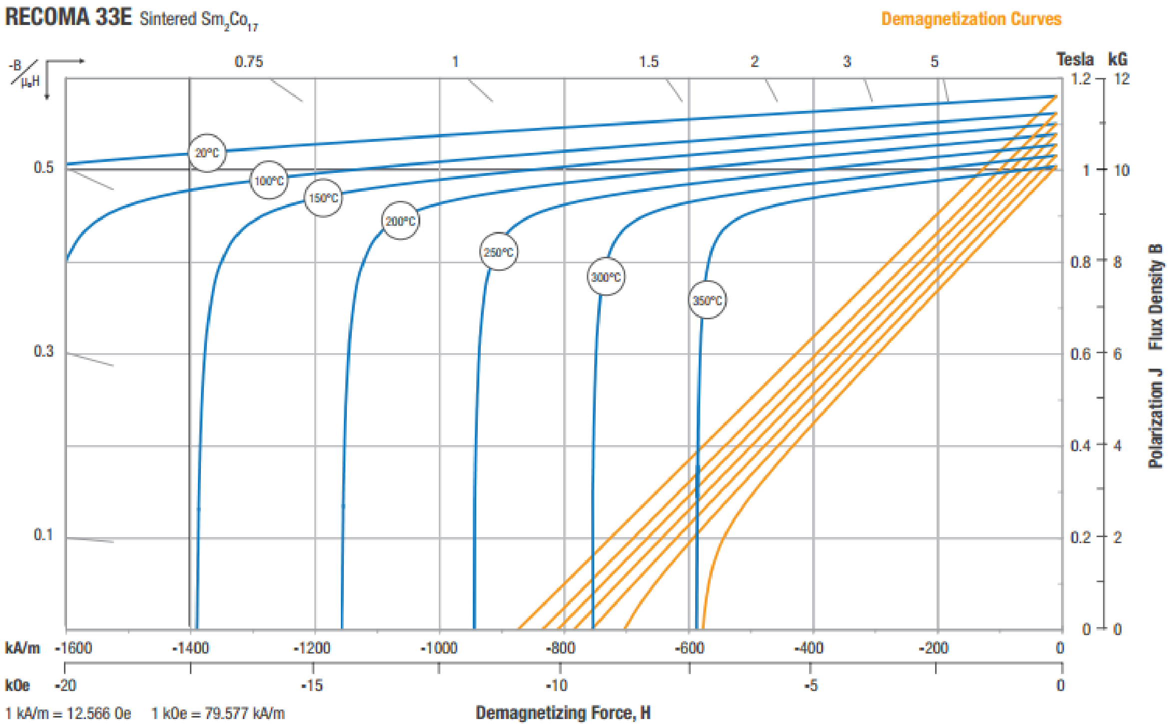

Recomma 33E magnetic properties

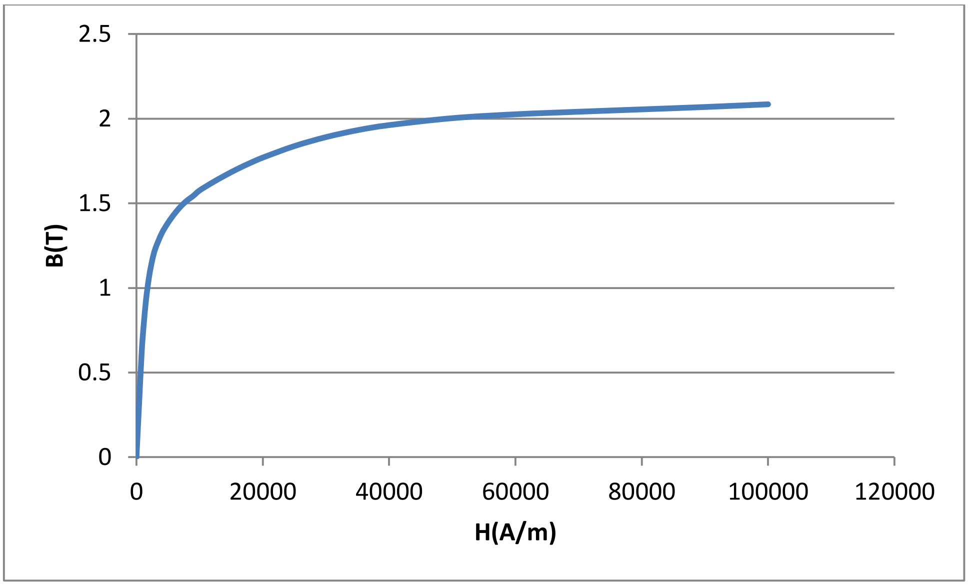

B-H curve of SMC material

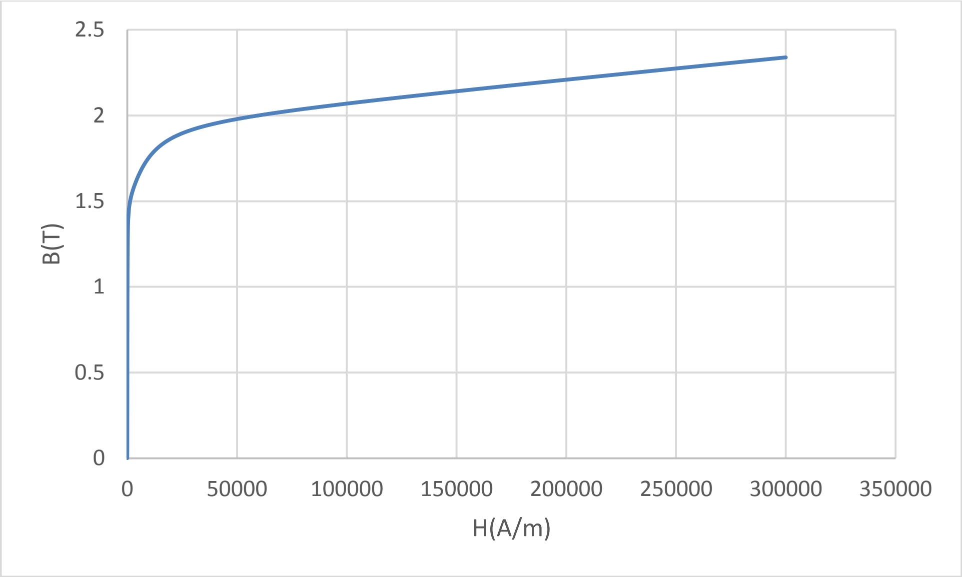

B-H curve of thin non-oriented silicon steel (N020) material

Appendix 2

MSSRM drawings

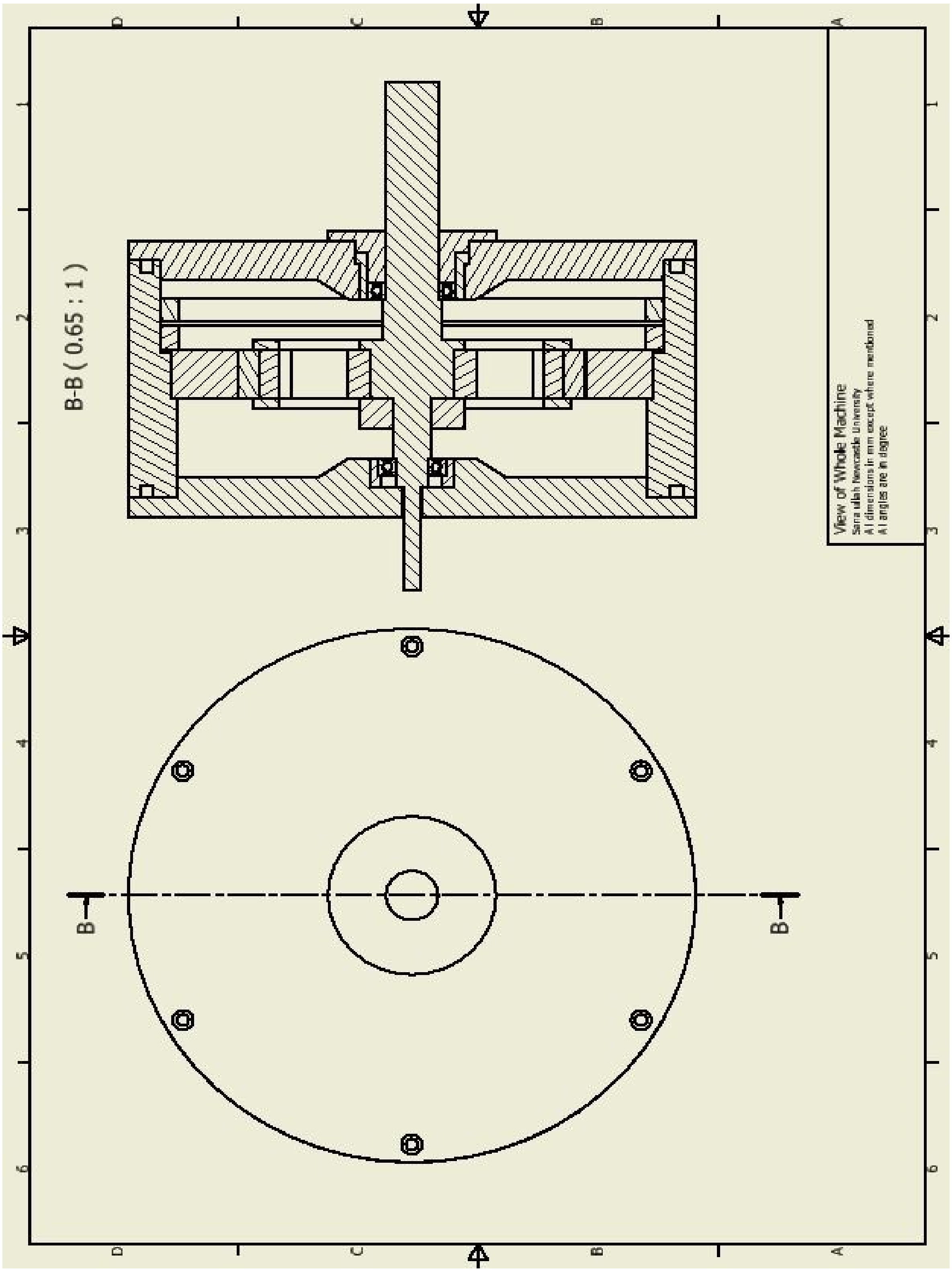

Full machine

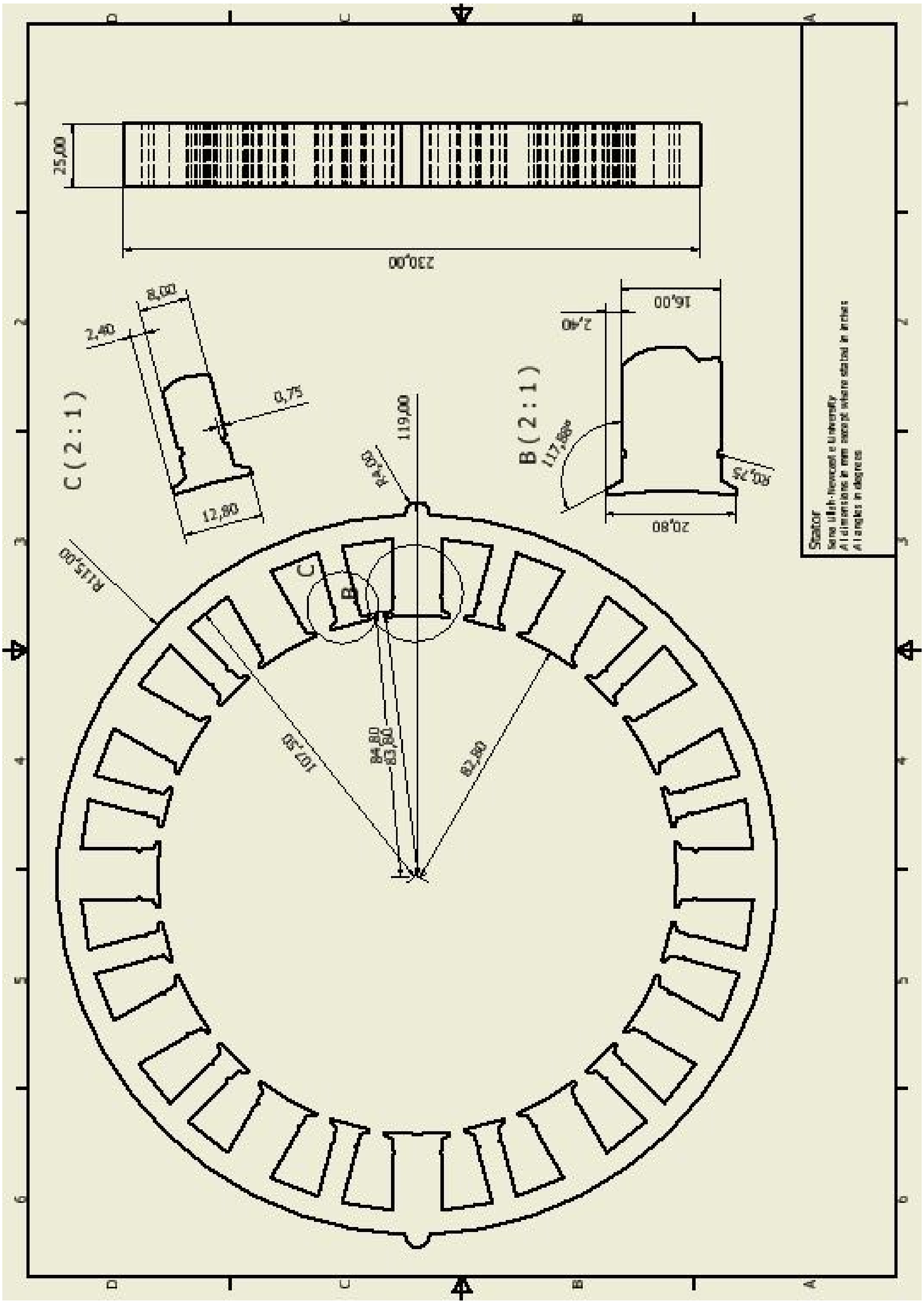
25,00
230,00
8,00
2,40
0,75
12,80
C (2 : 1)
16,00
2,40
B (2 : 1)
117,88°
R0,75
20,80
119,00
R4,00
R115,00
C
B
107,30
84,80
83,60
82,80
Stator

Stator

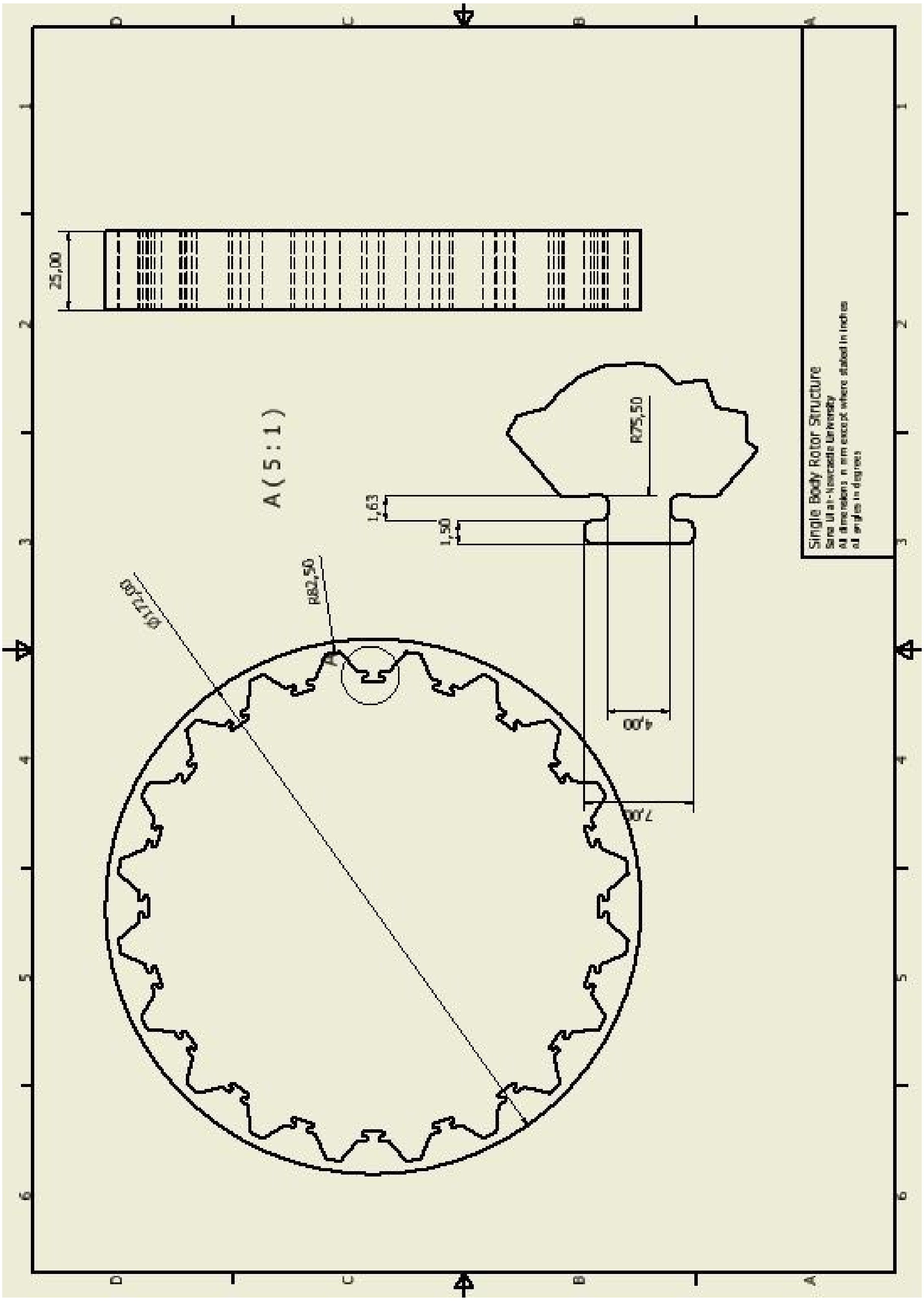

Rotor Single block

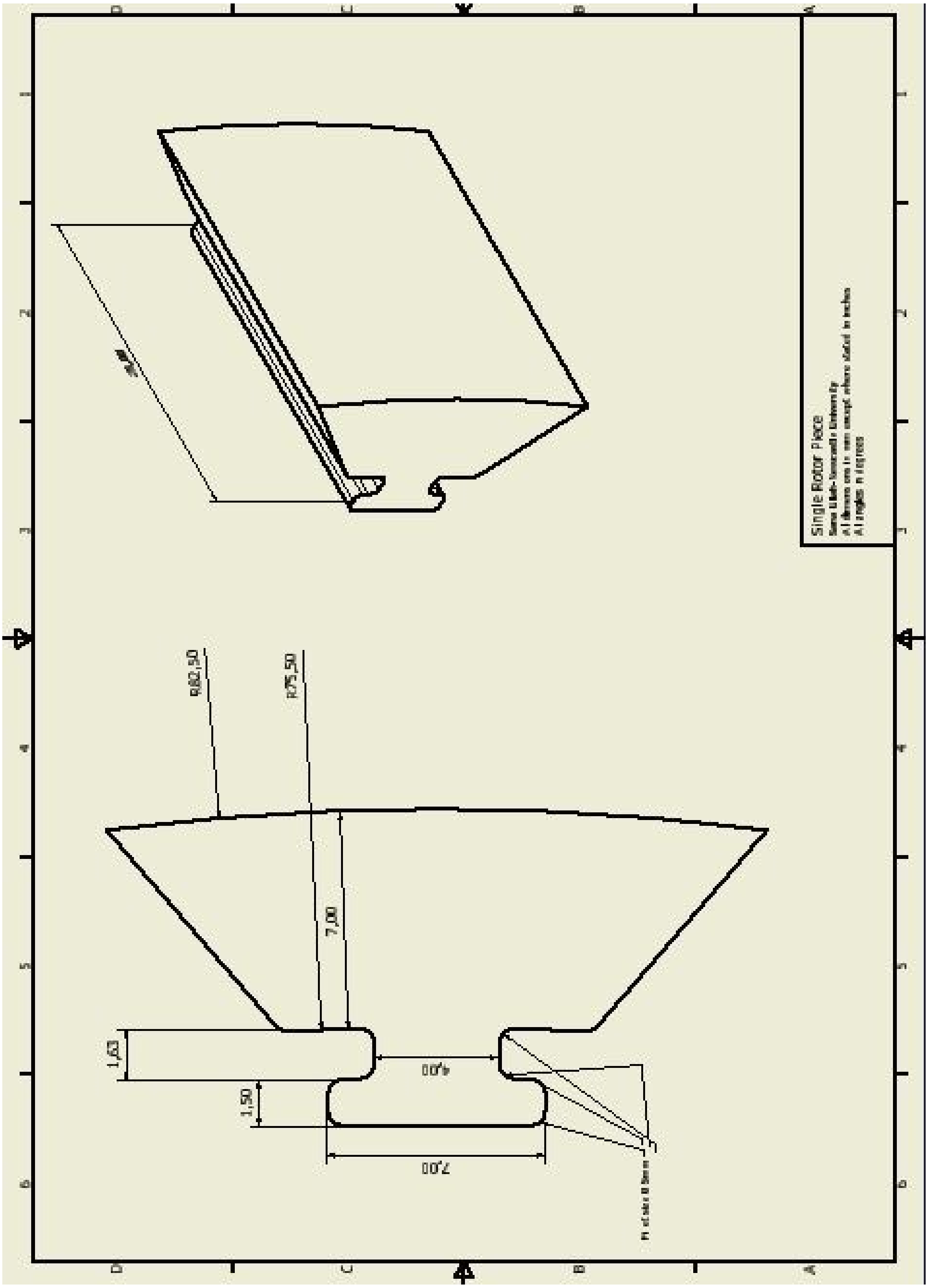

Rotor single segment

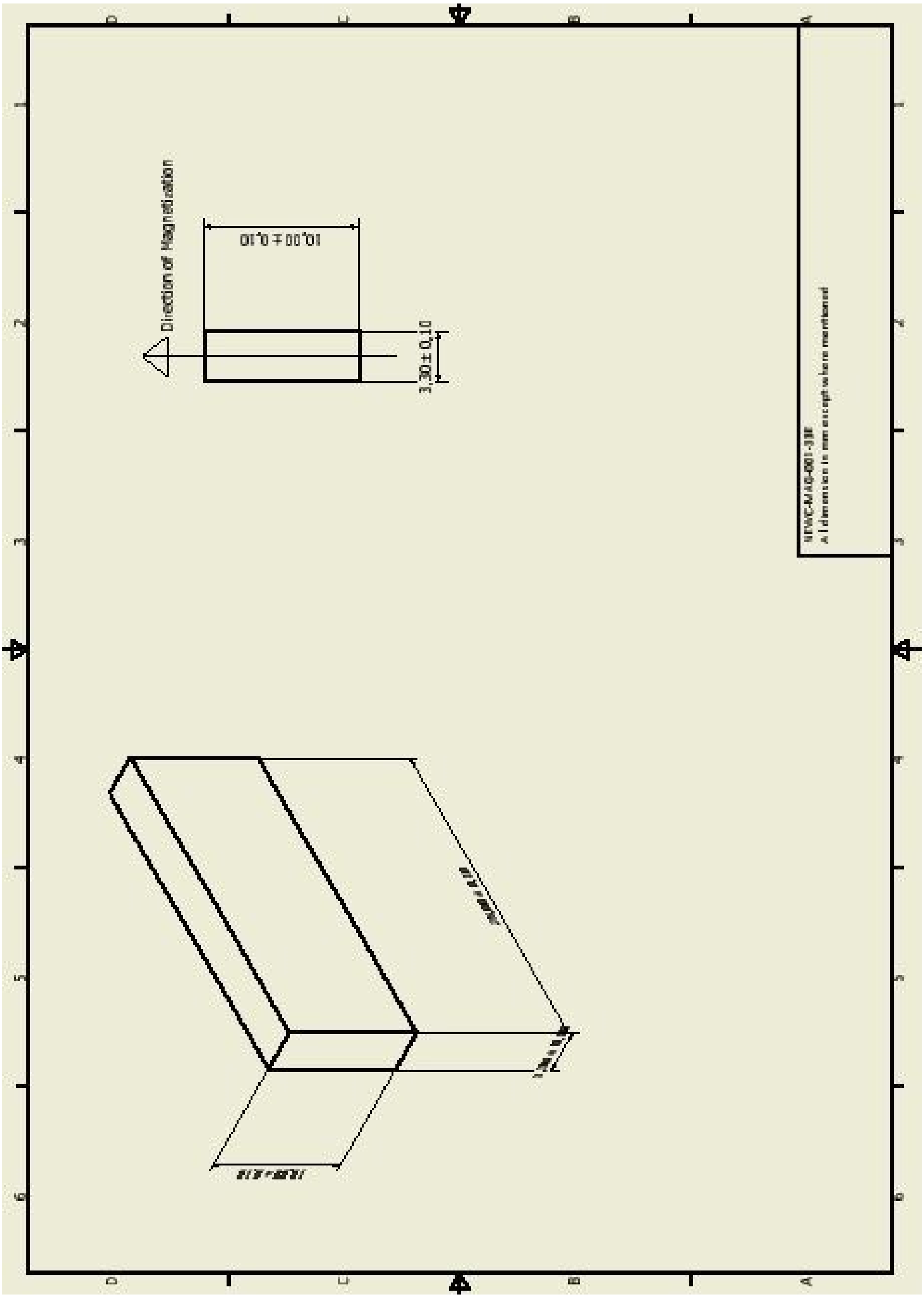

Magnet dimensions and direction of magnetization

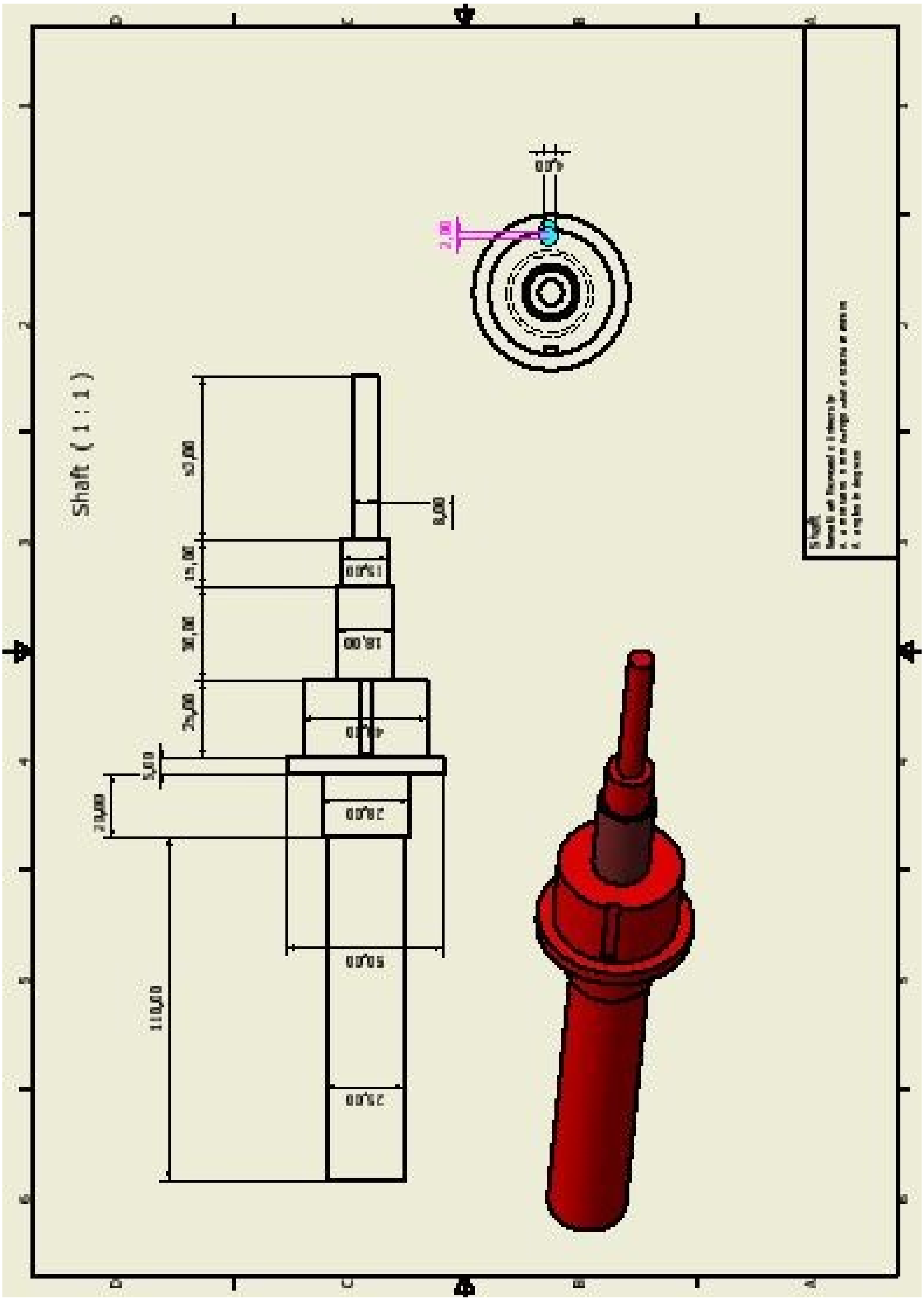
Shaft (1 : 1)
52,00
15,00
30,00
24,00
5,00
20,00
110,00
8,00
15,00
18,00
40,00
28,00
50,00
25,00
4,00
2,00

Rotor Shaft

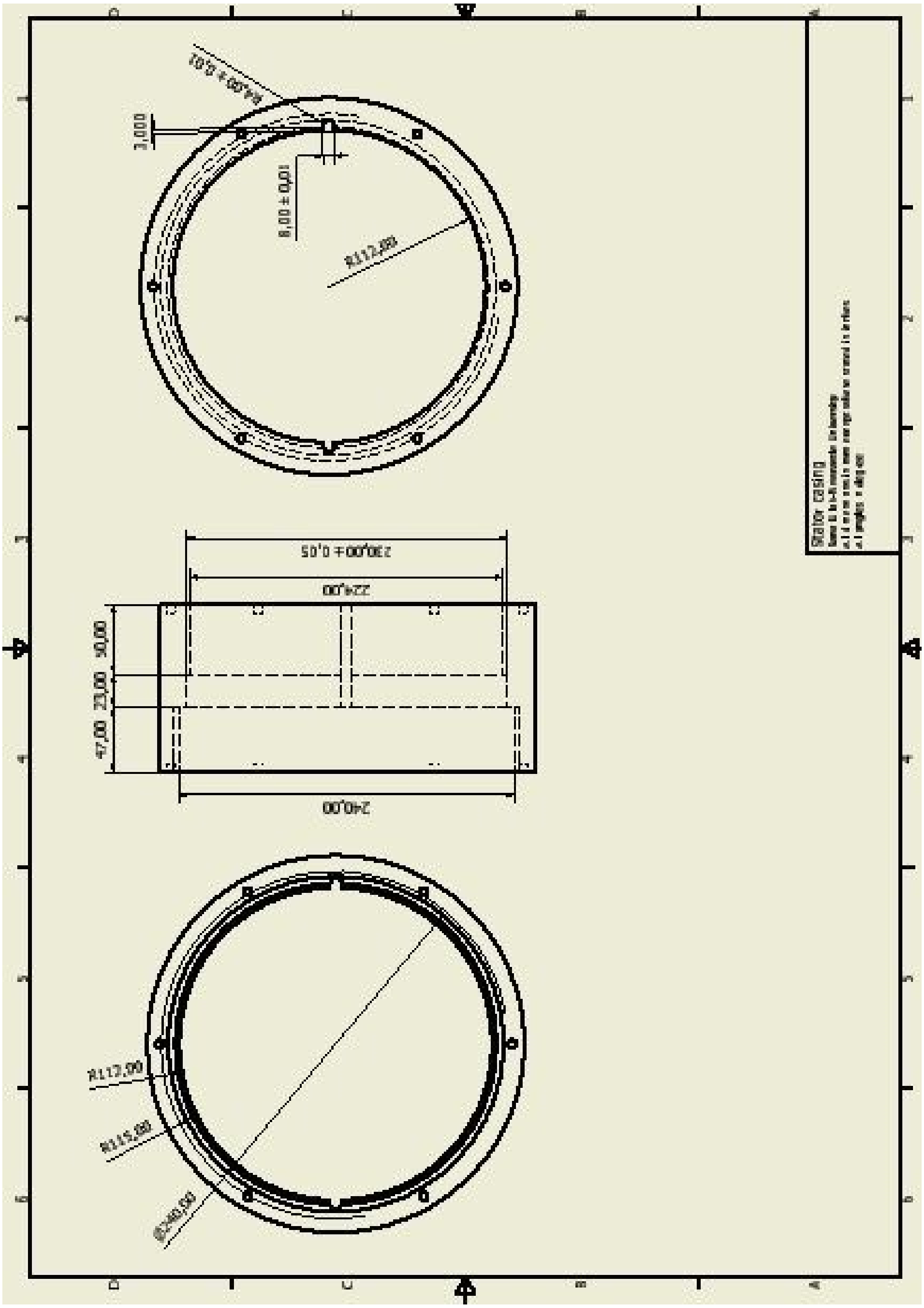

Stator casing

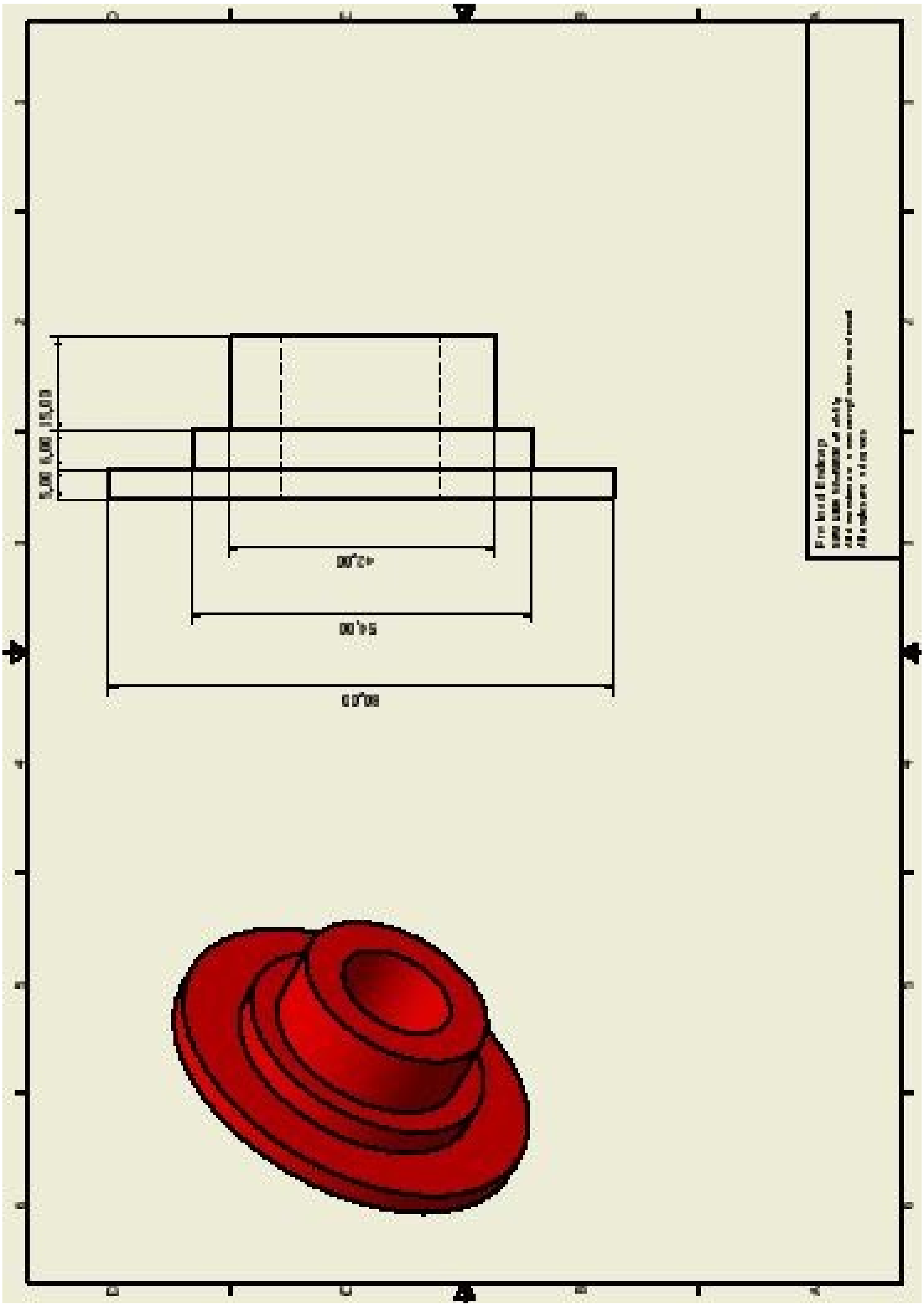

Pre load ring

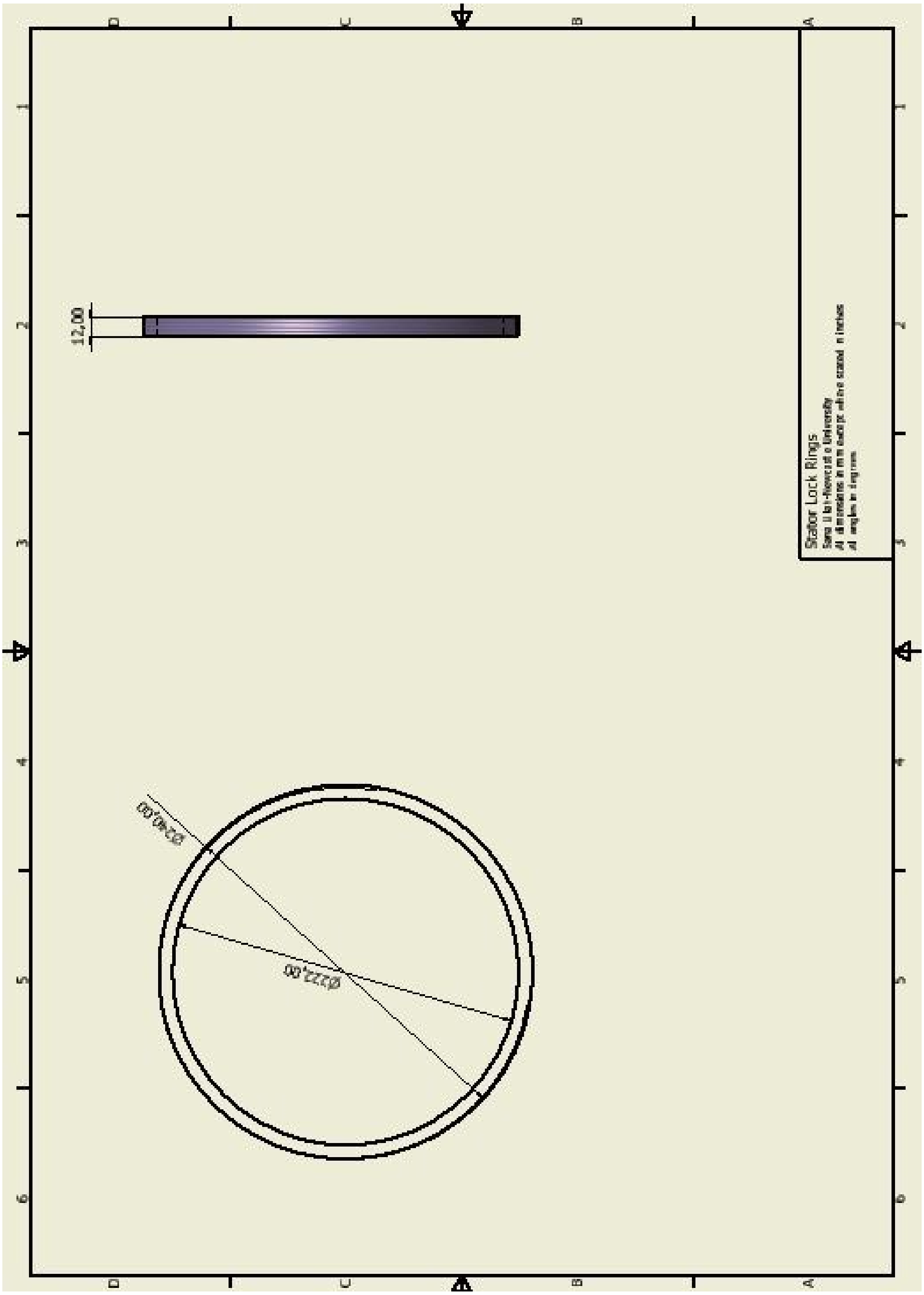

Stator lock ring

Appendix 3

Stator drawings

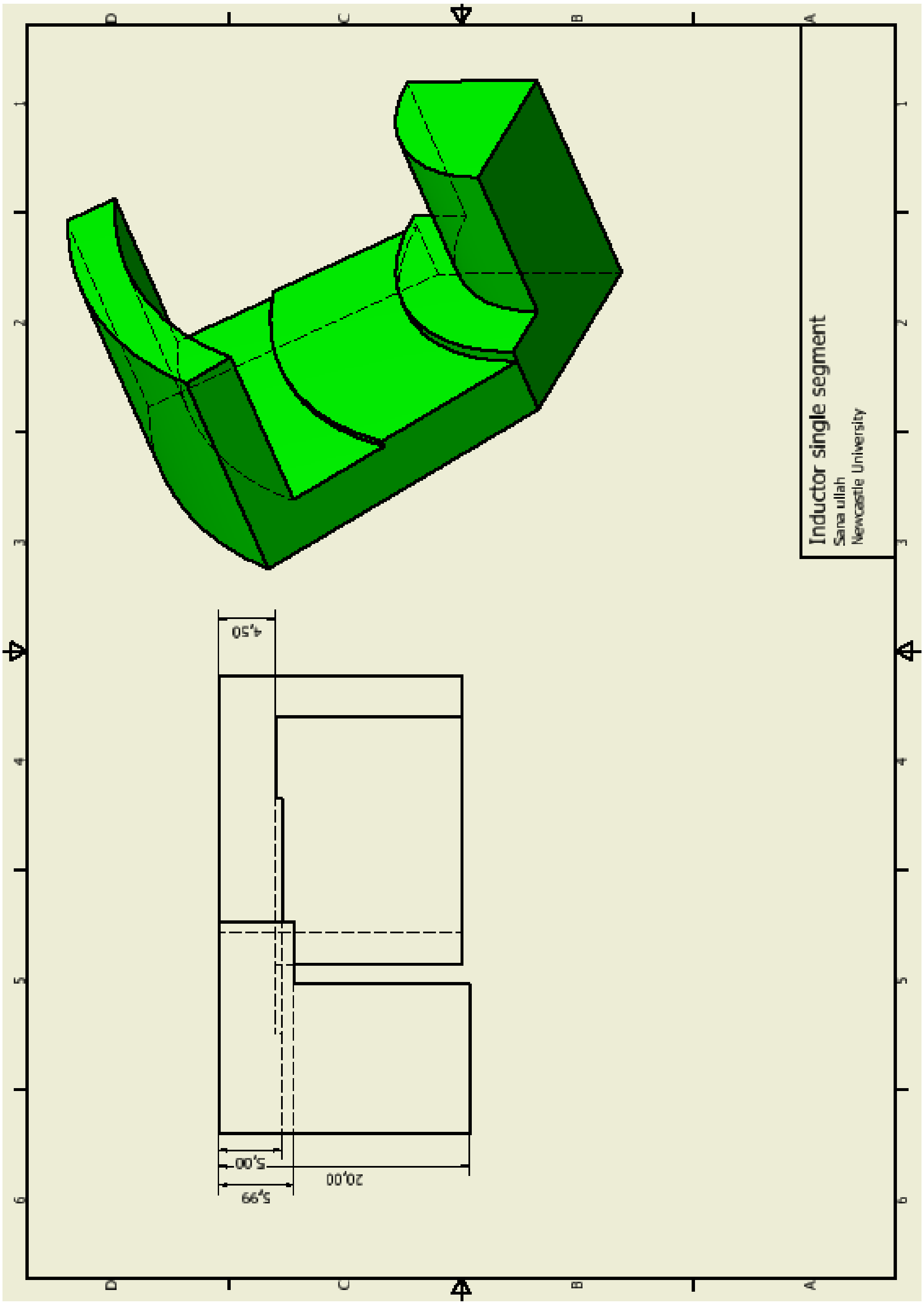

Inductor single segment

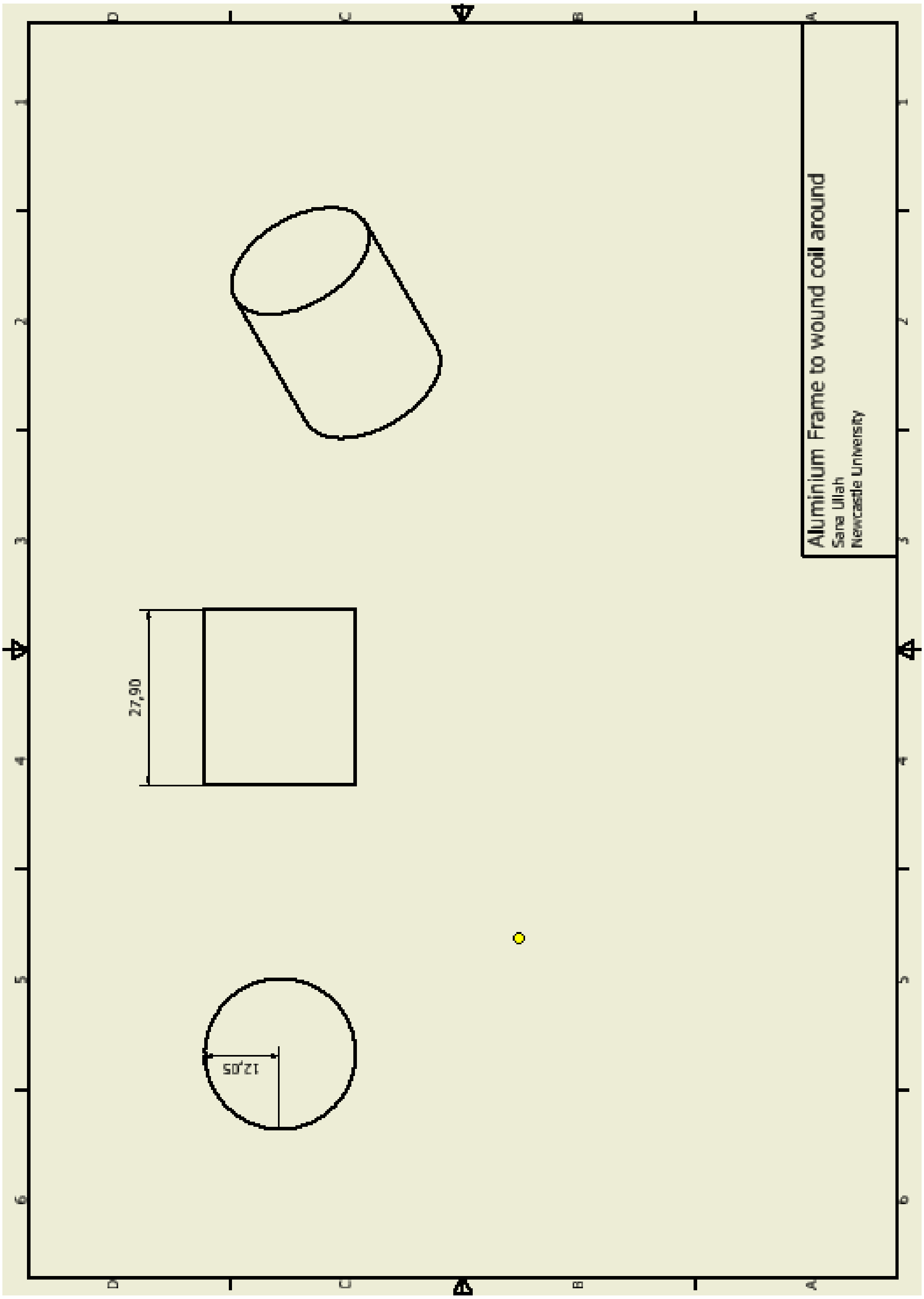

Aluminium block to wound coil around

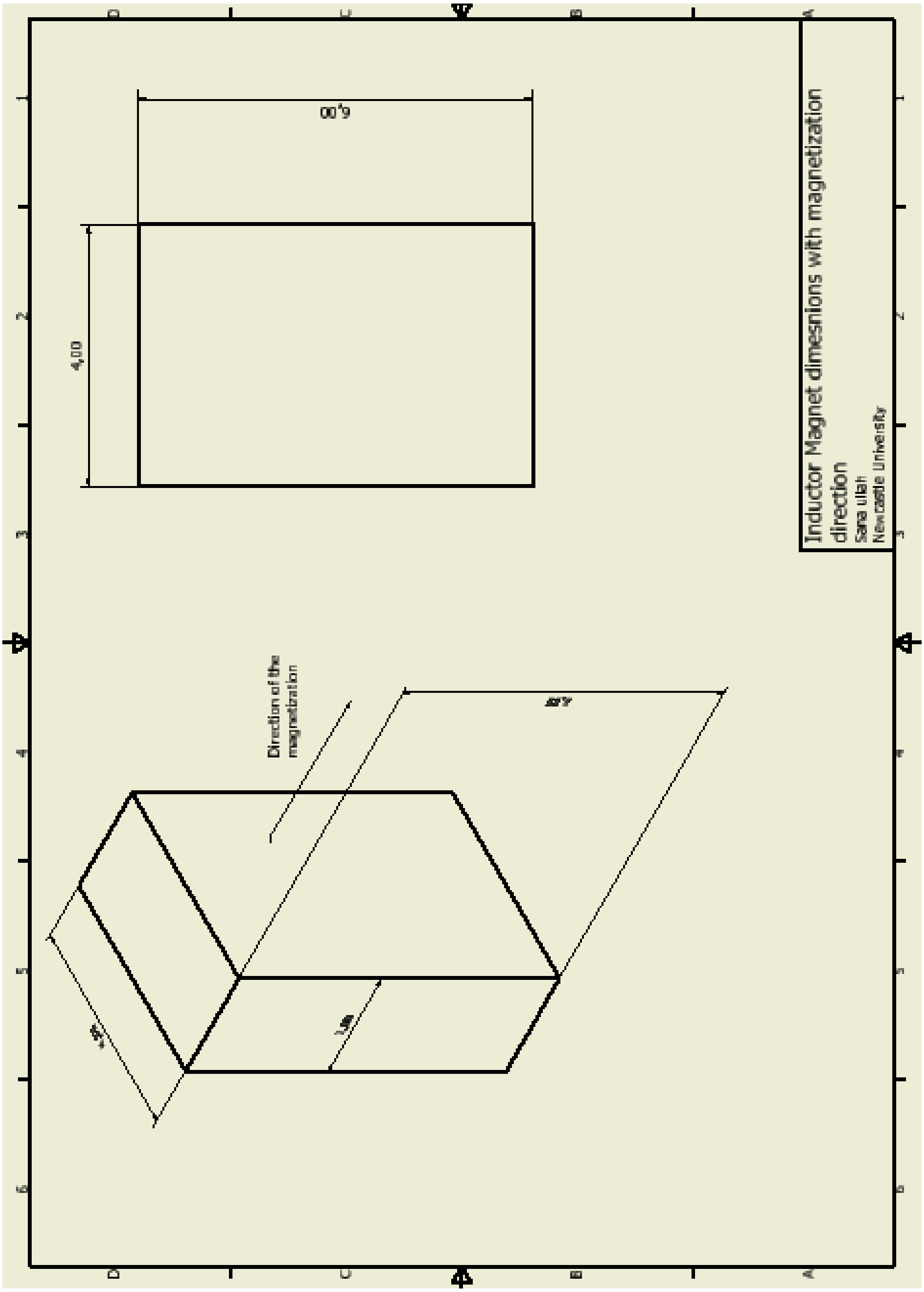

Inductor magnet dimensions with magnetization directions